



HELLENIC REPUBLIC

**National and Kapodistrian
University of Athens**

— EST. 1837 —

MEDICAL PHYSICS LABORATORY - MEDICAL SCHOOL

**Development of quality control protocol and software tool for
the correction of geometric distortions and signal
inhomogeneities in magnetic resonance images**

Eleftherios P. Pappas

PhD Thesis

Supervisors: Evangelos Georgiou

Pantelis Karaiskos

Ioannis Seimenis

Η παρούσα διδακτορική διατριβή εκπονήθηκε υπό τον ελληνικό τίτλο «Ανάπτυξη πρωτοκόλλου ποιοτικού ελέγχου και λογισμικού εργαλείου για τη διόρθωση χωρικών σφαλμάτων και ανομοιογενειών σήματος σε εικόνες μαγνητικής τομογραφίας», στο Εργαστήριο Ιατρικής Φυσικής της Ιατρικής Σχολής του Εθνικού και Καποδιστριακού Πανεπιστημίου Αθηνών.

ATHENS 2018

Ευχαριστίες

Η παρούσα διατριβή εκπονήθηκε στο Εργαστήριο Ιατρικής Φυσικής της Ιατρικής Σχολής του Εθνικού και Καποδιστριακού Πανεπιστημίου Αθηνών. Καθ' όλη τη διάρκεια εκπόνησής της είχα την ευκαιρία και την τύχη να γνωρίσω και να συνεργαστώ με πολλούς ανθρώπους, η συμβολή και η συμπαράσταση των οποίων τόσο σε επιστημονικό όσο και σε προσωπικό επίπεδο ήταν καθοριστικές. Μου είναι πλέον ξεκάθαρο ότι σε αυτό το ταξίδι απέκτησα μεν γνώση, αλλά απέκτησα και φίλους...

Υπό αυτό το πρίσμα, ευχαριστώ θερμά τον Καθηγητή κ. Ευάγγελο Γεωργίου, Διευθυντή του Εργαστηρίου Ιατρικής Φυσικής και κύριο επιβλέποντα της διατριβής, ο οποίος συνέβαλε αποφασιστικά στην προσπάθειά μου για ολοκλήρωση της παρούσας διατριβής και εξασφάλισε ένα άρτιο και δημιουργικό περιβάλλον, αναγκαία συνθήκη για την επιτυχή ολοκλήρωση μιας ερευνητικής προσπάθειας.

Μία ιδιαίτερη και εκ βάθέως ευχαριστία οφείλω στον Καθηγητή κ. Παντελή Καραϊσκό τόσο για την ανάθεση του θέματος και την εμπιστοσύνη που έδειξε στο πρόσωπό μου από την πρώτη κιόλας στιγμή, όσο και τη μόνιμη καθοδήγηση που μου προσέφερε. Δεν αποτέλεσε απλώς την επιστημονική πυξίδα που πάντα συμβουλευόμουν, αλλά ανέλαβε και στο αkéραιο την ευθύνη της χάραξης, επίβλεψης και καθοδήγησης στην εκπόνηση της διατριβής αυτής.

Βαθιά ευγνωμοσύνη θα ήθελα να εκφράσω και στον Καθηγητή του Δημοκρίτειου Πανεπιστημίου Θράκης, κ. Ιωάννη Σεϊμένη και να τον ευχαριστήσω θερμά για τη συνεχή καθοδήγησή του, την άψογη συνεργασία μας και την αμέριστη συμπαράσταση και βοήθεια που μου προσέφερε, καθώς και τις πολύ ενδιαφέρουσες συζητήσεις μας.

Ένα πολύ μεγάλο και ειλικρινές ευχαριστώ θα ήθελα επίσης να εκφράσω προς τα «τέταρτα μέλη» της τριμελούς επιτροπής μου, Αναπληρωτή Καθηγητή κ. Παναγιώτη Παπαγιάννη και Επίκουρο Καθηγητή κ. Ευάγγελο Παντελή. Η ενθάρρυνση, η συμβολή τους και η επιστημονική τους αρτιότητα συνέβαλαν τα μέγιστα στην εκπόνηση της παρούσας διατριβής. Επιπλέον, η καθημερινή μας αλληλεπίδραση απέδωσε

επιστημονικούς καρπούς οι οποίοι δεν εντάσσονται μόνο στα πλαίσια της παρούσας εργασίας, κάτι για το οποίο είμαι διπλά ευγνώμων.

Ευχαριστώ θερμά τον Επίκουρο Καθηγητή κ. Κωνσταντίνο Λουκά για τη διαρκή υποστήριξή του, τις χρήσιμες συζητήσεις μας και την άψογη συνεργασία μας στη διάρκεια όλων αυτών των ετών.

Ευχαριστώ θερμά, επίσης, τον Επίκουρο Καθηγητή κ. Βασίλειο Κουτουλίδη για την αποδοχή της συμμετοχής του στην κρίση της εργασίας μου και το χρόνο που αφιέρωσε στο σκοπό αυτό.

Η πυραμίδα είχε τα πιο γερά θεμέλια! Είχα την τύχη να γνωρίσω και να συνεργαστώ με υποψήφιους διδάκτορες και μεταδιδάκτορες που έβαλαν ανεξίτηλα τη σφραγίδα τους στην προσπάθεια εκπόνησης της εργασίας αυτής αλλά και στη διαμόρφωση του τρόπου σκέψης μου. Ειδικότερα, θα ήθελα να ευχαριστήσω τον Δρ Αργύρη Μουτσάτσο (γνωστό και ως «μέντορά μου») τόσο για τη μύησή μου στο θέμα όσο και την επιστημονική του καθοδήγηση και υπομονή του στα πρώτα βήματα της προσπάθειάς μου. Ευχαριστώ επίσης τη Δρ Βασιλική Πέππα (γνωστή και ως «διπλανή μου») για τις κυριολεκτικά χιλιάδες ώρες συζητήσεων, τις πολύτιμες συμβουλές και ιδέες της, καθώς και την άψογη πολύ-επίπεδη συνεργασία μας. Οφείλω ακόμη να ευχαριστήσω τους Δρ Κυβέλη Ζουράρη, Δρ Βασίλη Λαχανά και Δρ Λουκά Πετροκόκκινο για τη διαρκή συμπαράσταση και ενθάρρυνσή τους, καθώς και τις πολύτιμες συμβουλές τους. Τέλος, ένα ιδιαίτερο ευχαριστώ στον υποψήφιο διδάκτορα Μάνο Ζώρο για τη συνεργασία μας και την πολύ σημαντική συμβολή, υποδείξεις και βοήθειά του, αλλά και την υπομονή του σε μερικές περιπτώσεις.

Τέλος, ένα βαθύτατα ειλικρινές ευχαριστώ οφείλω στον αδερφό μου, Θεοχάρη, όχι μόνο για την ηθική του υποστήριξη όλα αυτά τα χρόνια, αλλά και για την τεχνική βοήθεια που προσέφερε χωρίς δισταγμό όποτε αυτό του ζητήθηκε.

Publications in international peer-reviewed journals

1. **Pappas EP**, Seimenis I, Dellios D, Kollias G, Lampropoulos KI, Karaiskos P. Assessment of sequence dependent geometric distortion in contrast-enhanced MR images employed in stereotactic radiosurgery treatment planning. *Phys Med Biol.* under review, 2018
2. **Pappas EP**, Peppas V, Hourdakis CJ, Karaiskos P, Papagiannis P. On the use of a novel Ferrous Xylenol-orange gelatin dosimeter for HDR brachytherapy commissioning and quality assurance testing. *Phys Medica.* 2018;45:162-169. [doi:10.1016/j.ejmp.2017.12.015](https://doi.org/10.1016/j.ejmp.2017.12.015).
3. **Pappas EP**, Zoros E, Moutsatsos A, Peppas V, Zourari K, Karaiskos P, Papagiannis P. On the experimental validation of model-based dose calculation algorithms for 192 Ir HDR brachytherapy treatment planning. *Phys Med Biol.* 2017;62(10):4160-4182. [doi:10.1088/1361-6560/aa6a01](https://doi.org/10.1088/1361-6560/aa6a01).
4. **Pappas EP**, Alshantiry M, Moutsatsos A, Lababidi H, Khalid A, Georgiou K, Karaiskos P, Georgiou E. MRI-Related Geometric Distortions in Stereotactic Radiotherapy Treatment Planning: Evaluation and Dosimetric Impact. *Technol Cancer Res Treat.* 2017;16(6):1120-1129. [doi:10.1177/1533034617735454](https://doi.org/10.1177/1533034617735454).
5. Peppas V, **Pappas EP**, Karaiskos P, Papagiannis P. Time resolved dose rate distributions in brachytherapy. *Phys Medica.* 2017;41:13-19. [doi:10.1016/j.ejmp.2017.04.013](https://doi.org/10.1016/j.ejmp.2017.04.013).
6. Zoros E, Moutsatsos A, **Pappas EP**, Georgiou E, Kollias G, Karaiskos P, Pantelis E. Monte Carlo and experimental determination of correction factors for gamma knife perfexion small field dosimetry measurements. *Phys Med Biol.* 2017;62(18):7532-7555. [doi:10.1088/1361-6560/aa8590](https://doi.org/10.1088/1361-6560/aa8590).
7. **Pappas EP**, Seimenis I, Moutsatsos A, Georgiou E, Nomikos P, Karaiskos P. Characterization of system-related geometric distortions in MR images

- employed in Gamma Knife radiosurgery applications. *Phys Med Biol.* 2016;61(19):6993-7011. [doi:10.1088/0031-9155/61/19/6993](https://doi.org/10.1088/0031-9155/61/19/6993).
8. **Pappas EP**, Moutsatsos A, Pantelis E, Zoros E, Georgiou E, Torrens M, Karaiskos P. On the development of a comprehensive MC simulation model for the Gamma Knife Perfexion radiosurgery unit. *Phys Med Biol.* 2016;61(3):1182-1203. [doi:10.1088/0031-9155/61/3/1182](https://doi.org/10.1088/0031-9155/61/3/1182).
 9. Peppas V, **Pappas E**, Major T, Takácsi-Nagy Z, Pantelis E, Papagiannis P. On the impact of improved dosimetric accuracy on head and neck high dose rate brachytherapy. *Radiother Oncol.* 2016;120(1):92-97. [doi:10.1016/j.radonc.2016.01.022](https://doi.org/10.1016/j.radonc.2016.01.022).
 10. Peppas V, **Pappas EP**, Karaiskos P, Major T, Polgár C, Papagiannis P. Dosimetric and radiobiological comparison of TG-43 and Monte Carlo calculations in ¹⁹²Ir breast brachytherapy applications. *Phys Medica.* 2016;32(10):1245-1251. [doi:10.1016/j.ejmp.2016.09.020](https://doi.org/10.1016/j.ejmp.2016.09.020).
 11. Peppas V, Pantelis E, **Pappas E**, Lahanas V, Loukas C, Papagiannis P. A user-oriented procedure for the commissioning and quality assurance testing of treatment planning system dosimetry in high-dose-rate brachytherapy. *Brachytherapy.* 2016;15(2):252-262. [doi:10.1016/j.brachy.2015.11.001](https://doi.org/10.1016/j.brachy.2015.11.001).
 12. Pantelis E, Peppas V, Lahanas V, **Pappas E**, Papagiannis P. BrachyGuide: A brachytherapy-dedicated DICOM RT viewer and interface to Monte Carlo simulation software. *J Appl Clin Med Phys.* 2015;16(1):208-218. [doi:10.1120/jacmp.v16i1.5136](https://doi.org/10.1120/jacmp.v16i1.5136).
 13. Karaiskos P, Moutsatsos A, **Pappas E**, Georgiou E, Roussakis A, Torrens M, Seimenis I. A simple and efficient methodology to improve geometric accuracy in gamma knife radiation surgery: Implementation in multiple brain metastases. *Int J Radiat Oncol Biol Phys.* 2014;90(5):1234-1241. [doi:10.1016/j.ijrobp.2014.08.349](https://doi.org/10.1016/j.ijrobp.2014.08.349).

Conference papers in peer-reviewed journals

1. **Pappas EP**, Dellios D, Seimenis I, Moutsatsos A, Georgiou E, Karaiskos P. Review and comparison of geometric distortion correction schemes in MR images used in stereotactic radiosurgery applications. *J Phys Conf Ser.* 2017;931:12031. [doi:10.1088/1742-6596/931/1/012031](https://doi.org/10.1088/1742-6596/931/1/012031).

Announcements at international peer-reviewed conferences

1. **E P Pappas**, D N Makris, E Zoros, G Kalaitzakis, T Boursianis, N Papanikolaou, C J Hourdakakis, K Zourari, V Lahanas, T G Maris, E Efstathopoulos, E Pappas, “*Personalized End-to-End QA in cranial SRS: evaluation of the phantom-to-patient dosimetric equivalency of a 3D printed phantom using film dosimetry*”, submitted for presentation at ASTRO annual meeting 2018, October 21 – 24, San Antonio, Texas, USA
2. **E P Pappas**, E Zoros, G Anagnostopoulos, G Antorkas, E Pantelis, P Karaiskos, “*Multi-detector dosimetry for QA in advanced radiotherapy modalities: a comparative study*”, ESTRO 37 (2018), April 20 – 24, Barcelona, Spain
3. **E P Pappas**, D Dellios, I Seimenis, A Moutsatsos, E Georgiou and P Karaiskos, “*Review and comparison of geometric distortion correction schemes in MR images used in stereotactic radiosurgery applications*”, BIOMEPP 2017, October 12 – 13, Athens Greece
4. A Logothetis, **E P Pappas**, E Zoros, E Pantelis, A Dimitriadis, I Paddick and P Karaiskos, “*Development of a Phase Space source model for Monte Carlo dosimetry in Gamma Knife applications*”, BIOMEPP 2017, October 12 – 13, Athens, Greece
5. A Logothetis, E Zoros, **E P Pappas**, E Pantelis, A Dimitriadis, I Paddick and P Karaiskos, “*Dosimetric validation of the Convolution and TMR 10 dose algorithms of the GammaPlan treatment planning system*”, BIOMEPP 2017, October 12 – 13, Athens, Greece
6. C Hourdakakis, K Zourari, Z Thrapsanioti, E Pantelis, C Antypas, P Pantelakos, E Zoros, D Makris, **E P Pappas**, E Pappas, “*End-to-end audit tests for advanced radiotherapy treatment modalities involving patient-specific 3D dosimetry phantoms*”, International Conference on Advances in Radiation Oncology (ICARO2) 2017, June 20 – 23, Vienna, Austria

7. **E P Pappas**, I Seimenis, D Dellios, A Moutsatsos, E Georgiou, P Karaiskos, *“Efficacy of vendor supplied distortion correction algorithms for a variety of MRI scanners”*, ESTRO 36 (2017), May 5 – 9, Vienna, Austria
8. E Zoros, **E P Pappas**, K Zourari, E Pantelis, A Moutsatsos, G Kollias, C I Hourdakakis, P Karaiskos, *“Experimental determination of correction factors for reference dosimetry in Gamma Knife Perfexion”*, ESTRO 36 (2017), May 5 – 9, Vienna, Austria
9. **E P Pappas**, E Zoros, K Zourari, C I Hourdakakis, P Papagiannis, P Karaiskos, E Pantelis, *“Investigation of dose-rate dependence at an extensive range for PRESAGE radiochromic dosimeter”*, ESTRO 36 (2017), May 5 – 9, Vienna, Austria
10. M Hillbrand, G Landry, G Dedes, **E P Pappas**, G. Kalaitzakis, C Kurz, F Dörringer, K Kaiser, M Würfl, F Englbrecht, O Dietrich, D Makris, E Pappas, K Parodi, *“A 3D polymer gel dosimeter coupled to a patient-specific anthropomorphic phantom for proton therapy”*, ESTRO 36 (2017), May 5 – 9, Vienna, Austria
11. I Seimenis, **E P Pappas**, A Moutsatsos, E Georgiou, P Karaiskos, *“Estimation and correction of susceptibility related distortions in MRI”*, European Congress of Radiology (ECR) 2017, March 1 – 5, Vienna, Austria
12. V Peppas, **E Pappas**, P Karaiskos, P Papagiannis, *“On the use of time resolved dose rate distributions in brachytherapy”*, European Congress of Medical Physics (ECMP) 2016, September 1 – 4, Athens, Greece
13. L Petrokokkinos, A Moutsatsos, **E P Pappas**, I Seimenis, E Pantelis, P Karaiskos, P Papagiannis, *“Dosimetric comparison of 3D chemical dosimeters for use in modern RT/SRS quality assurance”*, European Congress of Medical Physics (ECMP) 2016, September 1 – 4, Athens, Greece
14. **E P Pappas**, I Seimenis, A Moutsatsos, E Zoros, E Georgiou, P Karaiskos, *“Evaluation and correction of patient-induced distortion in MR images used in stereotactic radiosurgery”*, European Congress of Medical Physics (ECMP) 2016, September 1 – 4, Athens, Greece

15. A Moutsatsos, E Pantelis, C Antypas, L Petrokokkinos, **E P Pappas**, E Zoros, P Pantelakos, E Georgiou, P Karaiskos, “*On the use of presage detectors for the dosimetry of helical tomotherapy small fields*”, European Congress of Medical Physics (ECMP) 2016, September 1 – 4, Athens, Greece
16. M Alshanjity, **E P Pappas**, P Karaiskos, A Moutsatsos, K Alsafi, H Lababidi, E Georgiou, “*Assessment of total geometric distortion in MR images used in intracranial stereotactic radiosurgery*”, European Congress of Medical Physics (ECMP) 2016, September 1 – 4, Athens, Greece
17. G Kalaitzakis, N Papanikolaou, T Boursianis, **E P Pappas**, V Lahanas, D Makris, S Stathakis, L Watts, E Efstathopoulos, T G Maris, E Pappas, “*A quality assurance test for the validation of the spatial and dosimetric accuracy of a new technique for the treatment of multiple brain metastases*”, European Congress of Medical Physics (ECMP) 2016, September 1 – 4, Athens, Greece
18. E Zoros, **E P Pappas**, A Moutsatsos, E Pantelis, C Paraskevopoulou, E Georgiou, P Karaiskos, “*Monte Carlo determination of correction factors for dosimetric measurements in gamma knife perfexion small fields*”, European Congress of Medical Physics (ECMP) 2016, September 1 – 4, Athens, Greece
19. G Prentou, **E Pappas**, E Koutsouveli, P Nomikos, E Georgiou, P Karaiskos, “*Geometric, DVH and plan quality differences induced from different patient image registration methods used in gamma knife applications*”, European Congress of Medical Physics (ECMP) 2016, September 1 – 4, Athens, Greece
20. P Papanikolaou, L Watts, **E Pappas**, G Kalaitzakis, T Maris, N Kirby, K Rasmussen, A Gutierrez, S Stathakis, “*Dosimetric Validation of Spatially Fractionated Radiotherapy Using Gel Dosimetry*”, American Association of Physicists in Medicine (AAPM) Annual Meeting 2016, July 30 – August 3, Denver, Colorado, USA
21. **E P Pappas**, N Papanikolaou, G Kalaitzakis, T Boursianis, D Makris, V Lahanas, I Genitsarios, S Stathakis, L Watts, T Maris, E Pappas, “*Pseudo-In-Vivo Dose Verification of a New Mono-Isocentric Technique for the Treatment of Multiple*

Brain Metastases”, American Association of Physicists in Medicine (AAPM) Annual Meeting 2016, July 30 – August 3, Denver, Colorado, USA

22. P Karaiskos, **E P Pappas**, A Moutsatsos, E Zoros, G Kollias, E Georgiou, “*On the use of PRESAGETM 3D dosimetry for Gamma Knife treatment verification*”, 18th Leksell Gamma Knife Society meeting (LGKS) 2016, May 15 – 19, Amsterdam, The Netherlands

23. P Karaiskos, G Prentou, **E P Pappas**, E Georgiou, E Koutsouveli, C Skarleas, M Torrens, “*Influence of the degree of geometric uncertainty on the quality of Gamma Knife dose delivery*”, 18th Leksell Gamma Knife Society meeting (LGKS) 2016, May 15 – 19, Amsterdam, The Netherlands

24. V Peppas, **E Pappas**, V Lahanas, E Pantelis, P Papagiannis, “*End-User Oriented Tools and Procedures for Testing Brachytherapy TPSs Employing MBDCAs*”, American Association of Physicists in Medicine (AAPM) Annual Meeting 2015, July 12 – 16, Anaheim, California, USA

25. **E Pappas**, P Karaiskos, K Zourari, V Peppas, P Papagiannis, “*An Experimental Commissioning Test of Brachytherapy MBDC Dosimetry, Based On a Commercial Radiochromic Gel/optical CT System*”, American Association of Physicists in Medicine (AAPM) Annual Meeting 2015, July 12 – 16, Anaheim, California, USA

26. **E Pappas**, A Moutsatsos, E Zoros, V Peppas, K Zourari, P Karaiskos, P Papagiannis, “*A Physical Phantom for Experimental Commissioning and Performance Testing of 192Ir MBDCAs*”, American Association of Physicists in Medicine (AAPM) Annual Meeting 2015, July 12 – 16, Anaheim, California, USA

27. **E P Pappas**, P Karaiskos, A Moutsatsos, E Pantelis, E Georgiou, M Torrens, I Seimenis, “*Evaluation of stereotactic frame induced geometric distortions in clinically-used MR sequences*”, 12th International Stereotactic Radiosurgery Society Congress (ISRS) 2015, June 7 – 11, Yokohama, Japan

28. **E Pappas**, A Moutsatsos, E Pantelis, M Torrens, I Seimenis, P Karaiskos, “*On the development of an EGSnrc-based model for predicting the dosimetric properties of*

Gamma Knife Perfexion small fields”, 12th International Stereotactic Radiosurgery Society Congress (ISRS) 2015, June 7 – 11, Yokohama, Japan

29. **E Pappas**, A Moutsatsos, P Karaiskos, E Pantelis, E Georgiou, M Torrens, “*Stereotactic frame induced geometric distortions in MR images employed in Gamma Knife radiosurgery applications*”, European Conference on Medical Physics (ECMP) 2014, September 11 – 13, Athens, Greece
30. **E Pappas**, A Moutsatsos, E Pantelis, C Paraskevopoulou, E Georgiou, P Karaiskos, “*An EGSnrc-based model of the Gama Knife Perfexion unit for small field dosimetric calculations*”, European Conference on Medical Physics (ECMP) 2014, September 11 – 13, Athens, Greece
31. E Zoros, **E Pappas**, E Pantelis, “*Evaluation of the accuracy of the electron transport algorithms of the MCNP6 and EGSnrc Monte Carlo codes using Fano theorem*”, European Conference on Medical Physics (ECMP) 2014, September 11 – 13, Athens, Greece
32. L Petrokokkinos, A Moutsatsos, **E Pappas**, E Pantelis, P Karaiskos, P Papagiannis, “*Virtual dicom-CT based phantoms for the assessment of radiation therapy TPS volumetric accuracy*”, European Conference on Medical Physics (ECMP) 2014, September 11 – 13, Athens, Greece
33. A Moutsatsos, E Pantelis, **E Pappas**, P Papagiannis, “*Experimental dosimetry for model-based ^{192}Ir HDR brachytherapy treatment planning*”, European Conference on Medical Physics (ECMP) 2014, September 11 – 13, Athens, Greece
34. V Peppas, **E Pappas**, E Pantelis, P Papagiannis, “*A QA procedure for brachytherapy TPS employing model based dose calculations, based on Monte Carlo simulation and end use oriented tools*”, European Conference on Medical Physics (ECMP) 2014, September 11 – 13, Athens, Greece
35. **E Pappas**, A Moutsatsos, I Seimenis, E Karavasilis, M Torrens, E Georgiou, P Karaiskos, “*A new phantom for the assessment of MR related geometric distortions affecting Gamma Knife radiosurgery*”, International Conference on Medical Physics (ICMP) 2013, September 1 – 4, Brighton, UK

36. A Moutsatsos, L Petrokokkinos, **E Pappas**, E Pantelis, E Georgiou, M Torrens, P Karaiskos, “*Assessment of Gamma Knife small field output factors: a multi-detector approach*”, International Conference on Medical Physics (ICMP) 2013, September 1 – 4, Brighton, UK
37. V Peppas, K Zourari, **E Pappas**, E Pantelis, P Papagiannis, “*A comparison of conventional and contemporary dosimetry for a brachytherapy cohort of 68 APBI patients*”, International Conference on Medical Physics (ICMP) 2013, September 1 – 4, Brighton, UK
38. A Moutsatsos, P Karaiskos, E Karavasilis, **E Pappas**, E Pantelis, E Georgiou, I Seimenis, M Torrens, “*A methodology for assessing and improving the total geometric accuracy in gamma knife radiosurgery*”, 11th International Stereotactic Radiosurgery Society Congress (ISRS) 2013, June 16 – 20, Toronto, Canada

Abstract

Magnetic Resonance Imaging (MRI) is widely used in advanced radiotherapy applications and, especially, in stereotactic radiosurgery (SRS) treatment planning for intracranial applications. This is justified by the superior soft tissue contrast it exhibits as compared to Computed Tomography (CT) and its multi-contrast capability, which result in better tumor delineation and characterization. Especially for brain lesions, MRI has been established as the imaging modality of choice for both target and normal tissue delineation. This choice, however, comes at the expense of geometric accuracy since it is well known that MR images are geometrically distorted.

Following an analysis of the underlying theoretical background, in the second part of this thesis an evaluation of the MR-related geometric distortions is performed. To this end, a prototype phantom was designed and constructed to facilitate distortion characterization for the MR pulse sequences and imaging parameters clinically employed in SRS treatment planning, in MRI-based or MRI-only protocols. The phantom incorporates 947 Control Points (CPs) and was designed to accurately fit in a typical head coil, as well as the Leksell stereotactic frame, used for patient immobilization in SRS applications. System-related distortions were characterized both with and without the presence of the frame. In the absence of the frame and following compensation for field inhomogeneities, measured average CP displacement owing to gradient nonlinearities was 0.53 mm. In presence of the frame, contrarily, detected distortion was greatly increased (up to about 5 mm) in the vicinity of the frame base due to eddy currents induced in the closed loop of its aluminum material. Although the region with the maximum observed distortion may not lie within the SRS treatable volume, frame-related distortion was obliterated at approximately 90 mm from the frame base. Severe distortions observed outside the treatable volume could possibly impinge on the delivery accuracy mainly by adversely affecting the registration process (e.g., the position of the lower part of the N-shaped fiducials used to define the stereotactic space may be miss-registered). System-related distortion was also identified in patient MR images. Using corresponding CT angiography images as a reference, an offset of 1.1 mm was detected for two vessels lying in close proximity to the frame base, while excellent spatial agreement was observed for a vessel far apart from the frame base.

The same phantom was scanned at 1.5 and 3.0T and using three clinical MR imaging protocols for SRS treatment planning. B_0 inhomogeneity and gradient nonlinearity related geometric distortions were assessed in this study. Areas of increased distortion were identified at the edges of the imaged volume which was comparable to a brain scan. Although mean absolute distortion did not exceed 0.5 mm on any spatial axis, maximum detected CP displacement reached 2 mm.

Furthermore, the phantom was modified to incorporate two cylindrical inserts, simulating small brain metastases. The inserts were filled with various concentrations (0-20 mM) of Gd-DTPA (commonly administered in cranial SRS) in order to characterize contrast agent induced distortion. The reversed read gradient polarity was combined with the field mapping technique to distinguish between sources of distortion. Contrast agent was found to significantly affect insert position, with the centroid offset reaching on average 0.067 mm/mM (0.204 ppm/mM). Following Gd-DTPA administration, patient MR images involving a total of 10 brain metastases/targets were also studied using a similar methodology. Total target localization uncertainty was on average 0.54 mm (2.24 ppm) with the Gd-DTPA induced distortion being of the order of 0.5 mm for the MRI protocol used, in agreement with the phantom study.

In an effort to establish what could be considered as acceptable geometric uncertainty, highly conformal plans were utilized to simulate irradiation of targets of different diameters (5 to 50 mm). The targets were deliberately mispositioned by 0.5 up to 3 mm. Dose Volume Histograms (DVHs) and plan quality indices clinically used for plan evaluation and acceptance were derived and used to investigate the effect of geometrical uncertainty (distortion) on dose delivery accuracy and plan quality. The latter was found to be strongly dependent on target size. For targets less than 20 mm in diameter, a spatial displacement of the order of 1 mm could significantly affect (>5%) plan acceptance/quality indices. For targets with diameter greater than 2 cm the corresponding displacement was found greater than 1.5 mm.

In the last part of this thesis, distortion correction schemes were developed and/or evaluated. In specific, the efficacy of vendor-supplied distortion correction algorithms (accounting for gradient nonlinearity only) was initially assessed for a variety of scanners, following development of an advanced version of the prototype phantom for high-resolution distortion detection, incorporating nearly 2000 CPs. Moreover, the

novel average-image distortion correction methodology was developed and evaluated in both phantom and patient studies. The proposed technique is based on read gradient polarity reversal and, therefore, requires two MR scans. In specific, a new image is created after averaging the signal intensities of corresponding forward and reversed polarity images, on a pixel-by-pixel basis. The method was found efficient for sequence dependent distortion minimization. Furthermore, a comparison study was also conducted involving the more well-established signal integration method. All necessary custom routines were developed in-house. Both distortion correction techniques perform equally well, minimizing the mean and median residual distortions. However, the signal integration method requires a few hours of post-imaging computational time while the average-image method is simple and efficient.

Περίληψη

Η Απεικόνιση Μαγνητικού Συντονισμού (ΑΜΣ) χρησιμοποιείται ευρύτατα στις σύγχρονες ακτινοθεραπευτικές εφαρμογές και ιδιαίτερα στο σχεδιασμό πλάνου θεραπείας στη Στερεοτακτική Ακτινοχειρουργική (ΣΑ) για ενδοκρανιακές θεραπείες. Η επιλογή αυτή δικαιολογείται από την εξαιρετική αντίθεση μαλακού ιστού που προσφέρει η ΑΜΣ σε σχέση με την Υπολογιστική Τομογραφία (ΥΤ) καθώς επίσης και την ευελιξία στην αντίθεση εικόνας. Έτσι, με τη βοήθεια εικόνων ΑΜΣ επιτυγχάνεται καλύτερη περιγραφή και χαρακτηρισμός του όγκου-στόχου. Ειδικότερα για θεραπείες εγκεφαλικών μεταστάσεων και άλλων βλαβών, η ΑΜΣ αποτελεί την πρώτη επιλογή απεικονιστικής τεχνικής τόσο για τον όγκο-στόχο όσο και τους υγιείς ιστούς. Αυτή η επιλογή όμως έρχεται σε βάρος της γεωμετρικής ακρίβειας καθώς είναι ευρέως γνωστό ότι οι εικόνες ΑΜΣ φέρουν γεωμετρική παραμόρφωση.

Μετά από μία σύντομη παράθεση του σχετικού θεωρητικού υποβάθρου, στο δεύτερο μέρος της παρούσας εργασίας διενεργήθηκε αξιολόγηση των γεωμετρικών παραμορφώσεων που σχετίζονται με τις εικόνες ΑΜΣ. Για το σκοπό αυτό, σχεδιάστηκε και κατασκευάστηκε ένα ειδικό ομοίωμα για τον χαρακτηρισμό τους και εφαρμόστηκε σε ακολουθίες και παραμέτρους απεικόνισης ΑΜΣ που χρησιμοποιούνται κλινικά κατά το σχεδιασμό πλάνου θεραπείας στην ΣΑ, σύμφωνα με πρωτόκολλα θεραπείας που βασίζονται είτε στην ΑΜΣ μόνο, είτε επικουρικά. Το ομοίωμα φέρει 947 σημεία ελέγχου (ΣΕ) και σχεδιάστηκε ώστε να είναι συμβατό με το πηνίο κεφαλής καθώς και το Leksell στερεοτακτικό πλαίσιο που χρησιμοποιείται για την ακινητοποίηση του ασθενούς και τον ορισμό του στερεοτακτικού χώρου σε εφαρμογές ΣΑ. Οι παραμορφώσεις που επάγονται από το σύστημα αξιολογήθηκαν με και χωρίς την παρουσία του στερεοτακτικού πλαισίου. Μετά από απαλοιφή των παραμορφώσεων που σχετίζονται με τις ανομοιογένειες του στατικού μαγνητικού πεδίου, απουσία του στερεοτακτικού πλαισίου η μετρούμενη μέση παραμόρφωση που σχετίζεται με τη μη-γραμμικότητα των βαθμιδωτών πεδίων ήταν 0.53 mm. Αντίθετα, παρουσία του πλαισίου, ανιχνεύθηκε αύξηση της παραμόρφωσης αυτής (μέχρι και 5 mm) στην περιοχή γύρω από τη βάση του πλαισίου, λόγω των δεινορευμάτων που επάγονται στον κλειστό της βρόγχο από αλουμίνιο. Αν και η περιοχή μέγιστης παραμόρφωσης δεν βρίσκεται εντός του όγκου που μπορεί να ακτινοβοληθεί με ΣΑ, η εν λόγω παραμόρφωση εξαλείφεται σε απόσταση περίπου 90 mm από τη βάση του πλαισίου.

Οι έντονες παραμορφώσεις που παρατηρήθηκαν εκτός του όγκου που δύναται να ακτινοβοληθεί, μπορεί όμως να υποβαθμίσουν την ακρίβεια ακτινοβολήσης μέσω του επηρεασμού της χωρικής ευθυγράμμισης (π.χ., η θέση του κατώτερου μέρους του ειδικού σημαδιού σχήματος N που ορίζει τον στερεοτακτικό χώρο μπορεί να είναι χωρικά στρεβλωμένο). Οι παραμορφώσεις που σχετίζονται με το σύστημα απεικόνισης ανιχνεύθηκαν και σε εικόνες ασθενούς. Χρησιμοποιώντας αγγειογραφία ΥΤ ως εικόνα αναφοράς του ασθενούς, μια απόκλιση 1.1 mm εντοπίστηκε σε δύο αγγεία που βρίσκονται σε μικρή απόσταση από τη βάση του πλαισίου, ενώ εξαιρετική χωρική συμφωνία είχε ένα άλλο αγγείο ευρισκόμενο σε μεγάλη απόσταση από αυτήν.

Το ίδιο ομοίωμα απεικονίστηκε σε 1.5 και 3.0T με χρήση τριών διαφορετικών κλινικών πρωτοκόλλων ΑΜΣ για χρήση σε σχεδιασμό πλάνου θεραπείας στην ΣΑ. Αξιολογήθηκαν οι παραμορφώσεις που σχετίζονται με την ανομοιογένεια του B_0 μαγνητικού πεδίου και τη μη-γραμμικότητα των βαθμιδωτών πεδίων. Περιοχές αυξημένης παραμόρφωσης καταγράφηκαν στις παρυφές του χαρτογραφούμενου όγκου, ο οποίος ήταν συγκρίσιμος με μια τυπική σάρωση κεφαλής. Αν και η μέση απόλυτη παραμόρφωση δεν ξεπέρασε τα 0.5 mm σε κανένα χωρικό άξονα, η μέγιστη απόκλιση ΣΕ έφτασε τα 2 mm.

Στη συνέχεια, το ομοίωμα τροποποιήθηκε καταλλήλως ώστε να φέρει δύο κυλινδρικές δομές που προσομοιάζουν εγκεφαλικές μεταστάσεις. Οι δομές γεμίστηκαν με διάφορες συγκεντρώσεις (0-20 mM) του σκιαγραφικού Gd-DTPA (συχνά χορηγούμενο στην ΑΜΣ για ΣΑ εγκεφάλου) με σκοπό τον χαρακτηρισμό των παραμορφώσεων που επάγονται από το ίδιο το σκιαγραφικό. Η μέθοδος αναστροφής της πολικότητας της βαθμίδας κωδικοποίησης της συχνότητας συνδυάστηκε με την τεχνική χαρτογράφησης πεδίου ώστε να είναι δυνατός ο διαχωρισμός μεταξύ των πηγών παραμόρφωσης. Το σκιαγραφικό βρέθηκε ότι επηρεάζει σημαντικά τη θέση των δομών, με την απόκλιση να φτάνει κατά μέσο όρο τα 0.067 mm/mM (0.204 ppm/mM). Μετά από χορήγηση κλινικής δόσης του ίδιου σκιαγραφικού, εικόνες ΑΜΣ ασθενών με συνολικά 10 εγκεφαλικές μεταστάσεις/στόχους μελετήθηκαν εφαρμόζοντας παρόμοια μεθοδολογία. Η συνολική αβεβαιότητα στο χωρικό εντοπισμό των όγκων ήταν κατά μέσο όρο 0.54 mm (2.24 ppm) για το πρωτόκολλο ΑΜΣ που χρησιμοποιήθηκε, σε συμφωνία με τα αποτελέσματα του ομοιώματος.

Σε μια προσπάθεια να καθοριστεί ποια γεωμετρική αβεβαιότητα μπορεί να είναι ανεκτή, πλάνια θεραπείας υψηλής συμμόρφωσης χρησιμοποιήθηκαν για την προσομοίωση ακτινοβολήσης στόχων διαφόρων διαμέτρων (5 έως 50 mm). Χωρικές μεταθέσεις από 0.5 έως 3 mm εφαρμόστηκαν εσκεμμένα στους στόχους. Στη συνέχεια, υπολογίστηκαν ιστογράμματα δόσης-όγκου και δείκτες ποιότητας πλάνου που χρησιμοποιούνται κλινικά για την αξιολόγηση και αποδοχή πλάνων θεραπείας. Τα αποτελέσματα χρησιμοποιήθηκαν για τη διερεύνηση της επιρροής της γεωμετρικής αβεβαιότητας (παραμόρφωσης) στην ακρίβεια της εναπόθεσης της δόσης και στην ποιότητα του πλάνου. Η τελευταία βρέθηκε ότι εξαρτάται ισχυρά από τις διαστάσεις του στόχου. Για στόχους μικρότερους των 20 mm σε διάμετρο, μια χωρική μετατόπιση της τάξης του 1 mm μπορεί να επιφέρει σημαντική μεταβολή (>5%) στα κριτήρια ποιότητας/αποδοχής του πλάνου. Για στόχους διαμέτρου πάνω από 2 cm, η αντίστοιχη μετατόπιση βρέθηκε ότι είναι πάνω από 1.5 mm.

Στο τελευταίο μέρος αυτής της εργασίας, αξιολογήθηκαν ή/και αναπτύχθηκαν τεχνικές και αλγόριθμοι διόρθωσης της γεωμετρικής παραμόρφωσης. Συγκεκριμένα, η αποτελεσματικότητα των αλγορίθμων διόρθωσης (μόνο για τη μη-γραμμικότητα βαθμίδων) που παρέχονται από τους κατασκευαστές αξιολογήθηκε αρχικά για ποικιλία συστημάτων ΑΜΣ, μετά από το σχεδιασμό και κατασκευή μιας εξελιγμένης έκδοσης του ομοιώματος χαρτογράφησης παραμόρφωσης, με υψηλή διακριτική ικανότητα, το οποίο φέρει σχεδόν 2000 ΣΕ. Επίσης, η μεθοδολογία διόρθωσης μέσης-εικόνας αναπτύχθηκε και αξιολογήθηκε τόσο σε εικόνες ομοιώματος όσο και σε ασθενών. Η προτεινόμενη τεχνική βασίζεται στη μέθοδο αναστροφής της πολικότητας και για το λόγο αυτό απαιτεί δύο σαρώσεις ΑΜΣ. Συγκεκριμένα, η νέα εικόνα συντίθεται από τις μέσες τιμές των εντάσεων σήματος των αντίστοιχων εικόνων αντίθετης πολικότητας, υπολογισμένες πίζελ-προς-πίζελ. Η μέθοδος διόρθωσης αυτή βρέθηκε αποδοτική στην ελαχιστοποίηση παραμορφώσεων που εξαρτώνται από την ακολουθία που χρησιμοποιείται. Επιπλέον, διεξήχθη μια συγκριτική μελέτη που περιλάμβανε την πιο καλά καθιερωμένη μέθοδο διόρθωσης που βασίζεται στην ολοκλήρωση του σήματος, αφού αναπτύχθηκαν όλες οι απαραίτητες σχετικές ρουτίνες για την εφαρμογή της. Και οι δύο μέθοδοι διόρθωσης βρέθηκαν να αποδίδουν εξίσου καλά, ελαχιστοποιώντας τη μέση και διάμεσο εναπομείνουσα παραμόρφωση. Η μέθοδος ολοκλήρωσης σήματος, όμως, απαιτεί μερικές ώρες υπολογιστικού χρόνου μετά τη λήψη των εικόνων, ενώ η μέση-εικόνα είναι πιο αποδοτική και πιο απλή στην εφαρμογή της.

Table of Contents

Introduction, Motivation and Research Goals.....	24
PART A: THEORITICAL BACKGROUND	29
1 Introduction to Magnetic Resonance Imaging	30
1.1 Introduction – Historical overview	30
1.2 Nuclear Magnetic Resonance.....	31
1.2.1 Magnetic properties of the nucleus.....	31
1.2.2 Interaction of spin with external magnetic field	32
1.2.3 Excitation of a system of protons	33
1.2.4 T1 and T2 relaxation times	35
1.3 Spatial encoding	37
1.3.1 Slice selection	38
1.3.2 Phase encoding	39
1.3.3 Frequency encoding.....	40
1.4 MRI pulse sequences and imaging parameters	41
1.5 Weighted contrast in MRI	44
1.6 Contrast agents in MRI	45
1.6.1 Gd-based contrast agents	45
1.6.2 Other contrast agents	46
2 MR-related geometric distortions	47
2.1 Introduction	47
2.2 Gradient field nonlinearity	48
2.3 Static magnetic field inhomogeneity.....	49
2.4 Magnetic susceptibility difference	51
2.5 Chemical shift effect	54

2.6	Characterization of MR spatial distortion	56
2.7	Distorted image space	57
2.8	Methods for distortion assessment	59
2.8.1	The read gradient reversal method	59
2.8.2	The field mapping technique	60
2.8.2.1	Wrapped phase	61
2.8.2.2	1D phase unwrapping	62
2.8.2.3	Guided 3D phase unwrapping	65
2.9	Distortion correction	67
3	MRI in stereotactic radiosurgery treatment planning	69
3.1	Introduction	69
3.2	Historical overview of Stereotactic Radiosurgery	71
3.3	The Gamma Knife Perfexion system	72
3.3.1	The GK Perfexion treatment delivery unit	72
3.3.2	The Leksell stereotactic frame and stereotactic space	74
3.3.3	Dose calculation and image registration in the GammaPlan treatment planning system	77
3.4	MRI protocols for stereotactic radiosurgery treatment planning	78
3.5	Applying margins in stereotactic radiosurgery treatment planning	80
	PART B: MR DISTORTION ASSESSMENT.....	82
4	System-related geometric distortions in MR images employed in Gamma Knife radiosurgery applications	83
4.1	Introduction	84
4.2	Materials and methods	84
4.2.1	Phantom study	84
4.2.1.1	Phantom design.....	84
4.2.1.2	Frame modification.....	86

4.2.1.3	Image acquisition.....	87
4.2.1.4	Data analysis.....	88
4.2.1.5	Uncertainty estimation.....	89
4.2.2	Patient study	90
4.3	Results	91
4.3.1	Phantom study	91
4.3.2	Patient study	97
4.4	Discussion	99
4.5	Conclusion.....	104
5	Evaluation of MRI-related geometric distortions in stereotactic radiotherapy treatment planning at 1.5T and 3.0T	106
5.1	Introduction	106
5.2	Materials and Methods	107
5.2.1	The phantom	107
5.2.2	Distortion detection	108
5.2.3	Image acquisitions	109
5.3	Results	110
5.3.1	Distortion magnitude	110
5.3.2	Distortion distribution and directionality	113
5.4	Discussion	114
5.5	Conclusion.....	116
6	Patient-specific geometric distortion in MR images employed in stereotactic radiosurgery treatment planning.....	117
6.1	Introduction	118
6.2	Materials and Methods	119
6.2.1	Phantom study	119
6.2.1.1	Phantom description	119

6.2.1.2	MRI scanning	120
6.2.1.3	Read gradient polarity reversal technique	120
6.2.1.4	Field mapping technique	122
6.2.1.5	Contrast agent induced offset	123
6.2.2	Patient study	123
6.3	Results	124
6.3.1	Phantom study	124
6.3.2	Patient study	128
6.4	Discussion	131
6.5	Conclusion.....	135
7	Dosimetric impact.....	136
7.1	Introduction	136
7.2	Materials and Methods	136
7.3	Results	137
7.4	Discussion	140
7.5	Conclusion.....	141
	PART C: MR DISTORTION CORRECTION SCHEMES.....	143
8	Vendor-supplied distortion correction algorithms at 1.5T and 3.0 T.....	144
8.1	Introduction	145
8.2	Materials and Methods	146
8.2.1	High-resolution distortion detection phantom	146
8.2.2	Image acquisitions	147
8.3	Results and discussion.....	149
8.4	Conclusion.....	151
9	The average-image distortion correction method: implementation in multiple brain metastases.....	152

9.1	Introduction	153
9.2	Materials and Methods	153
9.2.1	Phantom study	153
9.2.2	Patient study	154
9.3	Results	155
9.3.1	Phantom study	155
9.3.2	Patient study	157
9.4	Discussion	161
9.5	Conclusions	163
10	Comparison of geometric distortion correction schemes in MR images used in stereotactic radiosurgery applications	164
10.1	Introduction	165
10.2	Materials and Methods	165
10.2.1	The phantom	165
10.2.2	Image acquisitions	165
10.2.3	Image processing	166
10.2.3.1	Signal integration correction method	166
10.2.3.2	Average-image correction method	167
10.3	Results and discussion.....	167
10.4	Conclusion.....	169
	Summary of Results, Overall Conclusions and Future Work.....	170
	Bibliography	174
	List of Figures.....	195
	List of Tables	204
	Appendix.....	206

Introduction, Motivation and Research Goals

Magnetic Resonance (MR) images exhibit superior soft tissue contrast with respect to computed tomography (CT) and, consequently, are being increasingly employed in radiotherapy treatment planning [1,2], either complementarily to CT, or even as the sole imaging modality (MRI-only treatment planning) [3]. The multi-contrast capabilities of MR allow for finer tumor localization and delineation. As an instance, contrast agents, such as gadolinium diethylenetriamine pentaacetic acid (Gd-DTPA) reduce T1 relaxation time, rendering even tiny brain lesions visible [4,5] in T1-weighted (T1w) images.

This is routinely exploited in radiotherapy treatment planning, including stereotactic radiosurgery (SRS) applications in which target localization accuracy becomes paramount [6–11]. SRS is a well-established treatment approach for the management of a wide variety of lesions, mainly in the brain. The use of SRS in the brain as part of either initial treatment or salvage of recurrent brain metastases has recently increased and so has the number of metastases considered treatable by SRS [12–24]. The efficiency SRS is based on the precise delivery of accurately registered dose distributions to the target, facilitating restriction of the absorbed dose to the surrounding critical structures. High dose levels with steep gradients are delivered in a single or a few dose fractions (single-fraction or fractionated SRS, respectively), setting strict spatial uncertainty tolerance levels.

MR images are inherently distorted with sources of distortion related to both the MR unit (system-related) [25–29] and the subject being scanned (patient-induced) [30–33]. In the former case, geometric distortions arise from gradient field nonlinearity and static magnetic field (B_0) inhomogeneity. MR scanner vendors equip their units with post-imaging correction algorithms which reduce gradient field nonlinearity distortions [34,35] (often referred to as sequence independent distortions [33]), although residual distortions are still significant in areas distant from the MR isocenter [26,27]. These distortions, however, are fairly reproducible with time and, therefore, can be predicted [27]. In a patient scan, residual gradient field nonlinearity related distortions can be

corrected for, following an a priori characterization with the aid of specially designed phantoms [33].

Patient-induced distortions are related to magnetic susceptibility differences [36] and the chemical shift effect [37]. However, the set of magnetic properties for a given patient cannot be predicted, in addition to not being constant in time. Therefore, patient-specific distortion characterization and/or correction has drawn considerable attention [10,30,32,33,38–40]. The vast majority of these studies rely on either the field mapping technique [41] or the read gradient polarity reversal method [42] which both burden the patient's imaging protocol with at least one extra sequence. In addition to susceptibility differences and chemical shift, both methodologies also account for B_0 inhomogeneity related distortion (all three collectively referred to as sequence dependent distortions [33]). Although tissue susceptibility effects within patient anatomy have been investigated in simulation studies [31,43,44], distortions exactly at the target locations (including the ones induced by MR contrast agents) have not been specifically studied. In an MR-only SRS treatment planning protocol, geometric accuracy in and around the target is paramount as minor spatial displacements could result in target under-dosage, especially for tiny lesions [9,10,45].

Gd-DTPA is a commonly used contrast agent in MR imaging for brain lesion localization in SRS treatment planning. Following an injection of 0.1 – 0.2 mmol/kg of Gd-DTPA, the contrast agent rapidly reaches the brain, where Gd remains intravascular. However, in high-grade tumors the blood-brain barrier is sufficiently disrupted to allow Gd leakage from the vessels. Since Gd is paramagnetic, accumulation of contrast agent results in local T1w signal enhancement by reducing tissue T1 relaxation times [1,46]. This mechanism is routinely exploited in MR imaging for SRS treatment planning by applying contrast enhanced 3D T1w Gradient Echo (GE) pulse sequences. However, the paramagnetic nature of Gd alters the local magnetic field due to its magnetic susceptibility (molar susceptibility in SI units: 0.3393 mL/mol [47]). Susceptibility inhomogeneities inherently induce geometric distortion in and around the susceptibility cavity with the spatial displacement of a given point varying according to the cavity size, shape and orientation with respect to B_0 as well as its location with respect to the cavity [31,36,47].

Apart from the above-mentioned sources of distortion, external devices such as localization frames utilized for patient immobilization and stereotactic space definition in SRS applications can also perturb the magnetic field. In Gamma Knife (GK) radiosurgery, the Leksell stereotactic system is used for these purposes. It consists of the CT and MR indicator boxes (used in CT and MR imaging, respectively), the Leksell stereotactic frame model G (frame), and other auxiliary apparatuses. The CT or MR indicator box is used to determine target coordinates using a system of N-shaped fiducials located at the Left (L), Right (R) and Posterior (P) sides of the patient. The frame consists of a rectangular base ring (frame base) and four posts which are attached to the patient's head using four pins. The indicator box is fixed on the ring using snap-on clips. The front piece of the frame base (i.e., Anterior (A) patient side) is removable and is either straight or curved [48,49]. In both cases the frame base forms a closed loop. It is well established that eddy currents can be induced in closed loops by both the radiofrequency (RF) and gradient fields of the MRI scanner, resulting in significant artifacts [50–52]. Although frame induced distortions and artifacts in MR images are generally acknowledged [48,50], a systematic characterization of the magnitude, directionality and range of the distortion field has not been documented.

Apart from MR-related geometric distortions, a series of other sources of spatial uncertainties can potentially compromise dose delivery in SRS applications, such as image registration uncertainties (on average 2 mm for MR/CT modalities, according to a multi-institutional study [53]), patient positioning uncertainties, patient/organ motion during treatment [54], as well as dose delivery system mechanical uncertainties. Magnitude of spatial accuracy and precision related to the above depends on the treatment modality employed, patient immobilization apparatus, positioning system used, etc. Discussion on the overall spatial uncertainty budget clearly stems from the need to identify and use an optimal margin about the gross target volume (GTV) for target definition in SRS treatment planning, which is of great importance in order to irradiate the GTV with the prescription dose and, on the other hand, to minimize toxicity and local recurrence, especially in cases where multiple targets are treated, such as in multiple brain metastases patients. Radiation-induced toxicity is directly associated with the irradiated brain volume [55–57]. According to a prospective clinical study, if the volume of brain receiving at least 10 Gy ($V_{10\text{Gy}}$) and 12 Gy ($V_{12\text{Gy}}$) is larger than 12.6 cm³ and 10.9 cm³, respectively, the risk of brain radionecrosis has been

reported to reach 47%. The rate is reduced to 10%, if V_{12Gy} drops to 8.5cm^3 [55]. Symptomatic or asymptomatic radiation induced brain necrosis, i.e., the disruption of healthy neurons due to cell necrosis, is the most common side effect in cranial SRS. The symptoms of radiation induced brain necrosis depend on the location and function of the brain at the injury site. These symptoms can range from headaches, fatigue, nausea, imbalance, extremity weakness/numbness, speech deficits, and seizures to a combination of the above [58]. On the other hand, any potential spatial dose delivery discrepancies to the GTV (due any spatial errors involved, such as MR image distortion at the target location) could compromise treatment efficiency, resulting to reduced local tumor control. Therefore, introduction of a margin of 1 mm around the GTV, defining the target, has been reported to significantly increase the tumor local control rate [17,59]. Applying larger (2 or 3 mm) margins significantly increases the risk for radiation induced toxicity (e.g., up to 25% for a 2mm-margin [60]) without warranting higher local control rates [17,61]. In other approaches, sub-millimeter or zero margins are applied, minimizing the risk of radionecrosis [60]. The discussion on margin restrictions becomes even more complicated if fractionated SRS is also considered [62] which has been reported to exhibit increased tolerance to necrosis, compared to single-fraction SRS schemes [63].

In any case, it is crucial to restrict the irradiated volume, e.g., the V_{12Gy} , at the lowest levels possible but without risking to compromise the treatment outcome. This very sensitive balance between the necessity for applying margins and the higher risk for radiation induced side effects in cranial SRS applications sets the motivation of this thesis to deal with MR images employed in SRS treatment planning with emphasis to frame-based single-fraction SRS for the management of multiple brain metastases.

Distortion detection and characterization (both sequence dependent and independent) in an MRI unit employed for treatment planning is valuable towards determination of the appropriate margins to be applied around the GTV [2]. As a step further, development of methods for efficient distortion correction/minimization can result in enhancement of the spatial accuracy of the SRS treatment protocol and, potentially, allow for further reducing the applied margins. Several distortion correction schemes have been presented in the literature [33,38,39,41,42], all requiring an extra imaging step and post-imaging process and, therefore, resulting in increased MR scanning time

and protocol complexity. To the best of our knowledge, no sequence dependent distortion correction/minimization procedure is routinely used in SRS clinical practice.

Following a literature review (Part A of this thesis), the research goals of this thesis are divided into two groups:

1. To perform a thorough characterization of the geometric distortions related to MR images employed in SRS (Part B of this thesis). More specifically, the scopes of this Part involve:
 - a. Characterization of the sequence independent geometric distortions
 - b. Evaluation of the spatial distortion induced by the presence of the stereotactic frame
 - c. Estimation of patient-induced distortion and especially the distortion related to the magnetic susceptibility of the Gd-based contrast agent
 - d. Estimation of the dosimetric impact associated with potential target geometric offset for clinical high conformal SRS treatment plans
2. To develop/evaluate and compare distortion correction/minimization schemes (Part C of this thesis). In particular, the aims of this Part are:
 - a. To evaluate the efficacy of vendor-supplied distortion correction schemes which take into account the gradient nonlinearity induced distortion only
 - b. To develop and implement a distortion correction/minimization methodology, which takes into account sequence dependent distortion and, thus, patient-induced distortion
 - c. To perform a comparative study involving the proposed methodology and a more well-established distortion correction technique such as the signal integration method

Achieving the above-listed goals could pave the way for introducing into clinical practice MR images of negligible geometric distortion even for cranial SRS applications, involving tiny peripheral brain lesions.

PART A: THEORITICAL BACKGROUND

1 Introduction to Magnetic Resonance Imaging

1.1 Introduction – Historical overview

MRI is one of the most advanced medical imaging modalities which is nowadays widely used in clinical practice for both diagnostic and radiotherapy applications. The superior soft tissue contrast it exhibits (compared to other imaging modalities such as the CT) along with the use of non-ionizing radiation constitute the main advantages of MRI for use in clinical practice.

MR imaging is based on the Nuclear Magnetic Resonance (NMR), a phenomenon first described in 1938 by Isaac Rabi. For his research, Rabi was awarded the Nobel prize in 1944. NMR was first observed in protons independently by Bloch and Purcell [64,65], and consequently shared the 1952 Nobel Prize [66]. In 1959, J. Singer proposed that NMR could be exploited to measure blood flow, while Richard Ernst developed Fourier transform (FT) NMR spectroscopy in 1966 [67], winning the 1991 Nobel Prize in Chemistry [66]. In 1971, R. Damadian discovered that certain mouse tumors were characterized by longer T2 relaxation times compared to normal tissues [68]. In 1973, P. Lauterbur proposed to use gradients of magnetic fields in order to distinguish between NMR signals originating from different locations [69], combining this with a form of reconstruction from projections. Selective excitation was proposed in 1974 by P. Mansfield [46]. Lauterbur and Mansfield shared the 2003 Nobel Prize in Physiology/Medicine, acknowledging that the use of gradients set the foundations of MRI [46]. The first MR images of humans were produced in 1977, depicting the thorax [66], while Clow and Young produced the first published human head image in 1978 [46]. General Electric introduced the first 1.5 T systems around 1984. Ever since, MRI units and procedures are increasing exponentially. Between June 2015 and June 2016,

in England alone, more than 3,000,000 MR procedures were performed in total, with approximately 600,000 MR procedures related to brain cancer imaging [70].

1.2 Nuclear Magnetic Resonance

1.2.1 Magnetic properties of the nucleus

The magnetic momentum of a nucleus, $\vec{\mu}$, is related to the kinetic momentum, \vec{J} , according to the relation:

$$\vec{\mu} = \gamma \vec{J} \quad (1)$$

where γ is the gyromagnetic ratio of the nucleus, $\gamma = g_n \beta / \hbar$, g_n is the Lande factor of the studied nucleus and $\beta = e \hbar / 2m_p$ is the nuclear Bohr magneton [71]. The kinetic momentum, \vec{J} , relates to the spin, \vec{I} , according to:

$$\vec{J} = \hbar \vec{I} \quad (2)$$

Only the projection of the nucleus magnetic moment in the z-direction (arbitrarily selected) is measurable and is simply:

$$\mu_z = \gamma J_z \quad (3)$$

Only the nuclei having a non-null magnetic moment—thus a non-null spin—are observable by the NMR phenomenon. The resulting spin of a nucleus depends on the number of protons and neutrons it contains. It is non-null if the number of protons is odd or if it is even with an odd number of neutrons. The NMR behavior may thus be different for isotopes of the same element. The NMR sensitivity of a given isotope takes into account its natural abundance and the amplitude of the NMR signal it produces, depending on its gyromagnetic ratio [71]. Since the majority of the body mass consists of water, hydrogen, ^1H , is the most abundant nucleus with non-zero spin. Clinical MR imaging relies on NMR signal from hydrogen and therefore the analysis in the following sections will be adapted accordingly.

1.2.2 Interaction of spin with external magnetic field

According to the quantum approach, in absence of external magnetic field, the projection of the nucleus magnetic moment, μ_z , can only be $\pm\gamma\hbar/2$, i.e., spin $I=1/2$ in equations (1) and (2). The energies corresponding to these two states are equal. Applying an external magnetic field B_0 along the z-axis will result in splitting the energy states, an effect known as Zeeman. This is illustrated in Figure 1-1.

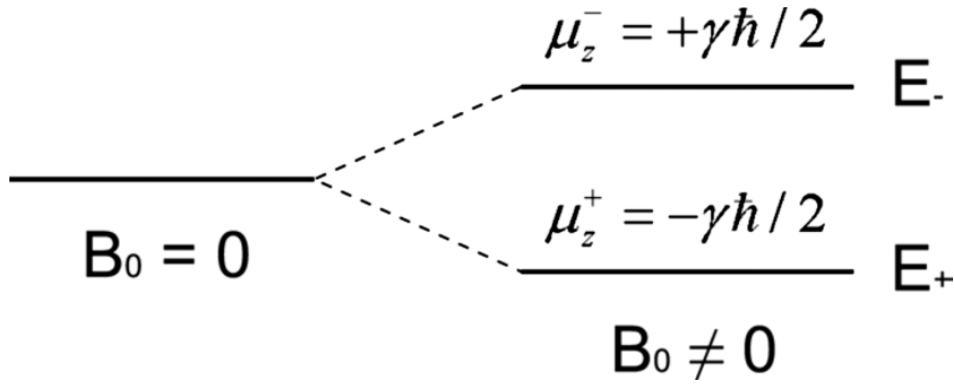


Figure 1-1: Illustration of the Zeeman effect for a proton in presence of external magnetic field B_0 . Adopted from [71].

The magnetic moment is discretized and leads to discrete energy values [72]:

$$E = -\vec{\mu}\vec{B} = -\mu_z B_z = -\gamma m_s \hbar B_z \quad (4)$$

with $m_s = +\frac{1}{2}$ when the spin is parallel to the magnetic field and $m_s = -\frac{1}{2}$ when the spin is anti-parallel.

Assuming that the external magnetic field B_0 is applied on the z-axis, the energy difference between the two energy levels is:

$$\Delta E = \frac{1}{2}\gamma\hbar B_0 + \frac{1}{2}\gamma\hbar B_0 = \gamma\hbar B_0 = \hbar\omega_0 \quad (5)$$

$$\text{where } \omega_0 = \gamma B_0 \quad (6)$$

is the Larmor precession frequency and corresponds to the frequency of a photon absorbed or emitted during transition of a proton spin between the two energy levels.

For a given population, N , of protons at a constant temperature, T , protons will be distributed to the two energy levels. Let N_+ and N_- be the number of protons at the energy levels E_+ and E_- (Figure 1-1), respectively, then according to Boltzmann statistic [71]:

$$\frac{N_+}{N_-} = e^{\hbar\omega_0/kT} \quad (7)$$

where k equals to the Boltzmann constant. For typical magnetic field strengths and temperatures, $N_+ > N_-$, i.e., an excess of just a few protons exhibit μ_z parallel to B_0 , corresponding to the lower energy state. Using Equation (7), it is obvious that the difference in population between the two energy levels is increased at higher magnetic field strengths, B_0 (and therefore, at increased ΔE), and at lower temperatures, T . However, population difference does not increase rapidly. As an instance, at a $B_0 = 1.5$ T, the ΔN is just 96 for every 10^6 protons.

In the classical approach, one can determine that the temporal gradient of the magnetic moment is given by [72]:

$$\frac{d\vec{\mu}}{dt} = \gamma\vec{\mu} \times \vec{B}_0 \quad (8)$$

By solving Equation (8) one can calculate that precession of the magnetic moment, $\vec{\mu}$, around the external magnetic field, \vec{B}_0 , at the Larmor frequency given by Equation (6).

1.2.3 Excitation of a system of protons

Suppose we have a system (a large number) of protons and examine it macroscopically, following application of an external constant magnetic field \vec{B}_0 . Magnetization, \vec{M} , describes the magnetic moment of the system and can be analyzed in isochromat components. An isochromat is a microscopic group of spins that resonate at the same frequency, i.e., within a volume where the magnetic field is absolutely homogenous.

The Magnetization, \vec{M} , is aligned with \vec{B}_0 , as shown in Figure 1-2(a). The system is at the equilibrium state. If a photon of specific frequency corresponding to ΔE is applied on x-axis, transitions between the energy levels will occur. In the classical approach, this is regarded as applying an external $\vec{B}_1(t)$ field on x'-axis, at the rotating frame

(Figure 1-2). Vector \vec{M} rotates around \vec{B}_1 (i.e., x' in the rotating frame) at an angular frequency of $\omega_1 = \gamma B_1$ (rotating frame), as shown in Figure 1-2(b), for as long as \vec{B}_1 is applied. Therefore, the flip angle (FA), is:

$$FA = \omega_1 t = \gamma B_1 t \quad (9)$$

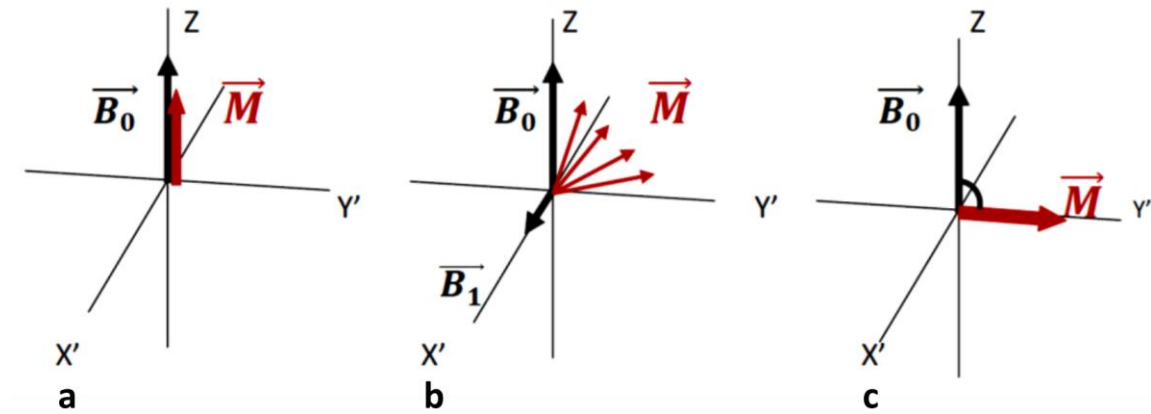


Figure 1-2: (a) System at the equilibrium state. Magnetization is aligned with B_0 . (b) A B_1 field is applied on x' -axis in the rotating frame. Magnetization rotates around B_1 . (c) B_1 field is disrupted at a specific time to result in a flip angle of 90° .

By varying the duration, t , of application of the $\vec{B}_1(t)$ field (or in some cases by varying its amplitude), one can choose to rotate the resulting Magnetization of the system of the protons with different FAs. The most used FAs are 90° and 180° , corresponding to 90° and 180° radiofrequency (RF) excitation pulses, respectively. In Figure 1-2(c), an FA of 90° is illustrated. After an RF pulse tuned at the Larmor frequency is applied, the proton system is out of equilibrium and it will return to equilibrium through transitions between the Zeeman energy levels (Figure 1-1). This could not be achieved by spontaneous transitions since their probability is negligible. In fact, the return to equilibrium is caused by interactions of the protons with their environment, in a process called relaxation [71].

1.2.4 T1 and T2 relaxation times

So far, the system of protons has been excited by photons of Larmor frequency, which were absorbed and resulted in the rotation of the Magnetization by an angle of $FA=90^\circ$. In the quantum approach this corresponds to protons transiting to the higher energy level E.. As always, an excitation is followed by a decay by emitting the photons. The characteristic times describing this decay are information fundamentally exploited in MR imaging.

At a random moment, the Magnetization vector, \vec{M} , is analyzed to two components; the longitudinal, \vec{M}_z , and the transversal, \vec{M}_{xy} . Bloch phenomenologically described the temporal evolution of the two components until they reach the equilibrium state [64]. In specific, longitudinal Magnetization, \vec{M}_z , increases exponentially with a characteristic time T1, as graphically illustrated in Figure 1-3. T1 represents the time when \vec{M}_z reaches the 63% of its maximum value. The exponential increase is described by:

$$M_z(t) = M_z(0)(1 - e^{-t/T_1}) \quad (10)$$

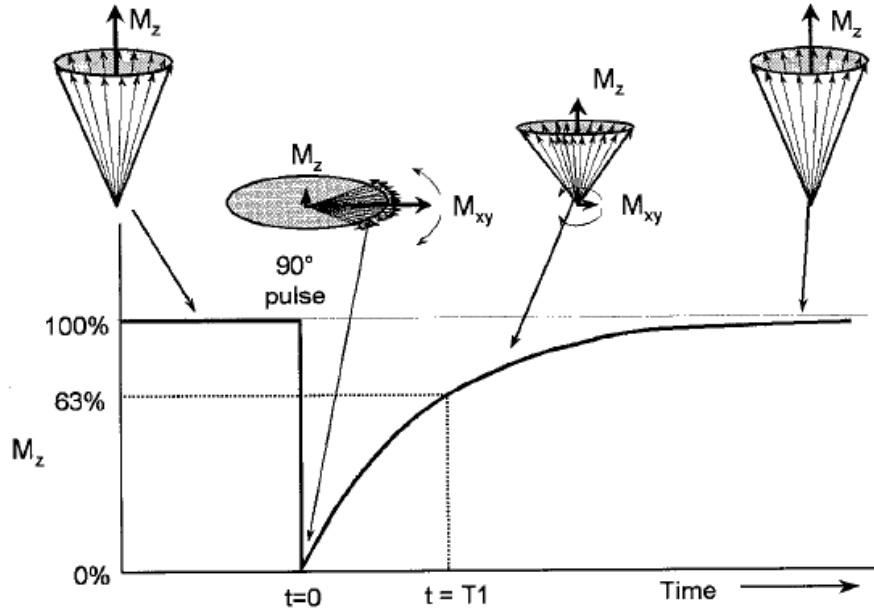


Figure 1-3: Graphical illustration of the exponential increase of the longitudinal Magnetization with T_1 characteristic time. Precession of isochromats is also shown.

In contrast, the transversal Magnetization, \vec{M}_{xy} , decreases exponentially with time. T_2 relaxation time represents the time when \vec{M}_{xy} drops to 37% of its initial maximum value. This is graphically illustrated in Figure 1-4 and described by the equation:

$$M_{xy}(t) = M_{xy}(0)e^{-t/T_2} \quad (10)$$

It should be noted that T_1 and T_2 relaxation times are not equal as they describe different decay procedures. T_1 is referred to as *spin-lattice relaxation time*, where lattice is the electromagnetic environment of the system of protons. T_1 characterizes procedures related to the energy balance between the system of protons and the lattice. On the other hand, T_2 relaxation time is also known as *spin-spin relaxation time* and describes the procedures that lead to changes to the entropy balance within the system of protons. More specifically, T_1 is associated with the dephasing rate of the system of spins and, thus, with the corresponding entropy increase. In pure water, T_1 and T_2 relaxation times are approximately 4 and 2 seconds, respectively. However, in most biological tissues, $T_2 \ll T_1$.

In a realistic case, decay is characterized by the T_2^* relaxation time (instead of T_2), which is even smaller and is related to the local magnetic field inhomogeneities which

result in different Larmor frequencies. T_2^* is also illustrated in Figure 1-4. Local magnetic field inhomogeneities result in shortened relaxation of the transversal Magnetization M_{xy} .

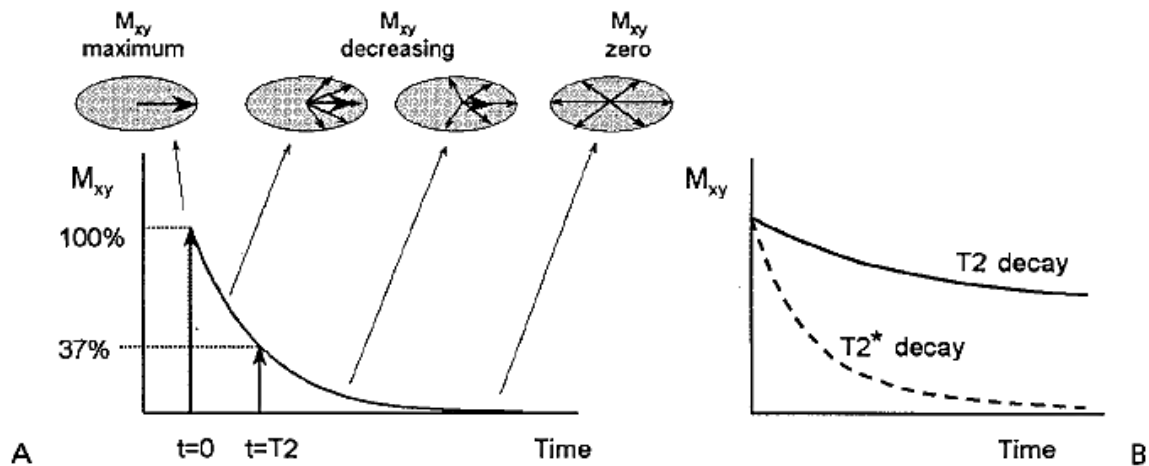


Figure 1-4: Graphical illustration of the T_2 relaxation time. Exponential reduction of the transverse Magnetization, M_{xy} , at a rate of $1/T_2$ (continuous line). In fact, the reduction will take place at a relaxation rate of $1/T_2^*$ (dashed line) due to local magnetic field inhomogeneities.

In an MRI, image contrast stems from the T_1 , T_2 or T_2^* relaxation times or the density of protons within the anatomical structures imaged.

1.3 Spatial encoding

NMR signal from the human body (or any object) is useless for imaging purposes, unless it contains information of the location it was emitted from. In other words, the signal must be tagged according to the position of the decaying system of proton spins within the subject/object. This is facilitated by introducing magnetic field gradients to the background static \vec{B}_0 field. This idea was introduced by Lauterbur in 1973 [69] (see also Section 1.1).

1.3.1 Slice selection

In a two-dimensional (2D) imaging sequence, the slice to be imaged is defined by applying an additional magnetic field gradient together with the excitation RF pulse. Assuming that the slice is transversal to the z-axis, then the total magnetic field, $\vec{B}_{0,tot}$, at a given z coordinate will be [71]:

$$B_{0,tot}(z) = B_0 + G_z(z) \quad (11)$$

where G_z is the gradient of the magnetic field on the z-axis. Therefore, the Larmor frequency of a proton now varies with z-location, according to Equations (6) and (11). By applying G_z simultaneously with the excitation pulse, a specific slice can be excited alone, allowing for slice selection. However, the RF pulse should contain only a narrow range of frequencies, corresponding to the slice location and the slice thickness selected to be imaged. This range of frequencies is known as the transmit bandwidth. The slice selection concept is graphically illustrated in Figure 1-5.

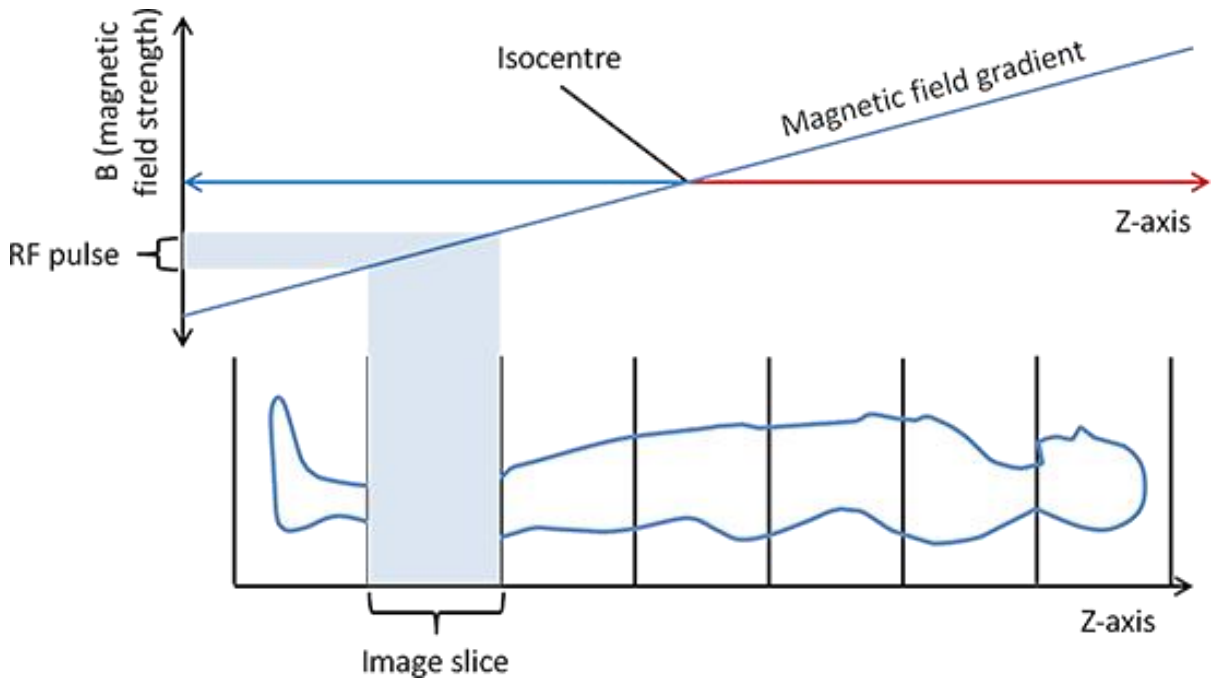


Figure 1-5: Graphical illustration of selective excitation of a slice transversal to the z-axis. Figure adopted from [radiologycafe.com educational site].

It should be noted that the slice selection gradient in a 2D imaging protocol is applied only along with the RF excitation pulse. Removing G_z results in restoring the Larmor frequency of the excited system of spins to the value corresponding to B_0 static magnetic field, i.e., $\omega_0 = \gamma B_0$.

1.3.2 Phase encoding

Following RF excitation, in presence of no gradient magnetic field (slice selection gradient is switched off soon after selective excitation), all precessing isochromats are in phase since they were excited simultaneously and now rotate at the same angular frequency. By applying a gradient magnetic field on one axis (assuming on y-axis for this analysis), Larmor precessing frequency varies with y coordinate and, therefore, dephasing of isochromats gradually occurs. The longer the gradient field duration, the more the isochromats dephase. The concept of identifying the location of the signal by variably dephasing the isochromats prior to read-out is graphically illustrated in Figure 1-6. The phase encoding gradient field is switched off prior to signal read-out and, thus, Larmor precessing frequency is restored to the initial $\omega_0 = \gamma B_0$ but the phase shift between isochromats still remains.

Without any applied gradient magnetic field at all, the isochromats are all in phase and a large signal can be obtained. On the other hand, if gradient field is switched on, the dephasing of isochromats increases with magnitude of the gradient applied. If the strength is large enough for all the isochromats to cancel each other out, no signal is obtained at all. Therefore, gradient strength and duration need to be carefully selected [46].

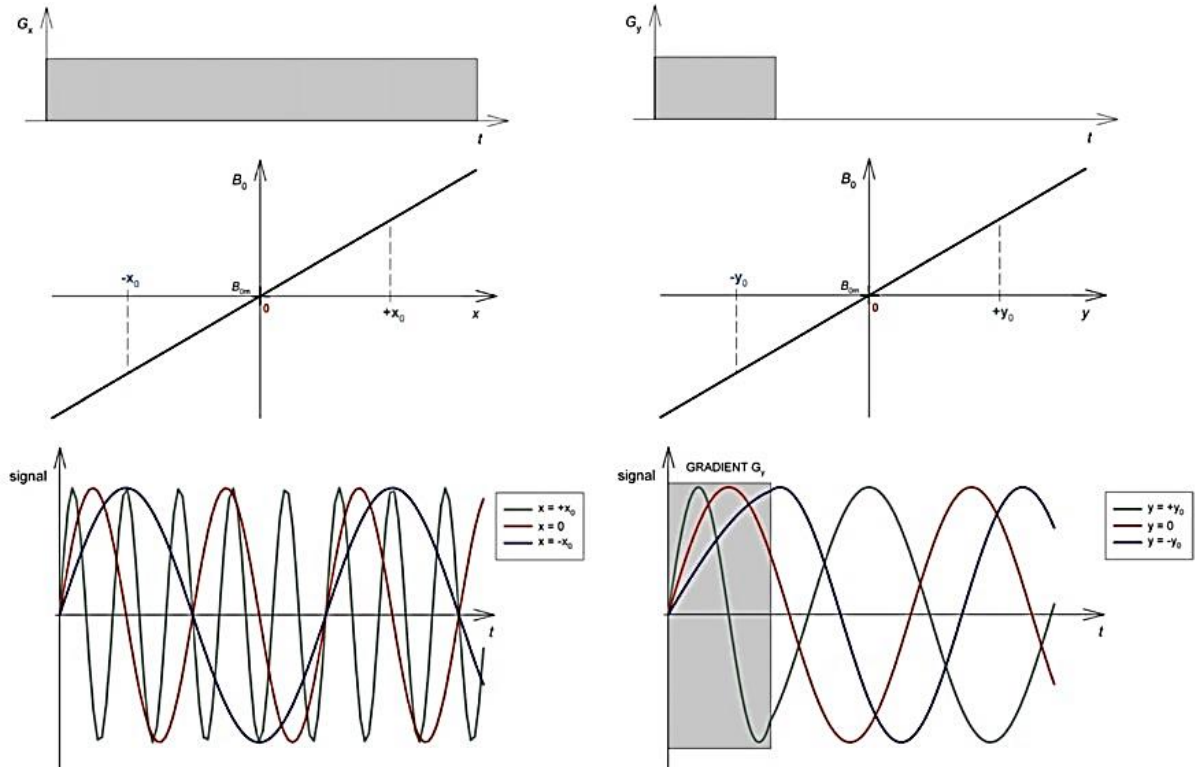


Figure 1-6: Graphical illustration of the phase encoding (left) and frequency encoding (right) principles by applying gradient magnetic fields on x and y axes, respectively. Figure adopted from [71].

1.3.3 Frequency encoding

There is no reason why this phase encode process cannot be re-applied to obtain the full image in other directions. The main practical difficulty is that such approach would take a considerably long time, although it is feasible. By applying a time consuming three-dimensional (3D) imaging can be performed with phase encoding process only. However, there is a quicker, more convenient and conceptually simpler method of encoding the second in-plane direction, referred to as frequency encoding [46].

In a similar approach to phase encoding, another gradient magnetic field is used to encode the y-coordinate of a volume emitting the decay signal. This time, the frequency domain is exploited. More specifically, the applied gradient magnetic field, G_y , results in a change of the Larmor precessing frequency according to the location on y-axis. Simultaneously, the signal is recorded. By analyzing the frequency of the recorded signal, the emission location on y-axis can be determined. The concept is illustrated in Figure 1-6.

To sum up, in a 2D imaging pulse sequence, a given volume within the subject/object is (i) selectively excited by the slice selection gradient simultaneously with RF excitation pulse, (ii) dephased by the phase encoding gradient prior to signal reception and (iii) its precessing frequency was changed simultaneously with signal read-out. The latter is the reason for referring to the frequency encoding axis also as the read gradient direction. These three processes define the location of signal emission within the subject/object and are based on switching gradient magnetic fields.

In a 3D imaging pulse sequence, there is no slice selection gradient. The complete 3D volume of interest is simultaneously excited at each repetition of the sequence with the entire volume regarded as a single slice in a similar way to a 2D imaging protocol. The z-axis is spatially encoded by also applying phase encoding gradient. Therefore, 3D imaging protocols are doubly phase encoded. Image reconstruction is performed by using 3D FT. Acquisition time in 3D imaging sequences is significantly shorter with improved signal to noise ratio compared to a 2D protocol for the same volume of interest.

1.4 MRI pulse sequences and imaging parameters

In MRI, a series of RF pulses and gradient fields are applied repetitively for complete image acquisition. This procedure is called *sequence*. A great deal of sequences has been introduced, each one filling the so-called *k-space* in a different way. k-space is the distribution of spatial frequencies and in simple terms is the raw data matrix which stores the encoded MR signals [46]. Applying gradients can be represented as trajectories in the k-space as shown in Figure 1-7. Depending on the application and image type, the optimum sequence can be selected. The most appropriate sequence and parameters used is usually a compromise between signal to noise ratio, acquisition time and image artifacts.

Any scanning protocol is characterized by a number of imaging parameters. Repetition Time (TR), Echo Time (TE), FA, the receiver bandwidth and number of inversion pulses are the most important ones.

TR is the time interval between two successive excitation pulses. Selection of a larger TR will allow more time for restoring the longitudinal Magnetization, M_z , between two consecutive RF excitation pulses. However, this will have a considerable impact on image acquisition time.

TE is defined as the time interval between excitation of the volume of interest by an RF pulse and decay signal read-out. TE along with TR control the transversal Magnetization, M_{xy} , at signal read-out. More specifically, higher TE will result in reduced transversal Magnetization, M_{xy} , at signal read-out. Within a time interval of one TR and depending on the MR application and sequence, it is possible to receive signal at different TEs, i.e., signal read-out several times after a single excitation.

Any sequence is a combination of excitation pulses, inversion pulses, number of echoes at TEs, gradients, etc. A few of the most common sequences are known as Gradient Echo (GE), Spin Echo (SE), Fast Low Angle Shot (FLASH), Fast Spin Echo (FSE) and Echo Planar Imaging (EPI). The principle of each one is graphically illustrated in Figure 1-7, where the different ways of filling the k-space are also shown.

After the k-space is filled in a 3D MR application, an inverse FT is applied to transform from the spatial frequencies domain, (k_x, k_y, k_z) , k-space to the image space.

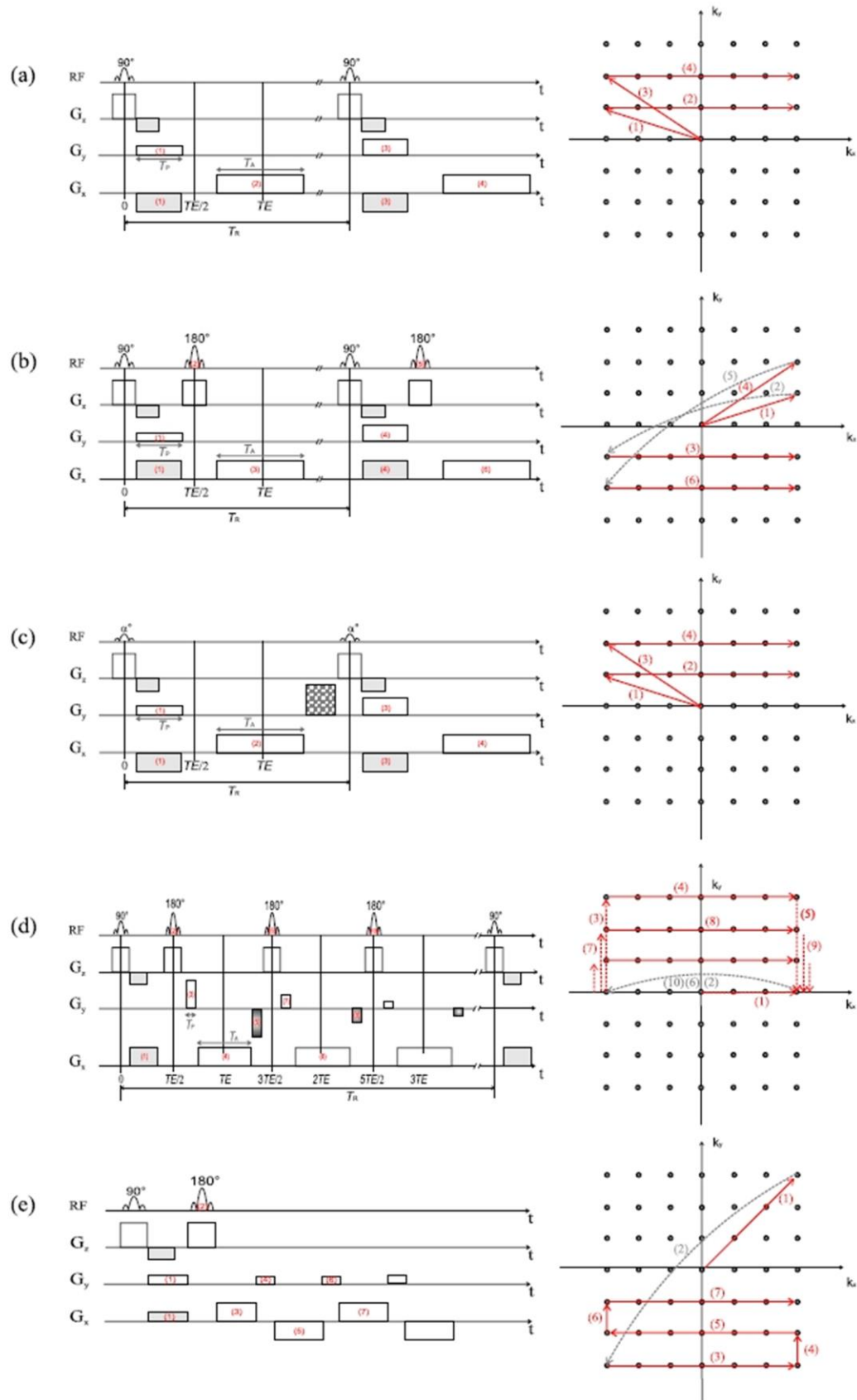


Figure 1-7: Excitation pulses, inversion pulses and gradient magnetic fields of some of the most common sequences in MR imaging, (a) Gradient Echo, (b) Spin Echo, (c) FLASH, (d) FSE and (e) EPI. Figure adopted from [71].

1.5 Weighted contrast in MRI

Contrast in an MR image depends on the sequence and parameters used, as well as the properties of the scanned subject. Selecting the appropriate sequence and adjusting the corresponding parameters enables multi-contrast capabilities. In specific, images can be acquired with contrast stemming from either different T1, T2 or T2* relaxation times or even differences in the proton density, p_m , in the voxels. In routine spin echo sequences (Figure 1-7), the signal intensity, $I(t)$, as a function of time is proportional to [73]:

$$I(t) \propto p_m \cdot (1 - e^{-TR/T_1}) \cdot e^{-TE/T_2} \quad (12)$$

or, equally:

$$I(t) \propto S_{pm} \cdot S_{T1} \cdot S_{T2} \quad (13)$$

Equation (13) involves three factors, S_{pm} , S_{T1} and S_{T2} each one related to either proton density, T1 or T2, respectively. By adjusting TE and TR relative to expected T1 and T2 relaxation times of the tissues, $I(t)$ can be weighted accordingly to highlight differences in T1, T2 or proton density or a mixture of the above [73], according to Equation (12). For instance, in routine SE brain imaging, selecting long TR and long TE will result in favoring the signal from T2 time (referred to as T2-weighted (T2w) images), although signal from proton density will also contribute. In a similar way, applying short TR and short TE values will enhance the contribution from T1 relaxation time (T1w images).

Moreover, by taking advantage of relaxation times dependence on magnetic susceptibility, flow rates of liquids, chemical shifts, etc. it is also possible to acquire images containing functional information of an organ (e.g., functional MRI for brain activity [74,75]), flow rates of blood in the vessels (e.g., phase contrast angiography [76]), 3D dosimetry information in radiotherapy [77] or even the relative abundance of a substance in a sample or tissue (i.e., NMR spectroscopy [76]). In other words, MRI provides endless possibilities for applications which lie beyond the conventional imaging of the patient anatomy.

However, in this thesis, T1w and T2w images are only considered as they are routinely used in intracranial radiotherapy treatment planning for target localization.

1.6 Contrast agents in MRI

For most imaging applications, MRI results in adequate natural contrast based on T1, T2 or proton density weighting. In some cases, however, contrast has to be enhanced with the external administration of contrast agents which can selectively reduce the relaxation times of tissues of interest and, hence, increase their contrast with surrounding tissues. Several contrast agents have been introduced in clinical practice. The most commonly used ones are based on the paramagnetic ion of Gadolinium (Gd).

1.6.1 Gd-based contrast agents

Paramagnetic ions are used as contrast agents acting both on T1 and T2 relaxation times. Gadolinium (Gd^{3+}) is the most commonly used one but, as being an ion, it is administered chelated by a molecule to avoid the toxicity of free ions [71], forming the group of the Gd-based contrast agents. Such contrast agents will mainly result in shortening T1 relaxation time in the tissues accumulated and, thus, significantly increasing the brightness in a T1w image. Gd is very routinely used in brain lesion detection, such as multiple brain metastases. Following injection into the body, it is distributed to all perfused tissues but, chelated in a large molecule, cannot cross the blood brain barrier quickly. In tumors, however, the barrier is disrupted which results in the Gd-based contrast agent leaking into the interstitial space, a mechanism which results in a significant increase in T1w signal from the tumor. Gd also reduces T2 relaxation time but the normal rate is still the dominant one [46]. The underlying mechanism that reduces relaxation times is related to the paramagnetic nature of Gd. Its magnetic susceptibility changes the local magnetic field in the vicinity of the molecule, acting as a local field inhomogeneity.

Dosage varies depending on the formulation, imaging application and body weight of the patient. Typical doses for brain lesion localization are 0.1 – 0.2 mmol per kg of

body mass, administered dissolved in saline. The main contra-indications for administration of such contrast agents are poor renal function and pregnancy. Gd-based contrast agents have been linked to nephrogenic systemic fibrosis as a side effect [78,79] which has led to regulatory recommendations by the authorities [46]. Moreover, Gd-based contrast agents have been reported to be deposited in the brain after repeated administrations, although the clinical significance and risks associated with this finding are still unknown [80,81].

1.6.2 Other contrast agents

Manganese (Mn^{2+}) is another paramagnetic ion which has also been used in clinical practice, acting in the same way as Gd-based contrast agents (i.e., significantly reducing T1 relaxation time), although it has not proven as popular.

Superparamagnetic iron oxide nanoparticles (SPIO contrast agents) have also been employed clinically, although they behave very differently compared to Gd-based contrast agents. They act mainly on reducing T2 and T2* relaxation times and, thus, lowering the signal in tissues in which they accumulate, in T2w or T2*-weighted images [46]. They have been used for tumor detection in the liver as they are absorbed by healthy tissues but not by the tumor and, therefore, the latter appears bright in a dark background [71].

2 MR-related geometric distortions

2.1 Introduction

In addition to common image quality indices (such as signal-to-noise ratio, contrast-to-noise ratio, etc.), an imaging modality's accuracy in localizing in space anatomical structures of interest is of paramount importance, especially in the case images are employed in radiosurgery treatment planning. It is well-known that MR images are inherently distorted. Distortion of a few millimeters is not expected to affect typical diagnostic applications. However, if the images are used to identify and delineate a target or a critical organ with minimum spatial error tolerance, then MR-related geometric distortion might set limitations or raise concerns. Particularly for intracranial SRS, spatial inaccuracies of the order of 1 mm may have a significant dosimetric impact (e.g. a significant reduction to the absorbed dose by the target), in cases where steep dose gradients exist (see Chapter 7). Therefore, significance of the geometric distortion depends on the application the image will be employed for.

MR-related geometric distortions have been reported to exceed 25 mm within a field-of-view of 24 cm in a 1.5T MR unit [28]. Spatial accuracy degradation is mainly exhibited at the edges of the imaged volume and increases with increasing field-of-view [33]. Geometric distortions mainly stem from static magnetic field, B_0 , inhomogeneity, gradient field nonlinearity, differences in the magnetic susceptibility of the object/subject being imaged and the chemical shift effect [2]. Other sources of distortions and/or artifacts are related to the eddy currents, temperature drift, aliasing, etc. [37,82–86] which will not be discussed as they lie beyond the scopes of this thesis.

2.2 Gradient field nonlinearity

As analyzed in Section 1.3, NMR signal is tagged with respect to its origin by applying gradient magnetic fields, G_x , G_y , G_z on the three dimensions. Gradient fields are enabled either during excitation (slice selection gradient in 2D pulse sequences), prior to (phase encoding gradient) or during (frequency encoding gradient) the NMR signal read-out at TE. Therefore, gradient fields are strongly associated with the coordinates of the voxel being imaged.

The gradient of the magnetic field is supposed to be uniform throughout the volume being imaged. In other words, when a gradient field is enabled on one dimension, magnetic field is supposed to increase or decrease linearly with respect to distance from the isocenter on this dimension. When the gradient field is enabled on x axis, G_x , the local magnetic field at location x should be:

$$B(x) = B_0 + G_x x \quad (1)$$

The MRI systems are designed to apply a constant G_x with respect to x and, therefore, $G_x \cdot x$ is expected to vary linearly with x location. The same concept applies to the other two dimensions, as well. This is fundamental for encoding the NMR signal in space (see Section 1.3).

However, a considerable deviation from the assumed linearity in space will result to mis-encoding of the signal and, consequently, to a geometric offset for the voxel in the MR image corresponding to the specific location. The image will appear distorted. This is illustrated in Figure 2-1(A). The dashed line represents the assumed linear gradient field while the solid line corresponds to the actual field which deviates from linearity around the position r_0 . The voxel will be imaged at location r'_0 .

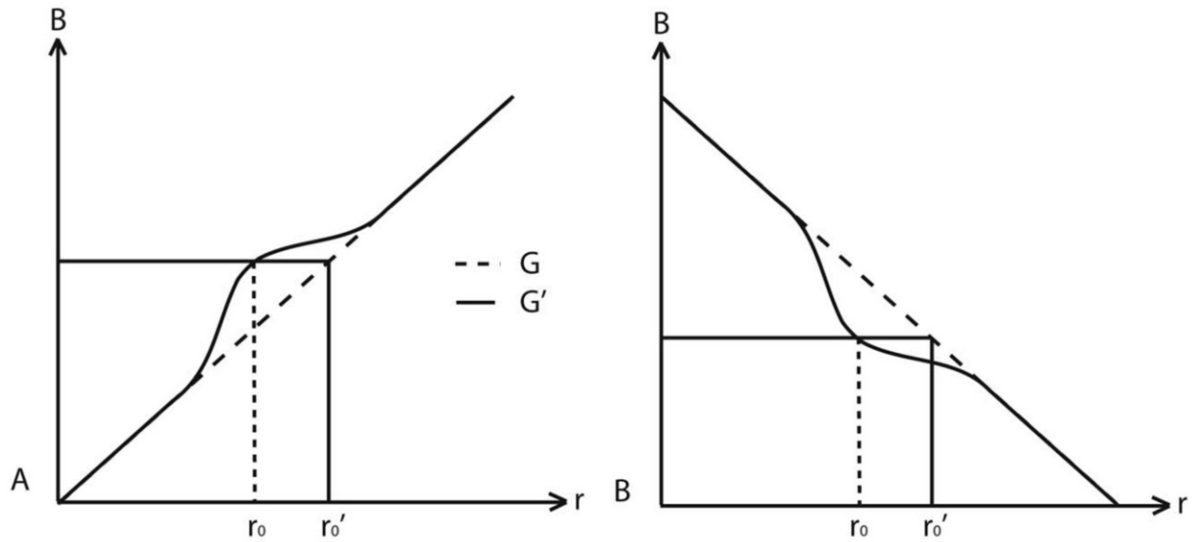


Figure 2-1: Deviation from the assumed gradient field linearity will result in image distortion. (A) Solid line represents the actual gradient field, while the dashed line corresponds to the assumed linear one. A voxel lying at the actual r_0 location will be imaged at the distorted r'_0 location. (B) The gradient field polarity is reversed (decreasing with distance r from the isocenter). This change did not affect the distorted space. Figure is adopted from [27].

In Figure 2-1(B), the polarity of the applied gradient magnetic field is reversed, i.e., gradient field is decreasing with increasing distance r from isocenter. The imaged location r'_0 will not be affected, $r'_0 > r_0$, which is the same as for the case shown in Figure 2-1(A) (gradient field is increasing with distance r). This remark is commonly exploited to differentiate between sources of geometric distortion [2,25–27].

2.3 Static magnetic field inhomogeneity

MRI strongly relies on the application of a static magnetic field, \vec{B}_0 , constant in magnitude and direction, in order to separate the energy levels of the spins, according to the Zeeman effect (see Section 1.2.2). Higher B_0 strength results in enhanced signal-to-noise or shorter scanning times.

A potential local inhomogeneity in the strength of the static magnetic field will result in a strength of B'_0 , which will directly affect the Larmor precessing frequency of the spins, according to the equation $\omega'_0 = \gamma B'_0$. This will also impact the spatial information,

as B'_0 will be summed with the gradient field to encode the location of the imaged volume, according to Equation (1). This is illustrated in Figure 2-2.

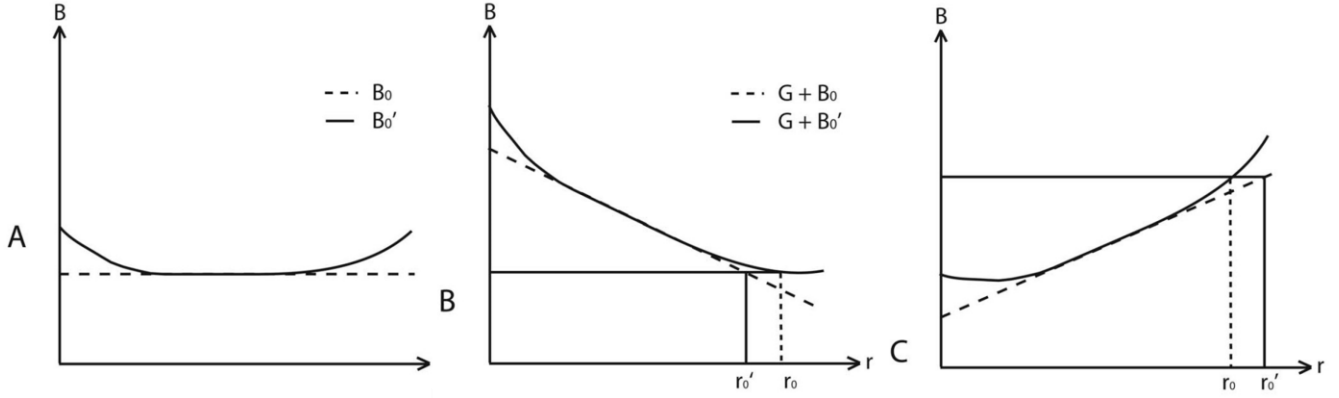


Figure 2-2: (A) The static magnetic field B_0 vector is not homogeneous at the edges of the imaged space. The dashed line represents the assumed homogeneous B_0 , while the solid line corresponds to the actual inhomogeneous B'_0 field. (B) The inhomogeneous field is summed with the linear gradient field, applied for spatial encoding. A voxel lying at the actual r_0 location will be imaged at the distorted r'_0 location, with $r'_0 < r_0$. (C) The gradient field polarity is reversed (increasing with distance r from MR isocenter). This change will directly affect the sign of the distortion in the acquired image, as $r'_0 > r_0$. Figure is adopted from [27].

As shown in Figure 2-2(B), the inhomogeneous B'_0 field, summed with a decreasing gradient field, G , results in a volume actually located at r_0 to be imaged at $r'_0 < r_0$. However, reversing the polarity of the gradient field (Figure 2-2), will result in a distorted image location at $r'_0 > r_0$. In other words, reversing the polarity of the gradient field will change the sign of distortion without affecting the distortion magnitude. This is in contrast to the corresponding remark made for the gradient field nonlinearity related distortion (see Section 2.2).

Another key difference between gradient field nonlinearity and B_0 inhomogeneity related distortions is that the latter is mainly exhibited on the frequency encoding direction (and the slice selection direction in 2D imaging protocols) in typical T1w images, while the former affects all dimensions.

2.4 Magnetic susceptibility difference

The magnetic susceptibility (commonly referred to as volume susceptibility [36]), χ , is an important magnetic property of a material. It indicates whether a material is attracted into or repelled out of a magnetic field. In short, when an external uniform magnetic field $\vec{B}_0 = \mu_0 \vec{H}_0$ is applied inside a material, the actual field \vec{B} inside the material is given by [47]:

$$\vec{B} = \mu_0(\vec{H} + \vec{M}) \quad (2)$$

where \vec{H} is measured in A/m, \vec{M} is the permanent magnetization or the induced magnetization (i.e., magnetic moment per unit volume of the substance measured in A/m), and μ_0 is the vacuum permeability ($4\pi \cdot 10^{-7}$) with units of Tm/A [47] in the SI system convention.

When a material is not permanently magnetized, that is, when \vec{M} is not a constant, the induced magnetization \vec{M} inside the material may be related to the \vec{H} field by a constant susceptibility χ through:

$$\vec{M} = \chi \vec{H} \quad (3)$$

According to Equation (3), the magnetic susceptibility, χ , is dimensionless. Combining Equations (2) and (3):

$$\vec{B} = \mu_0(1 + \chi)\vec{H} = \mu \vec{H} \quad (4)$$

where $\mu = \mu_0(1 + \chi)$ (5) is the magnetic permeability of the material.

Relative permeability, μ_r , is the ratio of the permeability of a specific material to the permeability of vacuum:

$$\mu_r = \frac{\mu}{\mu_0} \quad (6)$$

$$\stackrel{(5)}{\Rightarrow} \mu_r = 1 + \chi \quad (7)$$

Based on the macroscopic behavior under the influence of an external magnetic field, various materials are classified into diamagnetic, paramagnetic, and ferromagnetic materials. According to Equation (4), if the susceptibility $\chi > 0$, the material is

considered as paramagnetic and if $\chi < 0$, the material is diamagnetic. For vacuum, $\chi = 0$ [36,47]. Superconductors are characterized by the smallest susceptibility value, $\chi = -1$, while for soft ferromagnetic materials $\chi > 10^5$. However, for materials involved in MRI, $|\chi| \ll 1$. This is the practical reason for using magnetic susceptibility instead of the relative permeability, μ_r .

Table 2-1: Magnetic susceptibility (volume susceptibility) of various materials or substances found in vivo. Values from [36].

Material/tissue	Magnetic susceptibility
Pure water (37°C)	$-9.05 \cdot 10^{-6}$
Air (NTP)	$0.36 \cdot 10^{-6}$
Human tissues	$-11 \cdot 10^{-6}$ to $-7 \cdot 10^{-6}$
Liver	$\sim 0.0 \cdot 10^{-6}$
Whole blood (deoxygenated)	$-7.9 \cdot 10^{-6}$
Red blood cell (deoxygenated)	$-6.52 \cdot 10^{-6}$
Hemoglobin protein (without Fe ions)	$-9.91 \cdot 10^{-6}$
Cortical bone	$-12.82 \cdot 10^{-6}$
Lipids (stearic acid)	$-10 \cdot 10^{-6}$

Table 2-1 lists the magnetic susceptibility of various substances or materials found in vivo. Although most of the materials listed are diamagnetic (i.e., $\chi < 0$), significant variations in magnetic susceptibility are observed. According to Equations (3) and (4), the local magnetic field inside a substance depends on the local susceptibility and, consequently, B_0 uniformity is inevitably compromised by the presence of materials. As a result, the Larmor precessing frequency of spins inside a substance will also be affected. In an MR image, the center of a uniform material will be mis-encoded in space, resulting in a geometric offset which may or may not be significant depending on the susceptibility value. At material interfaces, due to the abruptly change in susceptibility, geometric distortion and artifacts might be observed in an MR image. More specifically, darker and brighter areas might appear along with surrounding tissues being distorted in the MR space. Figure 2-3 shows a characteristic example.



Figure 2-3: Cranial MRI scan of a patient with mascara on their eyelids. The susceptibility of mascara resulted in the front half of the globes appearing obscured. Figure adapted from [“MRI Artifacts: Mechanism and Control” by C. Ruan].

For the majority of soft tissues, we may assume that their magnetic susceptibility is equal to that of water. For a typical MRI scan for diagnostic purposes, differences in magnetic susceptibility such that $|\chi - \chi_{water}| < 10^{-5}$ are expected to cause minimum or negligible distortion in the image, even if they lie close to the anatomical site of interest [36]. However, if the MR image is employed in treatment planning for advanced radiotherapy applications, for which spatial accuracy is of paramount importance, more strict tolerances may be needed.

Susceptibility-related distortion depends on the employed MR pulse sequence and parameters selected. Moreover, the resulting geometric offset increases with increasing static magnetic field strengths [2], TEs used and with decreasing bandwidth [37]. To reduce susceptibility related artifacts, SE and FSE sequences with very short TEs should be preferred [86].

However, it should be noted that this type of distortion appears only in the frequency encoded direction (for non-EPI sequences) and the slice selection direction (only for 2D sequences). This results to the susceptibility-related distortion being dependent on the relative position of the materials being imaged. If the interface of materials with considerable susceptibility difference is perpendicular to the frequency encoded direction, the effect will be maximized. On the other hand, if the material interface is parallel to the frequency encoded direction, no distortion is expected [87,88]. This is illustrated in Figure 2-4.

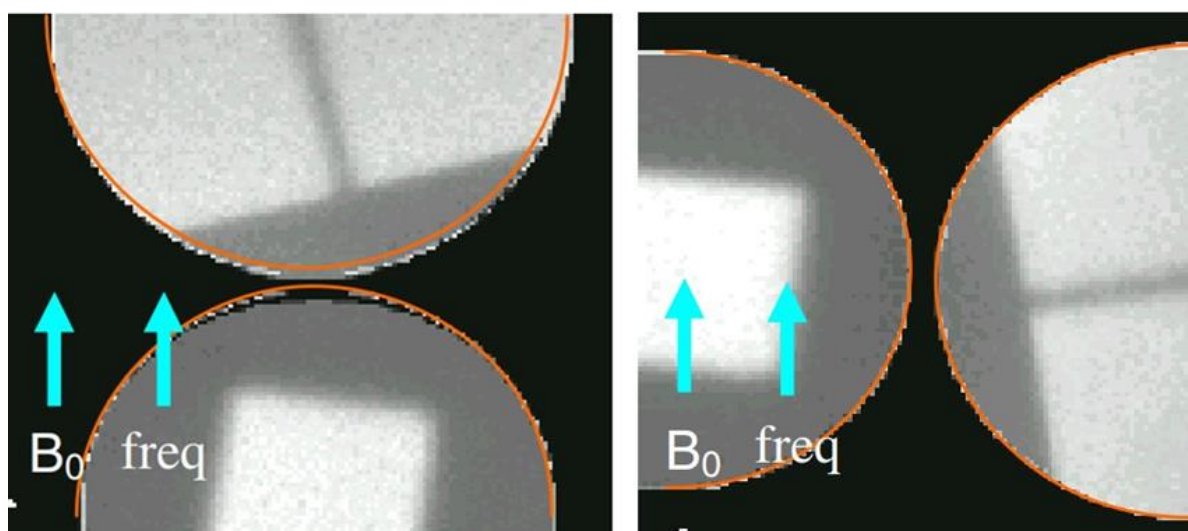


Figure 2-4: Susceptibility-related distortion depends on the orientation between frequency encoding direction and materials interface. (left) Interface is perpendicular to the frequency encoding direction. The actual shape of phantom containers (depicted by red the red contour) is deformed due to the difference in the magnetic susceptibility. (right) The material interface is parallel to the frequency encoding direction. The actual shapes match the ones identified in the image. Figure adopted from [87,88].

2.5 Chemical shift effect

An important physical phenomenon, which is similar to magnetic susceptibility in its electronic nature of origin, but has a different macroscopic manifestation in MRI, is the phenomenon of chemical shift. Chemical shift is more local and related to the time-averaged interaction of the electrons within a molecule (i.e., intramolecular) and/or between neighboring molecules (intermolecular) [47]. Rotating electrons, as charged

particles with spin, induce magnetic field which is anti-parallel to the main magnetic field. Therefore, the chemical shift effect causes a uniform and finite shift in the B_0 static magnetic field experienced by certain nuclei within the molecule. This shift will also impact the Larmor precessing frequency and is proportional to the applied external B_0 magnetic field [47].

At an external magnetic field of 1.5T, the Larmor frequency of a proton spin in the molecule of water is approximately 63.9 MHz, while for a proton spin in a fat molecule it is reduced by 210 Hz. These values apply for an object/subject being scanned at a temperature of 37°C. However, for a phantom at the room temperature of 22°C, the water-fat Larmor frequency shift is 224 Hz [89]. Therefore, large temperature drifts could also cause additional imaging issues in MRI [89–91].

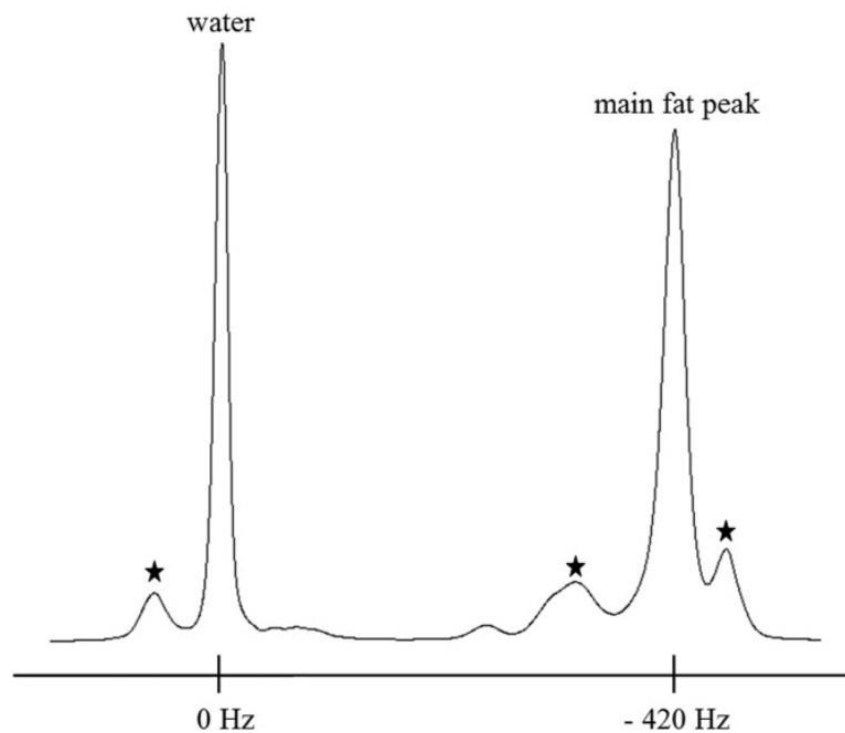


Figure 2-5: NMR spectrum for a mixture of water and fat placed at an external magnetic field of 3.0T. The main fat peak corresponds to a resonance frequency for fat of 420 Hz lower than that of water. Asterisks denote the secondary fat resonance peaks, some of which lie very close to the water resonance peak. Figure adopted from [89].

At a magnetic field of 3.0T, the above-mentioned water-fat shifts are doubled. Therefore, chemical shift related distortion is proportional to the applied external main magnetic

field strength. In a more in-depth analysis, it should be noted that fat exhibits a more complex NMR spectrum. It comprises of several secondary resonance peaks [89], denoted with asterisks in Figure 2-5. However, the secondary peaks' amplitudes are significantly lower than the main peak's amplitude and, therefore, they are often considered negligible.

Similar to the B_0 inhomogeneity and susceptibility related distortions, chemical shift has an impact only on the frequency encoding (for non-EPI pulse sequences) and the slice selection (only for 2D imaging protocols) directions.

2.6 Characterization of MR spatial distortion

According to the above analysis, sources of geometric distortion can be easily grouped based on common characteristics.

The most usual grouping is related to whether the distortion stems from the MRI unit used for image acquisition (system-related distortion) or the patient/object being scanned (patient-induced distortion). Apparently, B_0 inhomogeneity and gradient field nonlinearity are system-related sources of distortion, while chemical shift and susceptibility related distortions are patient-induced. Moreover, several other sources of distortion or artifacts belong to the former group, such as eddy currents, RF inhomogeneity, zipper artifact, slice-to-slice interference, aliasing, etc. Artifacts stemming from the patient's organ movement and temperature rise due to the presence of metal parts are also characterized as patient-induced [37,83–86].

However, a different grouping of sources of distortion is more suitable for the purposes of this thesis, i.e., distortion characterization and correction. In specific, distortions are distinct according to their dependence on the read gradient polarity selection. In the work of Baldwin et al [33], distortions that change sign with the reversal of the frequency encoding direction are referred to as sequence dependent, while the ones that are not affected are referred to as sequence independent. This definition has been adopted throughout this thesis. Based on the above analysis and this definition, gradient field nonlinearity related distortion is sequence independent, as shown in Figure 2-1. Since gradient nonlinearity is also system-related, corresponding distortion in three

dimensions can be measured for a specific MR unit using specially designed phantoms and predicted in subsequent patient scans [27].

Suppose that G_x , G_y and G_z are the three gradient strengths used to encode the entire 3D space. Potential gradient nonlinearities at (x, y, z) will result in corresponding local field shifts $\Delta B_{G_x}(x, y, z)$, $\Delta B_{G_y}(x, y, z)$ and $\Delta B_{G_z}(x, y, z)$ which will be constant, irrespective of the patient being imaged, anatomical site or the read gradient polarity selection. This is very significant as routine clinical practice can be relieved from time consuming gradient nonlinearity distortion measurements.

On the other hand, B_0 inhomogeneity, susceptibility differences and the chemical shift effect are sequence dependent types of distortion, since the read gradient polarity reversal will affect the sign of distortion. Moreover, sequence dependent distortions comprise both system-related and patient-induced distortions and, therefore, cannot be predicted prior to a patient scan. If ΔB_{SD} is the overall sequence dependent field shift, then:

$$\Delta B_{SD} = \Delta B_{B_0} + \Delta B_{MS} + \Delta B_{CS} \quad (8)$$

where ΔB_{B_0} , ΔB_{MS} and ΔB_{CS} are the induced local field shifts due to B_0 inhomogeneity, magnetic susceptibility difference and the chemical shift effect, respectively.

It should be mentioned again that sequence dependent distortion is exhibited only on the frequency encoded (i.e., read gradient) direction for non-EPI, 3D pulse sequences as the ones examined here. In contrast, sequence independent can be demonstrated on any axis.

2.7 Distorted image space

Assuming that the x-axis was selected as the frequency encoding direction in a 3D non-EPI pulse sequence, in absence of sources of field shifts, the magnetic field at a position x will be (Equation (1)):

$$B(x) = B_0 + G_x x$$

and using the relation for Larmor angular frequency, $\omega = -\gamma B$:

$$\omega(x) = -\gamma(B_0 + G_x x) \quad (9)$$

This is the ideal encoding of space, i.e., each frequency, $\omega(x)$, corresponds to a specific location on x-axis. Using FT, it is feasible to trace back the NMR signals recorded to their actual positions on x-axis, relying on their frequency information. However, this is just the ideal case. In practice, local field shifts originate from both sequence dependent and sequence independent types of distortion. Therefore, Equation (1) should be rewritten:

$$B(x) = B_0 + G_x x + \Delta B_{SD}(x, y, z) + \Delta B_{G_x}(x, y, z) \quad (10)$$

$$\Rightarrow \omega(x) = -\gamma(B_0 + G_x x + \Delta B_{SD}(x, y, z) + \Delta B_{G_x}(x, y, z))$$

$$\Rightarrow \omega(x) = -\gamma(B_0 + G_x (x + \frac{\Delta B_{SD}(x, y, z)}{G_x} + \frac{\Delta B_{G_x}(x, y, z)}{G_x})) \quad (11)$$

By comparing the ideal case represented by Equation (9) with the actual case of Equation (11), the voxel will be mapped at the distorted position, x' , because of the induced spatial offset, Δx_{tot} :

$$x' = x + \Delta x_{tot} = x + \Delta x_{SD} + \Delta x_{SI} = x + \frac{\Delta B_{SD}(x, y, z)}{G_x} + \frac{\Delta B_{G_x}(x, y, z)}{G_x} \quad (12)$$

where the first fraction represents the sequence dependent distortion, Δx_{SD} , and the second fraction corresponds to the sequence independent, Δx_{SI} , distortions involved.

In a similar way, for the phase encoded axes, y and z, the resulting distortions, Δy_{tot} and Δz_{tot} , will be:

$$y' = y + \Delta y_{tot} = y + \Delta y_{SI} = y + \frac{\Delta B_{G_y}(x, y, z)}{G_y} \quad (13)$$

$$z' = z + \Delta z_{tot} = z + \Delta z_{SI} = z + \frac{\Delta B_{G_z}(x, y, z)}{G_z} \quad (14)$$

For y and z axes, only sequence independent distortions are present.

Equations (12), (13) and (14) define the distorted image space (x', y', z') and constitute the basis for distortion mapping. Most importantly, they provide the necessary link to the undistorted image space, (x, y, z) , for distortion correction procedures.

2.8 Methods for distortion assessment

2.8.1 The read gradient reversal method

As explained above, sequence dependent distortions change sign with read gradient polarity reversal. Chang and Fitzpatrick [42] proposed a technique that exploits this characteristic for the purpose of distortion assessment. In specific, the authors proposed to acquire two image series with identical imaging parameters except for a reversal in the read gradient polarity. For instance, if according to the imaging protocol, the frequency encoding gradient, G_x , is applied from the L towards the R side of the patient (L→R), in the additional scan the gradient field is reversed (i.e., R→L) with all other imaging parameters remaining unchanged. Gradient field reversal will also reverse the sequence dependent distortions (i.e., same magnitude, opposite sign). Therefore:

$$\Delta x_{L \rightarrow R} = x'_{L \rightarrow R} - x = \frac{\Delta B_{G_x}(x, y, z)}{G_x} + \frac{\Delta B_{SD}(x, y, z)}{G_x} \quad (15)$$

$$\Delta x_{R \rightarrow L} = x'_{R \rightarrow L} - x = \frac{\Delta B_{G_x}(x, y, z)}{G_x} - \frac{\Delta B_{SD}(x, y, z)}{G_x} \quad (16)$$

with $\Delta B_{SD}(x, y, z) = \Delta B_{B_0} + \Delta B_{MS} + \Delta B_{CS}$, as defined in Equation (8), $x'_{L \rightarrow R}$ and $x'_{R \rightarrow L}$ are the positions in the distorted forward and reversed image scans, while x is the position in the actual undistorted space.

Subtracting or summing Equations (15) and (16), the sequence dependent, Δx_{SD} , and the sequence independent, Δx_{SI} , distortions will be:

$$\Delta x_{SD} = \frac{\Delta x_{L \rightarrow R} - \Delta x_{R \rightarrow L}}{2} = \frac{x'_{L \rightarrow R} - x'_{R \rightarrow L}}{2} \quad (17)$$

$$\Delta x_{SI} = \frac{\Delta x_{L \rightarrow R} + \Delta x_{R \rightarrow L}}{2} = \frac{x'_{L \rightarrow R} + x'_{R \rightarrow L}}{2} - x \quad (18)$$

In Equation (17), absence of the true position, x , in the undistorted space, allows for a straightforward evaluation of sequence dependent distortions, as long as $x'_{L \rightarrow R}$ and $x'_{R \rightarrow L}$ can be identified and matched in the two image scans. Knowledge of the true position, x , is not required. This is the most important advantage of the read gradient polarity reversal technique. On the other hand, distortion detection requires that

anatomical landmarks or distinct points, serving as Control Points (CPs) for $x'_{L \rightarrow R}$ and $x'_{R \rightarrow L}$ determination, are accurately identified, localized in the two image stacks and paired. Using specially designed phantoms for distortion detection [27,28,33,34,92–96], such CPs are well defined in space with adequate contrast for accurate localization in the image stacks. However, in a patient scan, identification of distinct landmarks serving as CPs is not straightforward, in addition to not being dense in space. This was addressed by Chang and Fitzpatrick [42] who used Runge-Kutta integration in the two image series. Reinsberg et al [39] proposed usage of mutual information and cross correlation-based image co-registration between the two MR scans.

For the assessment of sequence independent distortions, Δx_{SI} , Equation (18) requires that the true position, x , is determined. The latter can be performed by relying on other 3D imaging modalities that can be considered as golden standards in terms of geometric accuracy, such as the CT [26,27].

For use in clinical practice, the main drawback of this method is that it requires two image scans, effectively doubling the patient scanning time. It should be noted that the patient should not move during the image acquisitions which cannot be guaranteed in the case the treatment protocol does not involve an immobilization frame.

2.8.2 The field mapping technique

A different approach for sequence dependent distortion detection was proposed by Jezzard and Balaban [41] which, however, also involves an additional MR scan of the patient. It relies on the fact that the phase, φ , of the NMR signal depends on TE. More specifically, phase, φ_1 , at the position (x, y, z) and at time $t = TE_1$ is sensitive the local magnetic field perturbation due to sequence dependent distortions, $\Delta B_{SD}(x, y, z)$ and is given by:

$$\varphi_1(x, y, z, TE_1) = \varphi_0 - \gamma \cdot \Delta B_{SD}(x, y, z) \cdot TE_1 \quad (19)$$

where φ_0 is a constant phase offset, independent of time, induced by the local conductivity of the object being scanned [72]. In a similar way, phase, φ_2 , at the same position but at a time $t = TE_2$ is:

$$\varphi_2(x, y, z, TE_2) = \varphi_0 - \gamma \cdot \Delta B_{SD}(x, y, z) \cdot TE_2 \quad (20)$$

By subtracting Equations (19) and (20), and solving for the local magnetic field perturbation [72]:

$$\Delta B_{SD}(x, y, z) = \frac{\varphi_1 - \varphi_2}{\gamma(TE_2 - TE_1)} = \frac{\Delta\varphi(x, y, z, \Delta TE)}{\gamma(TE_1 - TE_2)} \quad (21)$$

Equation (21) is the basis of distortion detection using the field mapping technique. In order to extract $\Delta B_{SD}(x, y, z)$, a single scan is not sufficient and two gradient echo scans must be collected, with echo times TE_1 and TE_2 . If transient field effects are not a problem, one scan can be obtained with two echo times, a sequence often referred to as dual echo gradient echo. Otherwise, an interleaved scan can be run where the second echo time has the exact same gradient structure as the first echo. All phase encoding timings relative to the read gradient should be kept invariant, that is, both the read and phase encoding gradients are slid along as a group to the desired echo time [72].

Having determined the magnetic field perturbation map, $\Delta B_{SD}(x, y, z)$, calculation of the sequence dependent distortion map is straightforward (assuming the x-axis as the frequency encoding direction in a non-EPI 3D pulse sequence):

$$\Delta x_{SD} = \frac{\Delta B_{SD}(x, y, z)}{G_x} \quad (22)$$

where G_x is the strength of the frequency encoding gradient field in T/m.

The most important advantage in using the field mapping technique for measuring sequence dependent distortions is that it does not require distinct points (i.e., CPs) or landmarks to be identified, as is the case for the read gradient polarity reversal method. In fact, every voxel being imaged with adequate signal-to-noise ratio and reliable phase information serves as a CP. Therefore, it can be employed in both phantom and patient images. Although this method also burdens the patient scanning time, the required set of images can be parameterized to last a tolerable amount of time [33].

2.8.2.1 *Wrapped phase*

On the other hand, the field mapping technique, requires a time-consuming post-imaging process known as phase unwrapping.

In an MR image, the information for every voxel involves both the amplitude and phase of the signal received. Therefore, the signal, $S(x, y, z)$, corresponding to each voxel lying at (x, y, z) is represented by a complex number with imaginary, I , and real, R parts, or equally, with magnitude, M , and phase, φ :

$$S(x, y, z) = R + Ii = Me^{i\varphi} \quad (23)$$

Thus, in a typical MR scan, the acquired set of data that can be exported actually comprises of up to four image stacks, i.e., R , I , M and φ . The phase, φ , of the complex number is the angle of the decaying magnetization at the voxel location. However, this is not yet the phase information, φ_1 and φ_2 , required by Equation (21) because φ is wrapped in the $(-\pi, +\pi]$ interval [97,98]. Phase wrapping occurs when the transverse magnetization vector at a given location has in fact been around the circle one or more times. For example, if the wrapped phase is 45° , there is no way to tell if it is actually 405° , 765° , -315° or -675° , etc [47]. Mathematically, the principal value in the $(-\pi, +\pi]$ interval of the complex number argument is measured in an MR scan.

2.8.2.2 1D phase unwrapping

According to the above analysis, in order to derive the actual phase, unwrapped in the $(-\infty, +\infty)$ range some multiple of 2π should be added or subtracted [47]:

$$\varphi_{unwrapped} = \varphi_{wrapped} + (2\pi) \cdot n \quad (24)$$

where n is an integer.

Phase unwrapping is performed sequentially from one voxel to the next by examining whether the phase difference between an unwrapped voxel and a neighboring wrapped one is larger than $+\pi$ rad or less than $-\pi$ rad. In these two cases, an appropriate number of multiples of 2π are added or subtracted to the wrapped phase of the voxel in order for the difference to be less than π . This process is repeated for all neighboring still-wrapped voxels and then for the neighbors of the neighbors, etc. until all voxels in the image have been unwrapped.

Figure 2-6 presents the phase unwrapping concept in one dimension. In Figure 2-6(a), the actual phase values are given, while in Figure 2-6(b) the phase is wrapped in the

$(-\pi, +\pi]$ interval. Large phase discontinuities are observed at points A, B, C and D. Starting from the left-hand side towards the right, phase is $+\pi$ at point A and $-\pi$ at the neighboring point B. This abrupt change suggests that the phase has been wrapped and the actual phase is slightly larger than $+\pi$ rad. Thus, we add $+2\pi$ rad at point B in order to determine the actual phase at the corresponding point B shown in Figure 2-6(a). In a similar way, between points C and D phase is discontinuous ($-\pi$ at point C and $+\pi$ at point D). Therefore, phase is evidently wrapped at point C and we should add -2π rad in order to calculate the actual phase. This quantity will also be added to the wrapped phase of all subsequent points till the next wrap, in order to acquire the actual phase shown in Figure 2-6(a). Wrapping points like points B and D are called π -bounce points [97]. Such π -bounce points are also shown in a 2D image plane in Figure 2-7(a).

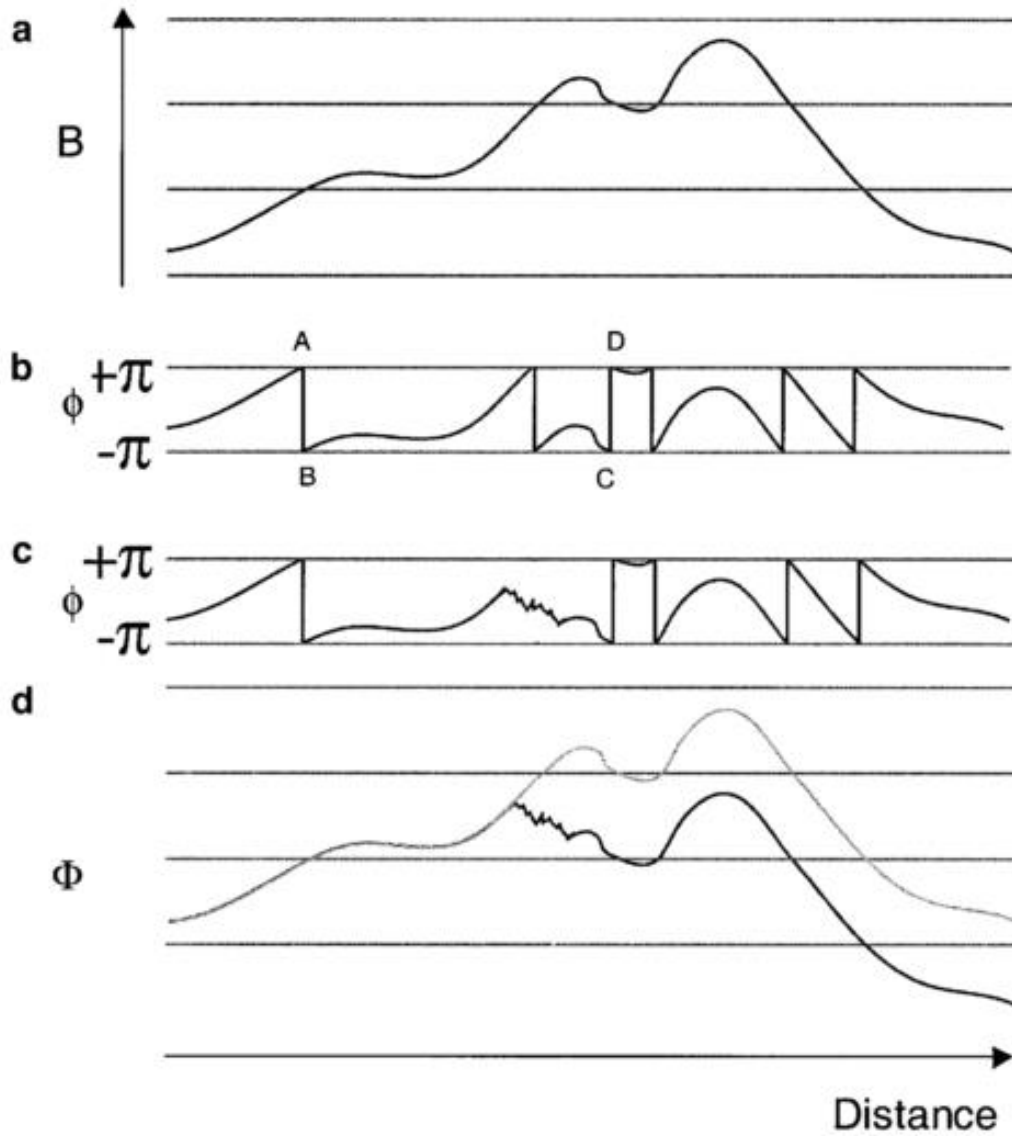


Figure 2-6: 1-D phase unwrapping. (a) Actual phase distribution. (b) Wrapped phase values. (c) Wrapped phase values including noise. (d) The noise resulted in errors in the unwrapping procedure. Consequently, the unwrapped phase distribution differs by 2π rad from the actual one. Furthermore, the unwrapping errors propagates to all subsequent points. Figure adopted from [97].

It is obvious how the unwrapping process diffuses from one point to the next. Changing the value of the phase at one point will propagate and affect the phase values of all the following points. Although in theory unwrapping is rather simple and straightforward, in practice several limitations exist. First of all, we have assumed that the local magnetic field does not abruptly vary in the above analysis. In such a case, a phase difference larger than π between two neighboring voxels could stem from actual very steep local magnetic field variations. However, mis-identifying this point as a wrapping point

would result in a large error of 2π rad to the unwrapped distribution. Furthermore, this error will propagate to all subsequently unwrapped points. In a more realistic case, the presence of noise in the acquired wrapped phase distribution has also been completely ignored in the analysis so far. For instance, if at a point where wrapping actually occurs (i.e., a π -bounce point) the local noise in the image is large enough to reduce the difference between wrapped and unwrapped voxels to less than π rad, then the wrapping point will not be identified and a multiple of 2π rad will not be added or subtracted. This error will also propagate to all subsequently unwrapped phase values. This is illustrated in Figure 2-6(d) where the π -bounce point before point D is obscured by increased noise levels in the acquired wrapped phase images (Figure 2-6(c)). As a result, all subsequently unwrapped phase values differ from the actual one by 2π rad. Therefore, even a small number of voxels with increased noise levels might catastrophically affect the unwrapped phase distribution.

2.8.2.3 Guided 3D phase unwrapping

In 1D phase unwrapping, unwrapping errors cannot be avoided and recovering of the lost phase information is impossible. In a 3D phase unwrapping process, there are several options for the unwrapping path to be followed and, therefore, areas that are prone to unwrapping errors (e.g., reduced signal-to-noise areas) can be unwrapped last. A correctly unwrapped phase distribution should be independent from the path followed. Several unwrapping algorithms have been proposed which differ with respect to the way the unwrapping path is chosen. A few of the most widely used ones are Jenkinson's method, Constantini's technique and Goldstein's branch cut method [99–102]. The main idea behind these algorithms is to select the unwrapping path that first deals with the most reliable areas of the image and leaves the areas suspected for unwrapping errors to be unwrapped last. Therefore, if unwrapping errors are introduced in the suspected areas, they will be contained locally and will not propagate to the rest of the image.

Cusack and Papadakis [97] proposed a 2D iterative phase unwrapping algorithm especially for MRI field mapping and distortion detection. It is a guided unwrapping algorithm which first defines a noise estimator field. This field is used to guide the

unwrapping path towards the less noisy areas of the image first. Three approaches to define the noise estimator field are proposed [97]:

1. The magnitude of the image acquired with the largest TE, negated.
2. For each voxel, the minimum magnitude of the voxel across the two images acquired with different TEs
3. The “pole field” of the image. As unwrapping is path independent in a noise-free map, the sum of signed phase wraps around any closed loop in the image should be zero. Breaking down any loop to small rectangular loops of 2x2 voxels, if there is noise in a region that destroys path independence, there will always be nonzero sums around at least one of these small loops. Points around a nonzero sum loop are referred to as “poles”. The distribution of poles in the image constitutes the pole field, serving as the noise estimator field.

Any of the above approaches perform equally well [97]. Therefore, in this work the simplest approach (1) was selected and developed in MATLAB. The algorithm was expanded to work in 3D, simply by extending the path selection option to the through-plane dimension.

Having defined the noise estimator field that will guide the unwrapping process in the developed algorithm, the next crucial step is to select the starting voxel(s), referred to as “seed(s)”. By definition, the phase of a seed is not wrapped, i.e., $n = 0$ in Equation (24). In order to ensure this prerequisite, the seed is selected to be at a region of minimum noise, away from material interfaces and close to the MR scanner’s isocenter. Then, the “current threshold” for the noise estimator is set to the lowest value found in the entire noise estimator field. The seed(s) is flagged as “unwrapped” and set as the “current voxel”. Then, the iterative part of the developed algorithm is summarized in the following steps:

1. For each voxel flagged as unwrapped
 - For each neighboring voxel:
 - If its noise field is below the current threshold, unwrap the neighboring voxel and flag it as unwrapped
 - If its noise field is above the threshold, continue
2. When this step is completed for all voxels flagged as unwrapped, increase the noise estimator field by a pre-defined step and repeat step (1)

The algorithm developed in MATLAB for the purposes of this thesis is given in the Appendix. It was employed to unwrap the phase difference between two TEs in order to use Equation (21) for distortion detection, implementing the field mapping technique. Figure 2-7 shows results obtained during the validation process of the developed routine, using a homogeneous cylindrical phantom and a 3.0T MR scanner.

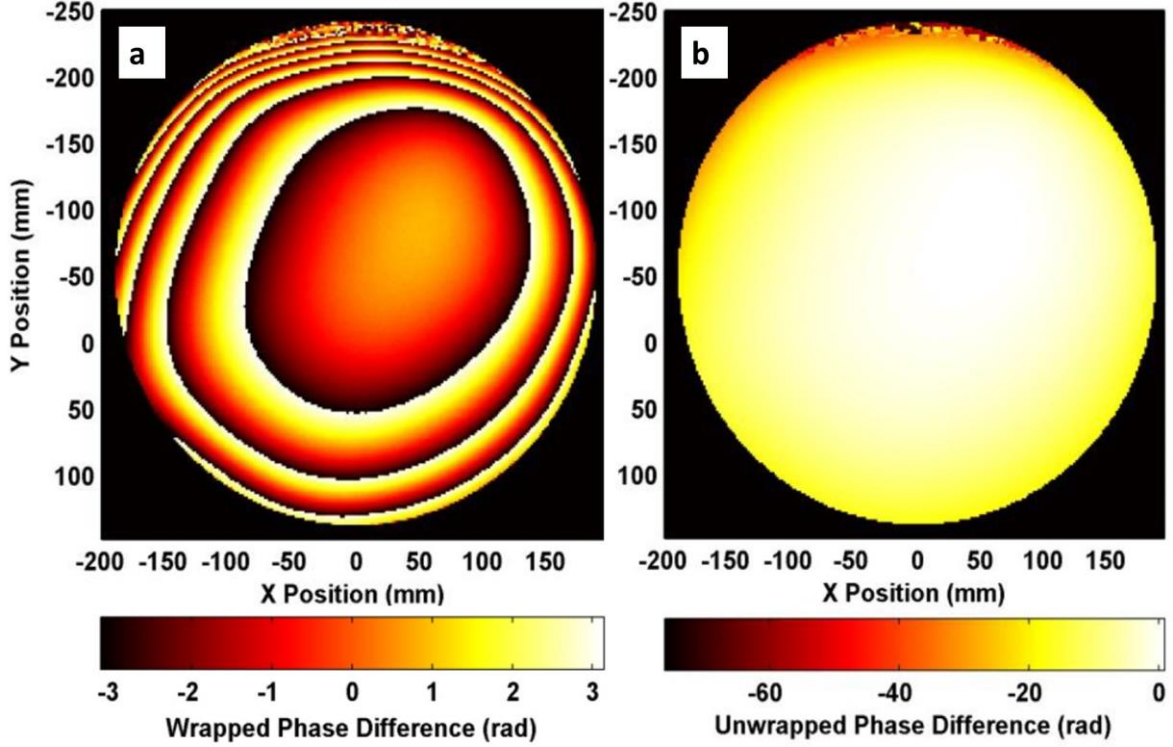


Figure 2-7: Indicative results of the 3D guided phase unwrapping algorithm. (a) Wrapped phase difference distribution for a large homogeneous cylindrical phantom and a 3.0T MR scanner. Several wrapping points are observed. An area of increased noise is detected at the top. (b) Corresponding unwrapped phase difference using the algorithm developed for the purposes of this thesis. Unwrapping errors are induced in the noisy area but did not propagate to the rest of the image.

2.9 Distortion correction

If the distortion map (i.e., $(\Delta x_{tot}, \Delta y_{tot}, \Delta z_{tot})$ in Equations (12), (13) and (14), respectively) has been determined in 3D, distortion correction is a simple 3D interpolation step between the distorted and undistorted image spaces [28]. Ideally the distortion map should involve all sources of MR-related geometric distortion, both sequence dependent and sequence independent. If they have been determined

separately, they are first combined into a single distortion map [33]. Moreover, if distortion maps have been calculated in a different gradient strength than the one of the image to be corrected, the distortion magnitudes for all axes should also be rescaled according to Equation (15). Prior to correction, the distortion map can be interpolated to the same resolution as the image to be corrected [33].

As a last step, following image correction, the signal of every voxel should also be corrected. In the distorted image space, a given voxel has been stretched or compressed to a different size, affecting its apparent density and brightness in the distorted image. In order to account for this effect, a rescale factor is applied to each voxel's intensity, known as the Jacobian determinant [28]. The Jacobian is directly calculated from the distortion map $(\Delta x, \Delta y, \Delta z)$ individually for each voxel lying at the location (x, y, z) , according to the equation [28]:

$$J(x, y, z) = \begin{vmatrix} 1 + \frac{\partial(\Delta x)}{\partial x} & \frac{\partial(\Delta x)}{\partial y} & \frac{\partial(\Delta x)}{\partial z} \\ \frac{\partial(\Delta y)}{\partial x} & 1 + \frac{\partial(\Delta y)}{\partial y} & \frac{\partial(\Delta y)}{\partial z} \\ \frac{\partial(\Delta z)}{\partial x} & \frac{\partial(\Delta z)}{\partial y} & 1 + \frac{\partial(\Delta z)}{\partial z} \end{vmatrix} \quad (25)$$

The signal intensity $S_{dist}(x', y', z')$ in the distorted image space will be corrected to $S_{true}(x, y, z)$ in the undistorted image space according to:

$$S_{true}(x, y, z) = J(x, y, z) \cdot S_{dist}(x', y', z') \quad (26)$$

As with all digital images, distortion distributions and corresponding signal intensities are discrete in space and, therefore, partial derivatives in Equation (25) can be calculated by the finite distortion differences between neighboring voxels [28].

3 MRI in stereotactic radiosurgery treatment planning

3.1 Introduction

In conventional radiotherapy applications, a CT scan is primarily used for treatment planning purposes as it provides an estimate of the electron density distribution in the patient, required for dose calculations by the treatment planning systems. MRI is often employed in order to take advantage of the superior soft tissue contrast it exhibits, which is necessary for tumor and soft tissue delineation [1,103]. Especially for brain tumor localization, MRI provides unsurpassed soft tissue contrast (as shown in Figure 3-1), following administration of appropriate contrast agents. Incorporating MRI in treatment planning also significantly reduces inter- and intra-observer contouring variability for many disease sites [103]. However, employing MRI in radiotherapy treatment planning comes at the expense of spatial accuracy due to the related geometric distortions.

The two imaging modalities are often combined, following a spatial co-registration procedure. In addition to MR-related geometric distortions, the registration process involved introduces an additional spatial uncertainty which has been reported to reach up to a few millimeters for cranial scans [53]. Patient positioning uncertainties, cranial/tumor motion during treatment [54], as well as dose delivery system mechanical uncertainties could also compromise radiation dose delivery accuracy. Nevertheless, in the vast majority of extracranial irradiations, spatial uncertainties are taken into account by introducing margins to the defined clinical target volumes. In specific, the contoured target is deliberately expanded in order to determine the planning target volume (PTV). Planning of radiation dose delivery and relevant dose distribution calculations are performed by regarding the PTV as the final target.

Over the last decades following the technological advancements, several advanced radiotherapy treatment techniques have emerged and are being increasingly used in clinical practice. Intensity Modulated Radiation Therapy (IMRT), Volume Modulated Arc Therapy (VMAT), SRS, Stereotactic Body Radiation Therapy (SBRT) as well as proton therapy (PT) are treatment delivery techniques which employ steep dose gradients to achieve high target conformance and coverage while sculpting dose away from critical organs. Higher dose conformity, however, requires and inspires stricter spatial uncertainty tolerances. This is particularly true for SRS applications, in which high dose levels are delivered in a single or few fractions. This thesis mainly focuses on the use of MR images in SRS treatment planning.

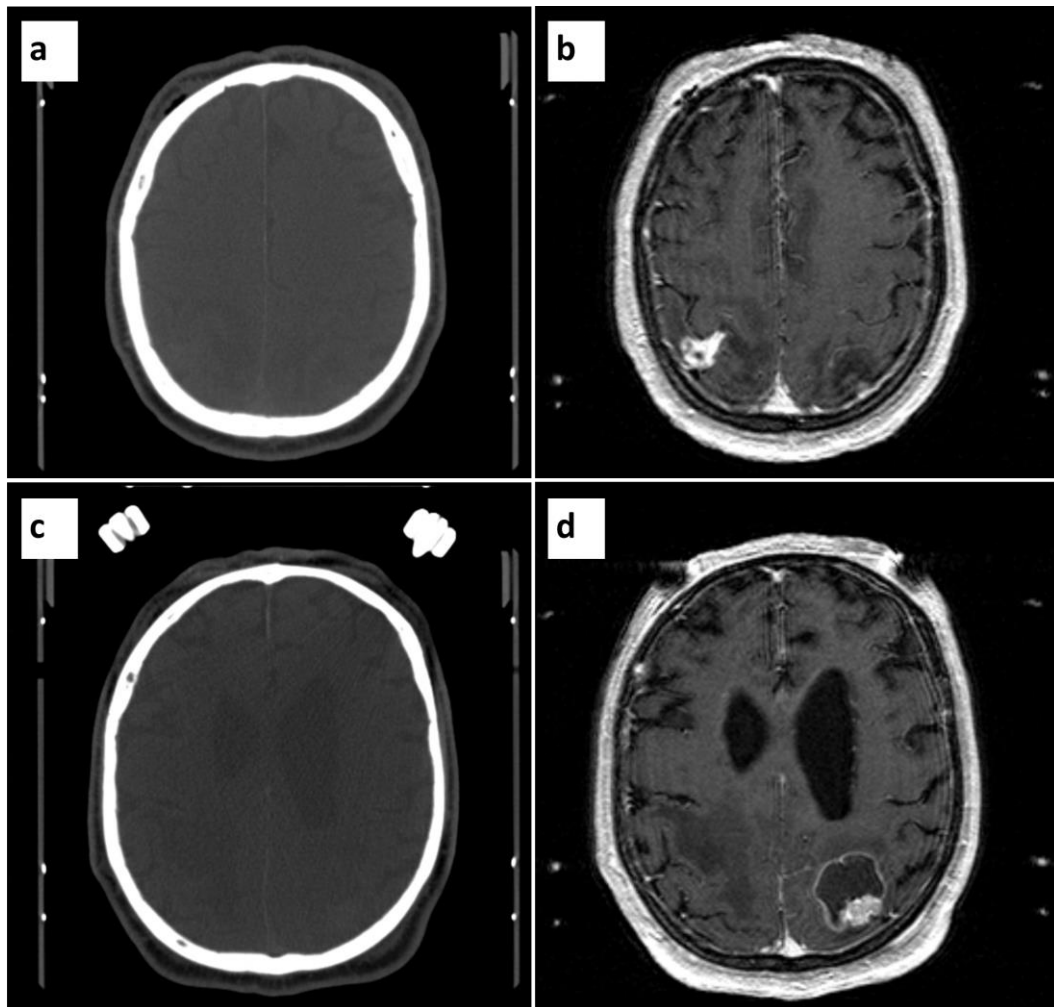


Figure 3-1: Examples of the superior soft contrast in MR compared to CT for brain tumor delineation. (a, c) Axial slices of a patient with multiple brain metastases. (b, d) Same slices acquired with MRI, following administration of contrast agent.

3.2 Historical overview of Stereotactic Radiosurgery

SRS is a well-established treatment approach for the management of a wide variety of lesions, mainly in the brain [7,13,22,23,104–107]. The efficiency of this technique is based on the precise delivery of accurately registered dose distributions to the target, facilitating restriction of the absorbed dose to the surrounding critical structures [108]. Using steep dose gradients, dose is delivered in a single or a few dose fractions [63].

Lars Leksell is considered as the pioneer in SRS. In 1951, he adapted methods employed in stereotactic surgery to external radiation dose delivery [109], even though stereotactic surgery was still in its early stages as well [110]. The first SRS procedures were done using an orthovoltage X-ray tube and a stereotactic frame mounted on the patients, for the treatment of trigeminal neuralgia [108]. He also invented the term stereotactic radiosurgery. Orthovoltage x-ray tubes were abandoned and efforts were made to apply SRS using proton beams. The invention of Gamma Knife (GK) in 1968 by Lars Leksell and his colleagues is certainly a milestone in the history of SRS. In the first model, the treatment delivery unit consisted of 179 ^{60}Co sources placed within a spherical sector, all focusing at a single point [111].

The development of linac-based SRS is set in the 1980's [112–117]. Compared to the GK, linear accelerators were less expensive, ubiquitous and provided a greater variety of collimators which allowed for the use of single isocenters when treating patients with larger targets. A debate regarding the merits of GK in comparison with linac-based SRS soon emerged [108]. In the 1990's, introduction of advanced stereotactic frames raised another debate related to fractionation [63,108]. Non-invasive frames allowed for SRS dose delivery in a few fractions in contrast to the conventional approach of single fraction SRS [118]. Fractionated SRS is often referred to as stereotactic radiation therapy (SRT), although this debate has not been settled yet [108,119].

In the same decade, a 6MV linear accelerator was attached to the end of a commercially available industrial robotic arm which led to the invention of the CyberKnife system by John Adler. The goal was to apply SRS to extracranial anatomical sites and, therefore, the stereotactic frame had to be omitted [108], introducing frameless SRS. CyberKnife

SRS has significantly evolved, proven successful for intracranial targets [120–122] while it has been applied to several other anatomical sites such as the spine, the lung and the prostate [123–125].

Today, apart from the GK and CyberKnife (commercialized by Elekta and Accuray, respectively), several other SRS treatment planning systems and/or treatment delivery units have been introduced by various vendors such as BrainLab, Varian and Radionics. Regarding the management of multiple brain metastases (i.e., the main focus of this thesis), SRS is being increasingly used as the sole treatment technique or adjuvant to whole brain radiation therapy (WBRT) [126], demonstrating longer survival rates compared to WBRT alone [127].

3.3 The Gamma Knife Perfexion system

For single-fraction SRS applications, the GK system is mainly comprised by the treatment delivery unit, the Leksell stereotactic frame and the GammaPlan treatment planning system.

In this section, the individual components are briefly described. Emphasis is given in the definition of the stereotactic space as well as the image registration procedure of the planning image coordinate system to the stereotactic space, as more relevant to the scopes of this thesis.

3.3.1 The GK Perfexion treatment delivery unit

Several GK models have been introduced in the market, including the models U, B, C, 4C and PerfexionTM [128]. The underlying concept behind all introduced GK treatment delivery units is the use of 192-201 ⁶⁰Co sources of high specific activity and a collimator system that focuses the emitted photon beams to a specific point within the stereotactic space, often referred to as the Unity Center Point (UCP). This design allows for multiple beam deliveries simultaneously, reducing the dose delivered to the surrounding healthy tissue and achieving high dose gradient in the vicinity of the UCP.

The current model of the GK irradiation unit is the Perfexion, in which sources configuration was entirely redesigned. Compared to previous models, where all (201) ^{60}Co sources are fixed on a truncated hemispherical surface exhibiting a constant source to focus distance (SFD) of ~400 mm, in Perfexion the 192 ^{60}Co sources are equally distributed over 8 sectors in a cylindrical configuration consisted of 5 rings exhibiting SFDs varying from 374 to 433 mm [128–132]. Each sector can be moved independently along a conical surface to facilitate alignment of the sources with any of the three available collimation channels, labeled as 4 mm, 8 mm and 16 mm. A graphical representation of the PFX sources configuration is given in Figures 3-2(a) and (b). Provided, however, that sectors' motion does not include rotations, accurate source-channel alignment is only achieved for the 4 mm collimator, whilst for the 8 mm and 16 mm collimators the corresponding alignment is hindered by a small geometric shift and tilt (see Figures 3-2(c) and (d)) [131].

Collimation channels are drilled on a 120 mm thick, cone-shaped shielding block made of tungsten [131]. There are 576 channels in total, 192 for each collimator size. Each channel comprises several coaxial cylinders of varying radii depending on collimator size and source ring. The radioactive sources consist of cylindrical ^{60}Co pellets of 1 mm radius and 1 mm height. The number of pellets and, hence, the total height of a source-cylinder varies from 10 to 20 pellets according to the specific activity of each pellet (with a nominal value of 17–18 pellets) in order to deliver an isotropic dose distribution at the UCP [133,134]. Each ^{60}Co source is housed by an aluminum-based bushing enclosed in a stainless steel capsule [131]. In Figures 3-2(c) and (d) the actual geometry of the sources in Perfexion is graphically illustrated.

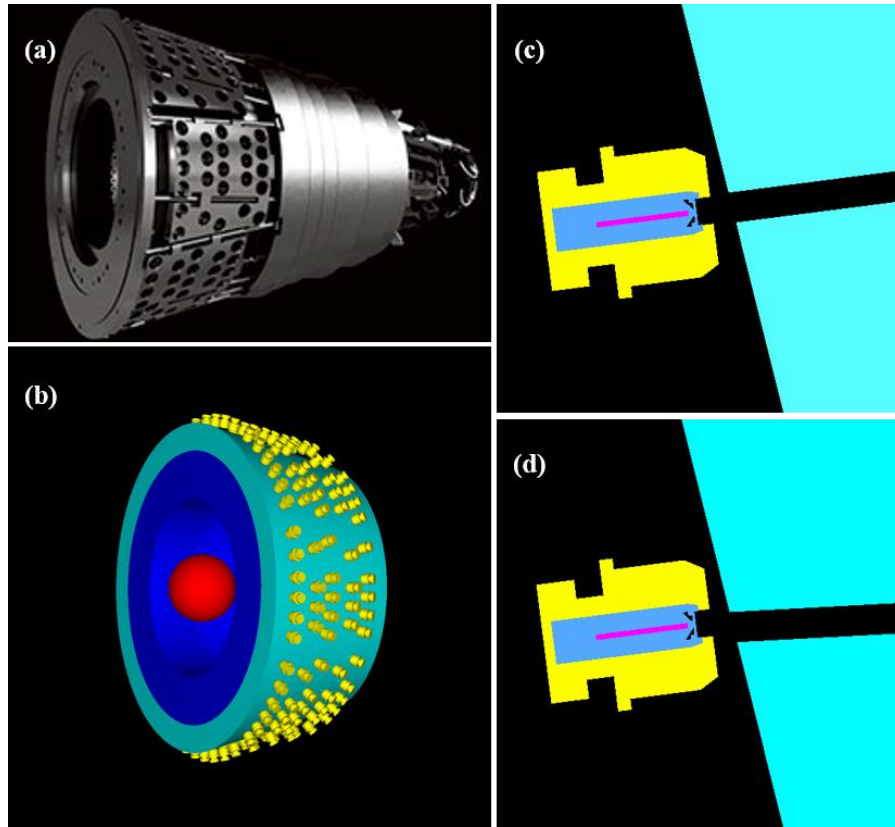


Figure 3-2: (a) A graphic illustration of the actual geometry of the Perfexion irradiation unit. Each sector accommodates 24 ^{60}Co sources, which are arranged in five rings and can be independently moved upon a conical surface to align with the channels of any of the three available collimator sizes. (b)–(d) Pictorial description of the comprehensive Perfexion simulation model developed for Monte Carlo dosimetric calculations. (b) A cross-sectional view (plane xz) of the simulation model geometry for the case that all sources are aligned with the 16 mm collimation channels. The following parts are distinguishable: (i) the source bushing (yellow), (ii) the primary collimator consisting mainly of Pb (cyan), (iii) the secondary collimation system consisting mainly of tungsten (dark blue) and (iv) the spherical phantom used to obtain dosimetry results (red). (c) A ^{60}Co source is accurately aligned with the collimation channel of the 4 mm collimator. The ^{60}Co pellets are depicted in magenta. (d) The same source has been moved and positioned to deliver a 16 mm shot. A small geometric shift and tilt is induced between the source's central axis and the collimation channel. In sub-figures (c) and (d), note that the capsule (light blue) interleaves the space between the source and the collimation channel, while this is not the case for the bushing part.

3.3.2 The Leksell stereotactic frame and stereotactic space

Efficiency of an SRS application relies on spatially accurate dose delivery to the target. Towards that end, stereotactic frames are often used for patient immobilization and definition of the stereotactic space, in which targets and critical organs have been registered during patient imaging and treatment planning. Such minimally-invasive frames are also used in stereotactic surgery. In fractionated SRS, however, frames are usually replaced by thermoplastic masks (facemasks) and accompanying patient motion detection systems [135].

In single-fraction GK SRS, the Leksell stereotactic frame model G is used for these purposes. It consists of the CT and MR indicator boxes (used in CT and MR imaging, respectively), the Leksell stereotactic frame model G (hereinafter, will be referred to as frame), and other auxiliary apparatuses [136]. The CT or MR indicator box is used to determine target coordinates using a system of N-shaped fiducials located at the L, R and P sides of the patient. The frame consists of a rectangular base ring (hereinafter, will be referred to as frame base) (shown in Figure 3-3) and four posts which are attached to the patient's head using four pins (shown in Figure 3-4). The indicator box is fixed on the ring using snap-on clips. The front piece of the frame base (i.e., A patient side) is removable and is either straight or curved [48,49]. In both cases the frame base forms a closed loop. In Figure 3-4, all the main parts comprising the Leksell frame are highlighted.

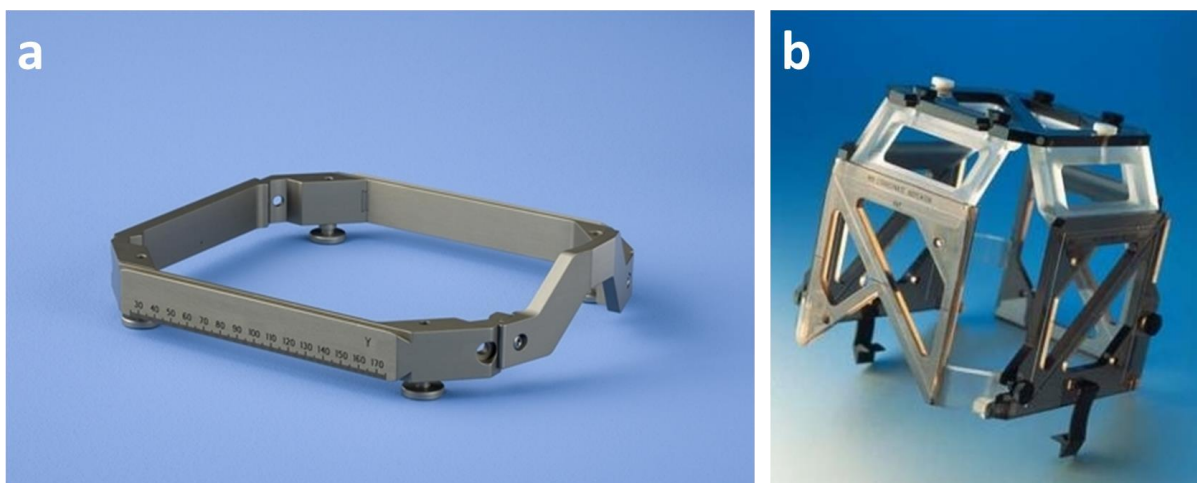


Figure 3-3: (a) The frame base of the Leksell stereotactic frame model G. (b) The MR indicator box. Images taken from [elekta.com].

The Leksell stereotactic space is defined by the MR and/or CT indicator boxes (Figure 3-3(b) and Figure 3-4) which incorporate the system of N-shaped fiducials. In particular, the fiducials provide adequate contrast in the CT or MR image stacks and, therefore, on any axial, sagittal or coronal slice they are identified as three bright marks on each side. An example of a CT and MR cranial image of a patient with the frame and the indicator box fixed is shown in Figure 3-1. Identification of the six marks and calculation of relative distances between them provides the necessary information of

the slice location within the stereotactic space. It is crucial that these marks are correctly identified and that the image is not severely distorted or defected in the vicinity of the fiducials, as this would result in mis-registering their locations [137].

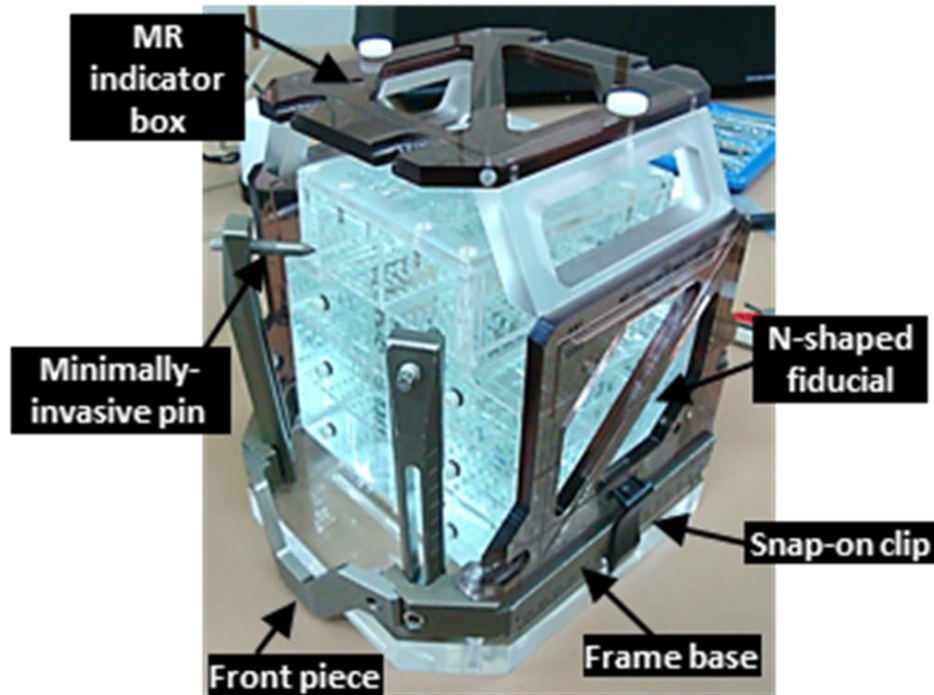


Figure 3-4: All parts comprising the Leksell stereotactic frame model G. The frame base and the MR indicator box are fixed on a distortion detection phantom.

In response to the increasing trend for fractionated SRS treatment schemes [63,135,138], the vendor has introduced frameless treatment protocols by incorporating a cone-beam CT to the Perfexion treatment delivery unit. Patient immobilization is performed using a thermoplastic mask system, while an infrared-based high-definition motion management camera is used for patient tracking during treatment [139]. The new model is commercialized as IconTM. Prior to treatment delivery of each fraction, a cone-beam CT scan of the patient is performed on the GK treatment couch, after having applied the thermoplastic mask [140,141]. The stereotactic space can be defined directly on the acquired cone-beam CT images. However, the spatial registration process is still not avoided, as the images need to be spatially co-registered with the MR images used in treatment planning for target and critical organ definition.

In frameless or not, fractionated or not, GK SRS applications, MR images play the most significant role which is target identification and accurate localization. Transformation from the MR coordinate system to the stereotactic space is performed by the GammaPlan treatment planning system.

3.3.3 Dose calculation and image registration in the GammaPlan treatment planning system

The GammaPlan treatment planning system [133,142] is provided by the GK vendor (Elekta). It comprises all the necessary tools for preparing an SRS treatment plan, calculating the 3D dose distribution and providing plan evaluation and acceptance metrics.

The TMR-10 is the most widely used version of the dose calculation algorithm, incorporated in GammaPlan version 10 and onwards. TMR-10 dose algorithm enables the calculation of dose at arbitrary points in the head. The algorithm models all tissues in the head as water, and, therefore, is referred to as “water-based” algorithm by the vendor [133]. In other words, TMR-10 does not take into tissue inhomogeneities, such as bone structures and air cavities (e.g., the sinuses) and considers the entire head as water. The 3D dose distribution in the head is calculated by using pre-calculated dose profiles (based on Monte Carlo calculations) and other parameters such as output factors for the three collimators [131,143], attenuation coefficients, virtual SFDs and others [133]. Since no tissue heterogeneities are considered, the distribution of CT numbers in the patient geometry is not required for TMR-10 calculations. The only requirement for dose calculations is the definition of the patient’s external contour. Although this approximation might raise concerns related to the accuracy of dose calculations in and around inhomogeneities, it enables MR-only treatment planning without the need and the uncertainty related to bulk Hounsfield Unit (HU) assignment. In the vast majority of single fraction GK SRS applications, MRI is the sole imaging modality for treatment planning purposes. The vendor has also introduced a collapsed-cone convolution algorithm, referred to as Convolution [142] in the GammaPlan version 10 and later. In contrast to TMR-10, this algorithm takes into account tissue inhomogeneities and, therefore, dose calculations are performed using a CT scan of the

patient's head. MRI only treatment planning is not an option when using the Convolution algorithm for dose calculation. Currently, the Convolution algorithm is not widely used in clinical practice.

One of GammaPlan's key features is the capability of spatially registering the MR or CT image coordinate system to the stereotactic space [137,144]. This can be achieved by automatically identifying in the image stack the system of N-shaped fiducials of the MR or CT indicator box. Location of N-shaped fiducials is fixed within the stereotactic space. The rigid transformation that best registers the fiducials defines the transformation matrix between the image stack coordinate system and the stereotactic space.

For frameless GK Icon applications, the spatial registration process is not fiducial-based. The rigid transformation matrix between cone-beam CT and MR images used in treatment planning is calculated using mutual information-based algorithm and the patient anatomy.

In a frame-based or frameless, single-fraction or fractionated GK SRS workflow, severely distorted MR images could significantly affect the transformation matrix calculated by GammaPlan.

3.4 MRI protocols for stereotactic radiosurgery treatment planning

Cranial SRS is routinely employed for the management of several lesions such as single or multiple brain metastases, acoustic neuromas, meningiomas, arteriovenous malformations, trigeminal neuralgia and others. In all these cases, MRI can provide unsurpassed soft-tissue contrast (compared to CT) between the lesion and surrounding healthy tissues, in adequately high 3D spatial resolution. Therefore, MRI is routinely used in SRS treatment planning for target localization and delineation, regardless of whether the treatment protocol is CT-based or MRI-only, fractionated or frame-based, etc.

In frame-based GK SRS, the frame and the indicator box define the stereotactic space (see Section 3.3.2) and, therefore, both need to be mounted on the patient during MR image acquisition. Thus, the first step of the MR scanning protocol is to fix the minimally invasive frame on the patient using the four pins. The MR indicator box is then mounted on the frame base using the clips. For MR signal acquisition, a specially designed head coil is always used which allows adequate space for the frame and the indicator box.

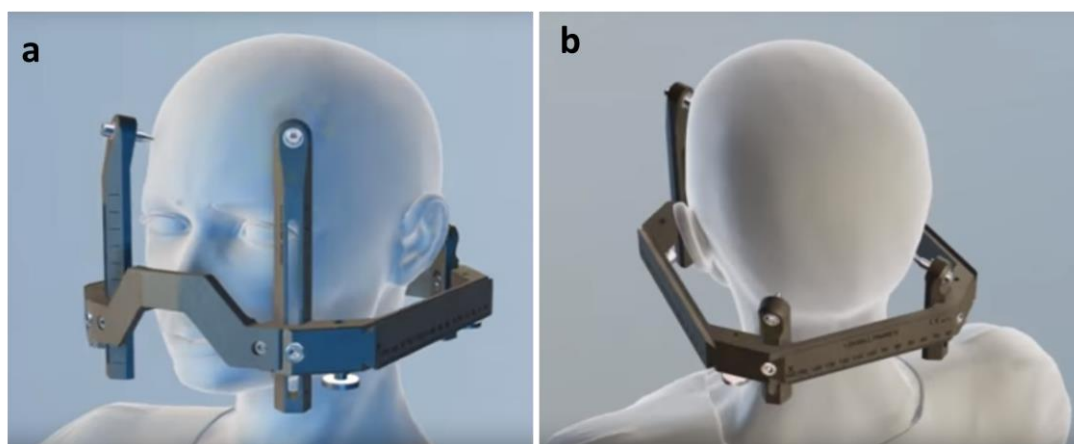


Figure 3-5: The minimally invasive Leksell stereotactic frame is firmly fixed on the patient using the four pins, prior to MR image acquisitions. The MR indicator box should also be fixed (not shown here). Images taken from [Elekta official youtube channel].

T1w contrast enhanced MR images are usually acquired, although additional T2 weighting pulse sequences can be used, depending on the clinical case. More specifically, the protocol often involves a gadolinium-enhanced 3D T1w GE pulse sequence with a high receiver bandwidth (e.g., 217 Hz/pixel in 1.5T) selected in order to minimize sequence dependent distortions. An intravenous injection of 0.1 – 0.2 mmol per kg of body mass of Gd-DTPA, which shortens the T1 relaxation time of brain lesions taking up such agents, is performed just before the imaging session. Depending on the MR manufacturer and model, the exact pulse sequence and parameters used may differ. In Philips scanners, protocols labelled as “T1-FFE” or “3D TFE” can be employed. In GE Healthcare, similar sequences are named “FSPGR BRAVO” or “FSPGR”, while for Hitachi and Siemens scanners one can use the “MP-RAGE” [46]. T2w images often involve the 3D balanced T2w fast field echo (3D T2w b-FFE) pulse

sequence which provides high spatial resolution images with a high signal-to-noise ratio and a high contrast-to-noise ratio and is supplementarily used for better visualization of the lower cranial nerves [145,146].

In frame-based, single-fraction GK applications, following the imaging session, the frame is not removed until the end of the treatment delivery. Re-fixing the frame would result in re-defining the stereotactic space and, thus, the determined target coordinates would no longer be applicable.

In frameless GK applications, the thermoplastic mask replaces the frame and the indicator box. Apart from that, the MR scanning protocol remains unchanged.

3.5 Applying margins in stereotactic radiosurgery treatment planning

In conventional radiotherapy, margins of several millimeters are usually applied around the identified clinical target volume, defining the target volume to be treated (acknowledging and tolerating potential spatial dose delivery discrepancies). However, this approach cannot be directly adopted in brain single-fraction SRS for single or multiple target(s) irradiation because radiation-induced toxicity is directly associated with the irradiated brain volume [55–57]. In specific, if the volume of brain receiving at least 10 Gy ($V_{10\text{Gy}}$) and 12 Gy ($V_{12\text{Gy}}$) is larger than 12.6 cm³ and 10.9 cm³, respectively, the risk of brain radionecrosis has been reported to reach 47%. The rate is reduced to 10%, if $V_{12\text{Gy}}$ drops to 8.5cm³ [55]. Symptomatic or asymptomatic radiation induced brain necrosis, i.e., the disruption of healthy neurons due to cell necrosis, is the most common side effect in cranial SRS. The symptoms of radiation induced brain necrosis depend on the location and function of the brain at the injury site. These symptoms can range from headaches, fatigue, nausea, imbalance, extremity weakness/numbness, speech deficits, and seizures to a combination of the above [58].

On the other hand, any potential spatial dose delivery discrepancies to the GTV (due any spatial errors involved, such as MR image distortion, spatial registration, patient positioning or motion) could compromise treatment efficiency, resulting to reduced local tumor control. Therefore, introduction of a margin of 1 mm around the GTV,

defining the target, has been reported to significantly increase (e.g., from 51% to 90% [59]) the tumor local control rate [17,59]. Applying larger (2 or 3 mm) margins significantly increases the risk for radiation induced toxicity (e.g., up to 25% for a 2mm-margin [60]) without warranting higher local control rates [17,61]. The discussion on margin restrictions becomes even more complicated if fractionated SRS is also considered [62] which has been reported to tolerate necrosis better compared to single-fraction SRS schemes [63].

In any case, it is crucial to restrict the irradiated volume, $V_{12\text{Gy}}$, at the lowest levels possible but without risking to compromise the treatment outcome. This very sensitive balance between the necessity for applying margins and the higher risk for radiation induced side effects in cranial SRS applications sets the motivation of this thesis to deal with MR images employed in SRS treatment planning.

PART B: MR DISTORTION ASSESSMENT

4 System-related geometric distortions in MR images employed in Gamma Knife radiosurgery applications

Summary

This work provides characterization of system-related geometric distortions present in MRIs used in GK frame-based SRS treatment planning.

A custom-made phantom, compatible with the Leksell stereotactic frame model G and encompassing 947 control points (CPs), was developed and utilized. MR images were obtained with and without the frame, thus allowing discrimination of frame-induced distortions. In the absence of the frame and following compensation for field inhomogeneities, measured average CP displacement owing to gradient nonlinearities was 0.53 mm. In presence of the frame, contrarily, detected distortion was greatly increased (up to about 5 mm) in the vicinity of the frame base due to eddy currents induced in the closed loop of its aluminum material. Frame-related distortion was obliterated at approximately 90 mm from the frame base. Although the region with the maximum observed distortion may not lie within the GK treatable volume, the presence of the frame results in distortion of the order of 1.5 mm at a 7 cm distance from the center of the Leksell space. Additionally, severe distortions observed outside the treatable volume could possibly impinge on the delivery accuracy mainly by adversely affecting the registration process (e.g., the position of the lower part of the N-shaped fiducials used to define the stereotactic space may be miss-registered). Images acquired with a modified version of the frame developed by replacing its front side with an acrylic bar, thus interrupting the closed aluminum loop and reducing the induced eddy currents, were shown to benefit from relatively reduced distortion.

System-related distortion was also identified in patient MR images. Using corresponding CT angiography images as a reference, an offset of 1.1 mm was detected

for two vessels lying in close proximity to the frame base, while excellent spatial agreement was observed for a vessel far apart from the frame base.

4.1 Introduction

In this Section, a systematic evaluation of system-related distortions arising from sequence independent distortions in MR images used in GK SRS treatment planning is presented. Emphasis is also placed on the geometric warping induced by the presence of the Leksell stereotactic frame (see Section 3.3.2). For this purpose, a novel prototype MRI phantom compatible with the Leksell stereotactic system was designed and constructed, whilst a suitable methodology was developed and implemented. Furthermore, a modified version of the Leksell stereotactic frame base was used and evaluated in terms of distortion induction. In addition, MR patient images from the brain stem region were studied with regard to distortions possibly associated with the stereotactic frame base.

4.2 Materials and methods

4.2.1 Phantom study

4.2.1.1 Phantom design

A custom-made acrylic-based phantom was designed and developed for intracranial MRI scans (Figure 4-1(a)). In particular, the phantom encompasses three axial planes, one coronal plane and one sagittal plane (4 mm thick each), on which 947 holes (3 mm in diameter) are drilled. The centers of mass of these holes serve as CPs for geometric distortion detection. More specifically, there is one CP every (10 ± 0.1) mm on every plane, while the axial planes are 4 cm apart from each other. The holes were drilled using a Computer Numerical Control (CNC) router which exhibits an excellent spatial accuracy of 0.1mm. Phantom's maximum external dimensions are approximately 17.4, 17.4 and 17.7 cm on the A-P (y-axis), L-R (x-axis) and S-I (z-axis) directions, respectively, although the shape is not rectangular (see Figures 4-1(a)-(c)). The

phantom's total size and shape were carefully designed so that it can fit in a typical head-coil (Figure 4-1(d)). CP distribution ensures that the edges of the available space are also monitored. The phantom is rigidly fixed on a 2cm-thick acrylic base for additional mechanical support which also serves as an adaptor to the Leksell mounting arm. The external size and shape of the phantom base is similar to the Leksell stereotactic frame. In terms of imaging, the phantom is both CT and MR compatible. In the latter case, however, it must be filled with standard copper sulfate solution, commonly used in MR phantoms [147,148].

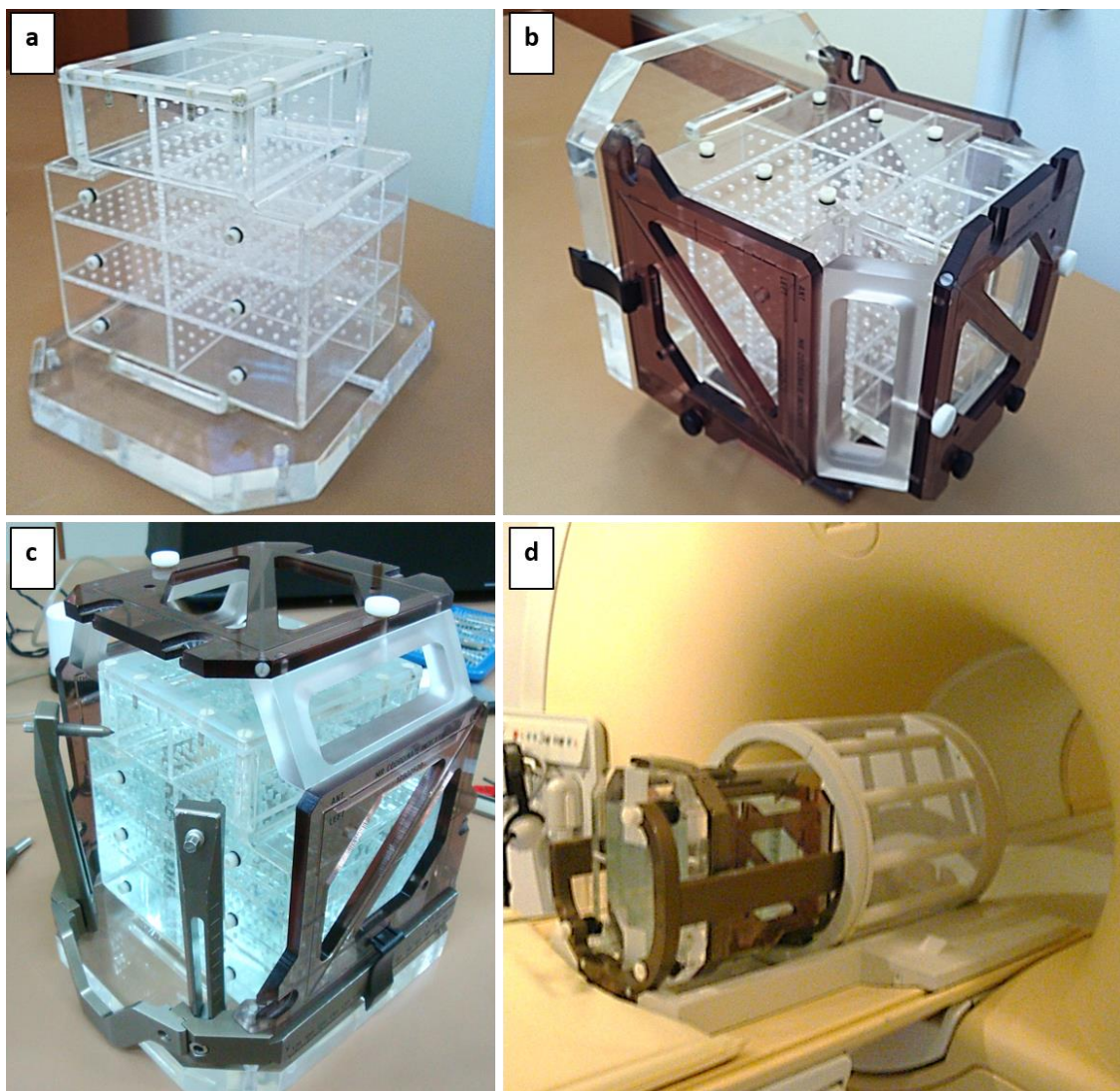


Figure 4-1: (a) The developed phantom. (b) The Leksell indicator box mounted on the phantom. (c) The Leksell stereotactic frame model G also fixed on the phantom. (d) The phantom being placed in the head coil used in intracranial MRI scanning for Gamma Knife radiosurgery treatment planning.

Additionally, the phantom was carefully designed to accurately fit to the Leksell indicator box and stereotactic frame (Figure 4-1(c)), employed during MRI scans for GK SRS treatment planning. However, the indicator box can also be attached to the phantom without the frame by mounting it directly on the thick acrylic base, as shown in Figure 4-1(b). This feature offers the possibility to evaluate for frame-induced geometric distortion by comparing CP displacements derived with and without the presence of the frame.

Table 4-1: Summary of the MR imaging protocol used in the phantom study

Scan Series #	Pulse sequence	Slice orientation	Read gradient axis & polarity	Pixel bandwidth (Hz/px)	Voxel size (mm ³)	Frame used
1	3D T1w GRE	Axial	A-P (y-axis)	217	0.82×0.82×1	nF
2	3D T1w GRE	Axial	P-A (y-axis)	217	0.82×0.82×1	nF
3	3D T1w GRE	Axial	A-P (y-axis)	217	0.82×0.82×1	F
4	3D T1w GRE	Axial	P-A (y-axis)	217	0.82×0.82×1	F
5	3D T1w GRE	Axial	L-R (x-axis)	217	0.82×0.82×1	F
6	3D T1w GRE	Axial	R-L (x-axis)	217	0.82×0.82×1	F
7	3D T1w GRE	Axial	A-P (y-axis)	217	0.82×0.82×1	mF
8	3D T1w GRE	Axial	P-A (y-axis)	217	0.82×0.82×1	mF
9	3D T2w b-FFE	coronal	S-I (z-axis)	145	0.53×0.53×0.8	nF
10	3D T2w b-FFE	coronal	S-I (z-axis)	145	0.53×0.53×0.8	F

Abbreviations: A = Anterior, P = Posterior, L = Left, R = Right, S = Superior, I = Inferior, nF = no Frame used, F = Frame used, mF = modified Frame used

4.2.1.2 Frame modification

A modified version of the aluminum frame base was also used. In particular, the exchangeable anterior side of the base was removed and replaced by an acrylic bar of

the same length. The acrylic interrupted the closed aluminum loop of the frame without compromising its mechanical integrity. This slight modification aimed at exploiting the fact that eddy currents induced in media without closed loops are much smaller than those in closed loops [36,50].

4.2.1.3 Image acquisition

The phantom, filled with the copper sulfate solution, was scanned by a Philips Achieva 1.5 T MRI scanner (Philips Medical Systems, The Netherlands, BV). The phantom was positioned so that the center of the indicator box (corresponding to (100,100,100) of the Leksell space) coincides with the MRI scanner's isocenter (corresponding to (0,0,0) of the MRI coordinate system). Table 4-1 summarizes the imaging protocol employed. In all MR sequences performed, the distortion correction option implemented in the manufacturer software, accounting mostly for gradient nonlinearities induced distortion, was – by default – enabled. Pulse sequences selected included a 3D T1w gradient recalled echo (3D T1w GRE) pulse sequence (TE = 4.6 msec, TR = 25 msec, FA = 30°, $0.82 \times 0.82 \times 1 \text{ mm}^3$ voxel size), as well as a 3D balanced T2w fast field echo (3D T2w b-FFE) pulse sequence (TE = 3msec, TR = 5msec, FA = 50°, $0.53 \times 0.53 \times 0.8 \text{ mm}^3$ voxel size). The 3D T1w GRE sequence used is an optimized sequence in terms of geometric distortions, signal-to-noise ratio and contrast-to-noise ratio, routinely used in patient imaging for target and organ at risk delineation. The 3D T2w b-FFE sequence provides high spatial resolution images with a high signal-to-noise ratio and a high contrast-to-noise ratio and is supplementarily used for better visualization of the lower cranial nerves [145,146]. To highlight sequence independent distortions arising from gradient nonlinearities, the aluminum frame was removed to exclude frame induced distortion and the reverse read gradient technique [42] was employed (Table 4-1, series #1-2) to eliminate sequence dependent distortions arising from susceptibility artifacts and B_0 inhomogeneity (see Section 4.2.1.4). To separately study frame induced distortions, additional scans were acquired with the frame mounted on the phantom, using either the clinically used assembly (i.e., with the exchangeable anterior aluminum side of the frame base on) (series #3-6) or its modified version (i.e., the exchangeable part replaced by an acrylic bar of the same length) (series #7-8). Moreover, the 3D T2w b-FFE sequence was run without and with the frame (series #9-

10) to investigate the source of the increased distortion regarding the position of the fiducials observed when this sequence is clinically used for optic nerve delineation in GK applications with the frame on. To increase clarity of the text, hereinafter, throughout this Chapter image series acquired with the frame fixed on the phantom will be labelled as “F”, without the frame as “nF” and with the modified frame as “mF”. Finally, the phantom was emptied and CT scanned in order to obtain the reference CP distribution. Data were acquired at 120 kVp by a SIEMENS SOMATOM Definition scanner (Siemens Healthcare, Erlangen, Germany) and images were reconstructed with a voxel size of $0.45 \times 0.45 \times 0.6 \text{ mm}^3$.

4.2.1.4 Data analysis

MR image series #1-2 nF, 3-6 F and 7-8 mF (Table 4-1) and the CT image stack were imported to MATLAB (The MathWorks, Inc., Natick, MA) for analysis. In-house routines were developed for CP localization and were applied to both MRI and CT datasets. As a first step, edge detection was performed exploiting the sufficient contrast between acrylic and copper sulfate solution in MR images, as well as acrylic (typical HU number of 220) and air in CT images (the phantom was CT-scanned empty). Figure 4-2 demonstrates an indicative axial slice of the performed MRI (specifically image series #1 nF) and CT scans located within a slab encompassing holes. A simple intensity thresholding step was adequate to cut off the holes resulting in a binary 3D image containing identified objects which consisted of CPs, areas of low signal-to-noise and random noise. The unique threshold level was selected after a try-and-error iterative procedure by the user in order to determine the optimum signal level that best cuts off noise and artifacts. Objects consisting of significantly lower or higher number of voxels than predefined limits were automatically excluded. A visual inspection of the identified objects was also performed by the user to ensure that obtained data did not involve any artifacts or considerable noise. CP locations were then determined as the centers of mass of the resulting 3D binary objects. Further, CPs identified in the forward read gradient polarity scan (series #1 nF, 3 F, 5 F, 7 mF) were paired with the corresponding ones in the reverse polarity scan (series #2 nF, 4 F, 6 F, 8 mF) by following the known design template. Finally, "average" CP distributions were obtained by calculating the average position of paired CP locations. Provided that the

bandwidth remains unchanged, this procedure eliminates sequence dependent distortion (i.e., stemming from B_0 inhomogeneity, chemical shift and susceptibility differences) which is known to change sign with respect to read gradient polarity [25,27,39,42,149,150], as analyzed in Chapter 2. This particular step was necessary to effectively cancel out phantom-induced distortion originating from susceptibility differences. Resultant "average" CP distributions, therefore, are associated with system-related distortion only, mainly stemming from gradient nonlinearities which are known to remain unaffected by read gradient reversal. This type of distortion can be revealed by comparing them with the reference CP locations identified in CT images. In view of that, the CT and MRI coordinate systems were co-registered. For this purpose, a rigid transformation was established after four CPs around the MRI scanner's isocenter were chosen and manually matched with the corresponding ones in the CT image stack. Accuracy of this step lies on two premises. First, CT images are characterized by negligible distortion and regarded as the reference dataset. This is a commonly followed approach [27,33,94–96]. Moreover, the four CPs manually selected to define the rigid transformation between the CT and MRI coordinate systems are subject to minimum distortion owed to gradient nonlinearities. This is considered to be true around the isocenter where scanners show optimum performance, while spatial accuracy deteriorates at the field of view edges [1,28,33,95].

4.2.1.5 *Uncertainty estimation*

Uncertainty in distortion detection and evaluation relates to inaccuracies of the CP localization algorithm applied to both CT and MR series. CP coordinates determination based on the centroid of binary 3D image objects can be achieved with sub-voxel (i.e., sub-mm for this study) accuracy as demonstrated elsewhere [25,94]. To estimate the uncertainty of the presented results, the accuracy of the CP localization algorithm was investigated. Specifically, distortion-free CPs should be (10 ± 0.1) mm apart in each plane according to the design template and assumed mechanical accuracy of the CNC router. MRI-averaged CPs were randomly chosen around the isocenter and the relative distances between all neighboring CPs were examined. A total of 40 relative distances were included. Deviations from the actual CP spacing provided an estimate of the algorithm's accuracy. The procedure was repeated for CT-identified CPs. In this case,

however, CP selection was not limited to the field-of-view center but, instead, expanded to the edges of the phantom.

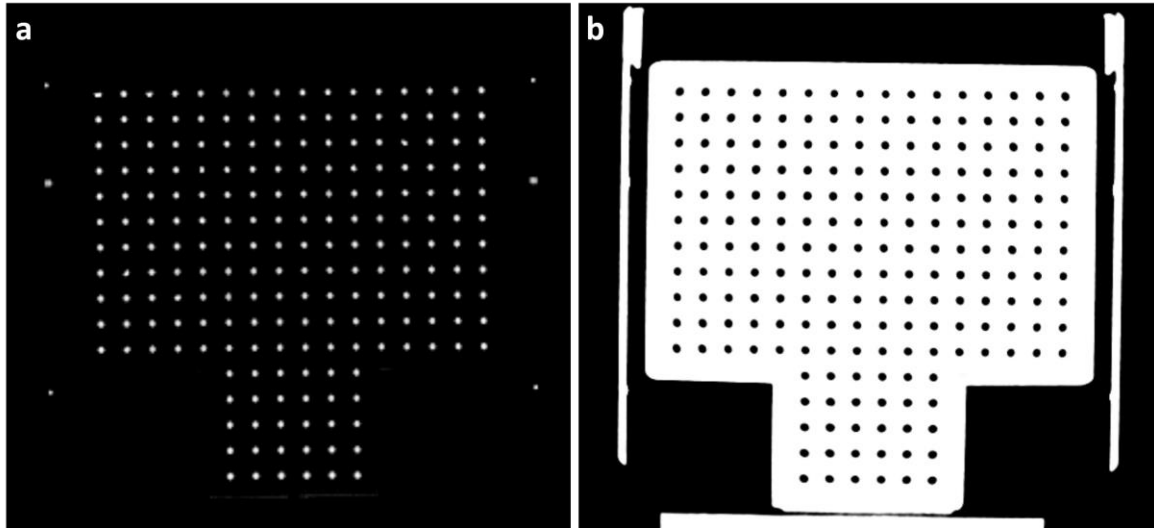


Figure 4-2: An indicative axial slice of the performed MR scan series #1 nF (a) and CT scan (b), depicting the high contrast between CPs and acrylic. The N shaped fiducials of the Leksell localization box are also visible. Presented images are not spatially co-registered.

4.2.2 Patient study

A recently proposed methodology [10] was employed to obtain patient MR images with minimal sequence dependent distortions. The technique is specifically presented and evaluated in Chapter 9. Briefly, this method involves two acquisitions with opposite read gradient directions and uses the two respective images obtained to deduce an “average” MR image, thus minimizing sequence dependent distortions. In the present study, the method was implemented to a patient referred to for arteriovenous malformation (AVM) by applying the 3D T1w GRE pulse sequence presented in Table 4-1 (series # 3-4 F). Both MR image series were obtained following an intravenous injection of 0.1 mmol/kg Gd-DTPA contrast agent (see Sections 1.6 and 3.4). Reference images were obtained by CT angiography (120 kVp, 200 mAs, reconstruction voxel size of $0.45 \times 0.45 \times 1 \text{ mm}^3$). Iodinated contrast was intravenously administered at 5 mL/s for a total of 80-90 mL, following an 80-mL bolus for triggering purposes. All MR and CT scans were performed with the head frame in place. The acquired CT series and the derived “average” image series were registered in the Leksell space by

exploiting the visible fiducial markers in the GammaPlan v.10 treatment planning system. Selected vessels were carefully contoured in two brain stem regions on the CT series and then copied and superimposed to the "average" MRI series. As mentioned above, CT images are supposed to be characterized by negligible distortion while "average" MR images eliminate sequence dependent distortions arising from susceptibility artifacts and B_0 inhomogeneities. Thus, taking into account MR sequence independent distortions due to gradient nonlinearities in the regions of interest, as quantified in the phantom study, frame induced distortions in these regions were assessed through geometric displacement between contours in the "ground truth" CT images and corresponding contours prescribed in the "average" MR images.

4.3 Results

4.3.1 Phantom study

Table 4-2 presents the maximum and mean absolute distortions owing to gradient nonlinearities and frame presence detected by comparing MRI-averaged CP distributions against corresponding CT-identified CP locations. Mean absolute distortion without the presence of the frame (series # 1-2 nF), thus reflecting gradient nonlinearity, was 0.53 mm, with only 2% of the CPs exceeding 1 mm. The largest CP displacements were detected at the corners of the examined space. Taking the sign into account, mean values of CP displacements in x (L-R direction), y (A-P direction) and z (S-I direction) axes were +0.21, +0.03 and +0.23 mm, respectively, suggesting a favored directionality towards positive values for the x and z axes. With respect to the Leksell space, points lying within 5 cm from its center (extracted from 283 corresponding CPs) present maximum gradient nonlinearity distortion of less than 1 mm (Table 4-3). This also stands true for points lying up to 7 cm from the Leksell space center, i.e., covering the vast majority of the Perfexion treatable region.

Mounting the frame on the phantom during MR scanning (series # 3-4 nF and 5-6 nF) resulted in a significant increase in mean CP displacements as shown in Table 4-2 (0.95 mm & 0.89 mm, respectively). Maximum values of absolute distortion greatly increased, especially in x and y axes (Table 4-2). Fraction of CPs exceeding 1 mm of

absolute distortion raised to about 30%. The distortion increase gets smaller with distance from the frame base. Thus, as shown in Table 4-3, for points lying within 5 cm from the center of the Leksell space (i.e., relatively away from the frame base), distortion is not significantly affected by the presence of the frame and it could be regarded as similar to that observed without the frame (i.e., a maximum distortion of the order of 1 mm was observed with or without the frame). However, for points lying up to 7 cm from the Leksell space center (i.e., points closer to the frame base are included), the maximum distortion increases to 1.64 mm (Table 4-3).

Table 4-2: Mean and maximum absolute distortion values measured in "average" MRI datasets. R corresponds to the total CP displacement (Euclidean distance)

"Average" Dataset	X – axis (mm)		Y – axis (mm)		Z – axis (mm)		R (mm)		CPs with > 1mm distortion
	Mean	Max	Mean	Max	Mean	Max	Mean	Max	
Series #									
1 – 2 nF	0.30	1.06	0.20	0.89	0.29	0.94	0.53	1.10	2%
3 – 4 F	0.48	2.98	0.52	5.69	0.38	1.13	0.95	5.74	28%
5 – 6 F	0.58	3.85	0.38	3.55	0.28	1.23	0.89	3.91	36%
7 – 8 mF	0.27	1.66	0.32	4.72	0.35	1.12	0.65	4.74	10%

Using the modified frame base (series # 7-8 mF) with the acrylic bar replacing the exchangeable anterior side of the base, frame-induced distortions were substantially decreased although not eliminated (Table 4-2). Maximum and mean absolute CP displacements were systematically lower in all axes compared to corresponding results with the original frame (series # 3-4 nF), whilst the fraction of CPs exceeding 1 mm of distortion was reduced to 10%. In respect to the Leksell space, points lying up to 7 cm from its center present a maximum distortion of 1.17 mm compared to a value of 1.64 mm with the original frame and 0.98 mm without the frame (Table 4-3).

Table 4-3: Mean and maximum absolute distortion values measured in "average" MRI datasets at radial distances up to 50 mm and 70 mm from the center of the Leksell space. R corresponds to the total CP displacement (Euclidean distance).

"Average"	Radius = 50mm		Radius = 70mm	
dataset	R (mm)		R (mm)	
Series #	Mean	Max	Mean	Max
1 – 2 nF	0.43	0.88	0.48	0.98
3 – 4 F	0.47	1.15	0.60	1.64
5 – 6 F	0.43	0.87	0.53	1.41
7 – 8 mF	0.39	1.13	0.48	1.17

Figure 4-3 provides an insight with respect to the spatial distribution and directionality of the detected distortions presented in Tables 4-2 and 4-3. In the absence of the frame (series #1-2 nF), vectors in Figures 4-3(a),(b) represent displacement between CT-detected CP locations and respective MRI-averaged ones for an axial and a coronal plane. Most vectors are hardly visible indicating inconsiderable distortion. In Figures 4-3(c)-(f), corresponding data are shown with the frame fixed on the phantom during the MRI scans (series # 3-4 F and 5-6 F). Severe frame-induced distortion is evident in regions neighboring the frame base (contoured in Figures 4-3(c)-(f)), while minimal or no displacement is observed in distant areas. Distortion magnitude decreases rapidly with respect to distance from the frame base. Distortion vectors did not change sign with respect to read gradient (or frequency encoding) axis (y in Figures 4-3(c),(d) and x in Figures 4-3(e),(f)) and were always directed towards the center of the frame base. It is evident that, as also presented in Table 4-2, choice of read gradient axis influences spatial distribution and maximum values of frame-induced distortion. As an instance, distortion vectors lying at the A side of the phantom in Figure 4-3(c) (read gradient on y (A-P) axis) are increased with respect to corresponding ones in Figure 4-3(e) (read gradient on x (L-R) axis). Contrarily, vectors close to the L and R sides of the frame in Figure 4-3(c) are smaller than corresponding ones in Figure 4-3(e).

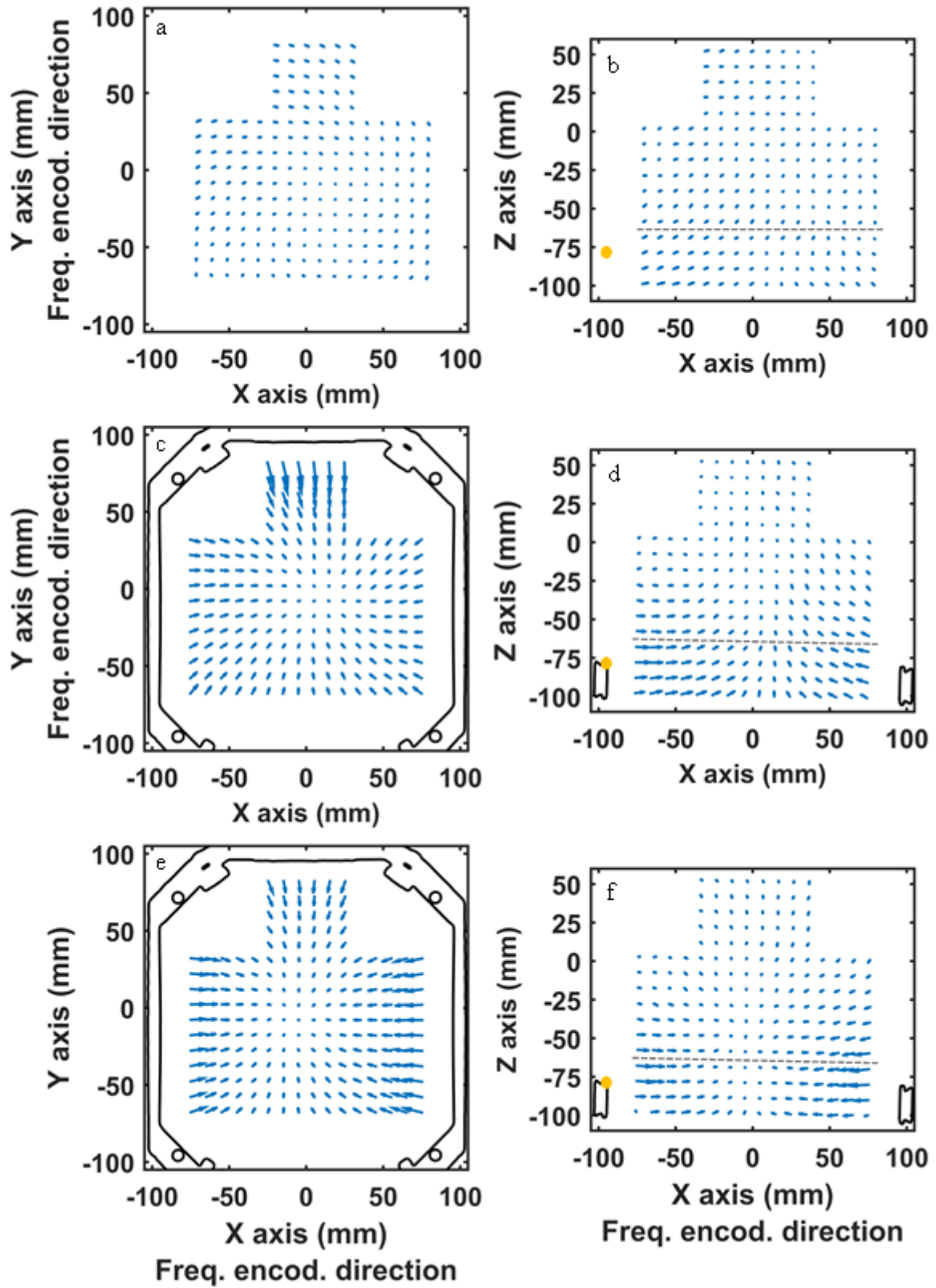


Figure 4-3: Distortion vectors for the axial (a),(c),(e) plane close to the phantom and frame base (see Figure 4-1) and the coronal (b),(d),(f) plane of the phantom. Initial points correspond to CT-identified CP locations while terminal points to MRI-averaged ones. Distortion vectors correspond to analysis performed for image series 1-2 nF

(a),(b), 3-4 F (c),(d) and 5-6 F (e),(f) (see Table 4-1). For figures (c)-(f), the contour of the frame base is also depicted. All vectors' lengths have been magnified by a factor of 3 to facilitate readability. The MR scanner's coordinate system is adopted. Note that in (c) and (e) frame base is projected on the axial plane as it actually lied at a distance of approximately 15 mm towards negative z axis. The gray dashed lines on figures (b),(d),(f) highlight location of the axial planes shown in figures (a),(c),(e), respectively. The yellow mark on frame base depicts the reference point for distances presented in Figure 4-4.

Figure 4-4 presents a quantitative analysis of distortion magnitude detected in the four "average" datasets. For the phantom's coronal plane shown in Figures 4-3(b) and (d), absolute distortion values for 72 CPs lying within a selected region of interest is presented against their radial distance from the reference point on the frame base (also depicted in Figure 4-3). Corresponding values related to distortion shown in Figure 4-3(b) (series #1-2 nF) are also included to facilitate comparison. In this case, it is noted that distortion slightly decreases with radial distance from the reference point, as the distance from the isocenter is shortened. For image series #3-4 F, distortion magnitude reaches unacceptable levels in the vicinity of the frame base and drops to corresponding values of image series #1-2 nF at a radial distance of approximately 90 mm. Similar results were obtained for image series #5-6 nF. Results related to the modified frame (series #7-8 mF) reflect the effected decrease in distortion magnitude for short radial distances (Figure 4-4).

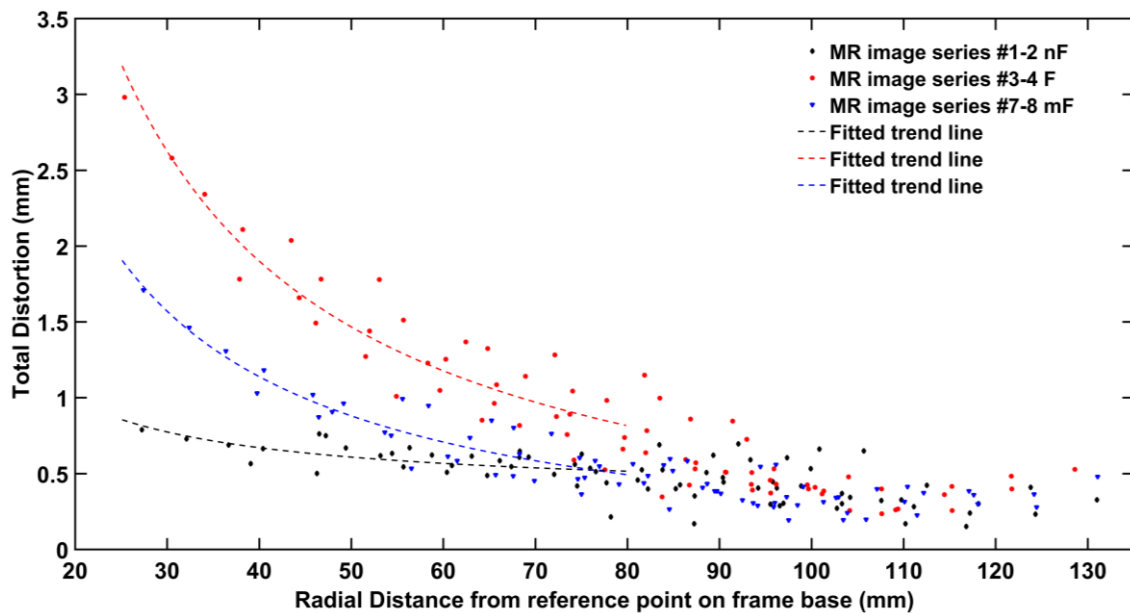


Figure 4-4: Total magnitude of detected CP displacements for three MRI-averaged datasets, image series #1-2 nF, 3-4 F and 7-8 mF. Distortion of 72 CPs is presented against their radial distance from the reference point on the

frame base (depicted in figure 3). Although the frame was not fixed in image series #1-2 nF, corresponding data using the same reference point are also included for comparison. Dashed lines correspond to fitted trend lines of the form $y=ax + b$ to guide the eye.

Figure 4-5 presents an indicative coronal slice of the phantom acquired with the 3D T2w b-FFE pulse sequence. In the presence of the frame (Figure 4-5(a)), the phantom's external shape appears deformed in the areas neighboring the frame base compared to its depiction without the frame (Figure 4-5(b)). Specifically, the phantom edges appear to incline towards the center of the frame base, in accordance with results presented in Figure 4-3. Shift of the indicator box N-shaped fiducials lying close the frame base is also pronounced (Figure 4-5(a)), breaking down co-linearity between fiducials premised to define the Leksell stereotactic space. In Figure 4-5(b), horizontal distance (L-R direction) between the inferior fiducial marks measures 189 mm. In the presence of the frame base (Figure 4-5(a)), this distance measures 184 mm. Moreover, the vertical distance (S-I direction) between corresponding marks also appears reduced by approximately 1 mm in Figure 4-5(a). It is noted however that distortion analysis based on the CPs revealed that distortion magnitude is comparable to that observed for image series #3-4 F and 5-6 F, thus being increased reaching unacceptable levels only in the vicinity of the frame base and dropped to corresponding values of image series #1-2 nF at a radial distance of approximately 90 mm.

Results of the performed uncertainty test are summarized in Table 4-4. Mean absolute deviation was found to be less than 0.1 mm for both MRI and CT datasets. In the most conservative approach for "average" MRI data, the method's accuracy is determined by adopting the maximum detected deviation among the 40 relative distances examined. Taking also into account the mechanical accuracy of 0.1 mm, the quadrature sum equals 0.2 mm. Consequently, spatial accuracy related to the CP localization algorithm for sequence independent distortion detection is 0.2 mm or better.

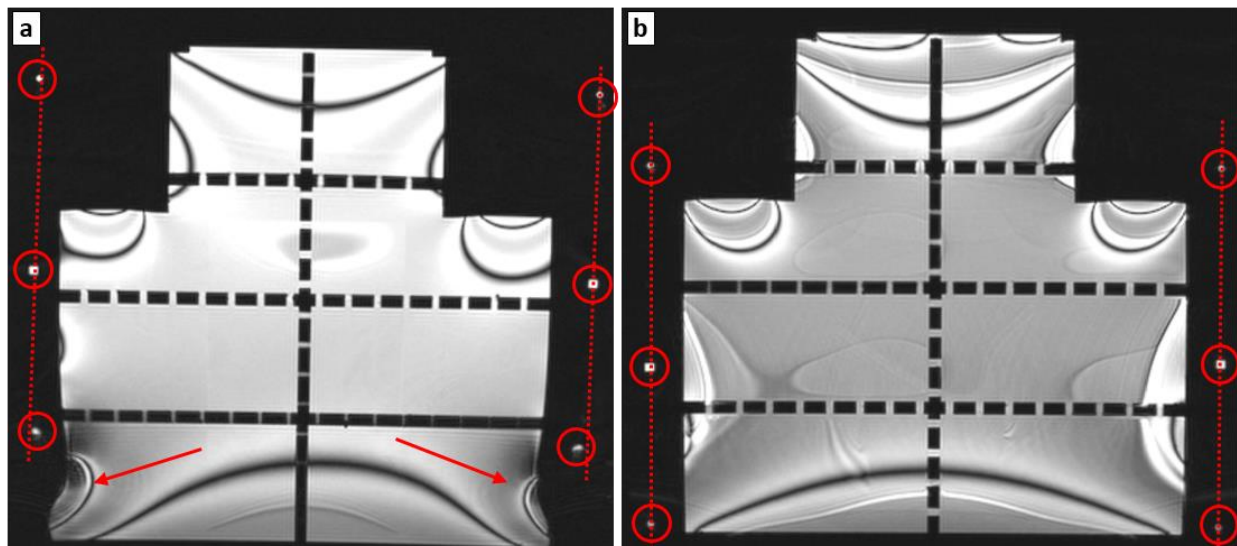


Figure 4-5: Coronal slice acquired by employing the 3D T2w b-FFE sequence with (a) and without (b) the frame fixed on the phantom (the one sagittal and the three axial acrylic planes are evident in both images). Fiducials from the indicator box are highlighted using red circles. Red dashed lines have been manually drawn to examine co-linearity between fiducials. Red arrows point to severe deformation of the phantom's external shape close to the frame base.

Table 4-4: Uncertainty related to the CP localization algorithm

Deviation between actual and measured		
CP distances (mm)		
Dataset	Mean \pm 1 std ^a	Max
MRI-averaged (series # 1-2 nF)	0.07 \pm 0.04	0.17
CT	0.04 \pm 0.02	0.10

^a one standard deviation of the average absolute value.

4.3.2 Patient study

Figures 4-6 and 4-7 present indicative axial images and sagittal reformats from the CT angiography, along with corresponding images from the “average”, Gd-enhanced MRI, performed on the AVM patient. In Figure 4-6, two feeding vessels lying close to the frame base (about 5 mm in Z axis and 80-90 mm in X and Y axes from the frame base), but still within the GK Perfexion treatable area, were contoured on the reference CT

images and superimposed to the “average” MRI ones. A geometric offset of 1.1 mm is observed between the "ground truth", CT-contoured vessels and the same vessels as identified in the "average" MRI series. Contrarily, as shown in Figure 4-7, for another vessel located at a significant distance from the frame base (more than 15 cm), CT-contours are in excellent geometrical agreement with the Gd-enhanced vessels.

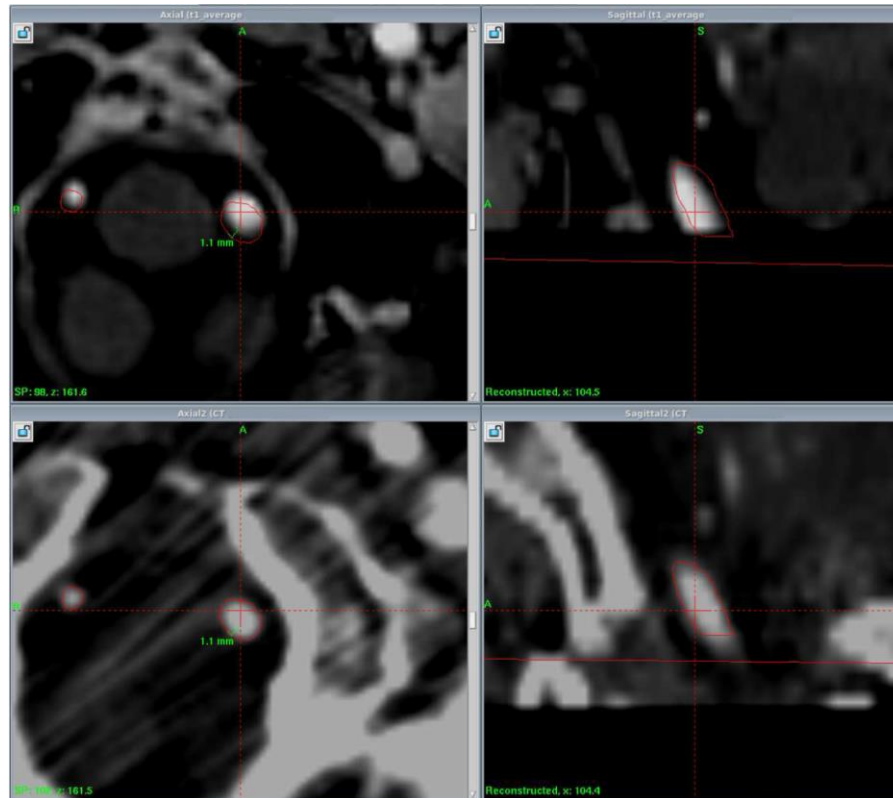


Figure 4-6: Snapshot of Leksell GammaPlan v.10 treatment planning system. Post-Gd axial image (left) and sagittal reformat (right) of the derived "average" MRI dataset (top row), along with corresponding CT-angiography images (bottom row) in the brain stem area of the scanned patient. The vertebral arteries lying in the vicinity of the frame base, but still within the treatable area with Perfexion, were contoured (red polygons) at the level of the foramen magnum on the CT series and superimposed to the MRI series.

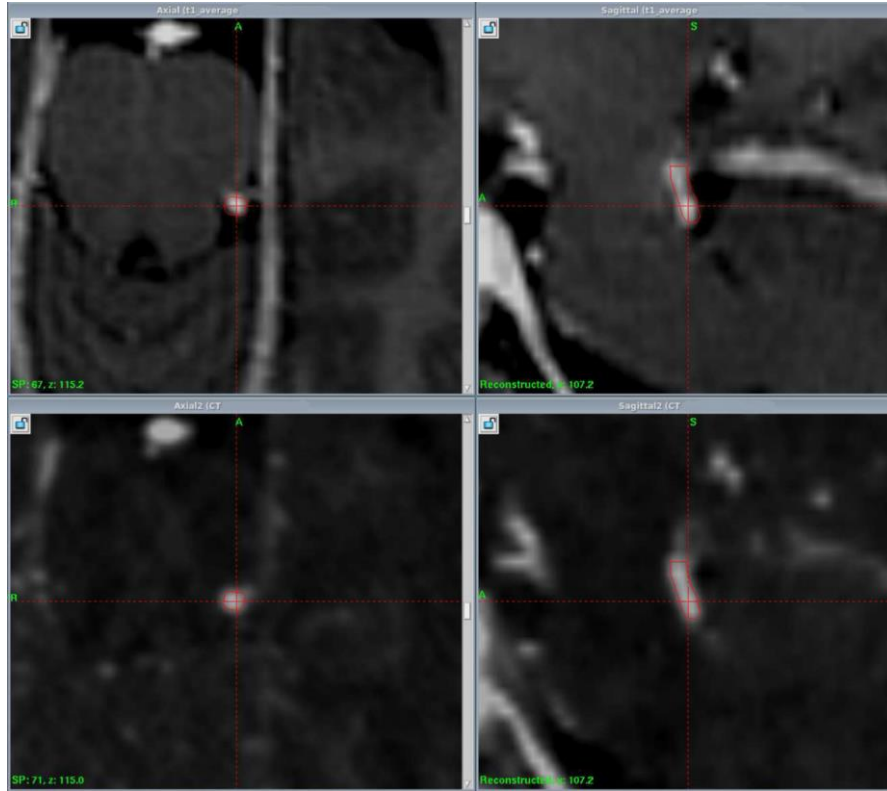


Figure 4-7: As in Figure 4-6, but in this case the contoured vessel (part of the superior cerebellar artery) is now lying at a significant distance (more than 15 cm) from the frame base.

4.4 Discussion

Several 3D phantoms for the detection and evaluation of MRI-related distortions have been presented in the literature. However, the vast majority are body-sized [27,28,33,92–96,151], focusing on large field-of-views which are more prone to geometric distortions. Despite the high demand for spatial accuracy in intracranial SRS, studies reporting on distortion associated with the hardware and imaging parameters specifically used in such applications are quite limited [25,152,153]. In specific, the cylindrical phantom (170 mm in diameter) used in Mack et al [152] and Zhang et al [153] encompasses 145 fiberglass rods which allow for distortion assessment on axial slices but are incapable of detecting through-plane distortion. In Moutsatsos et al [25] the authors filled a 16 cm diameter acrylic flask with polymer gel and irradiated it with 4mm GK shots at 26 predefined locations. The centers of mass of the polymerized areas served as CPs. Although this approach offers the attractive feature of reproducing every step in the GK treatment procedure and the phantom is easy to construct, it suffers from

the very limited number of CPs it can include and, thus, the inability of deriving detailed distortion maps. Moreover, frame-induced geometric inaccuracies were not specifically addressed in none of the above studies, possibly due to the lack of CPs in the vicinity of the frame base.

In the present work, a new phantom was designed and constructed while a suitable methodology was developed and implemented for the detection of MRI-related geometric distortions in intracranial SRS applications. The phantom was constructed by acrylic which is known to be easily machinable, MR-compatible [36] and cost effective. Grids of holes served as CPs for distortion assessment. The phantom's size was limited to the size of the Leksell indicator box and frame, while its shape was designed for monitoring the majority of the available space, with distortion assessment extending to areas lying a few millimeters away from the frame base. The ability of imaging the phantom with and without the stereotactic frame, offers the potential for a quantitative evaluation of the geometric distortion induced by the Leksell frame in remote regions with the GK Perfexion volume.

The CP localization algorithm developed in the present work consists of custom-made MATLAB routines. Although easy to develop, it is not an automated procedure. User interaction is required at several steps. First of all, decision on the signal intensity threshold to be applied for creating binary objects is not straightforward. It is a try-and-error procedure in order to determine signal level that best cuts off noise and artifacts while ensuring maximum number of voxels for every hole (i.e., CP). Still, visual inspection of the identified binary objects had to be performed and, in a few cases, manual removal of false positives was necessary. This step may be time consuming. Furthermore, in image series # 3 F and 4 F the algorithm failed to identify two neighboring CPs due to locally decreased signal. This would be of much greater concern in case a larger field of view was employed. The limitations of adopting a unique signal intensity threshold are discussed in Stanescu et al [94]. The authors proposed using a slice adapting threshold based on image histogram along with an unsharp masking step. Torfeh et al [95] also used an adaptive threshold but it was calculated within a region of interest around each CP. Implementing either approach in the proposed algorithm would probably lead to a more automated and faster CP identification procedure. This improvement would be important in the case of a larger phantom with a considerably increased number of CPs. The algorithm accuracy was

estimated by measuring relative distances of neighboring CP locations and was found to be 0.2 mm or better. Despite the relatively high accuracy in CP localization, the methodology followed for distortion evaluation may suffer from spatial registration errors between MRI and CT coordinate systems. This step might induce additional uncertainties in the case of non-negligible gradient distortion (i.e., owing to gradient nonlinearities) among the four CPs selected for registration. For the presented results, registration was performed based on carefully selected CPs around the MRI scanner's isocenter. Successful registration procedure was confirmed by comparing residual spatial errors between reference and transformed locations of the selected CPs.

The reverse read gradient technique can be used to evaluate both sequence dependent and sequence independent distortions [25,149]. The former is comprised of both system- and object-related distortions. Using the reverse read gradient technique in patients with multiple metastases treated with GK, Karaikos et al [10] reported sequence dependent distortions leading to target localization uncertainties of up to 1.3 mm (mean uncertainty of 0.51 ± 0.37 mm). This study is presented in Chapter 9. Other approaches have also been proposed for sequence dependent, patient-specific distortion evaluation. Susceptibility induced geometric errors can be numerically simulated in anatomical sites [31]. The field map technique [41] can be applied to acquire a detailed sequence dependent distortion map but it requires an additional image scan of the patient as well as a phase image unwrapping processing step [33,38,97,98]. However, phantom-induced distortions are not relevant in a clinical setup. Therefore, evaluation of sequence dependent distortions was beyond the scope of this work.

Sequence independent distortions constitute a purely system-related type of distortion which is mainly attributed to gradient nonlinearity. In this study, evaluation of gradient distortion was performed for a specific scanner employed in GK SRS applications using the phantom constructed and the reverse gradient technique. A mean absolute distortion (measured without the frame) of the order of 0.53 mm was detected, while hardly any CPs exhibited displacement of more than 1 mm. A number of authors have reported gradient distortions of several millimeters [28,33,94,96], but since gradient distortion magnitude is strongly dependent on the field-of-view, results are not directly comparable. Reduced gradient distortions were reported in Moutsatsos et al [25] where a field-of-view relative to intracranial MRI scans for GK SRS was used. In that work, gradient distortions reached 0.47 mm with an average of 0.23 mm within a spherical

phantom of 16 cm in diameter. However, a different MRI unit was used and CP locations were limited with respect to the field-of-view employed. Mounting the frame on the phantom significantly increased distortions in the vicinity of the frame base. The Leksell Coordinate Frame G investigated in this Chapter consists of a rectangular base with three permanently connected bars which cannot be disassembled, while the anterior bar of the frame is exchangeable so that differently-shaped front pieces (straight or curved) can be used. Since eddy currents can be induced in closed loops by both the RF and gradient fields, associated artifacts may be introduced [50–52]. Thus, frame induced distortions may constitute a concern in GK applications in which the treated area is close to the frame base. Results for the specific imaging conditions of this study indicate that frame induced distortion (i) does not show a directionality dependence on read gradient axis and is always directed towards the center of the frame base, (ii) reaches unacceptable levels in the first few centimeters from the frame base and obliterates at a radial distance of about 90 mm, (iii) is slightly larger along the read gradient (frequency encoding) axis compared to the phase encoding axis and at regions where the read gradient axis is perpendicular to the frame's proximal side and (iv) affects the position of the N-shaped fiducials used to define the stereotactic space and perform registration procedures.

Taking into account the above remarks, the following recommendations can be made in order to minimize frame induced distortion within regions of clinical importance. The frame can be mounted in a way that ensures maximum possible distance between the frame base and regions of interest (i.e., target and surrounding organs at risk). Read gradient axis can be selected to be parallel to the side of the frame base which is closest to the region of interest. The affected part of the N-shaped fiducials (if included in the MR image stack) and the distorted anatomical regions close to the frame base should not be taken into account in registration procedures using either the fiducial markers or the co-registration feature of GammaPlan, since frame induced geometric distortions may limit the accuracy of the registration process. Moreover, evaluation of frame induced distortion should be included in the quality assurance program for MRI scanners and specific MR imaging conditions employed in SRS.

Using the modified version of the frame resulted in a significant reduction of the detected distortion. The acrylic bar interrupts the pathway of the closed loop of the original frame, thus reducing eddy current effects. However, using a fragile material

such as acrylic instead of aluminum could compromise the frame's durability and long-term integrity.

A CT angiography of a patient provided the reference positions for a number of vessels. CT-based vessel contours were checked for geometric agreement with the same vessels in "average" MR images. A geometric offset of 1.1 mm was observed for vessel contours at a relatively close distance of about 9 cm from the proximal side of the frame base and within the treatable area of the Perfexion unit. Given that "average" MR images eliminate sequence dependent distortions arising from susceptibility artifacts and B_0 inhomogeneities and taking into account that the sequence independent distortion measured in the phantom study is of the order of 0.4 mm at the same region, the residual 0.7 mm could be attributed to frame induced distortion. Moreover, displacement directionality for both vessels in Figure 4-6 matches that of the frame induced distortion in Figure 4-3. Contrarily, a good spatial agreement was observed for a vessel lying at a great distance (more than 15 cm) from the proximal side of the frame base suggesting minimal gradient nonlinearities and frame induced distortions in that region in accordance to phantom study findings.

Distortion analysis presented above is only valid for the scanner and scanning conditions of this study. Therefore, quantitative results shown should only be treated as indicative for an imaging scheme commonly used in GK SRS treatment planning. Moreover, clinical interpretation of the presented results is not straightforward. Note that several CPs detected with severe distortion do not necessarily lie within the GK treatable volume (e.g., some were located within the plane defined by the frame base) and, consequently, their clinical impact could be considered to be insignificant. CPs at a distance up to 7 cm from the center of the Leksell space, thus covering the greatest part of the treatable volume, present a maximum distortion of the order of 1.5 mm with the frame mounted on the phantom compared to a corresponding value of 1 mm without the frame (Table 4-3). However, distortion in the fiducial markers commonly used to define the Leksell space, especially in the case of coronal MR images where the lower part of the N-shaped fiducials is always included, as well as distortion in image regions outside the treatable area, could adversely affect the accuracy of the image registration process and thus the treatment accuracy. An assessment of the effect of the detected distortions on the clinical outcome was not performed. In GK applications where steep dose gradients exist in all three directions, distortions of the order of 1 mm may have a

significant dosimetric impact, e.g., a significant reduction to the absorbed dose by the target [10,147]. Another limitation of this work is that geometric errors induced by B_0 static magnetic field inhomogeneities were not evaluated, despite constituting a system-related type of distortion. Nevertheless, these distortions are sequence dependent and are greatly reduced or canceled out during averaging of CP locations [25,27] or patient images [10]. Furthermore, a limitation of this study is the non-isotropic distribution of CPs over the phantom volume resulting in specific areas not being evaluated. Therefore, 3D distortion maps were not created in order to avoid introduction of interpolation errors.

Effectiveness of SRS applications relies on high fidelity tumor localization due to the steep dose gradients employed. System-related distortions were found to potentially affect both target positioning and image registration. In order to further increase spatial accuracy of SRS applications, further work is needed to fully characterize system-related distortions in patient MRIs used in such applications, especially the ones employing MRI-only treatment planning. The clinical impact of such distortions is partly investigated in Chapter 7, while determination of effective approaches and apparatuses for minimizing is studied in Part C of this thesis.

4.5 Conclusion

A novel phantom for distortion detection in GK SRS applications was designed and developed. The ability of employing the phantom with and without the Leksell stereotactic frame was exploited to highlight frame induced distortions in addition to gradient nonlinearity related ones. An evaluation of these distortions was performed for clinically employed pulse sequences. Gradient nonlinearity was found to induce mean distortion of about 0.5 mm, whilst maximum values of up to 1.1 mm are reached at the edges of the examined volume. Contrarily, mounting the stereotactic frame on the phantom resulted in a great increase in the detected distortion due to eddy currents induced in the closed loop of the aluminum frame base. Maximum values of about 5 mm are reached within a few centimeters from the frame base. However, frame induced distortion decreases rapidly with distance from the frame base, and the maximum distortion at a distance up to 7 cm from the Leksell space center, covering the greatest

part of the treatable volume, was found to be approximately 1.5 mm. Nevertheless, severe distortion observed outside the Perfexion treatable region could also affect treatment mainly through the registration process (e.g., the position of the lower part of the N-shaped fiducials used to define the stereotactic space was significantly affected) and thus this region should be excluded where possible during this process. A modified version of the frame was also studied and corresponding images were shown to suffer from relatively reduced distortion. Increased distortion in the vicinity of the frame base, but within the treatable volume, was also identified in patient images. Overall results of this work, suggest that assessment of frame induced distortion should be included in the quality assurance program for MRI protocols employed in SRS.

5 Evaluation of MRI-related geometric distortions in stereotactic radiotherapy treatment planning at 1.5T and 3.0T

Summary

The present work focuses on the assessment of total system-related geometric distortion inherent in MR images used in SRS treatment planning for a variety of MR scanners, field strengths and clinically used pulse sequences.

The geometric distortions for three clinical MR protocols (at both 1.5T and 3.0T) used for SRS treatment planning were evaluated using a recently proposed phantom and methodology. Areas of increased distortion were identified at the edges of the imaged volume which was comparable to a brain scan. Although mean absolute distortion did not exceed 0.5 mm on any spatial axis, maximum detected control point displacement reached 2 mm.

Overall results of this work suggest that efficacy of SRS applications could be compromised in case of very small targets lying distant from the scanner's isocenter (e.g., the periphery of the brain).

5.1 Introduction

The magnitude of geometric distortions in an MR image depends on the MR unit as well as on the parameters of the specific sequence used for patient imaging [2]. Distortions are minimal at the center of a closed-bore magnet and increase gradually toward the radial edges of the scanning volume [1,2,33,95]. As the static magnetic field strength increases geometric distortions are also increased. Even for a brain scan (where

a limited field-of-view is used) these distortions can be more than 3 mm [151,154]. In agreement with previous studies [147], it was recently showed that in SRS applications relatively small distortions of up to 1.3 mm in MR images may result in a significant underdosage (up to 30%) of specific very small targets [10]. Distortion magnitude increases as one moves away from the center of the magnetic field resulting in increased localization uncertainties for targets lying at the periphery of the brain. Therefore, the specific MRI protocol employed for radiotherapy treatment planning should be evaluated in terms of geometric accuracy, especially in applications delivering highly conformed dose distributions to irradiate targets lying at the periphery of the brain [155–157]. Although no specific tolerance in geometric uncertainty exists, since the impact of geometric distortion on dose delivery depends on several parameters including the target volume and the conformity of the irradiation technique, it is generally acknowledged that SRS applications require high geometric accuracy and precision [153,158–161]. Since MRI-related distortion has been recognized as one of the major contributors to geometric accuracy degradation in the entire dose delivery process, the implementation of MR distortion detection and assessment techniques could be of great importance [2,153,161].

In this work, we used the phantom and methodology presented and also used in Chapter 4 (and published in [26]) in order to evaluate spatial accuracy of three MR protocols clinically used for SRS/SRT treatment planning implemented in two different MR models with static magnetic fields of 1.5T and 3.0T. The acquired images were processed to assess and compare the total geometric accuracy of the employed protocols, as well as derive detailed distortion maps in various orientations.

5.2 Materials and Methods

5.2.1 The phantom

A custom-made phantom, recently developed by our group, was utilized (Figure 5-1(a)). Since the phantom has been extensively described in Chapter 4, its key characteristics will be presented in short. CPs for distortion detection are determined as the centers of mass of 947 3-mm diameter holes. The holes are distributed over three

axial, one sagittal and one coronal acrylic planes. On every plane, there is one CP every (10 ± 0.1) mm. The phantom's total size and shape were carefully designed so that it can fit in a typical head coil (Figure 5-1(b)) -in order to simulate an intracranial MR scan for SRS/SRT treatment planning-, while CP distribution ensures that an extended space is monitored and evaluated. In terms of imaging, the phantom is both CT and MR compatible provided for the latter case that it is filled with standard copper sulfate solution, commonly used in MR phantoms [26,147,148].

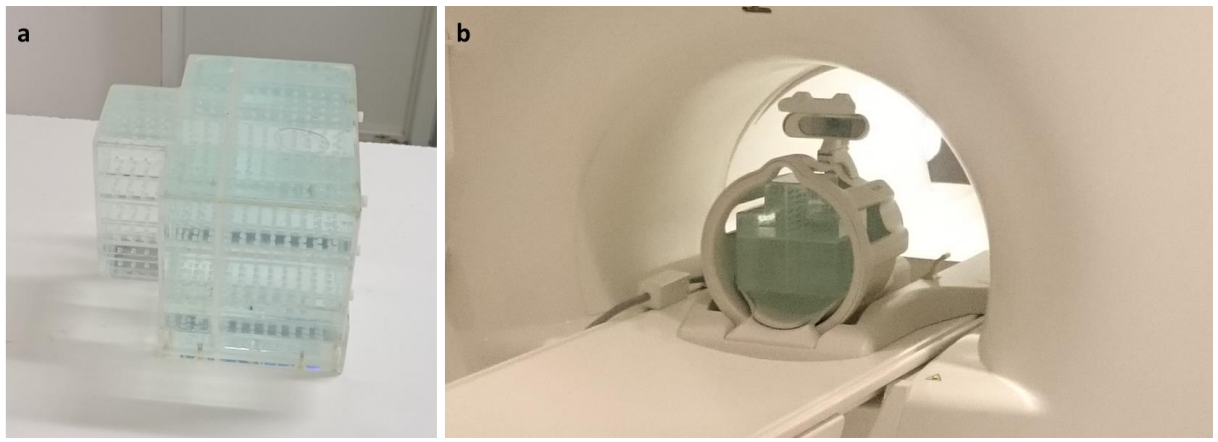


Figure 5-1: (a) The phantom utilized in this study filled with copper sulfate solution. (b) The phantom being MR scanned using the head coil.

5.2.2 Distortion detection

The procedure for distortion detection followed in this work is summarized in Figure 5-2. First, the phantom is filled with copper sulfate solution and MR scanned using the clinical protocol for SRS in order to obtain the evaluated CP distribution. CP locations are determined in the 3D DICOM coordinate system using the same CP localization algorithm as the one presented in Chapter 4 and published in Pappas et al [26]. Briefly, it consists of three steps (i) 3D edge detection, (ii) intensity thresholding and (iii) center of mass calculation and was implemented using in-house MATLAB (The MathWorks, Inc., Natick, MA) routines. Next, the phantom is CT scanned empty and the same procedure is followed to provide the reference CP distribution (Figure 5-2). The resulting CP distributions are registered to the same coordinate system after performing a rigid spatial co-registration. More specifically, a rigid transformation is established

after four CPs lying in the vicinity of the MR isocenter (where scanners are optimized to exhibit minimum geometric distortion [1,33]) are selected and manually matched with the corresponding ones in the CT dataset. This is a commonly adopted approach [27,33,94,96]. As a last step, identified CPs in the reference and evaluated datasets are paired by following their known design template. Geometric distortion is reflected as CP displacement on every axis and calculated as $d_i = i_{MR} - i_{CT}$, where $i = x, y, z$. The overall displacement was also calculated as $d_{tot}^R = \sqrt{d_x^2 + d_y^2 + d_z^2}$. Finally, by using interpolation methods, relevant distortion maps can be created on any orientation within the mapped area.

5.2.3 Image acquisitions

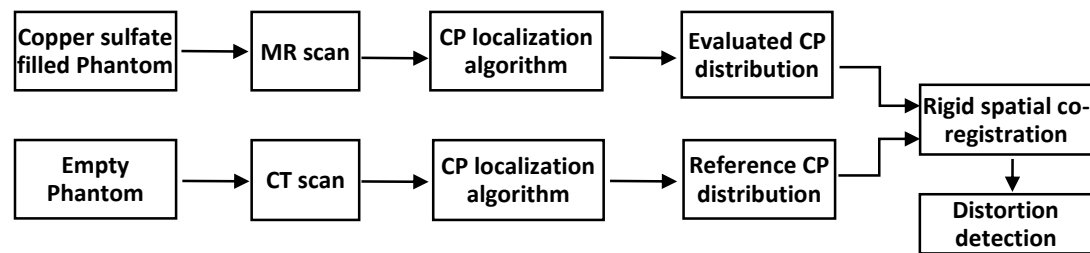


Figure 5-2: Overview of the workflow for distortion detection implemented in this study.

Two MR scanners were included in this study: a GE Optima MR450w with a static magnetic field of 1.5T and a SIEMENS Skyra 3.0T. Emphasis was given to evaluate the clinical protocols used specifically for SRS treatment planning. In particular, three sequences are employed in clinical routine labelled as “FSPGR BRAVO”, “FSPGR 3D T1w” and “T1w MPRAGE”. The corresponding clinically used head coils were also utilized (see also Section 3.4).

All specific details and imaging parameters were kept to their default clinically used values for SRS treatment planning and are summarized in Table 5-1. Pixel size was always $0.9375 \times 0.9375 \text{ mm}^2$. Prior to scanning, the phantom was filled with standard copper sulfate solution.

To obtain the reference CP distribution the phantom was also CT scanned. Images were acquired by a SIEMENS SOMATOM Definition scanner with a reconstruction pixel size of $0.45 \times 0.45 \text{ mm}^2$, slice thickness of 0.6 mm, operated at 120 kVp.

No stereotactic frame, localization box or any other apparatus was mounted on the phantom during MR (nor CT) scanning in order to avoid frame induced distortions [26] or susceptibility related artifacts.

Table 5-1: Protocol parameters of all the performed MR image acquisitions using both scanners included in this study.

MR Scanner Model	Protocol Name	Slice Thickness (mm)	TE/TR/FA (msec/msec/°)	Bandwidth (Hz/mm)	Frequency encoding direction
GE Optima MR450w 1.5T	FSPGR BRAVO	1	3.46/8.29/12	260.4	A-P (y-axis)
GE Optima MR450w 1.5T	FSPGR 3D T1w	1	2.18/6.60/15	260.4	A-P (y-axis)
SIEMENS Skyra 3.0T	T1w MPRAGE	1	2.13/2300/8	213.3	A-P (y-axis)

Abbreviations: TE: echo time; TR: Repetition time; FA: flip angle

5.3 Results

5.3.1 Distortion magnitude

Table 5-2 summarizes the detected CP offset between the MR and CT datasets on the three MR coordinate axes, d_i , as well as the total offset d_{tot}^R . In addition to minimum, maximum and mean detected distortion, Table 5-2 gives the percentage of CPs that were displaced by more than 1 mm. Mean absolute distortions are well below 0.5 mm on any axis for all three protocols.

Regarding the 1.5T GE scanner, increased distortion was detected on the z-axis (possibly due to increased z-gradient magnetic field nonlinearity, which could stem from a less effective performance of the automated distortion correction algorithms integrated in the scanner), while minimal distortion was observed on x and y axis, for

both protocols investigated. The 3.0T SIEMENS scanner is characterized by systematically higher mean distortion values (for the examined sequences) than the 1.5 T GE scanner. However, due to phantom repositioning, CP distribution within the imaged areas was not identical for the two scanners.

Table 5-2: Detected total distortion for the three imaging protocols of the GE and SIEMENS scanners included in this study. Percentage of CPs detected with more than 1 mm of absolute distortion (% CPs > 1 mm) is also given.

Axis		GE 1.5T		SIEMENS 3.0T
		FSPGR BRAVO	FSPGR 3DT1w	T1w MPRAGE
X axis (mm)	Range	-0.44 – 0.46	-0.57 – 0.54	-1.12 – 1.16
	Mean	-0.04	0.00	0.05
	Mean absolute	0.18	0.28	0.36
	% CPs > 1mm	0.00%	0.00%	0.63%
Y axis (mm)	Range	-0.70 – 0.55	-0.64 – 0.79	-1.16 – 1.84
	Mean	-0.14	0.00	0.03
	Mean absolute	0.29	0.23	0.46
	% CPs > 1mm	0.00%	0.00%	4.13%
Z axis (mm)	Range	-1.36 – 0.75	-1.93 – 1.02	-1.05 – 0.57
	Mean	-0.16	-0.06	-0.34
	Mean absolute	0.31	0.46	0.41
	% CPs > 1mm	0.08%	4.22%	0.21%
R (mm)	Range	0.04 – 1.37	0.05 – 1.99	0.06 – 1.92
	Mean	0.54	0.66	0.82
	% CPs > 1mm	1.06%	5.07%	10.37%

Figure 5-3 highlights the effect of increasing distortion magnitude with respect to increasing radial distance from the MR scanners' isocenter. In particular, total distortion magnitude detected with all 947 CPs is presented against radial distance from the

scanners' origin for both scanners and for all three imaging protocols. The mean as well as the spread of the detected CP displacement significantly increases with distance from the isocenter (Figure 5-3). Note that the range of radial distances investigated (up to approximately 135 mm) exceeds the typical size of a head. CP distribution within the phantom extended to the far off of the available space within the employed MR head coils.

Figure 5-3 also allows for a qualitative comparison of distortion magnitude between the three clinically used protocols. As seen, the “FSPGR BRAVO” sequence is slightly less prone to distortion compared to the other two protocols investigated.

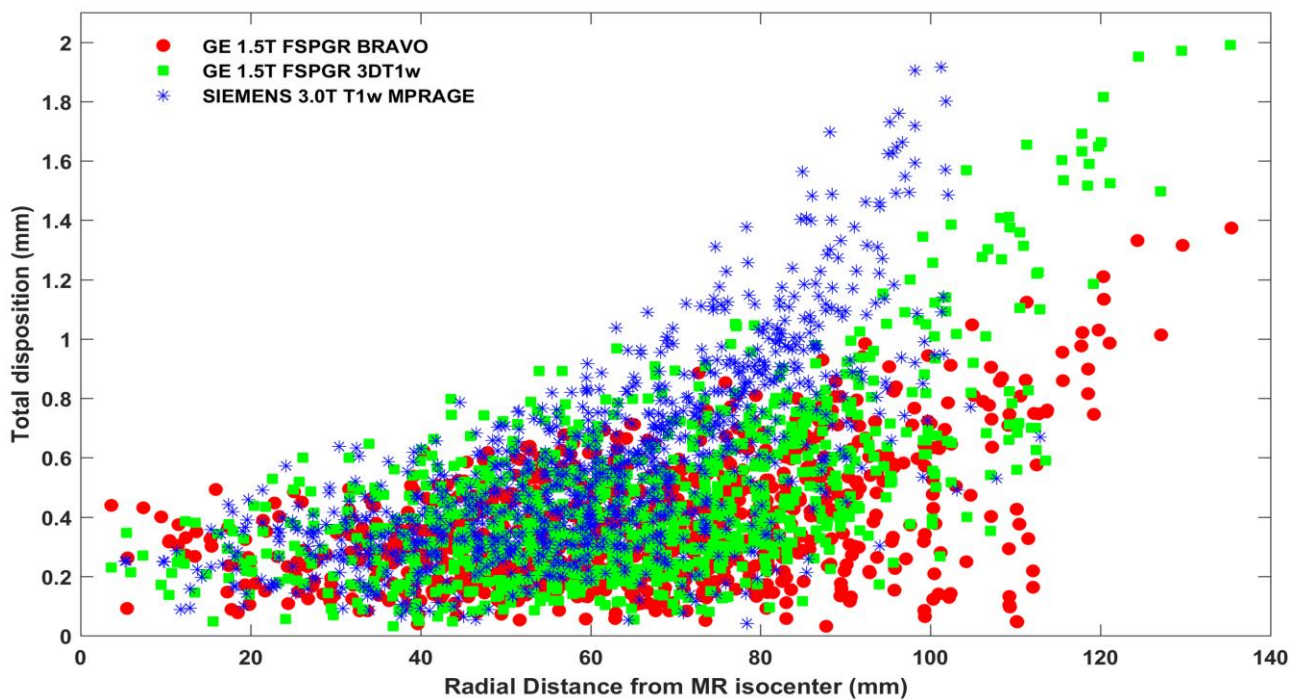


Figure 5-3: Total geometric distortion detected at all 947 CP locations for the three clinically used imaging protocols. Results are presented against radial distance from the corresponding MR scanner's isocenter.

5.3.2 Distortion distribution and directionality

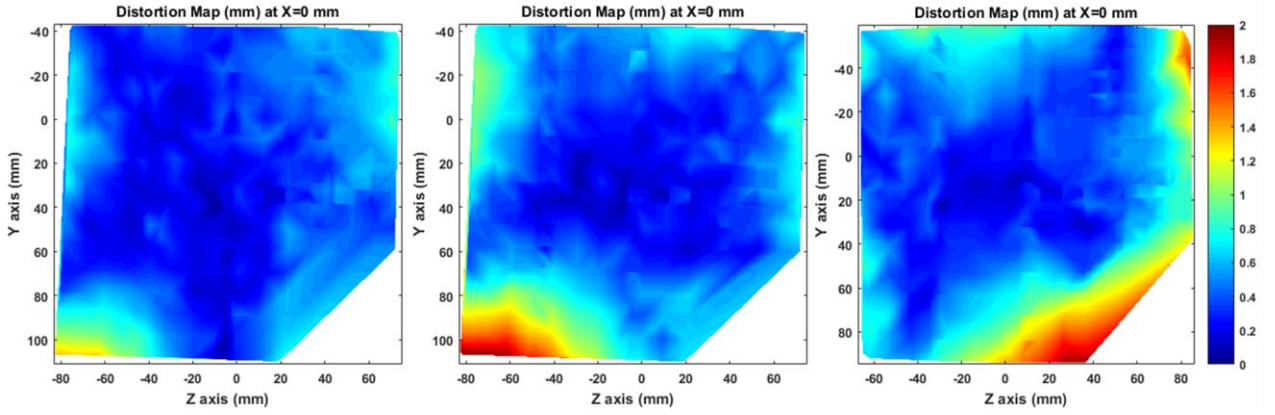


Figure 5-4: Total distortion maps (d_{tot}^R) on a sagittal plane at $x=0$ mm for FSPGR BRAVO (left), FSPGR 3DT1w (middle) and T1w MPRAGE (right).

A series of 3D total distortion maps (d_{tot}^R) have been created for all acquired image series. Inevitably, due to the interpolation procedure involved, accuracy of distortion maps deteriorates in regions distant from the CPs. Given that, y-z central planes carefully selected to lie in areas of high CP density (i.e., at $x=0$ mm) are presented in Figure 5-4. For all three MR protocols, detected distortion is minimal around the magnet's isocenter and greatly increases at the corners of the examined space.

Figure 5-5 provides an insight to the spatial distribution and directionality of the detected distortion. The distortion vectors' initial points correspond to CT-identified CP locations (i.e., "reference" locations) while terminal points to MRI-detected ones. Distortion vectors are projected on the y-z plane. The vectors' lengths are proportional to the detected distortion magnitude. As also shown in Table 5-2, distortion for the GE 1.5T scanner is excessive on the negative z-axis, while for the 3.0T scanner, distortion magnitude exhibits an almost symmetrical spatial distribution in all three axes.

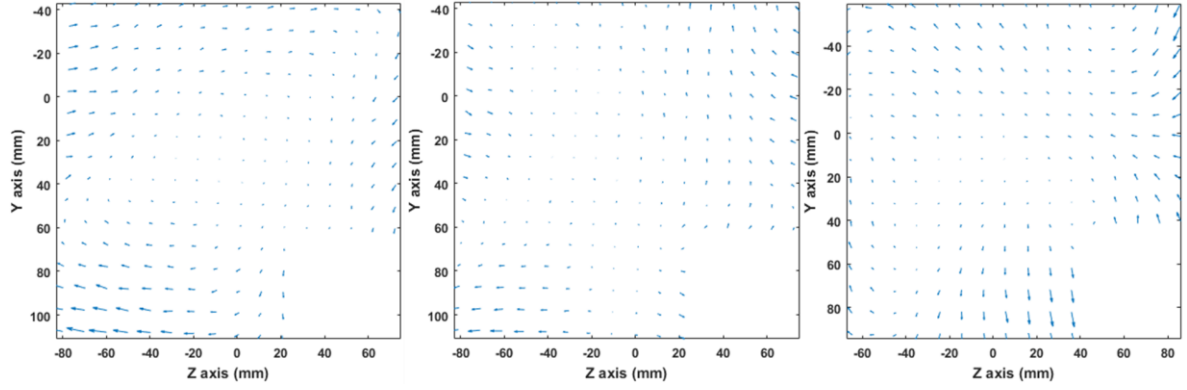


Figure 5-5: Distortion vectors on a sagittal plane at $x=0$ mm for FSPGR BRAVO (left), FSPGR 3DT1w (middle) and T1w MPRAGE (right). Vectors' lengths have been magnified by a factor of three to increase visibility.

5.4 Discussion

The phantom and CP localization algorithm used in this study are similar to those employed in Chapter 4. In this study, contrarily to the previous Chapter where the reversed gradient technique [25–27,33,42,94,95,162] was used to distinguish and characterize different sources of system-related geometric distortion (including those induced by stereotactic accessories such as the immobilization frame used in GK SRS applications [26]), distortion assessment relied entirely on one MR scan, as has been demonstrated elsewhere [35,147,151,154,163]. Consequently, both sequence independent (i.e., arising from gradient non-linearity) and sequence dependent distortions [25,33,149,150] (i.e., distortions related to B_0 inhomogeneity, chemical shift artifacts and susceptibility differences) were taken into account. However, chemical shift artifacts are not relevant in a phantom study while susceptibility induced distortions (stemming from PMMA-copper sulfate solution susceptibility difference) are uniform throughout the entire geometry and, inevitably, cancel out during the spatial registration step. Effectively, the approach followed in this study mainly takes into account machine-related distortions [151] (i.e., B_0 inhomogeneity and gradient nonlinearity). According to the results presented in Chapter 4, uncertainty in CP displacement detection is approximately 0.2 mm.

Three MR protocols used in SRS treatment planning (at 1.5T and 3.0T) were evaluated in terms of geometric accuracy. Although mean absolute distortion was found less than 0.5 mm in any orientation, CP total displacements of up to 2 mm were observed at the

edges of the imaged area. This suggests that regions of interest lying within a field-of-view relative to the size of a large head exhibit considerable levels of distortion and may compromise dose delivery accuracy [10]. Since distortion magnitude and orientation strongly depends on the imaging parameters used as well as the volume of interest and CP distribution within the imaged area, results cannot be directly compared with previous published studies. However, detected distortion of more than 1 mm (related to gradient nonlinearity alone) is generally acknowledged [26,96,149,162] for volumes similar to the one examined in the present study. In the study of Yu et al [154] a total geometric distortion of approximately 3 mm was reported for brain MRI scans used in GK SRS. For larger field-of-views (used in extracranial stereotactic body radiotherapy), MR-related geometric accuracy is studied using body-sized phantoms [27,28,92–96,151] with distortions reported reaching up to 25 mm. In a review article [2], a total of 11 studies investigating system-dependent geometric distortions were identified, with 5 of them reporting maximum detected distortion of less than 2 mm.

In addition to system-related distortion, patient-induced spatial inaccuracies should also be considered [2,33]. Several studies [10,26,164] have reported patient-related geometric uncertainties ranging up to 1.9 mm for MR protocols used in SRS treatment planning. In a simulation study, Stanescu et al [31] reported susceptibility induced distortion reaching up to 3.40 mm and 2.02 mm (for a 3.0T MR scanner employing 5 mT/m gradient strength) in air cavities and bone structures, respectively, in intracranial patient MR images. Depending on B_0 strength, bandwidth used, anatomical site investigated and orientation relative to B_0 , susceptibility induced distortion greatly varies [31]. Moreover, patient-induced distortion cannot be accurately predicted a priori since each patient is characterized by different magnetic susceptibility distributions which may also vary in time [2].

In the current practice, geometric distortions are commonly checked at a specific plane (2D distortion assessment) using the ACR phantom [165,166] for a typical T1w sequence using a passing criterion of 2 mm. In this work, a 3D distortion detection phantom coupled with a suitable methodology was implemented for the specific clinical protocols at 1.5T and 3.0T used for target localization and distortions of up to 2 mm were identified in an area covering an extended region of the field-of-views used in brain SRS applications. It is noted however that patient-induced distortions are not taken into account when phantoms are used to derive distortion maps.

An initial evaluation and periodic quality control related to MR geometric distortions for the specific MR units, sequences, clinical protocols and parameters is paramount, especially when they are used for the delineation of small targets in the periphery of the brain, where MR geometry accuracy deteriorates even in the relative small field-of-views involved (e.g., multiple brain metastases cases). Further work is still needed to fully characterize MR-related distortions and determine the acceptable levels of spatial error that do not considerably compromise dose delivery and target coverage. Towards that direction, Chapter 6 focuses on patient induced distortions [31,33,89,152,167] which should also be considered an additional source of geometric degradation.

5.5 Conclusion

Spatial distortions of up to 2 mm were detected for clinical MR protocols (at 1.5T and 3.0T) used in SRS treatment planning in regions away from scanner's isocenter. Necessity to evaluate and apply quality control procedures for the specific MR units and protocols employed in SRS was highlighted.

6 Patient-specific geometric distortion in MR images employed in stereotactic radiosurgery treatment planning

Summary

This work focuses on MR-related sequence dependent geometric distortions, which are associated with B_0 inhomogeneity and patient-induced distortion (susceptibility differences and chemical shift effects), in MR images used in stereotactic radiosurgery (SRS) applications. Emphasis is given to characterize distortion in target areas identified using Gd-DTPA paramagnetic contrast agent administration.

The prototype distortion detection acrylic-based phantom (presented in Chapter 4) was modified to accommodate two small cylindrical inserts simulating small brain targets. The inserts were filled with various concentrations of Gd-DTPA solutions (0-20 mM). The phantom was MR scanned at 1.5T unit using both the reversed read gradient polarity (to determine the overall distortion as reflected by the inserts centroid offset) and the field mapping (to determine B_0 inhomogeneity related distortion in the vicinity of the inserts) techniques. Post-Gd patient images involving a total of 10 brain metastases/targets were also studied using a similar methodology.

For the specific imaging conditions, contrast agent presence was found to significantly affect phantom insert position, with centroid offset extending up to 0.068 mm/mM (0.208 ppm/mM). The Gd-DTPA induced distortion in patient images was of the order of 0.5 mm for the MRI protocol used, in agreement with the phantom results. Total localization uncertainty of metastases-targets in patient images ranged from 0.35 mm to 0.87 mm, depending on target location, with an average value of 0.54 mm (2.24 ppm). This relative wide range of target localization uncertainty results from the fact that the B_0 inhomogeneity distortion vector in a specific location may add to or partly

counterbalance Gd-DTPA induced distortion, thus increasing or decreasing, respectively, the total sequence dependent distortion.

Although relatively small, the sequence dependent distortion in Gd-DTPA enhanced brain images can be easily taken into account for SRS treatment planning and target definition purposes by carefully inspecting both the forward and reversed polarity series.

6.1 Introduction

Within-patient, tissue susceptibility effects have been widely investigated in simulation studies [31,43,44]. However, distortions at SRS target locations, including those induced by Gd-based contrast agents, have not been specifically studied. The paramagnetic nature of Gd alters the local magnetic field due to its magnetic susceptibility (see Sections 1.6 and 3.4). Susceptibility difference inherently induces geometric distortion in and around a susceptibility cavity, with the spatial displacement of a given point varying according to the cavity location, size and orientation with respect to B_0 [31,36,47,72]. Susceptibility effects associated with Gd-enhanced lesions/targets in MRI-based SRS applications increase the localized total distortion and could result in target under-dosage, especially for tiny lesions [9,10,45].

A systematic characterization of system-related distortions arising from gradient field nonlinearities and eddy currents in the stereotactic frame was performed in Chapters 4 and 5. This study seeks to examine respective sequence dependent distortions. Emphasis is put on the geometric warping related to the magnetic susceptibility of the routinely administered Gd-DTPA contrast agent. To this purpose, the prototype phantom was modified to incorporate inserts filled with Gd-DTPA at various concentrations. Distortion evaluation was performed using the read gradient polarity reversal methodology in combination with the field mapping technique to assess and subtract background field variations. Furthermore, a similar methodology was applied to brain MR images in order to characterize and evaluate sequence dependent distortions at and in the vicinity of Gd-DTPA enhanced metastases. The effect of such distortions on SRS treatment planning and target definition is discussed.

6.2 Materials and Methods

6.2.1 Phantom study

6.2.1.1 Phantom description

The prototype phantom used for the studies presented in the previous Chapters was also employed here. For the purposes of the present study, the phantom was modified to accommodate two cylindrical inserts (inner dimensions of 8 mm diameter and 11 mm height, wall thickness of 1.8 mm), simulating two small brain metastases (Figure 6-1). The inserts were positioned towards the Superior (S) side of the phantom at a distance of 45 mm between them and lying only a few millimeters from control points (Figure 6-1(b)). Small plastic screws along with rubber flanges facilitated leakage proof filling with solutions, while acrylic posts ensured fixed position with respect to the removable top of the phantom (Figure 6-1(a)). In essence, the installed cylindrical inserts can be regarded as two additional CPs with the added capability to be filled with different solutions with respect to the body of the phantom.

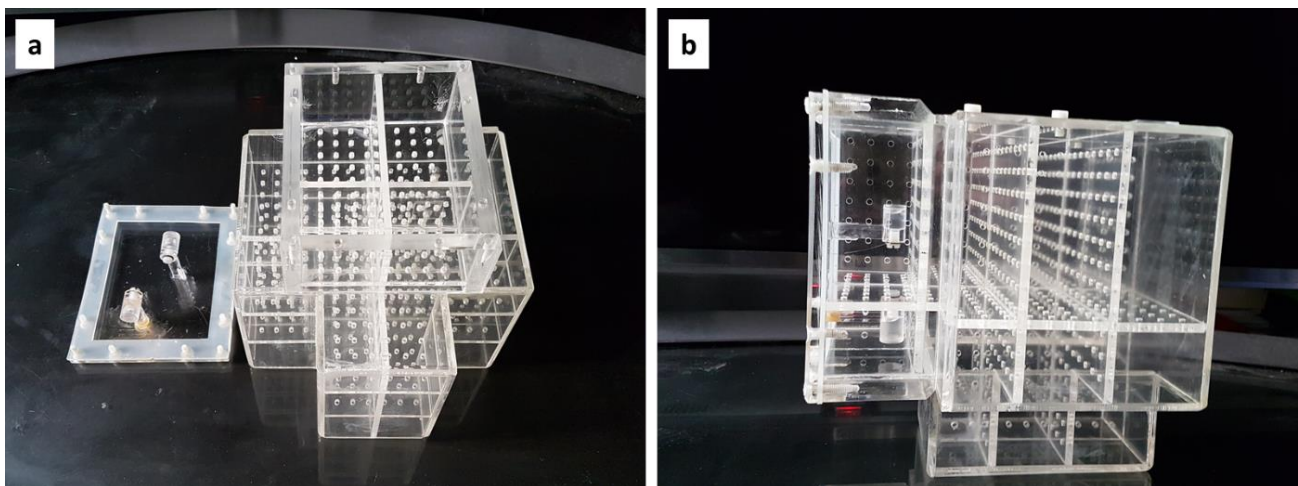


Figure 6-1: The distortion detection phantom used in this study. (a) Two cylindrical inserts were fixed on the removable top cap (S side of the phantom) shown on the left. (b) The phantom positioned at scanning orientation with the top mounted on.

In order to investigate the magnitude of distortion induced by the contrast agent, the inserts were filled with varying concentrations of Gd-DTPA solution in saline. In specific, both inserts were filled with saline (corresponding to zero concentration of Gd-DTPA), as well as 5, 10 and 20 mM of Gd-DTPA diluted in saline. Although contrast agent concentration rapidly varies within the brain and especially within tumors and vessels, concentrations considered here are typical with respect to the ones encountered in vivo and cover the range of concentrations found in the literature [91,168–170]. The phantom body was filled with standard copper sulfate solution [26,148] in order to achieve adequate signal intensity and high contrast with acrylic.

6.2.1.2 MRI scanning

All phantom scans were performed at 1.5T (Multiva, Philips Medical Systems, The Netherlands). The imaging protocol comprised of three 3D gradient recalled echo (GRE) pulse sequences with vendor-supplied distortion correction routines enabled. A phased array head coil was used for signal reception. Scanning parameters are summarized in Table 6-1 (image series #1-4). In all image series, reconstructed pixel size was $0.98 \times 0.98 \text{ mm}^2$ with a slice thickness of 1 mm.

6.2.1.3 Read gradient polarity reversal technique

The reversed read gradient polarity technique [25,27,33,42] was implemented in order to evaluate the contrast agent induced distortion. Briefly, this method relies on the fact that sequence dependent distortions (i.e., stemming from B_0 inhomogeneity, susceptibility differences and chemical shift artifacts [33]) change sign with respect to frequency encoded direction. Therefore, the technique requires that the phantom is MR scanned twice using identical imaging parameters except for the read gradient polarity (e.g., A – P and P – A) (for further details, refer to Section 2.8). The geometric offset between CPs identified in the two image series is twice the sequence dependent distortion magnitude [25].

Acquired images from series #1-4 (Table 6-1) were exported from the MR unit in dicom format and analyzed in MATLAB R2015b (The MathWorks, Inc., Natick, MA) using in-house routines. For every pair of image series (e.g., forward A-P polarity and

reversed P-A polarity), the cylindrical inserts were identified in the 3D image stack by exploiting the signal void of the inserts' acrylic walls. By applying a simple thresholding procedure, binary images were obtained facilitating the estimation of the centroid (geometric center) of each insert within the MRI coordinate system. In addition, all CPs incorporated in the phantom were identified in both the forward and reversed MRI scans, using the localization algorithm described in Chapter 4, characterizing system-related distortions [26]. Averaged (from the paired scans) CP or insert centroids were regarded as reference locations (assuming that polarity reversal results in the change of distortion sign without affecting the magnitude). Sequence dependent distortions (related to B_0 inhomogeneity and susceptibility effects) were estimated as the signed geometric offsets towards the polarity direction between reference locations (CP or insert centroids) and corresponding ones identified in the forward MRI scans. Residual sequence independent distortions (related to gradient field non-linearity [2,33]), after the application of the vendor-supplied distortion correction, are not taken into account since they do not change sign with respect to read gradient polarity.

Table 6-1: MR scanning protocol and parameters used in the phantom study.

Image series #	MRI pulse sequence	Receiver bandwidth (Hz/pixel)	TE/TR/FA (msec/msec/°)	Read gradient axis and polarity	Gd-DTPA concentration in inserts (mM)
1	T1w spoiled GRE	191	4.6/25/30	y-axis / A-P	0, 5, 10, 20
2	T1w spoiled GRE	191	4.6/25/30	y-axis / P-A	0, 5, 10, 20
3	T1w spoiled GRE	191	4.6/25/30	x-axis / R-L	0, 5, 10, 20
4	T1w spoiled GRE	191	4.6/25/30	x-axis / L-R	0, 5, 10, 20
5	1 st echo GRE	191	4.4/14/30	y-axis / A-P	0, 5, 10, 20
6	2 nd echo GRE	191	6.8/14/30	y-axis / A-P	0, 5, 10, 20
7	1 st echo GRE	191	4.4/14/30	x-axis / R-L	0, 5, 10, 20
8	2 nd echo GRE	191	6.8/14/30	x-axis / R-L	0, 5, 10, 20

6.2.1.4 Field mapping technique

In addition to the reversed gradient method, the well-established field mapping technique [30,33,41,98,171] for sequence dependent distortion assessment was also implemented for the same phantom within the same MR imaging session in order to validate the obtained results related to the CPs. Briefly, the method requires an additional imaging step which consists of a dual echo GE pulse sequence. Phase difference images are directly proportional to sequence dependent distortion, following a post-processing, time-consuming phase unwrapping step [97], according to equation (1), [30,33,171]:

$$\Delta B(x, y, z) = \frac{\Delta\phi(x, y, z, \Delta TE)}{\gamma \Delta TE} \quad (1)$$

where $\Delta TE = TE2 - TE1$ is the echo time difference between the two echoes of the two sequences and γ is the proton gyromagnetic ratio. Magnetic field variations can be transformed to sequence dependent distortions on the frequency encoding axis, e.g., Δy if y-axis is the read gradient axis, using equation (2):

$$\Delta y(x, y, z) = \Delta B(x, y, z) / G_{fe} \quad (2)$$

where G_{fe} is the read gradient field strength on y-axis. Equations (1) and (2) define the distortion sign convention used. A thorough analysis of the field mapping technique and the concerns involved was given in Section 2.8.2

In order to avoid severe phase wrapping, which could introduce phase unwrapping errors [97], selected ΔTE was 2.40 msec, at the expense of sensitivity. Imaging parameters used are summarized in Table 6-1 (image series #5-8). The resulting wrapped phase difference maps were unwrapped by implementing the methodology described in [97], with the negated magnitude serving as the noise estimator field for guided unwrapping (see Section 2.8.2.3). The developed routine is also given in the Appendix. In large areas of signal void, phase difference maps were dilated due to lack of phase information [98]. However, phase difference maps at low signal areas were discarded and not used in the analysis. This post imaging step required several hours of computational time, although real-time image unwarping has also been proposed [38].

Unwrapped phase difference maps were used to determine sequence dependent distortion at the CP locations within the 3D MR coordinate system as determined by

the analysis described in Section 6.2.1.3. Results were compared to the corresponding ones derived using the reversed read gradient polarity technique for cross-validation. Furthermore, the same methodology was followed to estimate B_0 inhomogeneity induced distortion exhibited in the vicinity of the cylindrical inserts filled with contrast agent solution.

6.2.1.5 Contrast agent induced offset

Net insert centroid offset stemming from Gd-DTPA susceptibility alone was deduced by subtracting the B_0 inhomogeneity related distortion at the respective insert region from the total distortion at the specific insert location as reflected by the total geometric offset of the insert centroid. The former was evaluated by the field mapping technique, whilst the latter was estimated as the signed geometric offset between reference insert centroid locations and corresponding ones identified in the forward MRI scans.

6.2.2 Patient study

Three patients referred to SRS for single or multiple brain metastases of variable sizes and locations were enrolled. All MR images were acquired at 1.5T (Achieva, Philips Medical Systems, The Netherlands), following an intravenous Gd-DTPA injection of 0.2 mmol/kg. The institution's standard clinical protocol for GK SRS applications was implemented, which included the utilization of the Leksell stereotactic frame for patient immobilization and image registration purposes. The imaging protocol involved both the read gradient polarity reversal and field mapping techniques employing a set of pulse sequences similar to those used in the phantom study. Specific acquisition parameters were the same as the ones presented in Table 6-1 for series #1, 2, 5 and 6 (only the y-axis was used as frequency encoding axis), apart from the receiver bandwidth which was set to 217 Hz/pixel.

Patient images, reconstructed using a voxel size of $0.82 \times 0.82 \times 1.5 \text{ mm}^3$, were exported in dicom format and analyzed in MATLAB using in-house developed routines. A total of ten brain metastases were identified and manually contoured by an experienced neurosurgeon in both the forward and reverse read gradient polarity series. Contoured lesions were treated as CPs for distortion detection at the respective

locations and, therefore, the followed approach was similar to that applied in the phantom study. Using the polarity reversal technique, the total sequence dependent distortion at a specific lesion location was calculated as half the geometric offset between the corresponding centroids in the MRI coordinate system. The field mapping technique was used to determine potential background field distortions in the vicinity of the identified lesions and, thus, to differentiate between contrast agent induced geometric offset and spatial degradation due to local B_0 inhomogeneities and chemical shift effects. Specifically, the mean distortion value within an unenhanced volume of interest close to a lesion was determined, and this value was subtracted from the total sequence dependent distortion estimated (using the polarity reversal method) for that lesion location to yield the net contrast agent induced offset.

6.3 Results

6.3.1 Phantom study

Table 6-2: Sequence dependent distortion magnitude for all 947 control points, detected using both methods.

	Frequency encoded direction	Mean \pm 1 std (mm)	Median (mm)	Max (mm)
Reversed read gradient polarity	A-P (y-axis)	0.21 ± 0.22	0.14	1.22
	L-R (x-axis)	0.30 ± 0.22	0.25	1.17
Field mapping	A-P (y-axis)	0.21 ± 0.16	0.19	1.05
	L-R (x-axis)	0.27 ± 0.16	0.24	1.12

Table 6-2 summarizes the results on CPs locations obtained following implementation of both read gradient reversal and field mapping techniques. Close agreement is observed between the two methods which supports the validity of the methodology and image processing routines employed in this study. Sequence dependent distortion

magnitude varies with respect to the distance from the MR scanner's isocenter and may exceed 1 mm. Taking into account that for the CPs close to the center of magnetic field the observed distortion is of the order of 0.1 mm, the observed sequence dependent distortion magnitudes mainly stem from B_0 inhomogeneities.

Regarding the cylindrical inserts filled with various concentrations of contrast agent, Figures 6-2 and 6-3 demonstrate relevant distortion maps derived from the field mapping technique, as well as acquired T1w axial images, for the read gradient direction in the y-axis and x-axis, respectively. Distortion maps (Figures 6-2(a),(d) and 6-3(a),(d)) are presented for an axial slice lying centrally to the cylindrical inserts. Inserts with no contrast agent do not disturb the local magnetic field (Figures 6-2(a) and 6-3(a)), while for the maximum concentration considered a steep distortion gradient is identified at the inserts borders (Figures 6-2(d) and 6-3(d)), where induced field variations associated with susceptibility differences are expected to be maximized [36,47]. The susceptibility related distortion gradient reaches its maximum values at the S and Inferior (I) inserts borders (not shown here). It should also be noted that B_0 inhomogeneity related distortion was not constant and slightly varied between different scanning sessions, as evidenced by comparing Figures 6-2(a) and 6-3(a) with Figures 6-2(d) and 6-3(d), respectively, depending on phantom positioning with respect to the MR isocenter and auto-shimming procedures potentially performed.

As shown in Figures 6-2(b),(c) and 6-3(b),(c), reversing the polarity of the read gradient direction does not evidently induce spatial offset of the inserts centroids in the case of no contrast agent presence. Contrarily, in the presence of the paramagnetic agent, inserts get mispositioned and, as demonstrated for the maximum concentration considered herein (Figures 6-2(e),(f) and 6-3(e),(f)), specific insert walls appear severely distorted.

Figure 6-4(a) presents the estimated net centroid offsets (i.e., owing to the Gd-DTPA contrast agent) for the cylindrical inserts for the MR scans with frequency encoding set on the y-axis. As expected, net centroid offset varies considerably with Gd-DTPA concentration. Relatively lower net centroid offsets were detected (up to 1 mm for the 20 mM concentration) with the frequency encoding direction on x-axis (Figure 6-4b),

suggesting a weaker correlation between centroid mispositioning and contrast agent concentration for this setup.

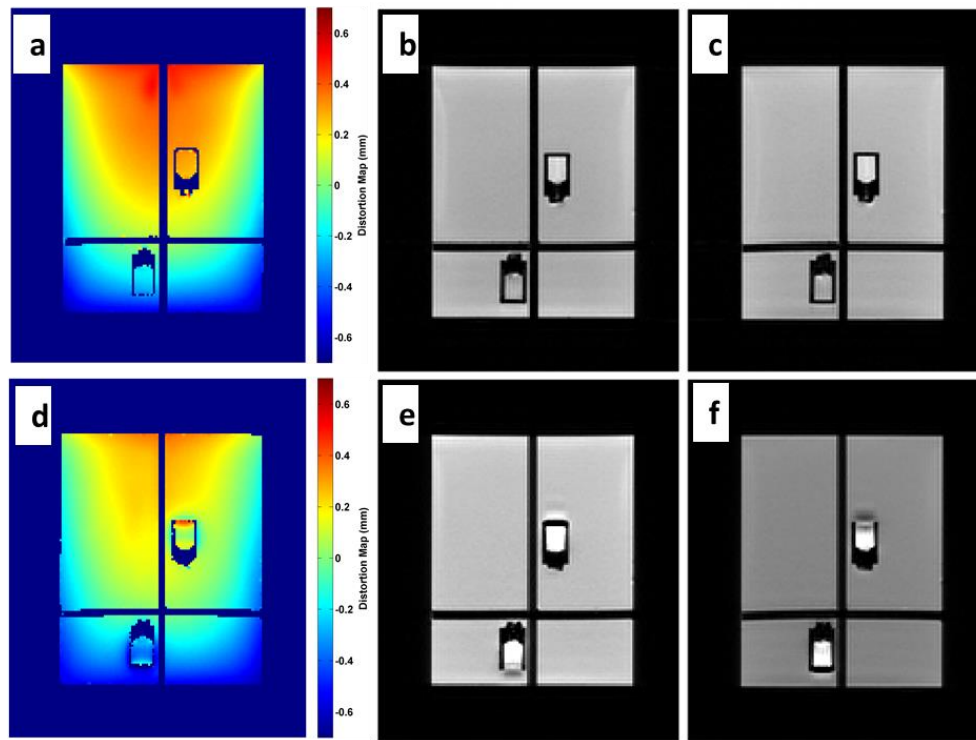


Figure 6-2: Axial slice intersecting the cylindrical inserts of the phantom with frequency encoded direction set on A-P (a),(b),(d),(e) and P-A (c),(f) directions. Inserts are filled with saline (no contrast agent) (top row) or 20 Mm of Gd-DTPA (bottom row). (a),(d) Distortion maps derived using the field mapping technique. (b),(c),(e),(f) T1w images of the same slice. Reversing read gradient polarity has no apparent effect on insert position but evidently displaces the contrast agent signal.

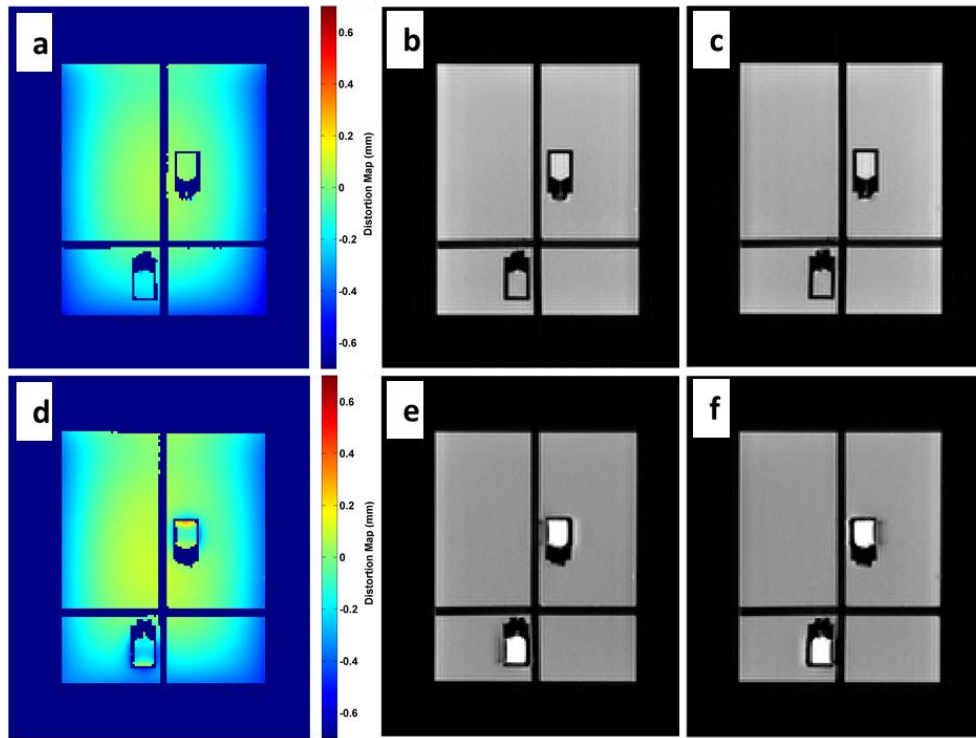


Figure 6-3: Axial slice intersecting the cylindrical inserts of the phantom with frequency encoded direction set on L-R (a),(b),(d),(e) and R-L (c),(f) directions. Inserts are filled with saline (no contrast agent) (top row) or 20 Mm of Gd-DTPA (bottom row). (a),(d) Distortion maps derived using the field mapping technique. (b),(c),(e),(f) T1w images of the same slice. Reversing read gradient polarity has no apparent effect on insert position but evidently displaces the contrast agent signal.

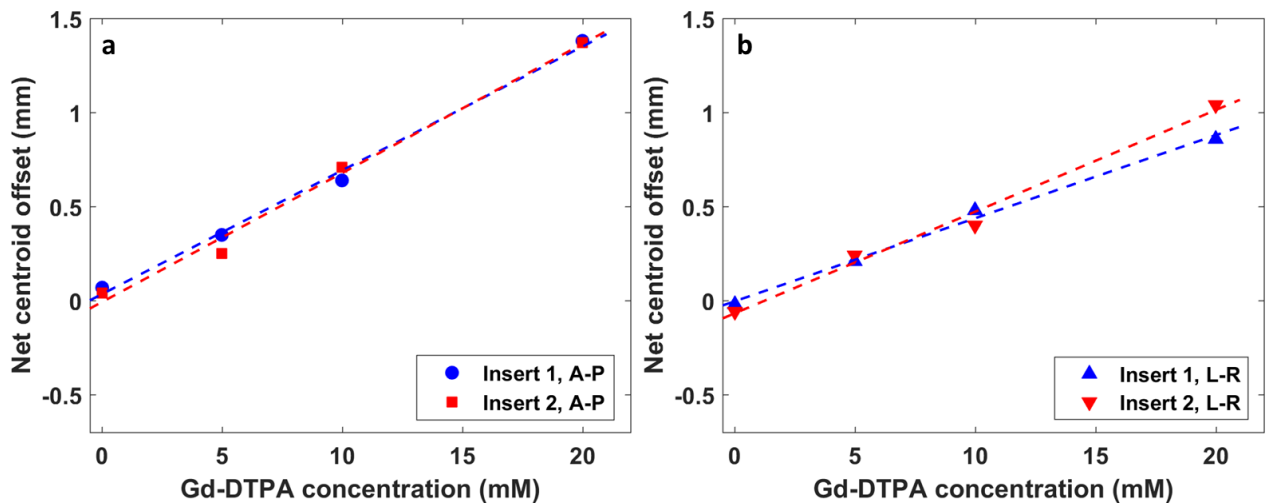


Figure 6-4: Estimated net centroid offset for both cylindrical inserts as a function of contrast agent concentration. (a) Frequency encoding direction set on the y-axis (P-A and A-P). (b) Frequency encoding direction set on the x-axis (L-R and R-L). Dashed lines were derived by linear fitting of the corresponding data.

For all datasets, a first order polynomial fit was applied in order to determine the centroid offset, D , induced per unit of contrast agent concentration, C , i.e., $\left|\frac{\partial D}{\partial C}\right|$, as reflected by the slopes of the curves shown in Figure 6-4. Obtained results are depicted in Figure 6-5. The error bars correspond to the uncertainty (at 67% confidence level) of the slope, as determined by the linear regression analysis. Significantly lower slopes were calculated for x-axis read gradient compared to y-axis read gradient. This could be attributed to the cylindrical shape of the inserts [36,47,72].

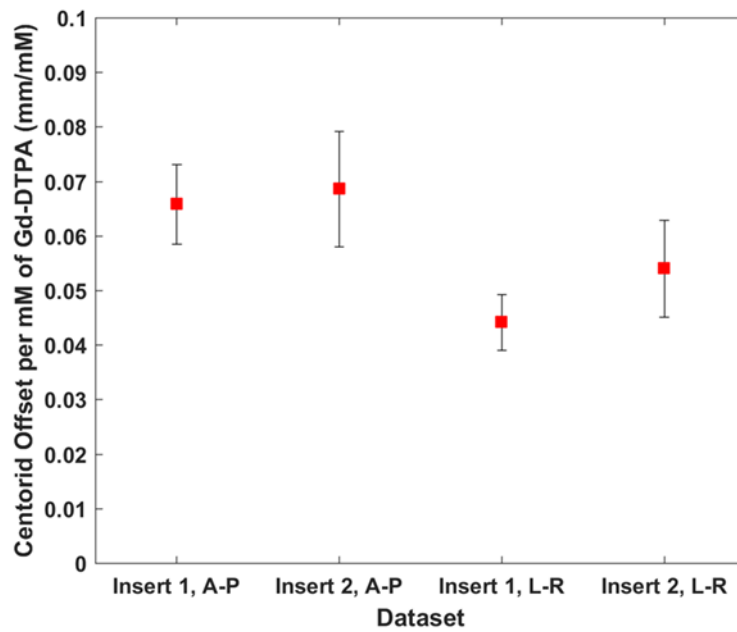


Figure 6-5: Fitted slopes for net centroid offset vs Gd-DTPA concentration. Error bars correspond to the uncertainty of the slopes (at 67% confidence level) as determined by linear regression analysis.

6.3.2 Patient study

Table 6-3 summarizes the results of the patient study conducted. For each lesion, the total centroid offset identified in every axis using the reversed read gradient polarity is given. This offset corresponds to the overall target localization uncertainty due to patient-induced geometric distortion in MR images. In phase encoding directions, i.e., x and z axes, maximum centroid offset hardly exceeds 0.1 mm and represents the uncertainty of the experimental methodology adopted. In the frequency encoding direction (y-axis), total centroid offset magnitude is on average 0.54 mm and exceeds 0.75 mm in two cases (2.24 and 3.11 ppm, respectively). It should be noted that these results represent the distance between reference lesion centroid locations and

corresponding ones identified in the forward polarity MR scan. Using the field mapping technique, distortion in the range of -0.12 up to 0.27 mm (Table 6-3) was detected in regions of interest close to the targets but with no Gd-DTPA enhancement, mainly due to local B0 magnetic field inhomogeneities. The directionality of this distortion either opposes or is the same with that of the susceptibility induced distortion, thus decreasing or increasing, respectively, the total uncertainty in target localization. Subtracting field mapping obtained distortion from the centroid offset in y-axis yields the net offset (i.e., centroid offset without effects from background field variations), which represents the Gd-DTPA susceptibility induced distortion. As presented in Table 6-3, the net offset ranges between 0.43 and 0.65 mm (1.78 and 2.68 ppm, respectively), with an average value of 0.51 mm (2.11 ppm).

Table 6-3: Patient study results. For each metastasis, the total centroid offset provided by the reversed polarity technique is presented, along with the distortion detected using the field mapping technique. Net centroid offset in y-axis is deduced by subtracting the detected background distortion from the total centroid offset in y-axis.

Patient #	Met #	Lesion characteristics			Total centroid offset (Reversed polarity)			Distortion close to lesion (Field mapping)	Net centroid offset (mainly related to Gd-DTPA)	
		Volume (mm ³)	Distance from MR isocenter (mm)	Location on z-axis (mm)	x-axis (mm)	y-axis (mm)	z-axis (mm)	y-axis (mm)	y-axis (mm)	y-axis (ppm)
1	1	1107	67.8	33.4	-0.04	0.80	0.07	0.27	0.53	2.19
2	2	471	69.0	6.3	0.00	0.52	-0.03	-0.12	0.65	2.68
	3	48.4	20.6	-5.7	0.01	0.47	0.00	0.01	0.46	1.92
	4	33.3	31.1	5.3	-0.02	0.35	-0.08	-0.12	0.47	1.96
3	5	18.2	35.0	5.3	-0.02	0.38	0.10	-0.10	0.49	2.02
	6	52.4	54.2	17.3	-0.07	0.38	0.01	-0.06	0.44	1.82
	7	20.2	49.5	38.3	-0.04	0.51	0.08	0.08	0.43	1.78
	8	20.2	83.7	48.8	0.04	0.72	0.08	0.20	0.52	2.14
	9	272	362.2	50.3	0.06	0.37	-0.12	-0.10	0.47	1.95
	10	212	541.8	66.0	-0.07	0.87	-0.09	0.24	0.63	2.61

Figure 6-6(a) presents the distortion field, as estimated by the field mapping technique, of an axial image depicting metastases #4 and #5 (Table 6-3). Figure 6-6(b) demonstrates the fusion of 3D T1w forward and reversed polarity MR scans. Matching pixels that exhibit different signal intensity in the two images are highlighted in color. Offsets between lesions in the two MR images are evident. A normalized signal intensity profile is given in Figure 6-6(c), quantifying the detected offset along a line passing through the two metastases. Field mapping results suggest a background field distortion of the order of -0.10 mm at this area (Table 6-3 and Figure 6-6(a)). Since the total centroid offset detected in the y-axis for the two metastases is slightly above +0.35 mm (Table 6-3), it is deduced that the Gd-DTPA induced centroid offset approaches +0.5 mm.

Contrarily, for metastasis #10 (Table 6-3), the background distortion in the vicinity of the lesion was found equal to +0.24 mm (Table 6-3 and Figure 6-7(a)). As a result, this distortion adds up to the estimated susceptibility induced offset (+0.63 mm, Table 6-3) resulting in a total centroid offset of +0.87 mm (Table 6-3 and Figure 6-7(b)). Therefore, the spatial shift between signal intensity profiles in Figure 6-7(c) is approximately double that shown in Figure 6-6(c).

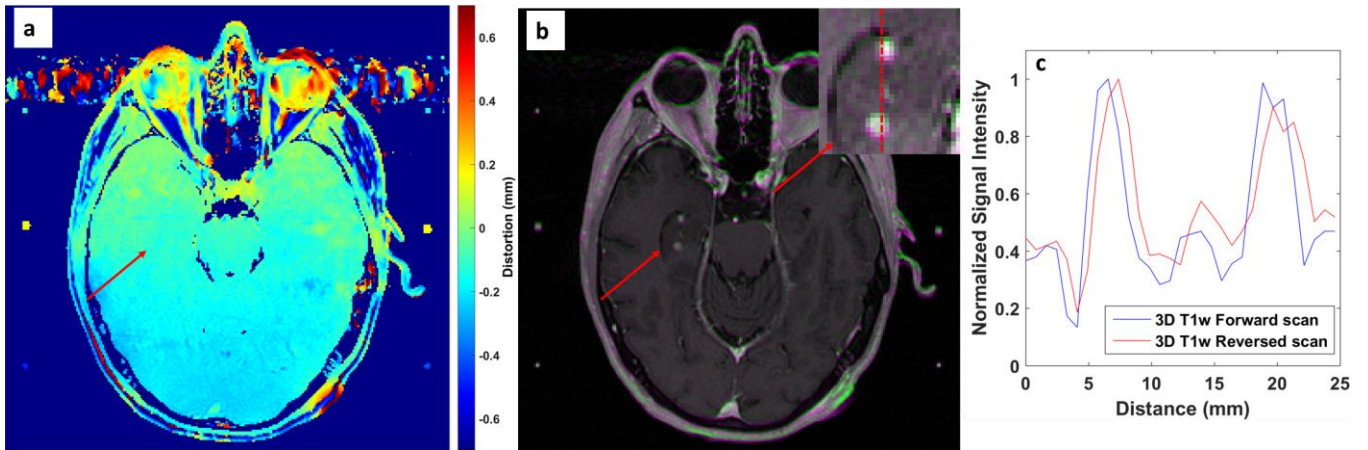


Figure 6-6: (a) Field mapping derived distortion map corresponding to an axial slice with two brain metastases (metastases #4 and 5 in Table 6-3). (b) Fused forward (A-P) and reversed (P-A) polarity MR images using the clinically employed MR protocol for SRS treatment planning. Corresponding pixels with different values are depicted in color (green and purple for higher values in forward and reversed images, respectively). The area of the two metastases is depicted magnified in the insert. The red arrow points to the area of the two metastases. (c) Normalized pixel intensity profiles for the two images along the red dashed line that runs parallel to the y-axis.

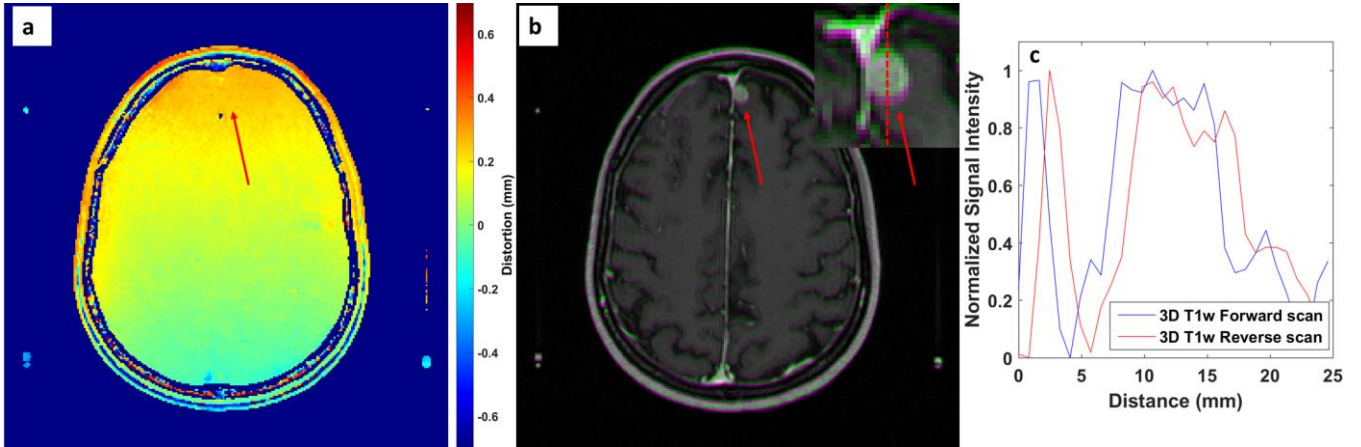


Figure 6-7: (a) Field mapping derived distortion map corresponding to an axial slice with one brain metastasis (met #10 in Table 6-3). (b) Fused forward (A-P) and reversed (P-A) polarity MR images acquired using the clinically employed MR protocol for SRS treatment planning. Corresponding pixels with different values are depicted in color (green and purple for higher values in forward and reversed images, respectively). The metastasis area is depicted magnified in the insert. The red arrow points to the metastasis location. (c) Normalized pixel intensity profiles for the two images along the red dashed line that runs parallel to the y-axis.

6.4 Discussion

Several studies have performed patient-specific distortion assessment in intracranial MR images, relying mainly on simulations or the field mapping technique. In specific, Stanescu et al [31] calculated geometric distortion stemming from susceptibility differences by assigning bulk susceptibility values in CT images of various anatomical sites, including the brain. Maximum calculated distortion reached 5.6 ppm at the air cavities. Wachowicz et al [43] calculated susceptibility induced distortion in the brain in a rotating magnet MR-linac design and reported maximum distortion of 7.1 ppm. The field mapping technique was implemented in 19 intracranial MR scans in the study of Wang et al [30]. Following phase unwrapping, the analysis revealed distortion less than 4.4 ppm near or around the sagittal sinuses. Although the above studies effectively detected or calculated patient-dependent intracranial distortion, MR-related geometric uncertainty in the brain lesion localization was not assessed. In SRS treatment planning, inaccuracies in localization and margin delineation of brain lesions constitute a major cause of concern [2,9,10,61]. The need to define an optimal margin around the GTV is of great importance in order to minimize radiation induced toxicity [60], especially

when multiple targets are treated such as in multiple brain metastases patients. A uniform margin of 1 mm has been reported to reduce risk of normal brain radionecrosis compared to a 3 mm margin [60,61]. In other approaches, sub-millimeter or zero margins are routinely applied, minimizing the risk of radionecrosis [60], but reducing or eliminating margins increases the risk of target underdosage and local recurrence. Geometric offsets of the order of 1 mm can result in considerable target underdosage, compromising treatment efficiency [9,10,147]. Furthermore, in SRS treatment planning based only on MRI (i.e., where MRI-CT spatial registration is not relevant [103]), patient-induced distortion in areas distant to the targets cannot considerably affect treatment planning and dose delivery. Therefore, this study focused on the characterization and evaluation of sequence dependent distortion in and around brain lesions, i.e., the high dose areas. A dedicated phantom and a limited number of patients, as well as pulse sequences and imaging parameters used clinically for SRS treatment planning, were employed to approximate real conditions.

In the phantom study of this work, both the read gradient polarity reversal and field mapping techniques were applied for sequence dependent distortion detection. Using the CPs of the phantom, results of both techniques were inter-compared for cross-validation. Although results were found in good agreement, the field mapping technique is less efficient since the phase unwrapping step is time-consuming and subject to unwrapping errors [97,98]. Brain lesions were simulated as small cylindrical inserts lying in the periphery of the phantom. The inserts were filled with Gd-DTPA solution of varying concentration to study the contrast agent induced susceptibility effect. Using the field mapping technique, distortion values were found to vary significantly inside and close to the susceptibility cavity. Since it is unclear how these distortions translate to geometric offset, this technique was not used to evaluate contrast agent induced displacement. However, it was used to evaluate B_0 inhomogeneity related distortion close to the inserts in order to derive, employing results obtained with the read gradient polarity reversal method, the net centroid offset owing to the Gd-DTPA contrast agent. As evidenced by data in Figures 6-2(a),(d) and 6-3(a),(d), the field mapping technique is robust even in the presence of miniature distortions (e.g., 0.1 mm). This may not stand true with the read gradient polarity reversal method (that is merely based on the subtraction of measurable offsets), especially in the case of reduced contrast or not well-defined boundaries.

Contrast agent presence was found to significantly affect phantom insert centroids, since mean values of 0.067 mm/mM and 0.054 mm/mM (corresponding to 0.205 ppm/mM and 0.165 ppm/mM, respectively) were estimated for read gradient direction in x-axis and y-axis, respectively. However, distortion magnitude in and around a susceptibility cavity is not constant and, in addition, it greatly depends on cavity size, shape, orientation with respect to B_0 and imaging parameters used [31,43,47,72]. Therefore, quantitative results provided should only be treated as indicative for the specific MR imaging sequence and scanning parameters (which are, however, clinically used in SRS treatment planning) and a cylindrical cavity with a size of the order of 700 mm³. In another phantom study [91], the authors measured a Gd-induced distortion of 0.109 ppm/mM for an infinitely long cylinder parallel to B_0 . Based on theoretical calculations for a spherical cavity, an offset of 0.218 ppm/mM is expected at the cavity border and no frequency shift at the center [91]. Also, it should be pointed out that higher concentrations do not necessarily result in greater overall sequence dependent distortion magnitudes (i.e. including B_0 inhomogeneity) at the insert locations. This is because the two distortion vector components, stemming from susceptibility differences due to the presence of the Gd-DTPA contrast agent and from B_0 inhomogeneity, respectively, may point to different directions.

In the patient study of this work, effort was made to characterize the distortion at brain metastases locations. A methodology similar to that used in the phantom study was implemented to dissociate distortion stemming from B_0 inhomogeneity and potential chemical shift effects from susceptibility induced distortion. B_0 inhomogeneity related distortion opposed susceptibility related offset at inferior brain areas, resulting in minimal overall centroid offsets. At S brain areas, however, B_0 inhomogeneity changed sign, increasing considerably the total distortion as reflected by overall centroid offset. Maximum detected overall centroid offset approached 0.9 mm (3.73 ppm) for the specific set of brain lesion locations examined and imaging parameters used. It should be noted that metastases lying in even more distant areas from MR isocenter are expected to exhibit even higher distortion magnitude due to further B_0 homogeneity degradation [33]. Since sequence dependent distortion scales linearly with B_0 [2], an almost double offset would be realized at 3.0T. Other sources of MR-related geometric degradation in SRS applications include gradient non-linearity and the stereotactic frame used for patient immobilization and image registration. For the lesion locations

considered herein, gradient non-linearity induced distortion, exhibited on any axis, can reach 0.8 mm [26].

Several caveats of the current study are noteworthy. Presented results are only valid for the specific scanner, magnetic field strength, acquisition parameters (e.g., echo time), contrast agent concentrations, target sizes, shapes and orientations with respect to B_0 assumed in this study. Moreover, in vivo contrast agent concentration varies with administration dosage and time [169,170,172]. Therefore, quantitative results should be treated as indicative for the experimental conditions used herein. The clinical significance of the presented results was not assessed. The extra imaging time required constitutes a major limitation of the proposed methodology. Sequence dependent distortion in areas away from targets (i.e., at low dose areas) was not evaluated, although it is expected to reach several millimeters at the air interfaces [30,31]. This remark also suggests that in certain clinical cases, such as acoustic neuromas where the target lies close to the bone-air interface, increased sequence dependent distortion could be exhibited. Residual sequence independent distortions were not considered, whilst no attempt was made to correct for detected distortions. A patient study of adequate sample size which will comprise of various clinical cases is warranted to assess the true clinical impact of sequence dependent distortions. Future work should also focus on the implementation and comparison of MR image correction schemes.

For the MRI protocol and imaging conditions used in this study, as well as the set of metastases locations examined, an average sequence dependent distortion of 0.54 mm (2.24 ppm) was estimated. Although this distortion magnitude may be regarded as relatively small, compared to the MR distortion or spatial uncertainty emanating from other sources, its effect on target localization in SRS treatment planning can be easily appreciated by simply acquiring an extra MR image series with reversed read gradient polarity. During target definition and treatment planning, both the forward and reversed polarity series, which are a priori spatially co-registered provided that the patient did not move, can be taken into account. The target contour or applied margins can be extended to cover the target identified in both image series. Another approach would be to correct acquired images for sequence dependent distortion and use the corrected series for target localization. To this purpose, several methods have been proposed [10,39,40,42,173]. However, implementation of these methods in routine clinical

practice is not straightforward, while it requires painstaking image processing steps which need to be validated.

6.5 Conclusion

Target mispositioning due to MRI distortion could adversely affect the efficiency of SRS planning, especially in locations where Gd-DTPA induced susceptibility and B_0 inhomogeneity add up to each other, thus resulting in increased overall distortion. The field mapping technique is suitable to provide sequence dependent distortion maps, but the reversed read gradient polarity method allows for a more straightforward and efficient visualization of the sequence dependent distortion at target locations. By carefully inspecting both the forward and reversed polarity image series during treatment planning and target/margin definition, sequence dependent distortion can be easily taken into consideration and partially dealt with.

7 Dosimetric impact

7.1 Introduction

In an effort to determine spatial accuracy tolerance specifically for SRS applications, the dosimetric impact of the geometric uncertainties was investigated by simulating distortions and studying their impact on Dose Volume Histograms (DVHs) and plan quality metrics clinically used for plan evaluation in highly conformal SRS applications.

7.2 Materials and Methods

In order to quantify the dosimetric effect of the detected distortion, a highly VMAT technique using multiple non-coplanar arcs [157,174,175] was utilized to irradiate targets of different diameters (5 to 50 mm). In specific, the Monaco v. 5.1.1 (ELEKTA Instrument AB, Stockholm, Sweden) treatment planning system based on X-ray Voxel Monte Carlo (XVMC) and constraint optimization algorithms with biological cost functions was used to plan a four non-coplanar arc arrangement (one full arc with couch angle 0° and three half arcs with couch angles 315° , 45° and 90°) with the 6 MV photon beam energy setting of an ELEKTA Axes linear accelerator equipped with beam modulator (4mm MLC leaves width). Dose calculations were performed on a rectangular grid of $(1\text{ mm})^3$ voxel size requiring MC statistical uncertainty of 1% (normalized standard deviation). A dose of 20 Gy was prescribed to cover the 95% of the volume of each target. DVHs and plan quality metrics commonly used in the clinical setting were calculated for the different diameter targets and exported to form a reference dataset. Reference dataset included – *inter alia* – i) the dose received by at least 95% of the target volume (D_{95}) used for target coverage evaluation ii) the Paddick's conformity index (CI) [176] used to evaluate the conformity of the prescription dose to the target volume, iii) the dose received by at least 50% of the target

(D_{50}), iv) the minimum (D_{\min}) and v) the mean dose (D_{mean}). Spatial offsets of 0.5 up to 3 mm towards either the x (L – R), y (A – P) or z (S – I) axes were deliberately added to the target locations and dose distributions were re-calculated. DVHs and the aforementioned metrics were calculated for the plans with the mispositioned target locations, then exported and compared with the reference dataset.

7.3 Results

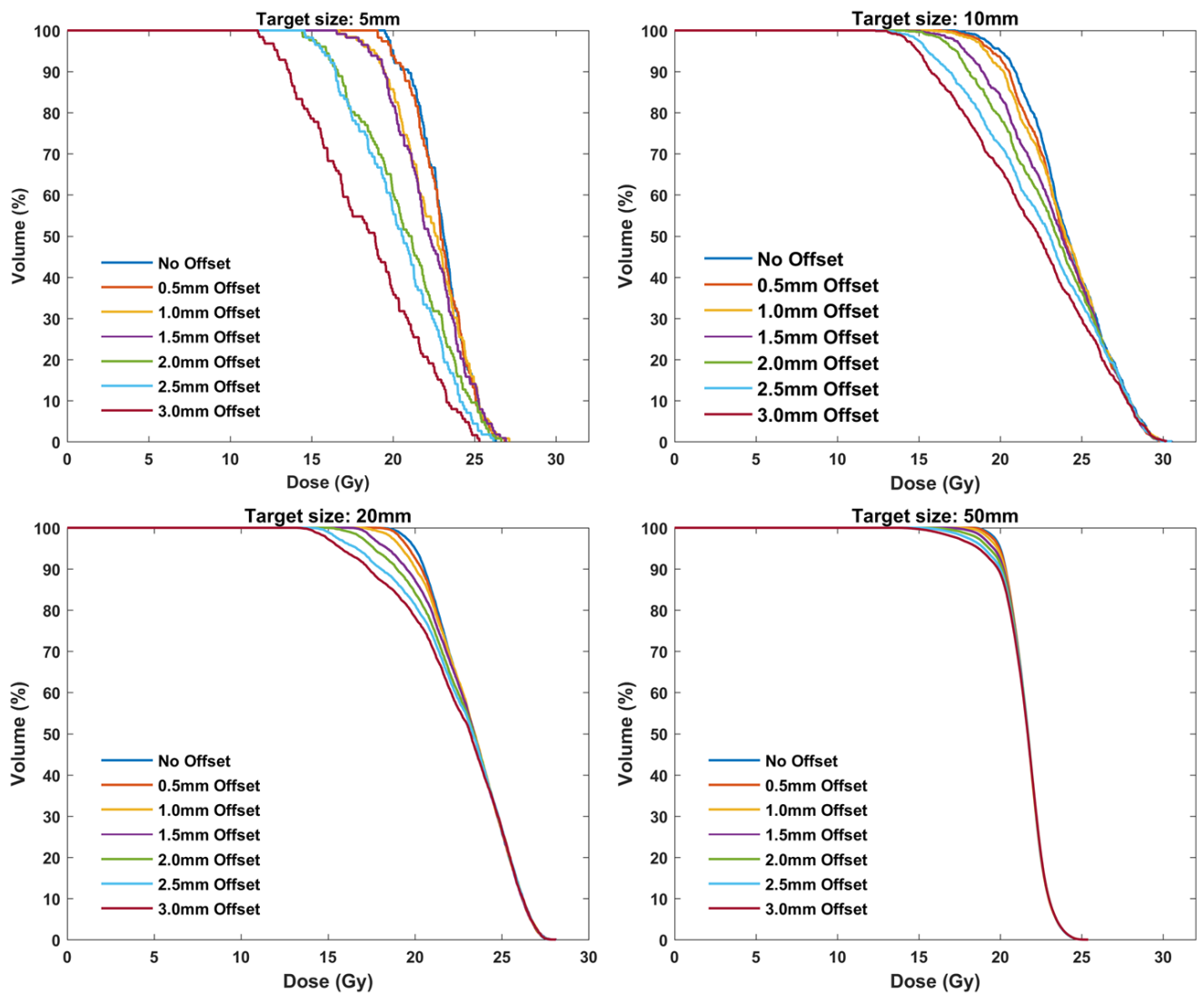


Figure 7-1: Calculated DVHs for the original plan (No Offset) as well as for the deliberately mispositioned targets towards the x direction (0.5 up to 3mm Offset) for four representative target sizes.

Figure 7-1 presents the impact of simulated geometric distortion (indicatively, along x-axis) on calculated DVHs for four representative target sizes (5, 10, 20 and 50 mm) and the highly conformal VMAT plans created using the four non-coplanar arcs technique. For the smallest target (5mm diameter) the effect is considerable even for a spatial offset of 1 mm. As seen, target coverage deteriorates with increasing geometric offset with the effect being more pronounced for smaller target sizes. Corresponding findings are also highlighted in Table 7-1. The D_{95} and the Paddick's CI [176] are tabulated for the original and x-axis mispositioned target locations. Both indices are very sensitive on both geometric distortion and target size, with their values rapidly decreasing as distortion magnitude increases and/or target size decreases. This trend is clearly shown in Figure 7-2 where the magnitude of the geometric uncertainty (distortion) resulting in D_{95} differences greater than 5% is plotted against target diameter. The D_{min} index is even more sensitive to distortion than the D_{95} , while D_{mean} and D_{50} are only affected for target sizes up to 10 mm. Similar DVH results were obtained for target misposition on y and z axes. However, the D_{95} value was found slightly more sensitive to distortion on z-axis for the smallest target sizes due to the increased dose gradient on this direction. This is illustrated in Figure 7-2 where target misposition that yields 5% difference on D_{95} is systematically lower for z-axis results.

Table 7-1: Effect of spatial offset towards the x direction on plan quality metrics for five target sizes.

Target size	X-Offset (mm)	D_{95} (Gy)	Difference (%)	Paddick's CI	Difference (%)
5mm	0.0	20.0	-	0.65	-
	0.5	19.8	-0.8	0.63	-2.4
	1.0	18.7	-6.7	0.53	-18.6
	1.5	18.5	-7.5	0.48	-26.3
	2.0	15.9	-20.6	0.26	-59.7
	2.5	15.6	-22.0	0.23	-65.1
	3.0	12.8	-36.1	0.10	-85.2
10mm	0.0	20.0	-	0.77	-
	0.5	19.5	-2.7	0.74	-3.3

	1.0	19.1	-4.4	0.70	-8.5
	1.5	17.8	-10.9	0.60	-21.9
	2.0	17.3	-13.5	0.53	-31.2
	2.5	15.5	-22.4	0.44	-42.7
	3.0	14.9	-25.3	0.38	-51.1
20mm	0.0	20.0	-	0.93	-
	0.5	19.7	-1.8	0.88	-4.7
	1.0	19.2	-3.8	0.84	-9.4
	1.5	18.4	-8.0	0.78	-15.4
	2.0	17.6	-11.8	0.73	-21.4
	2.5	16.7	-16.7	0.68	-26.6
	3.0	15.7	-21.3	0.63	-32.0
30mm	0.0	20.0	-	0.93	-
	0.5	19.9	-0.5	0.92	-1.7
	1.0	19.7	-1.4	0.90	-3.8
	1.5	19.3	-3.5	0.86	-7.7
	2.0	18.7	-6.3	0.83	-11.2
	2.5	17.8	-11.1	0.79	-15.6
	3.0	17.3	-13.7	0.75	-19.0
50mm	0.0	20.0	-	0.94	-
	0.5	19.9	-0.3	0.93	-1.0
	1.0	19.8	-0.9	0.91	-3.2
	1.5	19.6	-2.0	0.89	-5.5
	2.0	19.3	-3.4	0.87	-7.7
	2.5	19.0	-5.0	0.85	-10.3
	3.0	18.7	-6.7	0.83	-12.4

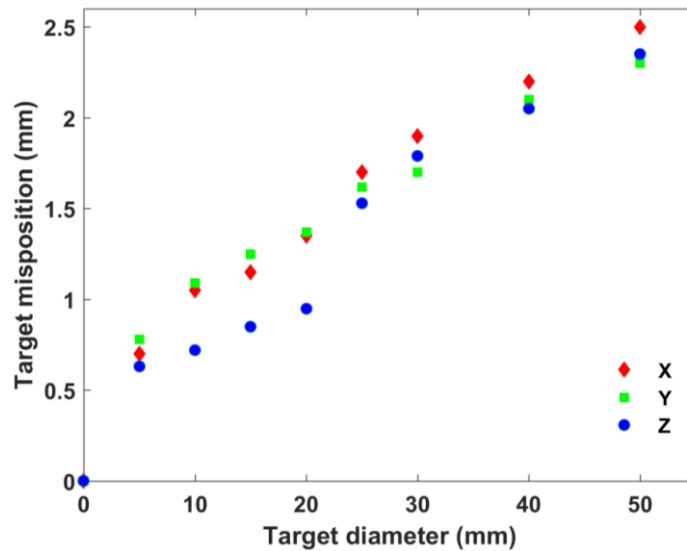


Figure 7-2: Geometric uncertainty on x, y and z axes resulting in difference greater than 5% in D_{95} value as a function of target diameter.

7.4 Discussion

To the best of our knowledge, no specific guidelines have been proposed with respect to the tolerance of geometric uncertainty in MRI series used in SRS treatment planning. Outdated guidelines [177] for radiotherapy QA suggest that geometric distortion of more than 2 mm requires consideration. Weygand et al [2] suggest that MR-related geometric distortions should be measured and accounted for when defining margins for determination of the planning target volume in MRI-guided radiotherapy applications. In this work, effort was made to quantitatively assess what could be considered unacceptable distortion. Therefore, an investigation of the induced dosimetric error with respect to target dose delivery was conducted by applying geometric offsets of 0.5 up to 3 mm for several spherical targets irradiated using a highly conformal VMAT technique with multiple non-coplanar arcs. It is clearly shown that the required geometric accuracy depends significantly on target size. Target coverage, expressed by the D_{95} value and in a greater extend by Paddick's CI (which takes into account both target coverage and the conformity of the prescription dose to the target volume [176]) are deteriorated (decreased) as the magnitude of geometric distortion increases and target size decreases. For targets less than 2 cm in diameter, a spatial displacement of the order of 1 mm could significantly affect both D_{95} and Paddick's CI values, with

differences being greater than 5% compared to the reference (non-distorted) plan. For targets with diameter up to 3 cm, D_{95} could be affected by spatial distortions of the order of 1.5 mm. For larger target diameters, geometric distortions greater than 2 mm are required to considerably (>5%) affect plan evaluation indices (Figure 7-2). Nevertheless, SRS applications are usually applied to irradiate multiple targets with diameters less than 3 cm, such as in multiple brain metastases cases [157,174,175,178], where small-sized targets could lie on the periphery of the brain where distortion greatly increases. If all sources of geometric uncertainties are considered (MRI system-related, MRI patient-induced, spatial registration, patient set-up, mechanical accuracy) and no margins are applied in treatment planning (a practice that is commonly followed in SRS applications [153,178]) deterioration of plan evaluation indices could reach unacceptable levels.

A limitation of this study is that the analysis of the dosimetric impact was not comprehensive. As an example, the spatial offsets investigated were only towards one axis while target shapes were always spherical. Induced dosimetric effects could considerably vary in case of non-uniform or different dose gradients and irregular target shapes. Furthermore, in a more realistic case, total distortion distribution is not uniform in the entire target volume, resulting to a deformable transformation of the structure. In the present study, only rigid transformations were applied, corresponding to uniform distortions. Moreover, MR-related geometric distortions do have a dosimetric impact to organs at risk as well, which is expected to depend on the magnitude and direction of distortion vectors at the location of each organ. However, this is beyond the scope of this work, which emphasizes in the corresponding impact on the target delivered dose distributions.

7.5 Conclusion

In highly conformal VMAT technique plans for SRS, it is concluded that the required geometric accuracy/tolerance level depends significantly on target size. Target coverage, expressed by the D_{95} value and in a greater extend by Paddick's CI are deteriorated (decreased) as the magnitude of geometric distortion increases and target size decreases. For targets less than 2 cm in diameter, a spatial displacement of the order

of 1 mm could significantly affect both D_{95} and Paddick's CI values, with differences being greater than 5% compared to the reference (non-distorted) plan. For targets with diameter up to 3 cm, D_{95} could be affected by spatial distortions of the order of 1.5 mm. For larger target diameters, geometric distortions greater than 2 mm are required to considerably (>5%) affect plan evaluation indices.

PART C: MR DISTORTION CORRECTION SCHEMES

8 Vendor-supplied distortion correction algorithms at 1.5T and 3.0 T

Summary

MR scanner manufacturers have equipped their units with distortion correction algorithms to mainly compensate for gradient nonlinearity induced spatial inaccuracies. The purpose of this study is to assess the efficacy of these algorithms by comparing distortion maps deduced with and without the optional distortion correction schemes enabled for a variety of MRI scanners.

A new custom acrylic-based phantom was designed and constructed in-house for distortion detection similar in concept with the prototype one but encompassing a substantially increased number of CPs. Its external dimensions were limited to approximately $17 \times 16 \times 16 \text{ cm}^3$ in order to accurately fit in a typical head coil while extending to the edges of the available space. On eleven axial planes, a total of 1978 holes were drilled, the centers of which serve as CPs for distortion detection. Center-to-center CP distance is 10 mm on x and y axis and 14 mm on z axis, resulting in adequately high CP density. The phantom was filled with copper sulfate solution and MR scanned at 1.5T (SIEMENS Avanto, Philips Achieva) and 3.0T (SIEMENS Skyra) using the corresponding standard clinical MR protocol for SRS treatment planning. All scans were repeated after disabling the vendor supplied distortion correction scheme. The phantom was emptied and CT scanned to provide the reference CP distribution. In-house MATLAB routines were developed for distortion assessment. Reference and evaluated CP distributions are spatially registered and compared to derive 3D distortion maps. This methodology does not consider uniform geometric distortion as it cancels out during the spatial registration step. This results in omitting uniform susceptibility-induced CP displacements and thus mainly takes into account machine-related distortions.

At central slices, around the scanners' isocenters minimum distortion was detected even with the correction algorithms disabled. However, at the edges of the available space distortion magnitude greatly increases and efficacy of algorithm becomes paramount. Maximum detected distortion reaches 3.1 mm for the SIEMENS 3.0T scanner but is reduced to 1.4 mm if the correction algorithm is enabled. For the 1.5T scanners, mean absolute CP displacement is reduced by approximately 0.6 mm, while exceeding 1mm prior to correction.

A methodology was developed and implemented to assess the accuracy of vendor supplied distortion correction schemes applied to SRS used MR protocols. Overall results of this work suggest that geometric distortions could be a concern around the edges of the field of view even with the correction algorithms enabled.

8.1 Introduction

All major MR scanner manufacturers have equipped their units with distortion correction algorithms applied as post-imaging steps [1]. These algorithms account for gradient nonlinearities induced geometric distortion, exhibited on any axis of the 3D coordinate system. However, the available distortion correction algorithms are either 2D or 3D, depending on the available options of each vendor. The former corrects only the in-plane distortions but does not account for any potential slice curving effects. Each output slice is computed from the voxels of the appropriate input slice only. On the other hand, the 3D algorithm uses voxels from several surrounding slices and, therefore, is able to compensate the slice curving effects as well [35]. In any case, distortion field is calculated by comparing the actual gradient field with the assumed linear one. It is measured for the specific MR unit (device-specific) and assumed stable with time. Moreover, gradient field nonlinearity is a sequence independent source of geometric distortion and, therefore, corresponding distortion field can be used to predict and correct distortion in images acquired with different imaging sequences [27].

Once the distortion field is determined, it can be used to correct the image series by applying a transformation from distorted image space to the undistorted one. As described in Section 2.9, this is actually an interpolation task [2] with several different

approaches presented, ranging from spherical harmonics to polynomial and spline interpolations [149,179–181].

The main advantage of vendor-supplied correction algorithms is that they can be applied automatically, if enabled, with a negligible impact on image reconstruction time [1] and no impact on scanning time.

In this study, the efficacy of these algorithms is investigated, as implemented in a variety of MR scanners and specifically in a Philips Achieva 1.5T, a SIEMENS Avanto 1.5T and a SIEMENS Skyra 3.0T. For this purpose, a dedicated distortion detection phantom with high CP density was designed and constructed based on the experience gained with the construction of the prototype phantom, used in the studies presented in the previous Chapters.

8.2 Materials and Methods

8.2.1 High-resolution distortion detection phantom

For the purposes of this study, a new phantom was designed and constructed based on the prototype phantom used in the previous Chapters. The new phantom was re-designed in order to incorporate more CPs and by increasing the CP density on the z-axis. Therefore, a CP grid resolution of $10 \times 10 \times 14 \text{ mm}^3$ was achieved by placing 11 acrylic planes of 4mm thickness in parallel on the x-y plane at a spacing of 14 mm. A 3D model of the phantom during the designing stage is presented in Figure 8-1, while the final constructed phantom is shown in Figure 8-2. On every acrylic plane, a number of 110 up to 206 holes (depending on the size of the plane) were drilled, defining CP locations for distortion detection. Subsequently, a total of 1978 CPs were encompassed in this high-resolution distortion detection version of the phantom. Its maximum external dimensions were deliberately kept relatively small (approximately $17 \times 16 \times 16 \text{ cm}^3$) so that it can fit in a typical head coil, in order to simulate an intracranial MR scan for SRS treatment planning purposes. Most importantly, the new phantom is also both CT and MR compatible. CT scan is performed with the phantom empty, exploiting the air-acrylic contrast in the CT image stack. On the other hand, prior to MR scanning

the phantom must be filled with the standard copper sulfate solution (commonly used in MR phantoms) in order to take advantage of the high acrylic-solution contrast.

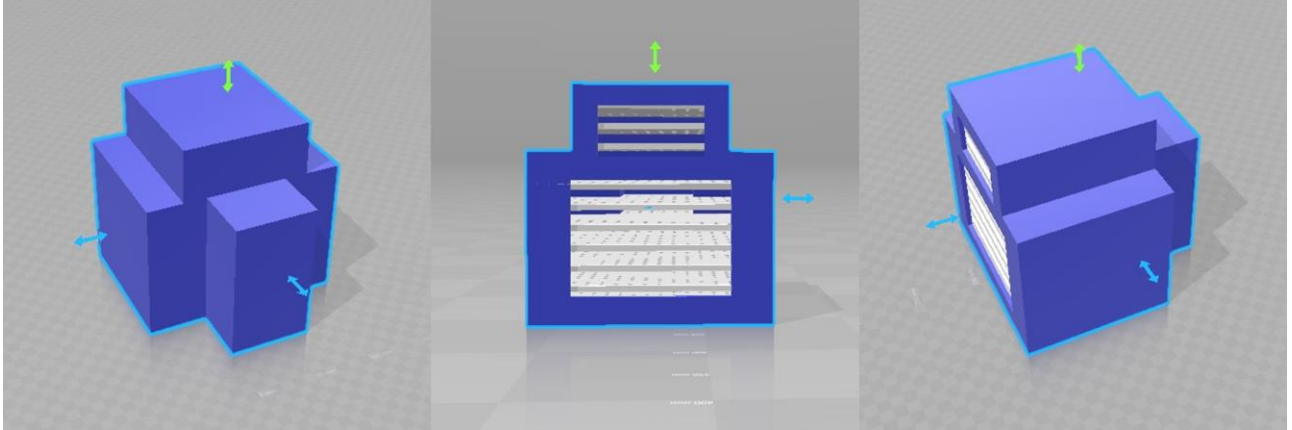


Figure 8-1: Views of the 3D model of the high-resolution distortion detection phantom during the designing stage.

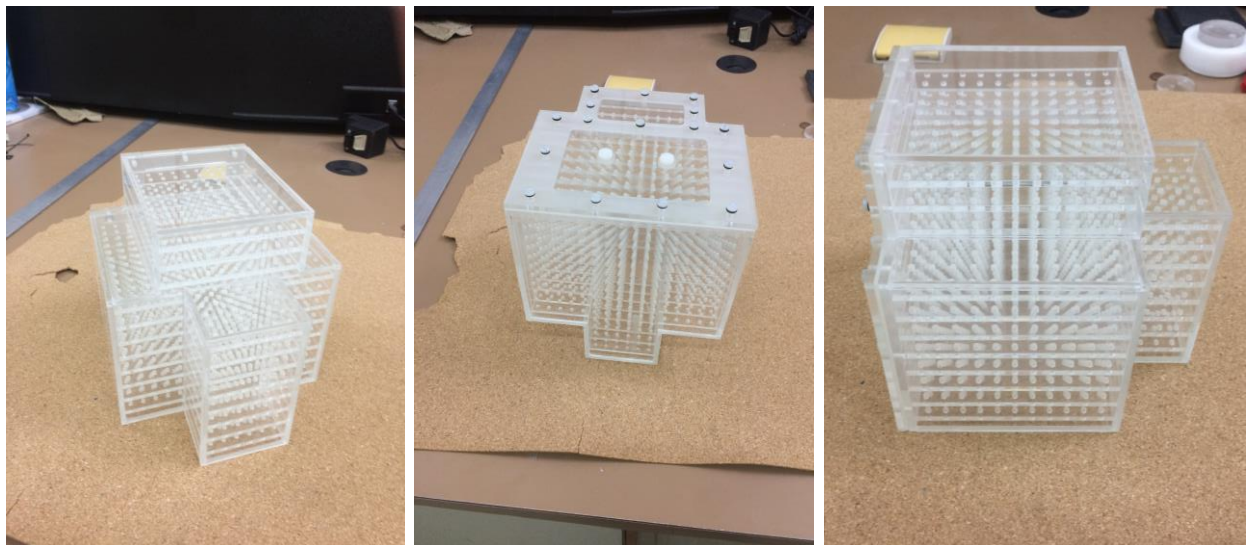


Figure 8-2: Pictures of the phantom developed for high resolution residual distortion detection.

8.2.2 Image acquisitions

The phantom was filled with copper sulfate solution and scanned using the standard clinical MR protocol and parameters for SRS treatment planning purposes. A variety of scanners were employed in this study as the vendor-supplied correction algorithms are device-specific [35]. Emphasis was given to involve both 1.5 and 3.0T scanners.

Specific details for the scanners and imaging protocols used are given in Table 8-1. All scans were repeated after disabling the vendor-supplied distortion correction scheme. The phantom was emptied and CT scanned to provide the reference CP distribution. In particular, a SIEMENS Sensation scanner was operated at 120 kVp to acquire an image stack with a reconstructed voxel size of $0.54 \times 0.54 \times 0.75 \text{ mm}^3$. An indicative axial and sagittal slice of the CT and MR images acquired are presented in Figure 8-3. CP localization for all image series was performed with sub-millimeter accuracy, according to the methodology described in Chapter 4 and [26].

Table 8-1: Specific details of MR scanners and imaging parameters used in this study.

MR unit	Series ID	Protocol Name	TE/TR/FA (msec/msec/°)	Voxel Size (mm ³)	Pixel Bandwidth (Hz/px)	Vendor-supplied distortion correction
Philips Achieva 1.5T	1	3D T1w FFE	4.6/25/30	0.82×0.82×1	217	OFF
	2	3D T1w FFE	4.6/25/30	0.82×0.82×1	217	ON
SIEMENS Avanto 1.5T	3	T1w MPRAGE	4.3/18/25	1×1×1	170	OFF
	4	T1w MPRAGE	4.3/18/25	1×1×1	170	ON
SIEMENS Skyra 3.0T	5	T1w MPRAGE	2.6/1900/9	0.45×0.45×1	3.0	OFF
	6	T1w MPRAGE	2.6/1900/9	0.45×0.45×1	1.4	ON

Spatial co-registration between MR and CT coordinate systems was performed by using the mutual information-based registration algorithm as implemented in the Monaco v. 5.1.1 (ELEKTA Instrument AB, Stockholm, Sweden) treatment planning system. Reference and evaluated CP distributions were spatially registered and compared to derive 3D distortion maps. This methodology does not consider uniform geometric distortion as it cancels out during the spatial registration step. This results in omitting uniform susceptibility-induced CP displacements and, thus, mainly takes into account machine-related distortions.

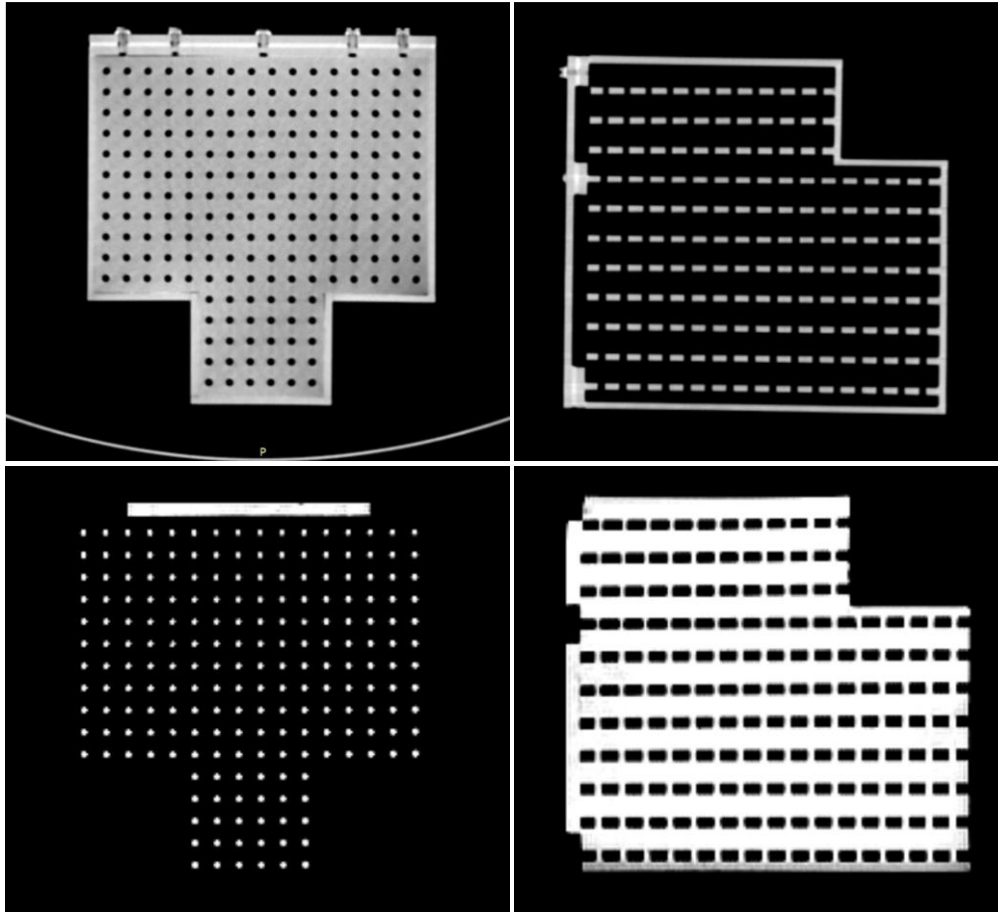


Figure 8-3: CT (top row) and MR (bottom row) scans of the high-resolution distortion detection phantom developed. Indicative central axial (left) and sagittal (right) slices are presented.

8.3 Results and discussion

Severe geometric distortion was observed in all MR images acquired with distortion correction algorithms disabled. Figure 8-4 presents an axial MR slice (at 1.5 and 3.0T) towards the S end of the phantom fused with corresponding CT image. Minimum distortion is observed at the center of the images, even with corrections disabled. However, severe geometric warping results in mismatching of the CP grid locations. After enabling vendor-supplied distortion correction schemes, CP locations are matched, while residual distortion is still evident at the edges of the field of view.

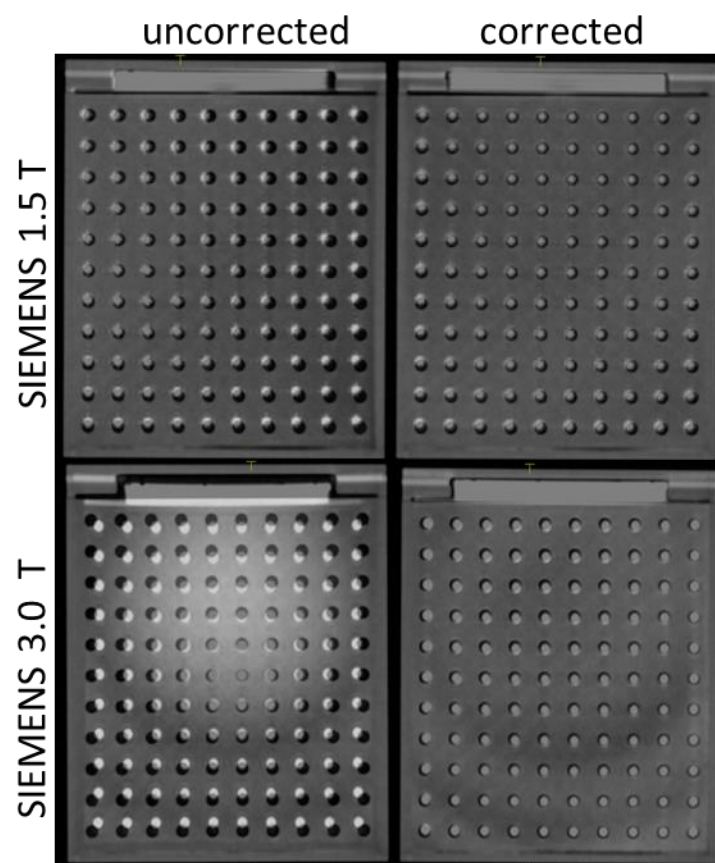


Figure 8-4: MR images fused with CT scans of the new phantom for a slice lying at the S side before (left) and after (right) having enabled the vendor-supplied distortion correction routines.

Table 8-2: Detected total absolute distortion for the three MR scanners included in this study, with and without having enabled the distortion correction scheme. Percentages of CPs detected with more than 1 mm of absolute distortion (% CPs > 1 mm) are also given.

MR unit	Series ID	Vendor-supplied distortion correction	Mean absolute distortion (mm)	Max absolute distortion (mm)	CPs > 1mm distorted (%)
Philips Achieva 1.5T	1	OFF	0.54	1.6	7.1
	2	ON	0.47	1.2	3.6
SIEMENS Avanto 1.5T	3	OFF	0.71	2.1	15.6
	4	ON	0.59	1.5	11.2
SIEMENS Skyra 3.0T	5	OFF	0.91	3.0	18.2
	6	ON	0.55	1.4	10.4

In Table 8-2, statistical analysis of the detected distortion for all images acquired using the three MR scanners, as well as residual distortion after enabling the vendor-supplied algorithms is given. Maximum detected distortion reaches 3 mm and was observed for the SIEMENS 3.0T but is reduced to less than 1.5 mm if the correction algorithm is enabled.

Results presented in Table 8-2 stem from B_0 inhomogeneity and gradient field nonlinearity and, thus, represent system-related distortions only. However, vendor-supplied distortion correction algorithms account only for gradient field nonlinearity distortions, without affecting the former. Susceptibility-related distortion is uniform throughout the image and therefore cancels out during the image registration process with CT coordinate system. Auto-shimming and higher order shimming procedures are available to minimize B_0 inhomogeneity related distortions [171], although they have to be employed on each scan separately, as constituting a sequence dependent type of distortion [33].

8.4 Conclusion

A methodology was developed and implemented to assess the accuracy of vendor supplied distortion correction schemes, applied to SRS-used MR protocols. Overall results of this work suggest that geometric distortions could be a concern around the edges of the field of view (even with the correction algorithms enabled) in SRS applications involving small target sizes, at least for the clinical MR protocols and units investigated.

9 The average-image distortion correction method: implementation in multiple brain metastases

Summary

The purpose of this study is to propose, verify, and implement a simple and efficient methodology for the improvement of total geometric accuracy in multiple brain metastases GK SRS.

The proposed methodology exploits the directional dependence of MRI-related spatial sequence dependent distortions, with respect to the read-gradient polarity during MRI acquisition. First, an extra MRI pulse sequence is acquired with the same imaging parameters as those used for routine patient imaging, aside from a reversal in the read-gradient polarity. Then, “average” image data are compounded from data acquired from the 2 MRI sequences and are used for treatment planning purposes. The method was applied and verified in a polymer gel phantom irradiated with multiple shots in an extended region of the GK stereotactic space. Its clinical impact in dose delivery accuracy was assessed in 15 patients with a total of 96 relatively small (<2 cm) metastases treated with GK radiation surgery.

Phantom study results showed that use of average MR images eliminates the effect of sequence dependent distortions, leading to a total spatial uncertainty of less than 0.3 mm, attributed mainly to gradient nonlinearities. In brain metastases patients, non-eliminated sequence-dependent distortions lead to target localization uncertainties of up to 1.3 mm (mean: 0.51 ± 0.37 mm) with respect to the corresponding target locations in the “average” MRI series. Due to these uncertainties, a considerable underdosage (5%-32% of the prescription dose) was found in 33% of the studied targets.

The proposed methodology is simple and straightforward in its implementation. Regarding multiple brain metastases applications, the suggested approach may substantially improve total GK dose delivery accuracy in smaller, outlying targets.

9.1 Introduction

In a relatively recent study, an experimental methodology based on the reversed read-gradient technique [27,42] was proposed for the assessment and characterization of the various geometric uncertainty components contributing to the entire GK treatment delivery, including MRI-related spatial distortions [25]. Results showed that frequency-encoding axis and read gradient polarity choices during MRI acquisition may affect the magnitude as well as the spatial components of the total GK geometric uncertainty. In this Chapter, an expeditious methodology to minimize sequence dependent distortions and, therefore, improve the total geometric accuracy of GK in multiple brain metastases applications, is proposed. The method requires simply the acquisition of an extra MRI sequence with the same imaging parameters as those used for routine patient imaging aside from a reversal in the read gradient polarity.

The proposed methodology was applied to: (1) a polymer gel phantom simulating a GK multiple metastases treatment for verification purposes; and (2) a clinical MRI dataset of 15 patients with a total of 96 relatively small brain metastases (<2 cm) and used to assess the impact of the suggested approach on total GK dose delivery accuracy.

9.2 Materials and Methods

9.2.1 Phantom study

This work implemented an end-to-end process proposed and used for the experimental assessment and characterization of total geometrical uncertainty in clinical GK applications [25]. Briefly, a custom-made PMMA spherical phantom (16 cm in diameter) filled with normoxic polymer gel [25] was used to accurately reproduce every link in the GK treatment chain, from patient imaging and treatment planning to patient

positioning and dose delivery using the patient positioning system of a GK Perfexion model. A total of 26 single-shot dose distributions (25 Gy maximum dose) covering the whole phantom volume were planned on pre-irradiation CT images of the phantom, using the Leksell GammaPlan version 9.0 treatment planning system. The phantom was irradiated using the 4 mm collimator and was subsequently imaged at 1.5 T (Intera model; Philips Best, The Netherlands) using a 3D turbo spin echo, T2w sequence (TE = 160 msec, TR = 2700 msec, $1 \times 1 \times 1 \text{ mm}^3$ acquisition/reconstruction voxel size). Two similar scans with the read-gradient polarity switched in opposite directions (i.e., forward and reverse) were acquired. A simple algorithm was developed to provide an “average” image series by compounding the forward- and reverse-acquired image series. Averaging of corresponding forward and reverse signal intensities was implemented on a pixel-by-pixel basis. The resulting average and original forward and reverse image series was independently used for treatment planning purposes.

Forward, reverse, and average series images were registered in the Leksell coordinate system by using the fiducial points generated in each image by the N-shaped rods on the Leksell indicator box. To qualitatively assess the geometrical uncertainties in each series, each shot was contoured on every MR series using the segmentation tool incorporated in the GammaPlan treatment planning system. Segmentation was based on the visible radiation-induced polymerization area after thresholding all 3 series at the same gray scale level. To quantitatively evaluate the geometrical uncertainties for each shot in the 3 series, the centers of the 26 shots served as CPs. These points were identified as the centers of mass (CM) of the radiation-induced polymerization area corresponding to each delivered shot. CM coordinates were determined with submillimeter accuracy using an in-house developed image processing algorithm [25]. The magnitude of the total geometric uncertainty, d_R^{tot} , for each CP was determined as the geometric deviation of its CM location in a given series (i.e., the CM coordinates of the radiation-induced polymerization volume) with respect to its reference location, dictated by the planned coordinates of the corresponding dose distribution.

9.2.2 Patient study

The above-described methodology was applied to 15 patients with a total number of 96 metastases treated with GK and using MRI for treatment planning purposes. The study

was approved by the hospital's Institutional Review Board. All metastases considered were of relatively small volume, exhibiting a diameter of less than 2 cm (85% and 52% of metastases had a diameter of <1 cm and <0.5 cm, respectively). Patients were scanned at 1.5 T with a double dose Gd-enhanced 3D T1w gradient recalled echo pulse sequence (TE = 4.6 msec, TR = 25 msec, $0.91 \times 0.91 \times 1.5 \text{ mm}^3$ acquisition voxel size, $0.82 \times 0.82 \times 1.5 \text{ mm}^3$ reconstruction voxel size, forward read gradient polarity, 9 minutes scanning time), routinely used for target definition in multiple metastases cases. An extra sequence was acquired with the same imaging parameters as those in the clinically used sequence aside from a reversal in the read gradient polarity (reverse scan). Using the above-mentioned in-house built algorithm, we produced an average MRI series for every patient.

Forward, reverse, and average series images were registered in the Leksell stereotactic space, as in the phantom study. Metastases targets were contoured independently in each series by the same experienced physician. To eliminate variability, this task was performed automatically by applying identical grayscale threshold levels in the different MRI series by using the GammaPlan's segmentation tool. Highly conformal patient plans based on the forward series were subsequently produced. In most of these plans, a single 4 or 8 mm shot was used for each metastasis, and the prescription isodose (50%-80%) was chosen so that the prescription dose of 25 Gy covered 99% of the target volume (i.e., $V_{25\text{Gy}} = 99\%$, and $D_{99\%} = 25 \text{ Gy}$), as determined in the forward series. Corresponding $V_{25\text{Gy}}$ and $D_{99\%}$ values were also determined for all targets contoured in the average series. Geometric uncertainties associated with the forward (i.e., the clinically used) series were determined by comparing the shot position (i.e., center coordinates) covering the target in the forward series with the corresponding shot position covering the same target in the average series.

9.3 Results

9.3.1 Phantom study

Figure 9-1 presents central views in axial, coronal, and sagittal planes of the radiation induced polymerization area corresponding to the 4 mm shot with reference coordinates

$[x, y, z] = [100, 100, 100]$ (defining the UCP location) as shown in the forward, reverse, and average image series (top, middle, and bottom row), respectively, following image spatial co-registration. The polymerization area simulating a target was contoured independently in the forward (Figure 9-1, red), reverse (Figure 9-1, blue), and average (Figure 9-1, green) images by using identical gray-scale threshold levels (volumes of 0.047, 0.046, and 0.047 cm³, respectively, were calculated). All contours, along with the planned dose distribution (Figure 9-1, yellow), were superimposed on all images for comparison. The mismatch between the planned dose distribution (Figure 9-1, yellow) and the contoured target in the forward and reverse series is evident and exhibits directionality. The close coincidence between the planned dose distribution and the contour of the polymerization distribution in the average series suggests that the geometric effect of MRI-related distortions is remarkably suppressed for that image series.

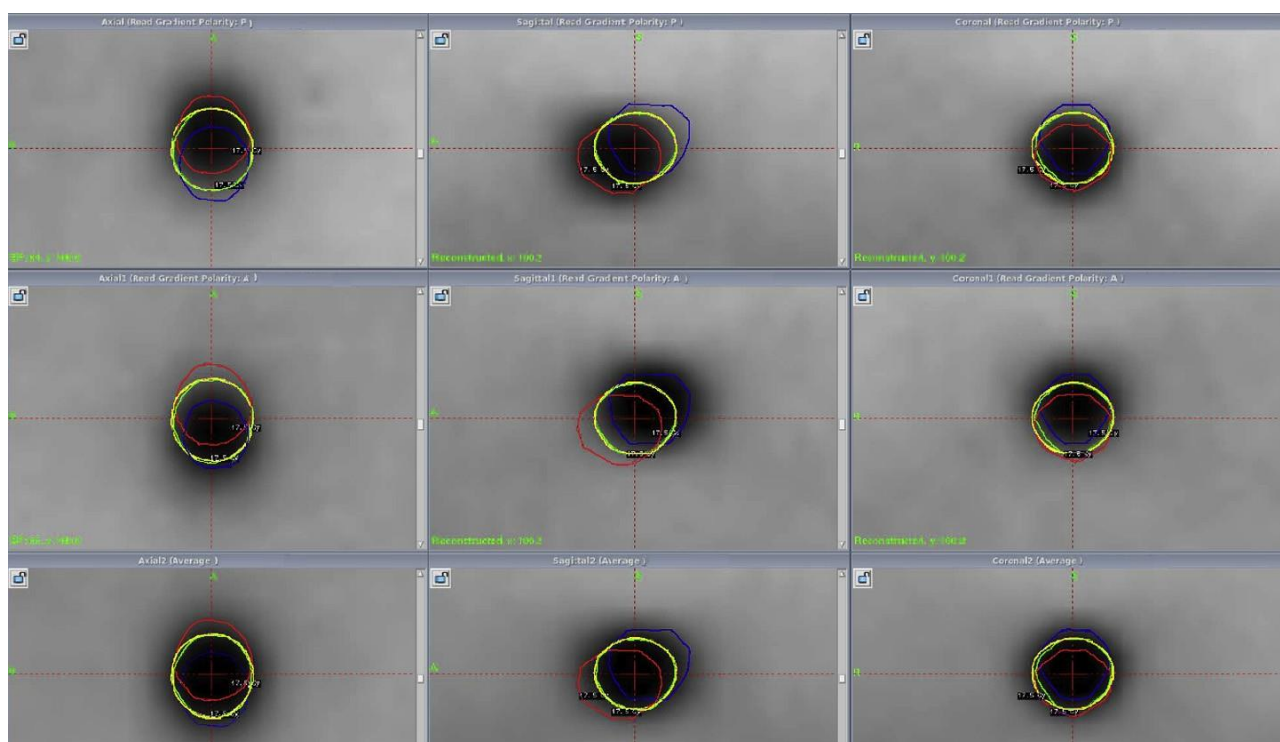


Figure 9-1: Print-screen images from the GammaPlan treatment planning system presenting the central axial (left column), sagittal (middle column), and coronal (right column) planes of the radiation-induced polymerization distribution corresponding to the 4mm shot with reference coordinates $(x, y, z) = (100, 100, 100)$ as shown in forward (top row), reverse (middle row), and average images (bottom row). The target contour defined independently in forward, reverse, and average series following registration in the stereotactic space is marked with red, blue, and green, respectively. The prescription isodose, as planned in the forward MR series, is shown in yellow.

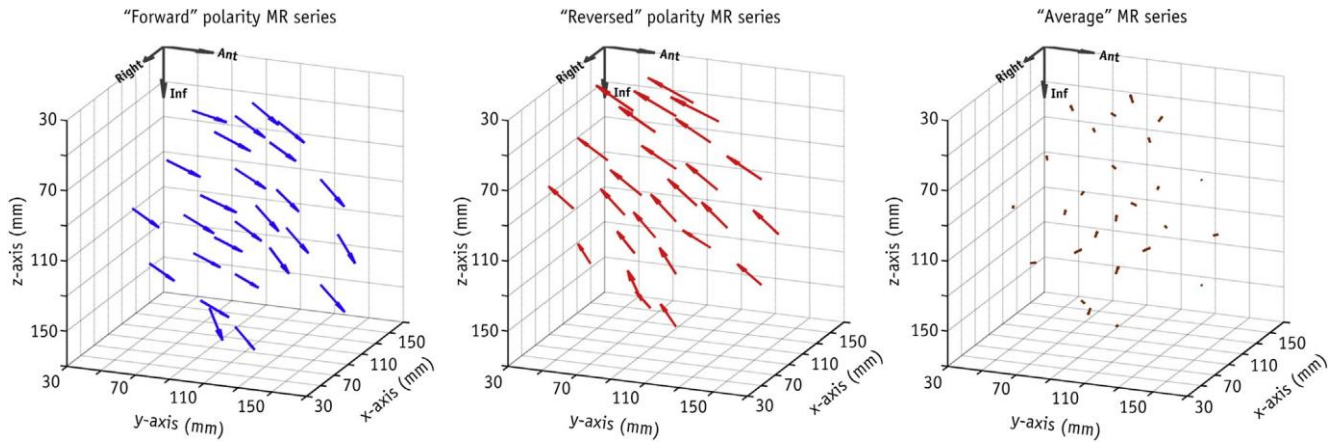


Figure 9-2: The geometrical uncertainty vector d_R^{tot} determined for the 2 series acquired with forward (left) and reverse polarity (middle), as well as for their average series (right). Distortion measurements are presented as a spatial distribution of scaled vectors: the origin of each vector coincides with the reference coordinates of the corresponding shot's CM, whereas its length, denoting the measured distortion magnitude, is scaled to the length of the gray vectors residing on $(x, y, z) = (170, 30, 30)$, which corresponds to a 1.5 mm distortion. For reasons of clarity, the length of the presented vectors was scaled by a factor of 20.

Total spatial uncertainty vectors, d_R^{tot} , were determined for forward, reverse, and average series. Results are presented in Figure 9-2 as a spatial distribution of scaled vectors: the origin of each vector coincides with the reference coordinates of the corresponding shot in the stereotactic space, whereas its length denotes the measured distortion magnitude d_R^{tot} . Although the magnitude of the observed total geometric distortions is comparable to the MRI voxel dimensions (i.e., 1 mm), they exhibit a clear directionality with respect to the read gradient polarity selected during acquisition. Phantom studies with 0.5 mm voxel dimensions resulted in similar geometric uncertainties (e.g., for the target presented in Figure 9-1, the total geometric uncertainty, d_R^{tot} , was calculated to be 0.88 and 0.84 mm, using a pixel size of a $1 \times 1 \times 1$ and $0.5 \times 0.5 \times 0.5$ mm³, respectively). In contrast, the use of the average MRI series resulted in residual distortions of less than 0.3 mm (0.04-0.3 mm) with no noticeable directionality.

9.3.2 Patient study

To evaluate geometric uncertainties in target localization associated with the forward MRI sequence used clinically, the apparent target locations in forward images were

compared with corresponding target locations in average images. In accordance with phantom results, the geometric deviation exhibited a directional dependence on the read gradient polarity. Figure 9-3 presents a representative metastasis located centrally and anteriorly (shot coordinates in GammaPlan covering the target in the forward series $[x, y, z] = [98.1, 183.5, 98.2]$), as shown in the forward, reverse, and average images (top, middle, and bottom row), respectively. The target was independently contoured in each series (Figure 9-3, red, blue, and green for forward, reverse, and average, respectively) by using identical grayscale threshold levels (respective volumes of 0.45, 0.47, and 0.47 cm^3 were calculated). For this target metastasis, deviations of 0.6 mm in the y axis (P – A direction) and 1.1 mm in the z axis (S – I direction) were found between forward and average images. Such geometric uncertainties may have a considerable dosimetric impact on brain target metastases treated with GK single shot dose distributions. The plan created in the forward series with the 25 Gy prescription isodose (Figure 9-3, yellow contour) covering 99% of the target volume ($V_{25\text{Gy}} = 99\%$ and/or $D_{99\%} = 25\text{ Gy}$) actually underdosed this target. In the average series, only 90% of the target volume received the 25 Gy prescription dose (target $V_{25\text{Gy}} = 90\%$), with the dose delivered to the target being 18 Gy ($D_{99\%} = 18\text{ Gy}$). In this case, therefore, a dose difference of ~ 30% was realized.

For the 96 metastases considered, target localization geometrical uncertainties from 0 to 1.3 mm (mean: $0.51 \pm 0.37\text{ mm}$) were observed in the forward series routinely used for target delineation and planning purposes in multiple brain metastases cases. Due to these uncertainties, the target coverage of the 25 Gy prescription dose ($V_{25\text{Gy}}$) was found to be <94% (instead of the 99% prescribed in the forward series) for 33% of the targets (32 of 96 metastases) in the average images. The actual $D_{99\%}$ value (dose covering the 99% of the target in the average series) delivered in these targets was between 17 and 23.8 Gy (instead of the 25 Gy prescribed dose), which corresponds to an underdosage (dose difference) ranging from 5% to 32%. The mean underdosage for all studied targets was 8%. Table 9-1 summarizes geometrical uncertainty and underdosage values for all 15 patients investigated. Because target contouring was performed in an automatic way by using identical grayscale threshold levels in all datasets, target contouring variability was eliminated, with target volumes being similar in all series (average volumes of 0.29, 0.29, and 0.30 cm^3 were calculated for forward,

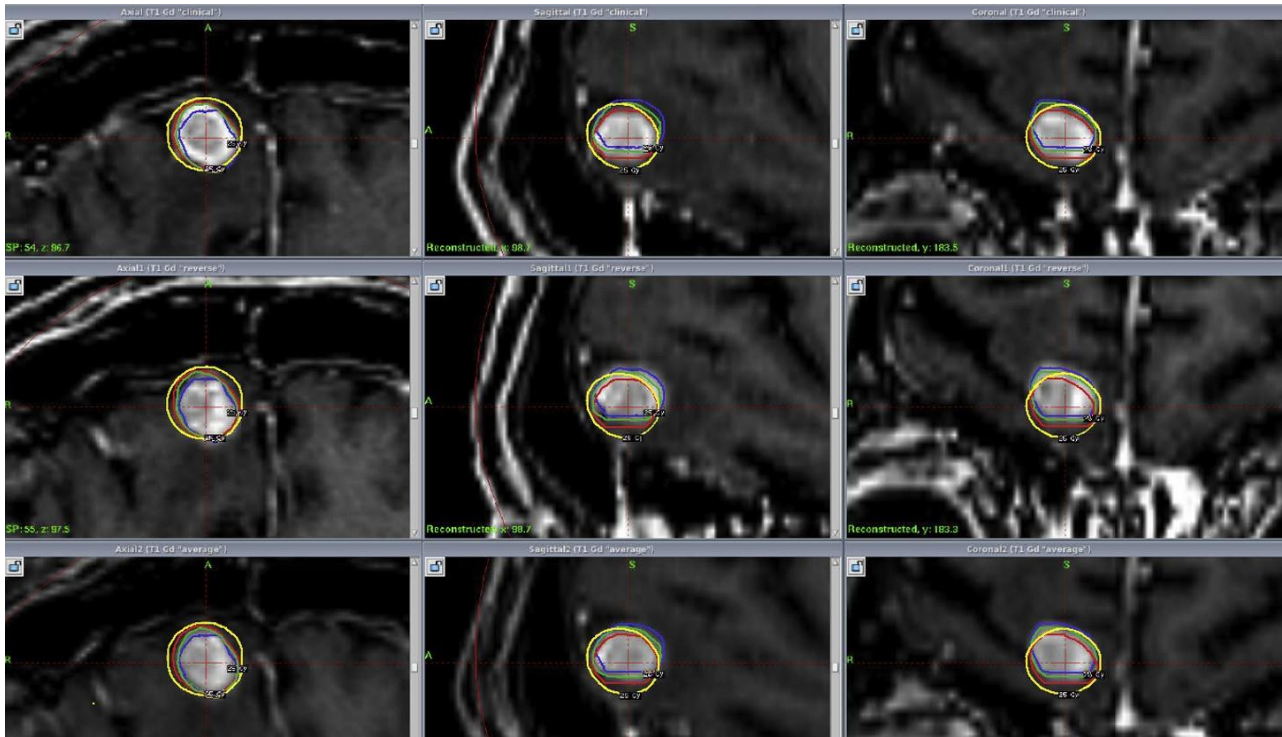


Figure 9-3: Print-screen images from the GammaPlan treatment planning system presenting the central axial (left column), sagittal (middle column), and coronal (right column) views of a 1 cm metastasis as shown in forward (top row), reverse (middle row), and average images (bottom row). The target contour defined independently in forward, reverse, and average series following registration in the stereotactic space is marked with red, blue, and green, respectively. The prescription isodose, as planned in the forward MR series, is shown in yellow.

reverse, and average series, respectively). Use of different grayscale threshold levels produced geometric distortions that were changed slightly; however, they presented the same directionality and resulted in similar underdosages of specific targets.

The delivered dose and target coverage differences are generally larger for smaller metastases as well as for metastases positioned in A and/or P brain regions, where the greater geometric uncertainties were observed. This is shown in Figure 9-4, which presents the geometric uncertainties as well as the corresponding target dose differences determined for a patient plan with 19 metastases performed in the forward series.

Table 9-1: Results (range and mean values) for the geometry uncertainties in x, y, and z axis directions (dx, dy and dz), as well as for the total spatial uncertainties, d_R^{tot} , along with resultant percentage dose difference values DD (%). In all MR scans, frequency encoding was performed along the y-axis.

Patient ID	No. of targets	Range								Mean \pm 1std								Dose difference	
		dx		dy		dz		dtot		dx		dy		dz		dtot		Range	Mean \pm 1 std
1	19	0	- 0	-0.2	- 0.9	-0	- 1.1	0	- 1.25	0	\pm 0	0.3	\pm 0.27	0.35	\pm 0.35	0.51	\pm 0.37	0	- 32
2	2	0	- 0	0	- 0.4	0	- 0.5	0	- 0.64	0	\pm 0	0.2	\pm 0.28	0.25	\pm 0.35	0.32	\pm 0.45	0	- 10
3	3	0	- 0	0.1	- 0.6	0.1	- 0.6	0.1	- 0.8	0	\pm 0	0.37	\pm 0.25	0.4	\pm 0.26	0.54	\pm 0.36	0	- 10
4	8	0	- 0	-0.1	- 0.4	0	- 0.4	0.1	- 0.5	0.02	\pm 0.05	0.11	\pm 0.2	0.18	\pm 0.18	0.28	\pm 0.18	0	- 9
5	3	0	- 0	0.4	- 0.6	0.1	- 0.4	0.54	- 0.61	0	\pm 0	0.5	\pm 0.1	0.23	\pm 0.15	0.57	\pm 0.04	6.2	- 14
6	5	0	- 0	0.1	- 0.4	0.2	- 0.5	0.22	- 0.57	0	\pm 0	0.26	\pm 0.13	0.3	\pm 0.14	0.41	\pm 0.15	0	- 10.4
7	7	0	- 0	0	- 0.6	0	- 0.4	0	- 0.64	0	\pm 0	0.32	\pm 0.24	0.13	\pm 0.14	0.36	\pm 0.27	0	- 21
8	7	0	- 0	0	- 0.4	0	- 0.5	0	- 0.58	0	\pm 0	0.19	\pm 0.16	0.19	\pm 0.2	0.28	\pm 0.22	0	- 22
9	2	0	- 0	0.4	- 0.6	0.2	- 0.4	0.44	- 0.72	0	\pm 0	0.5	\pm 0.14	0.3	\pm 0.14	0.58	\pm 0.19	8	- 15
10	7	0	- 0	0.2	- 0.7	0.2	- 0.5	0.28	- 0.86	0	\pm 0	0.48	\pm 0.2	0.32	\pm 0.12	0.58	\pm 0.21	0	- 24
11	10	-0.1	- 0	0	- 0.6	0.1	- 0.6	0.14	- 0.63	-0.02	\pm 0.04	0.22	\pm 0.17	0.27	\pm 0.16	0.38	\pm 0.18	0	- 11
12	5	0	- 0	-0.2	- 0.8	0	- 0.7	0	- 1.1	0	\pm 0	0.36	\pm 0.44	0.2	\pm 0.29	0.5	\pm 0.42	0	- 25
13	3	-0.2	- 0	0.1	- 0.2	0	- 0.4	0.1	- 0.5	-0.07	\pm 0.11	0.17	\pm 0.06	0.13	\pm 0.23	0.26	\pm 0.2	2	- 16
14	13	-0.2	- 0	0.1	- 1	-0	- 0.7	0.1	- 1.1	-0.01	\pm 0.05	0.49	\pm 0.24	0.23	\pm 0.26	0.59	\pm 0.28	0	- 25
15	2	0	- 0.1	0.2	- 0.3	0.6	- 0.7	0.64	- 0.76	0.05	\pm 0.07	0.25	\pm 0.07	0.65	\pm 0.65	0.7	\pm 0.09	12	- 20
Total	96	-0.2	- 0.1	-0.2	- 1	-0	- 1.1	0	- 1.3	0	\pm 0.04	0.31	\pm 0.25	0.26	\pm 0.24	0.45	\pm 0.29	0	- 32

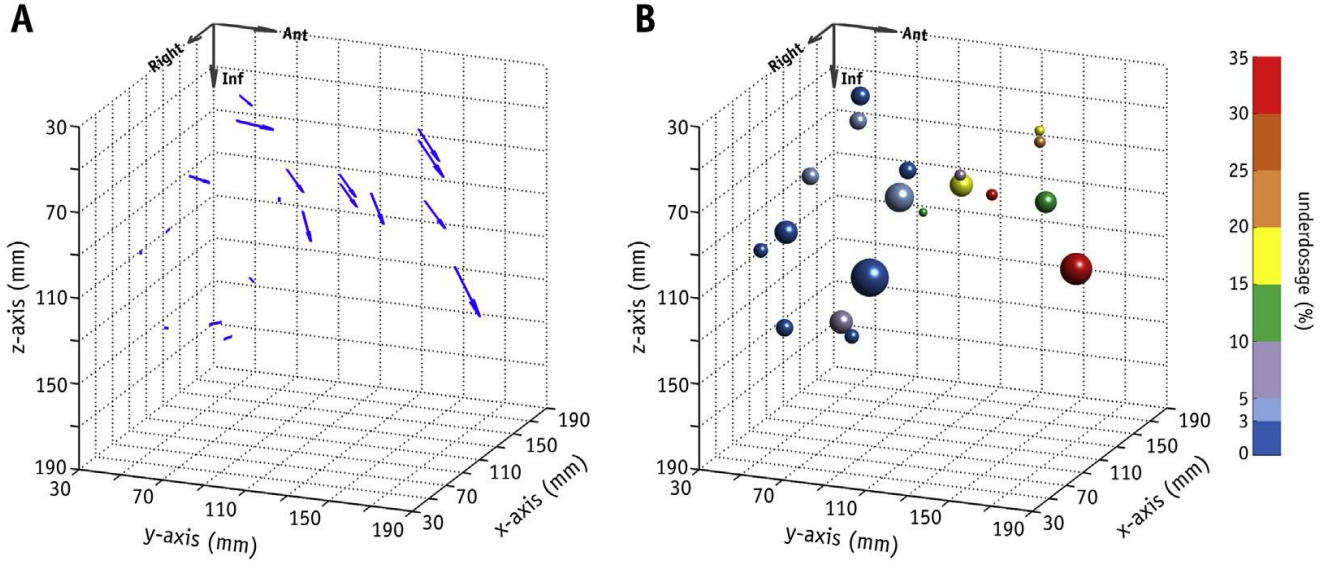


Figure 9-4: Geometric uncertainty and underdosage results associated with the forward series in a patient with 19 metastases. (a) The geometric uncertainty vectors, d_R^{tot} , are presented as scaled vectors similarly to those shown in Figure 9-2. (b) Target underdosage results were derived from target coverage of the prescription dose in the average images (the center and the diameter of each sphere coincides with the center and diameter of a target metastasis, whereas its color denotes the percentage of underdosage according to the presented color bar).

9.4 Discussion

In a previous phantom study using the reverse gradient technique [25], it was demonstrated that certain MRI acquisition parameters, such as the frequency encoding axis and read gradient polarity, significantly affect the sequence-dependent distortions due to the directional dependence of field inhomogeneities. The same parameters influence the direction of the total geometric uncertainty vector associated with the entire GK treatment delivery process, which also includes the image registration step. This was confirmed in MRI units from different vendors and various field strengths (0.5-3.0 T). Applying the same technique in multiple metastases patients, a similar behavior regarding the spatial geometric uncertainties and their directionality is revealed. These uncertainties may significantly affect the target coverage in highly conformal plans, especially for tiny and/or outlying targets. To ensure adequate prescription dose coverage for these targets, an additional margin of ~ 1.0 mm can be prescribed. This approach, however, will increase the 12 Gy volume of normal brain tissue and, consequently, the brain toxicity risk [60].

Although several methods with strong theoretical background have been proposed for reducing the MRI-related distortions [33,39–42,182], none of them, to our knowledge, has been clinically applied in SRS and, particularly, in GK SRS applications. All these methods involve specialized and time-consuming (up to several hours [33]) image post-processing steps and analysis in addition to additional scanning. The proposed methodology is time efficient (~ 1 min post-processing time) and easily implemented. As shown in the phantom study, it can substantially reduce the geometric uncertainty in MR-based GK applications. Moreover, the patient study revealed that the use of average images can increase the delivery accuracy and target coverage of the prescription dose in GK multiple metastases cases at the cost of an additional 10 minutes of scanning time. Similar results have been observed in a limited number of patients requiring highly conformal treatments of other intracranial lesions, such as arteriovenous malformations and meningiomas, where Gd-enhanced, T1w images are also used for target delineation. Although an in-house-built algorithm was used to provide the average image series in this work, a GammaPlan user can appreciate the methodology's potential benefit by simply fusing the corresponding forward and reverse series after they have been independently registered in the Leksell stereotactic space.

The proposed average method takes into account and eliminates only sequence dependent spatial distortions and does not treat sequence independent distortions resulting from gradient nonlinearities. The latter depend on the performance of the specific gradient coil set installed on the MRI unit used. However, these distortions are minimal in the investigated Leksell space and equal to the residual geometric uncertainties associated with the average series in Figure 9-2(c) (< 0.3 mm). Preliminary phantom studies revealed that the efficacy of the proposed average method may depend on the magnitude of sequence dependent distortions. In regions with high levels of sequence dependent distortions (higher than twice the imaging pixel size), not met in MR images investigated in this study, the target volumes in the average images can be larger than the corresponding volumes defined in the forward images by using the same threshold levels. Thus, the method needs to be evaluated further in GK applications other than brain metastases and/or with different background field inhomogeneities.

As an alternative to the preclusive use of MR images, CT images, known to present minimal geometric distortion, can be used to perform image registration in the LCS, with MR images being used solely for target delineation. In this case, however, an extra step is required (i.e., the co-registration between MR and CT images), which adds an additional uncertainty on the order of 1 mm [144,183]. Furthermore, untreated MRI geometric distortions may limit the accuracy and, therefore, the usefulness of CT/MR co-registration [182,184].

9.5 Conclusions

There is an inherent geometric uncertainty in GK applications induced by MRI sequence dependent spatial distortions. Both phantom and patient studies revealed geometrical uncertainties, presenting a directional dependence with respect to the selected read gradient direction. The uncertainty magnitude depends on target size and position, that is, it is greater for smaller targets and/or targets located in the brain periphery. Due to this uncertainty, specific targets may be considerably underdosed when MR images are used for both target delineation and planning purposes. The proposed methodology, based on the use of average image data resulting from corresponding MRI series acquired with opposite read gradient polarities, may improve geometric accuracy and, consequently, total GK dose delivery accuracy.

10 Comparison of geometric distortion correction schemes in MR images used in stereotactic radiosurgery applications

Summary

The scope of this work is to review, evaluate and compare the efficacy of two proposed correction approaches; the average-image method (presented and evaluated in Chapter 9) and the more well-established signal integration technique. A specially designed phantom which incorporates 947 CPs for distortion detection was utilized (presented in Chapter 4). The phantom was MR scanned at 1.5T using the head coil and the clinically employed pulse sequence for SRS treatment planning. An additional scan was performed with identical imaging parameters except for reversal of read gradient polarity. In-house MATLAB routines were developed for implementation of the signal integration and average-image distortion correction techniques. The mean CP locations of the two MR scans were regarded as the reference CP distribution. Residual distortion was assessed by comparing the corrected CP locations with corresponding reference positions. Mean absolute distortion on frequency encoding direction was reduced from 0.34 mm (original images) to 0.15 mm and 0.14 mm following application of signal integration and average-image methods, respectively. However, a maximum residual distortion of 0.7 mm was still observed for both techniques. The signal integration method relies on the accuracy of edge detection and requires 3-4 hours of post-imaging computational time. The average-image technique is a more efficient (processing time of the order of seconds) and easier to implement method to improve geometric accuracy in such applications.

10.1 Introduction

Several sequence dependent distortion correction schemes have been presented [10,33,39,40], all requiring an extra imaging step and, therefore, resulting in additional scanning time. An efficient approach for distortion correction in 3D imaging protocols is to take advantage of the fact that sequence-dependent distortions are polarity dependent [33], in the sense that distortion changes sign with the polarity of the frequency encoding gradient field. Correction methods that rely on read gradient reversal account for all sequence dependent sources of distortion including static magnetic field inhomogeneity, susceptibility differences and chemical shift artifacts but disregard distortion induced by gradient nonlinearities (sequence independent distortion [33]). In this work, the prototype head phantom was employed to investigate and compare the efficacy of two proposed sequence dependent distortion correction schemes; the average-image method and the signal integration technique, both relying on read gradient polarity reversal.

10.2 Materials and Methods

10.2.1 The phantom

The prototype head-size MR phantom was implemented to study the efficacy of distortion correction techniques. The phantom was MR scanned filled with copper sulfate solution, yielding high-contrast with acrylic and facilitating CP localization. However, differences in magnetic susceptibility between the solution and acrylic also result in object-induced geometric distortions, which come in addition to existing static magnetic field inhomogeneity related spatial distortions [2,33].

10.2.2 Image acquisitions

The filled phantom was positioned in the center of the head coil of a Philips Multiva 1.5T scanner (Philips Medical Systems, The Netherlands). A clinically used for intracranial SRS treatment planning 3D T1w Fast Field Echo (FFE) pulse sequence was

employed using a reconstruction voxel size of $0.98 \times 0.98 \times 1 \text{ mm}^3$, a bandwidth of 191 Hz/pixel and selecting the y-axis (i.e., A – P) as the frequency encoding direction. Since sequence dependent distortion correction schemes are based on the reversal of read gradient polarity [33], an identical pulse sequence was added to the imaging protocol after reversing the read gradient direction (i.e., P – A), doubling the scanning time. The MR imaging protocol was repeated by applying the frequency encoding direction on the x-axis (i.e., L – R and R – L directions). 3D sequence independent distortion correction routines, provided by the MR scanner vendor, were enabled and applied to all sequences acquired, thus, minimizing distortions due to gradient nonlinearities which are not corrected nor accounted for by any of the correction schemes involved in this comparative study.

10.2.3 Image processing

Using in-house MATLAB (The MathWorks, Inc., Natick, MA) routines, forward and reversed polarity image scans were processed to determine the distortion of the original images. In particular, the mean CP location identified in the opposed polarity MR scans was considered as the reference (undistorted) CP position. Distortion of the original image was determined by the spatial offset between CP location in the forward image scan and the corresponding reference location.

10.2.3.1 Signal integration correction method

The signal integration technique for sequence-dependent distortion correction is described in detail in the work of Morgan et al [40]. Briefly, the method relies on the fact that the integral of the image signal along the frequency encoding direction is not affected by spatial distortion and, therefore, matching points between the forward and the reversed polarity MR scans are identified at the locations where the two integrals equalize, yielding the distortion map. In addition, the original image is also corrected for the pixel intensity for the transformation between the undistorted and distorted image spaces, using the Jacobian determinant of the distortion map [28]. Further details related to the calculation of the Jacobian determinant were given in Section 2.9.

10.2.3.2 Average-image correction method

The average image method was presented and evaluated for a series of GK SRS multiple brain metastases cases in Chapter 9. Briefly, it simply combines the forward and reversed polarity images into a new image in which pixel intensity is the average of the original images. Consequently, post-image processing is minimal (of the order of seconds) and straightforward. However, no signal intensity corrections can be applied since distortion maps cannot be determined.

Following implementation of both distortion correction methods, residual distortions were assessed as the CP offsets between the reference and the corresponding corrected CP locations.

10.3 Results and discussion

Table 10-1: Statistical analysis for distortion detected for the original and corrected images.

Frequency encoding direction	Image	Range (mm)	Mean \pm 1std	Mean abs \pm 1std	Median (mm)
			(mm) ^a	(mm) ^b	
y-axis (A-P)	Original	-0.16 – 1.07	0.34 \pm 0.23	0.34 \pm 0.23	0.35
	Average-Image	-0.75 – 0.49	-0.02 \pm 0.20	0.14 \pm 0.15	0.00
	Signal Integration	-0.59 – 0.77	0.05 \pm 0.22	0.15 \pm 0.16	0.00
x-axis (L-R)	Original	-0.12 – 1.06	0.32 \pm 0.25	0.33 \pm 0.24	0.27
	Average-Image	-0.70 – 0.74	-0.05 \pm 0.18	0.12 \pm 0.14	-0.01
	Signal Integration	-0.56 – 0.68	-0.03 \pm 0.18	0.13 \pm 0.13	0.01

^a Mean detected distortion \pm 1 standard deviation

^b Mean detected distortion magnitude \pm 1 standard deviation

Detected distortion for the original images identified using all 947 CPs is presented in Table 10-1. The mean distortion in the entire volume scanned is 0.3 mm irrespective of selection of frequency encoding direction, while the maximum distortion exceeds 1 mm. After applying the correction techniques, mean and median distortion reduces to practically zero. However, the maximum detected CP offset reaches 0.7 mm which could be attributed to non-systematic errors of the CP localization algorithm occurring in areas of reduced signal. Implementation of the signal integration method requires a few hours of post-imaging computational time while the average-image method is more efficient (processing time of the order of seconds).

Figure 10-1 depicts the distortion magnitude and orientation for the original and corrected images with the frequency encoding gradient set on y-axis. For the original image (Figure 10-1(a)), distortion is mainly directed towards the frequency encoding direction due to the combined effect of susceptibility differences and static magnetic field inhomogeneity. For both corrected images (Figures 10-1(b),(c)), distortion on y-axis is negligible while minimal residual distortion is observed at random orientations.

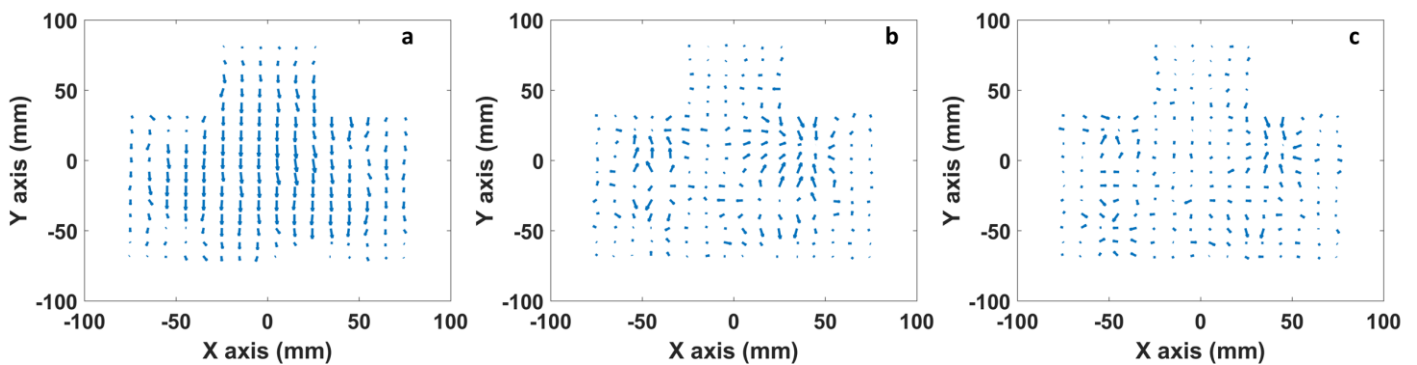


Figure 10-1: Distortion vectors (magnified by a factor of 15 to facilitate readability) for an indicative axial plane of the phantom corresponding to the original (a), as well as the average-image (b) and signal integration (c) corrected images with the read gradient direction set on the y-axis.

Figure 10-2 presents histograms of the identified distortion using all 947 CPs in all image series for direct comparison. While for the original images, distortion distribution is shifted towards the positive distortion direction, residual distortion identified in the corrected images is distributed around zero.

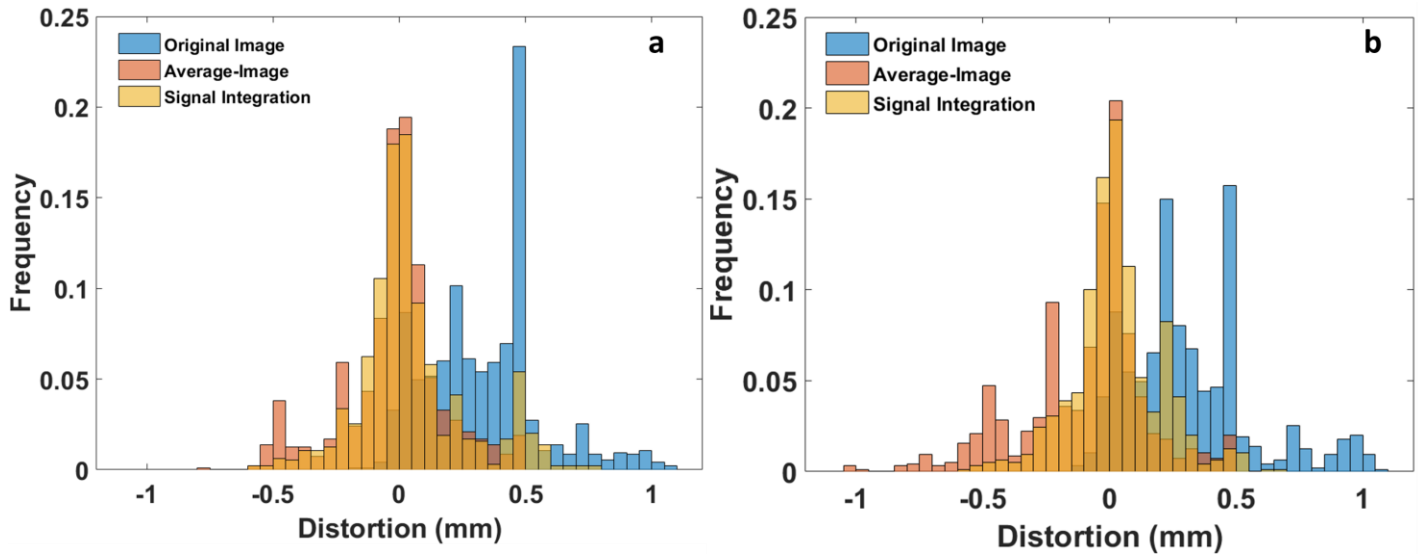


Figure 10-2: Histograms of the identified distortion for the original and corrected images with the read gradient direction set on y-axis (a) and x-axis (b).

10.4 Conclusion

Both sequence-dependent distortion correction techniques perform equally well, minimizing the mean and median residual distortions. However, the signal integration method requires a few hours of post-imaging computational time while the average-image method is simple and efficient.

Summary of Results, Overall Conclusions and Future Work

In this thesis, MR-related geometric distortions were evaluated with emphasis given to the MR protocols and hardware used for cranial SRS treatment planning procedures. Two novel phantoms (a prototype and an advanced version), both similar in concept, were designed and constructed towards this end. Accompanying methodologies and image processing routines were also developed. In most cases, the detected distortion was also appreciated in patient images.

In particular, using the prototype phantom and a 1.5T MR unit, gradient nonlinearity was found to induce mean distortion of about 0.5 mm, whilst maximum values of up to 1.1 mm are reached at the edges of the examined volume. Frame induced distortion was characterized and found to affect spatial accuracy in frame-based GK applications, including the registration procedure between MR image coordinate system and the stereotactic space. Distortion of several millimeters was detected within a few centimeters from the frame base while the range of the frame induced distortion also reached the GK Perfexion treatable area, suggesting that target localization might also be affected in some cases. Frame induced distortion was also acknowledged in patient MR images, using CT angiography as a reference.

Using the same phantom, the overall geometric distortion was measured for three MR pulse sequences and scanners clinically used in SRS, while also involving a 3.0T unit. Mapping of distortion magnitude and directionality was performed using the head coil but without mounting a stereotactic frame to the phantom, in order to focus on B_0 inhomogeneity and gradient nonlinearity distortions only. Although mean absolute distortion did not exceed 0.5 mm on any spatial axis, maximum detected CP displacement reached 2 mm. This analysis also served as a comparative study between the three clinically used MR pulse sequences.

The next step involved patient-induced distortions assessment with emphasis to susceptibility induced distortion related to the paramagnetic nature of the Gd-based contrast agent. The prototype phantom was modified to incorporate two small

cylindrical inserts simulating brain metastases. The inserts were filled with various concentrations (0-20mM) of the Gd-DTPA contrast agent. Using a composite methodology, Gd-induced distortion was separated from B_0 inhomogeneity and gradient nonlinearity related distortions. The inserts centroids were on average displaced by 0.204 ppm/mM which corresponds to 0.067 mm/mM for the specific imaging conditions and parameters employed. However, since distortion magnitude strongly depends on the susceptibility cavity size, shape, orientation with respect to B_0 and imaging parameters used, these results should only be regarded as indicative for an SRS realistic clinical scenario.

In MR images of patients with single or multiple brain metastases, the distortion directly affecting the target locations was assessed. Target displacement stemming from sequence dependent distortions (including the Gd-induced one) ranged from 0.35 mm to 0.87 mm, depending on target location, with an average value of 0.54 mm (2.24 ppm). This relative wide range of target localization uncertainty results from the fact that the B_0 inhomogeneity distortion vector in a specific location may add to or partly counterbalance Gd-DTPA induced distortion, thus increasing or decreasing, respectively, the total sequence dependent distortion. Although relatively small, these distortions are present exactly at target locations, directly affecting dose delivery accuracy.

Effort was made to determine levels of spatial uncertainty tolerance levels in realistic VMAT plans by simulating linac-based SRS applications. Corresponding results were strongly dependent on target size. In specific, for targets less than 2 cm in diameter, a spatial displacement of the order of 1 mm could significantly affect both D_{95} and Paddick's CI values, with differences being greater than 5% compared to the reference (non-distorted) plan. For targets with diameter up to 3 cm, D_{95} could be affected by spatial distortions of the order of 1.5 mm. For larger target diameters, geometric distortions greater than 2 mm are required to considerably (>5%) affect plan evaluation indices.

A methodology was developed and implemented to assess the accuracy of distortion correction routines, incorporated in the MR units by the vendors. These algorithms account for gradient nonlinearity related distortion only. Clinical 1.5T and 3.0T MR protocols were evaluated using the advanced version of the novel phantom. Results of

this work suggest that geometric distortions could still be a concern around the edges of the field of view even with the correction algorithms enabled.

The average-image methodology for distortion minimization was developed and implemented in a phantom as well as patient images with multiple brain metastases. The technique was found effective in minimizing sequence dependent distortion in and around the target locations. In a comparative study, the average-image and the more well-established signal integration methods were implemented to correct phantom images. Residual distortion was evaluated using reference CP locations. Both correction techniques were found to perform equally well, minimizing the mean and median residual distortions, although the average-image method is clearly more efficient and easier to implement.

Overall results of this thesis suggest that the total MR-related geometric distortion could potentially result in target mis-positioning by more than 1 mm, especially for targets lying at the periphery of the brain, closer to the edges of the field of view. Registration procedures are also affected by MR distortions, adding up to the overall uncertainty. Such levels of spatial uncertainty might exceed the margins often applied around the GTV during target definition in SRS. This remark is even more pronounced if other sources of spatial degradation are also considered (e.g., image registration uncertainty, inter-fraction patient positioning, intra-fraction organ/patient motion, dose delivery mechanical uncertainty). Concerns are raised with respect to under-dosage of tiny peripheral targets which can result in reduced local tumor control, as well as increased risk of radiation induced toxicity (e.g., brain necrosis).

The need for introduction of MR scanners, imaging protocols and post-imaging routines that exhibit improved geometric accuracy is highlighted by the results of this work. Alternatively, MR distortion correction techniques could be considered for application in routine clinical practice, following thorough validation and quality control procedures.

In any case, it is crucial that strict quality assurance protocols for MR-related geometric accuracy in MR units and sequences employed in SRS treatment planning are established and routinely performed. Relevant procedures, guidelines and tolerance levels need to be determined first. Existing societal standards for MRI quality control need to be updated to meet the stringent spatial accuracy demands in SRS.

Future work should focus on addressing the above concerns. Towards this end, patient specific sequence dependent distortion assessment presented in this thesis can be expanded to other SRS clinical cases (besides multiple brain metastases), such as acoustic neuromas where the target lies close to the bone-air interface and, therefore, increased distortion could be exhibited. The effect of sequence dependent distortion in areas away from targets should be also assessed as it is expected to reach several millimeters at the air interfaces. The consequent impact on image registration (both frame-based and anatomy-based) procedures is unknown. The link between spatial uncertainty tolerance levels, the lesion size and anatomical site and plan quality characteristics is currently missing. A patient study of adequate sample size which will comprise of various clinical cases and anatomical sites is warranted to assess the true clinical impact of spatial uncertainty. Moreover, introduction of distortion correction methodologies in clinical practice should be preceded by the development of corresponding quality control procedures for verification, benchmarking and periodic residual distortion detection. Phantoms and techniques similar to the ones developed for the purposes of this thesis could be considered.

Bibliography

- [1] Schmidt MA, Payne GS. Radiotherapy planning using MRI. *Phys Med Biol* 2015;60:R323–61. doi:10.1088/0031-9155/60/22/R323.
- [2] Weygand J, Fuller CD, Ibbott GS, Mohamed ASR, Ding Y, Yang J, et al. Spatial precision in magnetic resonance imaging-guided radiation therapy: The role of geometric distortion. *Int J Radiat Oncol Biol Phys* 2016;95:1304–16. doi:10.1016/j.ijrobp.2016.02.059.
- [3] Johnstone E, Wyatt JJ, Henry AM, Short SC, Sebag-Montefiore D, Murray L, et al. A systematic review of synthetic CT generation methodologies for use in MRI-only radiotherapy. *Int J Radiat Oncol* 2017;100:199–217. doi:10.1016/j.ijrobp.2017.08.043.
- [4] Hanssens P, Karlsson B, Yeo TT, Chou N, Beute G. Detection of brain micrometastases by high-resolution stereotactic magnetic resonance imaging and its impact on the timing of and risk for distant recurrences. *J Neurosurg* 2011;115:499–504. doi:10.3171/2011.4.JNS101832.
- [5] Nagai A, Shibamoto Y, Mori Y, Hashizume C, Hagiwara M, Kobayashi T. Increases in the number of brain metastases detected at frame-fixed, thin-slice MRI for gamma knife surgery planning. *Neuro Oncol* 2010;12:1187–92. doi:10.1093/neuonc/noq084.
- [6] Winey B, Bussi  re M. Geometric and dosimetric uncertainties in intracranial stereotactic treatments for multiple nonisocentric lesions. *J Appl Clin Med Phys* 2014;15:122–32. doi:10.1120/jacmp.v15i3.4668.
- [7] Roper J, Chanyavanich V, Betzel G, Switchenko J, Dhabaan A. Single-Isocenter Multiple-Target Stereotactic Radiosurgery: Risk of Compromised Coverage. *Int J Radiat Oncol Biol Phys* 2015;93:540–6. doi:10.1016/j.ijrobp.2015.07.2262.
- [8] Jin H, Keeling VP, Ali I, Ahmad S. Dosimetric effects of positioning shifts using

- 6D-frameless stereotactic Brainlab system in hypofractionated intracranial radiotherapy. *J Appl Clin Med Phys* 2016;17:5682. doi:10.1120/jacmp.v17i1.5682.
- [9] Pappas EP, Alshantiry M, Moutsatsos A, Lababidi H, Alsafi K, Georgiou K, et al. MRI-Related Geometric Distortions in Stereotactic Radiotherapy Treatment Planning: Evaluation and Dosimetric Impact. *Technol Cancer Res Treat* 2017;16:1120–9. doi:10.1177/1533034617735454.
- [10] Karaiskos P, Moutsatsos A, Pappas E, Georgiou E, Roussakis A, Torrens M, et al. A simple and efficient methodology to improve geometric accuracy in gamma knife radiation surgery: Implementation in multiple brain metastases. *Int J Radiat Oncol Biol Phys* 2014;90:1234–41. doi:10.1016/j.ijrobp.2014.08.349.
- [11] Massager N, Abeloos L, Devriendt D, Op de Beeck M, Levivier M. Clinical evaluation of targeting accuracy of gamma knife radiosurgery in trigeminal neuralgia. *Int J Radiat Oncol Biol Phys* 2007;69:1514–20. doi:10.1016/j.ijrobp.2007.05.013.
- [12] Yan E., Sneed P., McDermott M., Kunwar S, Wara W., Larson D. Number of brain metastases is not an important prognostic factor for survival following radiosurgery for newly-diagnosed nonmelanoma brain metastases. *Int J Radiat Oncol* 2003;57:S131–2. doi:10.1016/S0360-3016(03)00836-8.
- [13] Yamamoto M, Kawabe T, Sato Y, Higuchi Y, Nariai T, Barford BE, et al. A case-matched study of stereotactic radiosurgery for patients with multiple brain metastases: comparing treatment results for 1–4 vs ≥ 5 tumors. *J Neurosurg* 2013;118:1258–68. doi:10.3171/2013.3.JNS121900.
- [14] Shu HKG, Sneed PK, Shiau CY, McDermott MW, Lamborn KR, Park E, et al. Factors influencing survival after gamma knife radiosurgery for patients with single and multiple brain metastases 1996;2:335–42.
- [15] Serizawa T, Saeki N, Higuchi Y, Ono J, Iuchi T, Nagano O, et al. Gamma knife surgery for brain metastases: indications for and limitations of a local treatment protocol. *Acta Neurochir (Wien)* 2005;147:721–6. doi:10.1007/s00701-005-0540-4.

- [16] Petrovich Z, Yu C, Giannotta SL, O’Day S, Apuzzo MLJ. Survival and pattern of failure in brain metastasis treated with stereotactic gamma knife radiosurgery. vol. 97, 2002, p. 499–506.
- [17] Nataf F, Schlienger M, Liu Z, Foulquier JN, Grès B, Orthuon A, et al. Radiosurgery With or Without A 2-mm Margin for 93 Single Brain Metastases. *Int J Radiat Oncol Biol Phys* 2008;70:766–72. doi:10.1016/j.ijrobp.2007.11.002.
- [18] Muacevic A, Kufeld M, Wowra B, Kreth F-W, Tonn J-C. Feasibility, safety, and outcome of frameless image-guided robotic radiosurgery for brain metastases. *J Neurooncol* 2010;97:267–74. doi:10.1007/s11060-009-0023-1.
- [19] Chidel MA, Suh JH, Reddy CA, Chao ST, Lundbeck MF, Barnett GH. Application of recursive partitioning analysis and evaluation of the use of whole brain radiation among patients treated with stereotactic radiosurgery for newly diagnosed brain metastases. *Int J Radiat Oncol Biol Phys* 2000;47:993–9. doi:10.1016/S0360-3016(00)00527-7.
- [20] Chang WS, Kim HY, Chang JW, Park YG, Chang JH. Analysis of radiosurgical results in patients with brain metastases according to the number of brain lesions: is stereotactic radiosurgery effective for multiple brain metastases? 2010;113 Suppl:73–8.
- [21] Caballero JA, Sneed PK, Lamborn KR, Ma L, Denduluri S, Nakamura JL, et al. Prognostic factors for survival in patients treated with stereotactic radiosurgery for recurrent brain metastases after prior whole brain radiotherapy. *Int J Radiat Oncol Biol Phys* 2012;83:303–9. doi:10.1016/j.ijrobp.2011.06.1987.
- [22] Serizawa T, Yamamoto M, Sato Y, Higuchi Y, Nagano O, Kawabe T, et al. Gamma Knife surgery as sole treatment for multiple brain metastases: 2-center retrospective review of 1508 cases meeting the inclusion criteria of the JLGK0901 multi-institutional prospective study. 2010;113 Suppl:48–52.
- [23] Lippitz B, Lindquist C, Paddick I, Peterson D, O’Neill K, Beaney R. Stereotactic radiosurgery in the treatment of brain metastases: the current evidence. *Cancer Treat Rev* 2014;40:48–59. doi:10.1016/j.ctrv.2013.05.002.
- [24] Likhacheva A, Pinnix CC, Parikh NR, Allen PK, McAleer MF, Chiu MS, et al.

- Predictors of survival in contemporary practice after initial radiosurgery for brain metastases. *Int J Radiat Oncol Biol Phys* 2013;85:656–61. doi:10.1016/j.ijrobp.2012.05.047.
- [25] Moutsatsos A, Karaiskos P, Petrokokkinos L, Sakelliou L, Pantelis E, Georgiou E, et al. Assessment and characterization of the total geometric uncertainty in Gamma Knife radiosurgery using polymer gels. *Med Phys* 2013;40:31704. doi:10.1118/1.4789922.
- [26] Pappas EP, Seimenis I, Moutsatsos A, Georgiou E, Nomikos P, Karaiskos P. Characterization of system-related geometric distortions in MR images employed in Gamma Knife radiosurgery applications. *Phys Med Biol* 2016;61:6993–7011. doi:10.1088/0031-9155/61/19/6993.
- [27] Baldwin LLN, Wachowicz K, Thomas SDS, Rivest R, Fallone BG. Characterization, prediction, and correction of geometric distortion in 3 T MR images. *Med Phys* 2007;34:388. doi:10.1118/1.2402331.
- [28] Doran SJ, Charles-Edwards L, Reinsberg SA, Leach MO. A complete distortion correction for MR images: I. Gradient warp correction. *Phys Med Biol* 2005;50:1343–61. doi:10.1088/0031-9155/50/7/001.
- [29] Gustafsson C, Nordström F, Persson E, Brynolfsson J, Olsson LE. Assessment of dosimetric impact of system specific geometric distortion in an MRI only based radiotherapy workflow for prostate. *Phys Med Biol* 2017;62:2976–89. doi:10.1088/1361-6560/aa5fa2.
- [30] Wang H, Balter J, Cao Y. Patient-induced susceptibility effect on geometric distortion of clinical brain MRI for radiation treatment planning on a 3T scanner. *Phys Med Biol* 2013;58:465–77. doi:10.1088/0031-9155/58/3/465.
- [31] Stanescu T, Wachowicz K, Jaffray DA. Characterization of tissue magnetic susceptibility-induced distortions for MRIgRT. *Med Phys* 2012;39:7185–93. doi:10.1118/1.4764481.
- [32] Adjeiwaah M, Bylund M, Lundman JA, Thellenberg Karlsson C, Jonsson JH, Nyholm T. Quantifying the effect of 3T MRI residual system and patient-induced susceptibility distortions on radiotherapy treatment planning for prostate

- cancer. *Int J Radiat Oncol* 2017. doi:10.1016/j.ijrobp.2017.10.021.
- [33] Baldwin LLN, Wachowicz K, Fallone BG. A two-step scheme for distortion rectification of magnetic resonance images. *Med Phys* 2009;36:3917. doi:10.1118/1.3180107.
 - [34] Wang D, Strugnell W, Cowin G, Doddrell DM, Slaughter R. Geometric distortion in clinical MRI systems: Part I: Evaluation using a 3D phantom. *Magn Reson Imaging* 2004;22:1211–21. doi:10.1016/j.mri.2004.08.012.
 - [35] Karger CP, Höss A, Bendl R, Canda V, Schad L. Accuracy of device-specific 2D and 3D image distortion correction algorithms for magnetic resonance imaging of the head provided by a manufacturer. *Phys Med Biol* 2006;51:N253–61. doi:10.1088/0031-9155/51/12/N04.
 - [36] Schenck JF. The role of magnetic susceptibility in magnetic resonance imaging: MRI magnetic compatibility of the first and second kinds. *Med Phys* 1996;23:815. doi:10.1118/1.597854.
 - [37] Bernstein MA, Huston J, Ward HA. Imaging artifacts at 3.0T. *J Magn Reson Imaging* 2006;24:735–46. doi:10.1002/jmri.20698.
 - [38] Crijns SPM, Raaymakers BW, Lagendijk JJW. Real-time correction of magnetic field inhomogeneity-induced image distortions for MRI-guided conventional and proton radiotherapy. *Phys Med Biol* 2011;56:289–97. doi:10.1088/0031-9155/56/1/017.
 - [39] Reinsberg SA, Doran SJ, Charles-Edwards EM, Leach MO. A complete distortion correction for MR images: II. Rectification of static-field inhomogeneities by similarity-based profile mapping. *Phys Med Biol* 2005;50:2651–61. doi:10.1088/0031-9155/50/11/014.
 - [40] Morgan PS, Bowtell RW, McIntyre DJO, Worthington BS. Correction of spatial distortion in EPI due to inhomogeneous static magnetic fields using the reversed gradient method. *J Magn Reson Imaging* 2004;19:499–507. doi:10.1002/jmri.20032.
 - [41] Jezzard P, Balaban RS. Correction for geometric distortion in echo planar images

- from B0 field variations. *Magn Reson Med* 1995;34:65–73.
- [42] Chang H, Fitzpatrick JM. A technique for accurate magnetic resonance imaging in the presence of field inhomogeneities. *IEEE Trans Med Imaging* 1992;11:319–29. doi:10.1109/42.158935.
 - [43] Wachowicz K, Stanescu T, Thomas SD, Fallone BG. Implications of tissue magnetic susceptibility-related distortion on the rotating magnet in an MR-linac design. *Med Phys* 2010;37:1714–21. doi:10.1118/1.3355856.
 - [44] Lundman JA, Bylund M, Garpebring A, Thellenberg Karlsson C, Nyholm T. Patient-induced susceptibility effects simulation in magnetic resonance imaging. *Phys Imaging Radiat Oncol* 2017;1:41–5. doi:10.1016/j.phro.2017.02.004.
 - [45] Seibert TM, White NS, Kim GY, Moiseenko V, McDonald CR, Farid N, et al. Distortion inherent to magnetic resonance imaging can lead to geometric miss in radiosurgery planning. *Pract Radiat Oncol* 2016;6:e319–28. doi:10.1016/j.prro.2016.05.008.
 - [46] McRobbie DW, Moore EA, Graves MJ. *MRI from Picture to Proton*. Cambridge University Press; 2017.
 - [47] Haacke EM, Reichenbach JR. *Susceptibility Weighted Imaging in MRI: Basic Concepts and Clinical Applications*. Wiley-Blackwell; 2014.
 - [48] Lozano AM, Gildenberg PL, Tasker RR. *Textbook of Stereotactic and Functional Neurosurgery, Volume 1*. Springer Science & Business Media; 2009.
 - [49] Benedict SH, Schlesinger DJ, Goetsch SJ, Kavanagh BD. *Stereotactic Radiosurgery and Stereotactic Body Radiation Therapy*. CRC Press; 2014.
 - [50] Camacho CR, Plewes DB, Henkelman RM. Nonsusceptibility artifacts due to metallic objects in MR imaging. *J Magn Reson Imaging* 1995;5:75–88. doi:10.1002/jmri.1880050115.
 - [51] Graf H, Steidle G, Martirosian P, Lauer UA, Schick F. Metal artifacts caused by gradient switching. *Magn Reson Med* 2005;54:231–4. doi:10.1002/mrm.20524.
 - [52] Graf H, Steidle G, Martirosian P, Lauer UA, Schick F. Effects on MRI due to

- altered rf polarization near conductive implants or instruments. *Med Phys* 2006;33:124–7. doi:10.1118/1.2132571.
- [53] Ulin K, Urie MM, Cherlow JM. Results of a multi-institutional benchmark test for cranial CT/MR image registration. *Int J Radiat Oncol Biol Phys* 2010;77:1584–9. doi:10.1016/j.ijrobp.2009.10.017.
- [54] Gurney-Champion OJ, McQuaid D, Dunlop A, Wong KH, Welsh LC, Riddell AM, et al. MRI-based assessment of 3D intrafractional motion of head and neck cancer for radiation therapy. *Int J Radiat Oncol* 2017;100:306–16. doi:10.1016/j.ijrobp.2017.10.016.
- [55] Minniti G, Clarke E, Lanzetta G, Osti M, Trasimeni G, Bozzao A, et al. Stereotactic radiosurgery for brain metastases: analysis of outcome and risk of brain radionecrosis. *Radiat Oncol* 2011;6:48. doi:10.1186/1748-717X-6-48.
- [56] Blonigen BJ, Steinmetz RD, Levin L, Lamba MA, Warnick RE, Breneman JC. Irradiated Volume as a Predictor of Brain Radionecrosis After Linear Accelerator Stereotactic Radiosurgery. *Int J Radiat Oncol Biol Phys* 2010;77:996–1001. doi:10.1016/j.ijrobp.2009.06.006.
- [57] Korytko T, Radivoyevitch T, Colussi V, Wessels BW, Pillai K, Maciunas RJ, et al. 12 Gy gamma knife radiosurgical volume is a predictor for radiation necrosis in non-AVM intracranial tumors. *Int J Radiat Oncol Biol Phys* 2006;64:419–24. doi:10.1016/j.ijrobp.2005.07.980.
- [58] Patel U, Patel A, Cobb C, Benkers T, Vermeulen S. The management of brain necrosis as a result of SRS treatment for intra-cranial tumors. *Transl Cancer Res* 2014;3:373–82. doi:10.21037/2950.
- [59] Noël G, Simon JM, Valery CA, Cornu P, Boissarie G, Hasboun D, et al. Radiosurgery for brain metastasis: Impact of CTV on local control. *Radiother Oncol* 2003;68:15–21. doi:10.1016/S0167-8140(03)00207-X.
- [60] Ma L, Sahgal A, Larson DA, Pinnaduwa D, Fogh S, Barani I, et al. Impact of millimeter-level margins on peripheral normal brain sparing for gamma knife radiosurgery. *Int J Radiat Oncol Biol Phys* 2014;89:206–13. doi:10.1016/j.ijrobp.2014.01.011.

- [61] Kirkpatrick JP, Wang Z, Sampson JH, McSherry F, Herndon JE, Allen KJ, et al. Defining the optimal planning target volume in image-guided stereotactic radiosurgery of brain metastases: Results of a randomized trial. *Int J Radiat Oncol Biol Phys* 2015;91:100–8. doi:10.1016/j.ijrobp.2014.09.004.
- [62] Choi CYH, Chang SD, Gibbs IC, Adler JR, Harsh IV GR, Lieberman RE, et al. Stereotactic radiosurgery of the postoperative resection cavity for brain metastases: Prospective evaluation of target margin on tumor control. *Int J Radiat Oncol Biol Phys* 2012;84:336–42. doi:10.1016/j.ijrobp.2011.12.009.
- [63] Minniti G, Scaringi C, Paolini S, Lanzetta G, Romano A, Cicone F, et al. Single-fraction versus multifraction (3×9 gy) stereotactic radiosurgery for large (>2 cm) brain metastases: A comparative analysis of local control and risk of radiation-induced brain necrosis. *Int J Radiat Oncol Biol Phys* 2016;95:1142–8. doi:10.1016/j.ijrobp.2016.03.013.
- [64] Bloch F, Hansen WW, Packard M. The Nuclear Induction Experiment. *Phys Rev* 1946;70:474–85. doi:10.1103/PhysRev.70.474.
- [65] Purcell EM, Torrey HC, Pound R V. Resonance Absorption by Nuclear Magnetic Moments in a Solid. *Phys Rev* 1946;69:37–8. doi:10.1103/PhysRev.69.37.
- [66] Ai T, Morelli JN, Hu X, Hao D, Goerner FL, Ager B, et al. A historical overview of magnetic resonance imaging, focusing on technological innovations. *Invest Radiol* 2012;47:725–41. doi:10.1097/RLI.0b013e318272d29f.
- [67] Ernst RR. Nuclear magnetic double resonance with an incoherent radio-frequency field. *J Chem Phys* 1966;45:3845–61. doi:10.1063/1.1727409.
- [68] Damadian R. Tumor Detection by Nuclear Magnetic Resonance. *Science* (80-) 1971;171:1151–3. doi:10.1126/science.171.3976.1151.
- [69] Lauterbur PC. Image formation by induced local interactions: Examples employing nuclear magnetic resonance. *Nature* 1973;242:190–1. doi:10.1038/242190a0.
- [70] Dixon S. Official Diagnostic Imaging Dataset Statistical Release 2016.

- [71] Gossuin Y, Hocq A, Gillis P, Quoc Lam V. Physics of magnetic resonance imaging: From spin to pixel. *J Phys D Appl Phys* 2010;43:213001. doi:10.1088/0022-3727/43/21/213001.
- [72] Brown RW, Cheng Y-CN, Haacke EM, Thompson MR, Venkatesan R. *Magnetic Resonance Imaging: Physical Properties and Sequence Design*. Wiley; 2014.
- [73] Yokoo T, Bae WC, Hamilton G, Karimi A, Borgstede JP, Bowen BC, et al. A quantitative approach to sequence and image weighting. *J Comput Assist Tomogr* 2010;34:317–31. doi:10.1097/RCT.0b013e3181d3449a.
- [74] Bandettini PA, Wong EC, Hinks RS, Tikofsky RS, Hyde JS. Time course EPI of human brain function during task activation. *Magn Reson Med* 1992;25:390–7. doi:10.1002/mrm.1910250220.
- [75] Menon RS. Imaging function in the working brain with fMRI. *Curr Opin Neurobiol* 2001;11:630–6. doi:10.1016/S0959-4388(00)00260-9.
- [76] Meaney JFM, Boyle G, O’Keeffe S. Contrast-enhanced magnetic resonance angiography: Current status, theoretical limitations and future potential. *Radiography* 2007;13:e31–44. doi:10.1016/j.radi.2007.09.002.
- [77] Baldock C, De Deene Y, Doran S, Ibbott G, Jirasek A, Lepage M, et al. Polymer gel dosimetry. *Phys Med Biol* 2010;55:R1–63. doi:10.1088/0031-9155/55/5/R01.
- [78] Ranga A, Agarwal Y, Garg KJ. Gadolinium based contrast agents in current practice: Risks of accumulation and toxicity in patients with normal renal function. *Indian J Radiol Imaging* 2017;27:141–7. doi:10.4103/0971-3026.209212.
- [79] Khawaja AZ, Cassidy DB, Al Shakarchi J, McGrogan DG, Inston NG, Jones RG. Revisiting the risks of MRI with Gadolinium based contrast agents-review of literature and guidelines. *Insights Imaging* 2015;6:553–8. doi:10.1007/s13244-015-0420-2.
- [80] Kanda T, Nakai Y, Oba H, Toyoda K, Kitajima K, Furui S. Gadolinium

- deposition in the brain. *Magn Reson Imaging* 2016;34:1346–50. doi:10.1016/j.mri.2016.08.024.
- [81] Gulani V, Calamante F, Shellock FG, Kanal E, Reeder SB, International Society for Magnetic Resonance in Medicine. Gadolinium deposition in the brain: summary of evidence and recommendations. *Lancet Neurol* 2017;16:564–70. doi:10.1016/S1474-4422(17)30158-8.
- [82] Bihan D Le, Poupon C. Artifacts and pitfalls in diffusion MRI. *J Magn ...* 2006;24:478–88. doi:10.1002/jmri.20683.
- [83] Erasmus LJ, Hurter D, Naudé M, Kritzing HG, Acho S. A Short Overview of MRI Artefacts. *SA J Radiol* 2004;8:13–7. doi:10.1021/jp1019944.
- [84] Smith T, Nayak K. MRI artifacts and correction strategies. *Imaging* 2010;2:445–57.
- [85] Heiland S. From A as in Aliasing to Z as in Zipper: Artifacts in MRI. *Clin Neuroradiol* 2008;18:25–36. doi:10.1007/s00062-008-8003-y.
- [86] Stadler A, Schima W, Ba-Ssalamah A, Kettenbach J, Eisenhuber E. Artifacts in body MR imaging: their appearance and how to eliminate them. *Eur Radiol* 2007;17:1242–55. doi:10.1007/s00330-006-0470-4.
- [87] Deene Y De. Fundamentals of MRI measurements for gel dosimetry. *J Phys Conf Ser* 2004;3:87–114. doi:10.1088/1742-6596/3/1/009.
- [88] Deene Y De. Review of quantitative MRI principles for gel dosimetry. *J Phys Conf Ser* 2009;164:12033. doi:10.1088/1742-6596/164/1/012033.
- [89] Bley TA, Wieben O, Francois CJ, Brittain JH, Reeder SB. Fat and water magnetic resonance imaging. *J Magn Reson Imaging* 2010;31:4–18. doi:10.1002/jmri.21895.
- [90] Deene Y De, Wagter C De. Artefacts in multi-echo T2 imaging for high-precision gel dosimetry: III. Effects of temperature drift during scanning. *Phys Med Biol* 2001;2697.
- [91] Hijnen NM, Elevelt A, Pikkemaat J, Bos C, Bartels LW, Grüll H. The magnetic

- susceptibility effect of gadolinium-based contrast agents on PRFS-based MR thermometry during thermal interventions. *J Ther Ultrasound* 2013;1:8. doi:10.1186/2050-5736-1-8.
- [92] Tanner SF, Finnigan DJ, Khoo VS, Mayles P, Dearnaley DP, Leach MO. Radiotherapy planning of the pelvis using distortion corrected MR images: the removal of system distortions. *Phys Med Biol* 2000;45:2117–32. doi:10.1088/0031-9155/45/8/305.
- [93] Jovicich J, Czanner S, Greve D, Haley E, van der Kouwe A, Gollub R, et al. Reliability in multi-site structural MRI studies: effects of gradient non-linearity correction on phantom and human data. *Neuroimage* 2006;30:436–43. doi:10.1016/j.neuroimage.2005.09.046.
- [94] Stanescu T, Jans HS, Wachowicz K, Fallone BG. Investigation of a 3D system distortion correction method for MR images. *J Appl Clin Med Phys* 2010;11.
- [95] Torfeh T, Hammoud R, McGarry M, Al-Hammadi N, Perkins G. Development and validation of a novel large field of view phantom and a software module for the quality assurance of geometric distortion in magnetic resonance imaging. *Magn Reson Imaging* 2015;33:939–49. doi:10.1016/j.mri.2015.04.003.
- [96] Walker A, Liney G, Holloway L, Dowling J, Rivest-Henault D, Metcalfe P. Continuous table acquisition MRI for radiotherapy treatment planning: Distortion assessment with a new extended 3D volumetric phantom. *Med Phys* 2015;42:1982. doi:10.1118/1.4915920.
- [97] Cusack R, Papadakis N. New robust 3-D phase unwrapping algorithms: Application to magnetic field mapping and undistorting echoplanar images. *Neuroimage* 2002;16:754–64. doi:10.1006/nimg.2002.1092.
- [98] Cusack R, Brett M, Osswald K. An Evaluation of the Use of Magnetic Field Maps to Undistort Echo-Planar Images. *Neuroimage* 2003;18:127–42. doi:10.1006/nimg.2002.1281.
- [99] Jenkinson M. Fast, automated, N-dimensional phase-unwrapping algorithm. *Magn Reson Med* 2003;49:193–7. doi:10.1002/mrm.10354.

- [100] Goldstein RM, Zebker HA, Werner CL. Satellite radar interferometry: Two-dimensional phase unwrapping. *Radio Sci* 1988;23:713–20. doi:10.1029/RS023i004p00713.
- [101] Kaplan ST, Ulrych TJ. Phase Unwrapping: A Review of Methods and a Novel Technique. *Let It Flow – 2007 CSPG CSEG Conv* 2007:534–7.
- [102] Mario Costantini T. A novel phase unwrapping method based on network programming. *IEEE Trans Geosci Remote Sens* 1998;36:813–21. doi:10.1109/36.673674.
- [103] Owringi AM, Greer PB, Glide-Hurst CK. MRI-only treatment planning: benefits and challenges. *Phys Med Biol* 2018;63:05TR01. doi:10.1088/1361-6560/aaaca4.
- [104] De Salles AAF, Gorgulho AA, Pereira JLB, McLaughlin N. Intracranial stereotactic radiosurgery: concepts and techniques. *Neurosurg Clin N Am* 2013;24:491–8. doi:10.1016/j.nec.2013.07.001.
- [105] Chao ST, De Salles A, Hayashi M, Levivier M, Ma L, Martinez R, et al. Stereotactic Radiosurgery in the Management of Limited (1-4) Brain Metastases: Systematic Review and International Stereotactic Radiosurgery Society Practice Guideline. *Neurosurgery* 2017. doi:10.1093/neuros/nyx522.
- [106] Yamamoto M, Serizawa T, Shuto T, Akabane A, Higuchi Y, Kawagishi J, et al. Stereotactic radiosurgery for patients with multiple brain metastases (JLGK0901): a multi-institutional prospective observational study. *Lancet Oncol* 2014;15:387–95. doi:10.1016/S1470-2045(14)70061-0.
- [107] Yamamoto M, Ide M, Nishio S, Urakawa Y. Gamma Knife radiosurgery for numerous brain metastases: is this a safe treatment? *Int J Radiat Oncol* 2002;53:1279–83. doi:10.1016/S0360-3016(02)02855-9.
- [108] Chin LS, Regine WF, editors. *Principles and Practice of Stereotactic Radiosurgery*. New York, NY: Springer New York; 2008. doi:10.1007/978-0-387-71070-9.
- [109] Leksell L. The stereotaxic method and radiosurgery of the brain. *Acta Chir Scand*

- 1951;102:316–9. doi:10.1002/14651858.CD002091.pub2.Interventions.
- [110] Solberg TD, Medin PM. Quality and safety in stereotactic radiosurgery and stereotactic body radiation therapy: can more be done? *J Radiosurgery SBRT* 2011;1:13–9.
 - [111] Larsson B, Lidén K, Sarby B. Irradiation of small structures through the intact skull. *Acta Radiol Ther Phys Biol* 1974;13:512–34.
 - [112] Friedman WA, Bova FJ. The University of Florida radiosurgery system. *Surg Neurol* 1989;32:334–42.
 - [113] Podgorsak EB, Olivier A, Pla M, Lefebvre PY, Hazel J. Dynamic stereotactic radiosurgery. *Int J Radiat Oncol Biol Phys* 1988;14:115–26.
 - [114] Lutz W, Winston KR, Maleki N. A system for stereotactic radiosurgery with a linear accelerator. *Int J Radiat Oncol Biol Phys* 1988;14:373–81.
 - [115] Hartmann GH, Schlegel W, Sturm V, Kober B, Pastyr O, Lorenz WJ. Cerebral radiation surgery using moving field irradiation at a linear accelerator facility. *Int J Radiat Oncol Biol Phys* 1985;11:1185–92.
 - [116] Betti OO, Derechinsky VE. Hyperselective Encephalic Irradiation with Linear Accelerator. In: Gybels J, Hitchcock ER, Ostertag C, Rossi GF, Siegfried J, Szikla G, editors. *Adv. Stereotact. Funct. Neurosurg.* 6, Vienna: Springer Vienna; 1984, p. 385–90.
 - [117] Colombo F, Benedetti A, Pozza F, Avanzo RC, Marchetti C, Chierego G, et al. External stereotactic irradiation by linear accelerator. *Neurosurgery* 1985;16:154–60.
 - [118] Andrews DW, Silverman CL, Glass J, Downes B, Riley RJ, Corn BW, et al. Preservation of cranial nerve function after treatment of acoustic neurinomas with fractionated stereotactic radiotherapy. Preliminary observations in 26 patients. *Stereotact Funct Neurosurg* 1995;64:165–82. doi:10.1159/000098746.
 - [119] Pollock BE, Lunsford LD. A call to define stereotactic radiosurgery. *Neurosurgery* 2004;55:1371–3.

- [120] Mehta VK, Le Q-T, Chang SD, Chenery S, Adler JR. Image Guided Stereotactic Radiosurgery for Lesions in Proximity to the Anterior Visual Pathways: A Preliminary Report. *Technol Cancer Res Treat* 2002;1:173–9. doi:10.1177/153303460200100302.
- [121] Ishihara H, Saito K, Nishizaki T, Kajiwara K, Nomura S, Yoshikawa K, et al. CyberKnife radiosurgery for vestibular schwannoma. *Minim Invasive Neurosurg* 2004;47:290–3. doi:10.1055/s-2004-830095.
- [122] Chang SD, Murphy M, Geis P, Martin DP, Hancock SL, Doty JR, et al. Clinical experience with image-guided robotic radiosurgery (the Cyberknife) in the treatment of brain and spinal cord tumors. *Neurol Med Chir (Tokyo)* 1998;38:780–3.
- [123] King CR, Lehmann J, Adler JR, Hai J. CyberKnife radiotherapy for localized prostate cancer: Rationale and technical feasibility. *Technol Cancer Res Treat* 2003;2:25–9. doi:10.1177/153303460300200104.
- [124] Whyte RI, Crownover R, Murphy MJ, Martin DP, Rice TW, DeCamp MM, et al. Stereotactic radiosurgery for lung tumors: preliminary report of a phase I trial. *Ann Thorac Surg* 2003;75:1097–101.
- [125] Gerszten PC, Welch WC. Cyberknife radiosurgery for metastatic spine tumors. *Neurosurg Clin N Am* 2004;15:491–501. doi:10.1016/j.nec.2004.04.013.
- [126] Sahgal A, Ruschin M, Ma L, Verbakel W, Larson D, Brown PD. Stereotactic radiosurgery alone for multiple brain metastases? A review of clinical and technical issues. *Neuro Oncol* 2017;19:ii2–ii15. doi:10.1093/neuonc/nox001.
- [127] Halasz LM, Uno H, Hughes M, D’Amico T, Dexter EU, Edge SB, et al. Comparative effectiveness of stereotactic radiosurgery versus whole-brain radiation therapy for patients with brain metastases from breast or non–small cell lung cancer. *Cancer* 2016;122:2091–100. doi:10.1002/cncr.30009.
- [128] Monaco EA, Grandhi R, Niranjana A, Lunsford LD. The past, present and future of Gamma Knife radiosurgery for brain tumors: The Pittsburgh experience. *Expert Rev Neurother* 2012;12:437–45. doi:10.1586/ern.12.16.

- [129] Bhatnagar JP, Novotny J, Niranjana A, Kondziolka D, Flickinger J, Lunsford D, et al. First year experience with newly developed Leksell Gamma Knife Perfexion. *J Med Phys* 2009;34:141–8. doi:10.4103/0971-6203.54848.
- [130] Lindquist C, Paddick I. The Leksell Gamma Knife Perfexion and comparisons with its predecessors. *Neurosurgery* 2007;61:130–40. doi:10.1227/01.neu.0000289726.35330.8a.
- [131] Pappas EPP, Moutsatsos A, Pantelis E, Zoros E, Georgiou E, Torrens M, et al. On the development of a comprehensive MC simulation model for the Gamma Knife Perfexion radiosurgery unit. *Phys Med Biol* 2016;61:1182–203. doi:10.1088/0031-9155/61/3/1182.
- [132] Novotny J, Bhatnagar JP, Quader MA, Bednarz G, Lunsford LD, Huq MS. Measurement of relative output factors for the 8 and 4 mm collimators of Leksell Gamma Knife Perfexion by film dosimetry. *Med Phys* 2009;36:1768–74. doi:10.1118/1.3113904.
- [133] Elekta AB. A new TMR dose algorithm in Leksell GammaPlan ®. White Paper 2011:1–28.
- [134] Pipek J, Novotný J, Kozubíková P. A modular Geant4 model of Leksell Gamma Knife Perfexion™. *Phys Med Biol* 2014;59:7609–23. doi:10.1088/0031-9155/59/24/7609.
- [135] Karam SD, Tai A, Strohl A, Steehler MK, Rashid A, Gagnon G, et al. Frameless Fractionated Stereotactic Radiosurgery for Vestibular Schwannomas: A Single-Institution Experience. *Front Oncol* 2013;3. doi:10.3389/fonc.2013.00121.
- [136] Rojas-Villabona A, Miszkiewicz K, Kitchen N, Jäger R, Paddick I. Evaluation of the stability of the stereotactic Leksell Frame G in Gamma Knife radiosurgery. *J Appl Clin Med Phys* 2016;17:75–89. doi:10.1120/jacmp.v17i3.5944.
- [137] Park JH, Han JH, Kim CY, Oh CW, Kim DG, Suh TS, et al. Effect of fiducial marker defects on stereotactic target localization in the Leksell stereotactic system. *Med Biol Eng Comput* 2011;49:775–82. doi:10.1007/s11517-011-0773-8.

- [138] McTyre E, Helis CA, Farris M, Wilkins L, Sloan D, Hinson WH, et al. Emerging Indications for Fractionated Gamma Knife Radiosurgery. *Neurosurgery* 2016;80:210–6. doi:10.1227/NEU.0000000000001227.
- [139] Stieler F, Wenz F, Abo-Madyan Y, Schweizer B, Polednik M, Herskind C, et al. Adaptive fractionated stereotactic Gamma Knife radiotherapy of meningioma using integrated stereotactic cone-beam-CT and adaptive re-planning (a-gkFSRT). *Strahlentherapie Und Onkol* 2016;192:815–9. doi:10.1007/s00066-016-1008-6.
- [140] Li W, Cho Y Bin, Ansell S, Laperriere N, Ménard C, Millar BA, et al. The Use of Cone Beam Computed Tomography for Image Guided Gamma Knife Stereotactic Radiosurgery: Initial Clinical Evaluation. *Int J Radiat Oncol Biol Phys* 2016;96:214–20. doi:10.1016/j.ijrobp.2016.04.011.
- [141] Aldahlawi I, Prasad D, Podgorsak MB. Evaluation of stability of stereotactic space defined by cone-beam CT for the Leksell Gamma Knife Icon. *J Appl Clin Med Phys* 2017;18:67–72. doi:10.1002/acm2.12073.
- [142] Elekta AB. The Convolution algorithm in Leksell GammaPlan ® 10. White Pap 2011:1–8.
- [143] Zoros E, Moutsatsos A, Pappas EP, Georgiou E, Kollias G, Karaiskos P, et al. Monte Carlo and experimental determination of correction factors for gamma knife perfexion small field dosimetry measurements. *Phys Med Biol* 2017;62:7532–55. doi:10.1088/1361-6560/aa8590.
- [144] Watanabe Y, Han E. Image registration accuracy of GammaPlan: a phantom study. *J Neurosurg* 2008;109 Suppl:21–4. doi:10.3171/JNS/2008/109/12/S5.
- [145] Moon W-J, Roh HG, Chung EC. Detailed MR imaging anatomy of the cisternal segments of the glossopharyngeal, vagus, and spinal accessory nerves in the posterior fossa: the use of 3D balanced fast-field echo MR imaging. *AJNR Am J Neuroradiol* 2009;30:1116–20. doi:10.3174/ajnr.A1525.
- [146] Aydın H, Altın E, Dilli A, Sipahioğlu S, Hekimoğlu B. Evaluation of jugular foramen nerves by using b-FFE, T2-weighted DRIVE, T2-weighted FSE and post-contrast T1-weighted MRI sequences. *Diagn Interv Radiol* 2011;17:3–9.

doi:10.4261/1305-3825.DIR.2744-09.3.

- [147] Jursinic PA, Rickert K, Gennarelli TA, Schultz CJ. Effect of image uncertainty on the dosimetry of trigeminal neuralgia irradiation. *Int J Radiat Oncol Biol Phys* 2005;62:1559–67. doi:10.1016/j.ijrobp.2005.01.059.
- [148] Gunter JL, Bernstein MA, Borowski BJ, Ward CP, Britson PJ, Felmlee JP, et al. Measurement of MRI scanner performance with the ADNI phantom. *Med Phys* 2009;36:2193–205. doi:10.1118/1.3116776.
- [149] Tadic T, Jaffray DA, Stanescu T. Harmonic analysis for the characterization and correction of geometric distortion in MRI. *Med Phys* 2014;41:112303. doi:10.1118/1.4898582.
- [150] Tavares WM, Tustumi F, da Costa Leite C, Fernel Gamarra L, Amaro E, Teixeira MJ, et al. An image correction protocol to reduce distortion for 3-T stereotactic MRI. *Neurosurgery* 2014;74:121–7. doi:10.1227/NEU.0000000000000178.
- [151] Wang D, Doddrell D, Cowin G. A novel phantom and method for comprehensive 3-dimensional measurement and correction of geometric distortion in magnetic resonance imaging. *Magn Reson Imaging* 2004;22:529–42. doi:10.1016/j.mri.2004.01.008.
- [152] Mack A, Wolff R, Scheib S, Rieker M, Weltz D, Mack G, et al. Analyzing 3-tesla magnetic resonance imaging units for implementation in radiosurgery. *J Neurosurg* 2005;102 Suppl:158–64.
- [153] Zhang B, MacFadden D, Damyanovich AZ, Rieker M, Stainsby J, Bernstein M, et al. Development of a geometrically accurate imaging protocol at 3 tesla MRI for stereotactic radiosurgery treatment planning. *Phys Med Biol* 2010;55:6601–15. doi:10.1088/0031-9155/55/22/002.
- [154] Yu C, Petrovich Z, Apuzzo ML, Luxton G. An image fusion study of the geometric accuracy of magnetic resonance imaging with the Leksell stereotactic localization system. *J Appl Clin Med Phys* 2001;2:42–50. doi:10.1120/1.1327416.
- [155] Régis J, Tamura M, Guillot C, Yomo S, Muraciolle X, Nagaje M, et al.

- Radiosurgery with the world's first fully robotized Leksell Gamma Knife PerfeXion in clinical use: a 200-patient prospective, randomized, controlled comparison with the Gamma Knife 4C. *Neurosurgery* 2009;64:346-55-6. doi:10.1227/01.NEU.0000337578.00814.75.
- [156] Bolsi A, Fogliata A, Cozzi L. Radiotherapy of small intracranial tumours with different advanced techniques using photon and proton beams: a treatment planning study. *Radiother Oncol* 2003;68:1–14.
- [157] Narayanasamy G, Stathakis S, Gutierrez AN, Pappas E, Crownover R, Floyd JR, et al. A Systematic Analysis of 2 Monoisocentric Techniques for the Treatment of Multiple Brain Metastases. *Technol Cancer Res Treat* 2016. doi:10.1177/1533034616666998.
- [158] Schell MC, Bova FJ, Larson DA, Leavitt DD, Lutz WR, Podgorsak EB, et al. Report of Radiation Therapy Committee Task Group 42 AAPM Report No 54: Stereotactic Radiosurgery. 1995.
- [159] Heck B, Jess-Hempfen A, Kreiner HJ, Schöpgens H, Mack A. Accuracy and stability of positioning in radiosurgery: long-term results of the Gamma Knife system. *Med Phys* 2007;34:1487–95.
- [160] Ertl A, Saringer W, Heimberger K, Kindl P. Quality assurance for the Leksell gamma unit: considering magnetic resonance image-distortion and delineation failure in the targeting of the internal auditory canal. *Med Phys* 1999;26:166–70.
- [161] Mack A, Mack G, Scheib S, Czempel H, Kreiner HJ, Lomax NJ, et al. Quality Assurance in Stereotactic Radiosurgery/Radiotherapy according to DIN 6875-1. *Stereotact Funct Neurosurg* 2005;82:235–43. doi:10.1159/000083175.
- [162] Price RG, Kadbi M, Kim J, Balter J, Chetty IJ, Glide-Hurst CK. Technical Note: Characterization and correction of gradient nonlinearity induced distortion on a 1.0 T open bore MR-SIM. *Med Phys* 2015;42:5955–60. doi:10.1118/1.4930245.
- [163] Huang KC, Cao Y, Baharom U, Balter JM. Phantom-based characterization of distortion on a magnetic resonance imaging simulator for radiation oncology. *Phys Med Biol* 2016;61:774–90. doi:10.1088/0031-9155/61/2/774.

- [164] Poetker DM, Jursinic PA, Runge-Samuelson CL, Wackym PA. Distortion of magnetic resonance images used in gamma knife radiosurgery treatment planning: implications for acoustic neuroma outcomes. *Otol Neurotol* 2005;26:1220–8.
- [165] Chen CC, Wan YL, Wai YY, Liu HL. Quality assurance of clinical MRI scanners using ACR MRI phantom: Preliminary results. *J Digit Imaging* 2004;17:279–84. doi:10.1007/s10278-004-1023-5.
- [166] Ihalainen TM, Lönnroth NT, Peltonen JI, Uusi-Simola JK, Timonen MH, Kuusela LJ, et al. MRI quality assurance using the ACR phantom in a multi-unit imaging center. *Acta Oncol (Madr)* 2011;50:966–72. doi:10.3109/0284186X.2011.582515.
- [167] Crijns SPM, Bakker CJG, Seevinck PR, de Leeuw H, Lagendijk JJW, Raaymakers BW. Towards inherently distortion-free MR images for image-guided radiotherapy on an MRI accelerator. *Phys Med Biol* 2012;57:1349–58. doi:10.1088/0031-9155/57/5/1349.
- [168] Weisskoff RM, Kühne S. MRI susceptometry: Image-based measurement of absolute susceptibility of MR contrast agents and human blood. *Magn Reson Med* 1992;24:375–83. doi:10.1002/mrm.1910240219.
- [169] Fan X, Medved M, Karczmar GS, Yang C, Foxley S, Arkani S, et al. Diagnosis of suspicious breast lesions using an empirical mathematical model for dynamic contrast-enhanced MRI. *Magn Reson Imaging* 2007;25:593–603. doi:10.1016/j.mri.2006.10.011.
- [170] De Rochefort L, Nguyen T, Brown R, Spincemaille P, Choi G, Weinsaft J, et al. In vivo quantification of contrast agent concentration using the induced magnetic field for time-resolved arterial input function measurement with MRI. *Med Phys* 2008;35:5328–39. doi:10.1118/1.3002309.
- [171] Jackson EF, Bronskill MJ, Drost DJ, Och J, Sobol WT, Clarke GD. AAPM Report No. 100 Acceptance Testing and Quality Assurance Procedures for Magnetic Resonance Imaging Facilities Report of MR Subcommittee Task Group I. 2010.

- [172] Lind E, Knutsson L, Kämpe R, Ståhlberg F, Wirestam R. Assessment of MRI contrast agent concentration by quantitative susceptibility mapping (QSM): application to estimation of cerebral blood volume during steady state. *Magn Reson Mater Physics, Biol Med* 2017;30:555–66. doi:10.1007/s10334-017-0637-9.
- [173] Pappas EP, Dellios D, Seimenis I, Moutsatsos A, Georgiou E, Karaiskos P. Review and comparison of geometric distortion correction schemes in MR images used in stereotactic radiosurgery applications. *J Phys Conf Ser* 2017;931:12031. doi:10.1088/1742-6596/931/1/012031.
- [174] Audet C, Poffenbarger BA, Chang P, Jackson PS, Lundahl RE, Ryu SI, et al. Evaluation of volumetric modulated arc therapy for cranial radiosurgery using multiple noncoplanar arcs. *Med Phys* 2011;38:5863–72. doi:10.1118/1.3641874.
- [175] Iwai Y, Ozawa S, Ageishi T, Pellegrini R, Yoda K. Feasibility of single-isocenter, multi-arc non-coplanar volumetric modulated arc therapy for multiple brain tumors using a linear accelerator with a 160-leaf multileaf collimator: A phantom study. *J Radiat Res* 2014;55:1015–20. doi:10.1093/jrr/rru042.
- [176] Singh VP, Kansai S, Vaishya S, Julka PK, Mehta VS. Early complications following gamma knife radiosurgery for intracranial meningiomas. *J Neurosurg* 2000;93 Suppl 3:57–61. doi:10.3171/jns.2000.93.supplement.
- [177] Kutcher GJ, Coia L, Gillin M, Hanson WF, Leibel S, Morton RJ, et al. Comprehensive QA for radiation oncology: report of AAPM Radiation Therapy Committee Task Group 40. *Med Phys* 1994;21:581–618. doi:10.1118/1.597316.
- [178] McDonald D, Schuler J, Takacs I, Peng J, Jenrette J, Vanek K. Comparison of radiation dose spillage from the Gamma Knife Perfexion with that from volumetric modulated arc radiosurgery during treatment of multiple brain metastases in a single fraction. *J Neurosurg* 2014;121:51–9. doi:10.3171/2014.7.GKS141358.
- [179] Janke A, Zhao H, Cowin GJ, Galloway GJ, Doddrell DM. Use of spherical harmonic deconvolution methods to compensate for nonlinear gradient effects on MRI images. *Magn Reson Med* 2004;52:115–22. doi:10.1002/mrm.20122.

- [180] Caramanos Z, Fonov VS, Francis SJ, Narayanan S, Pike GB, Collins DL, et al. Gradient distortions in MRI: Characterizing and correcting for their effects on SIENA-generated measures of brain volume change. *Neuroimage* 2010;49:1601–11. doi:10.1016/j.neuroimage.2009.08.008.
- [181] Maikusa N, Yamashita F, Tanaka K, Abe O, Kawaguchi A, Kabasawa H, et al. Improved volumetric measurement of brain structure with a distortion correction procedure using an ADNI phantom. *Med Phys* 2013;40:62303. doi:10.1118/1.4801913.
- [182] Sumanaweera TS, Adler JR, Napel S, Glover GH. Characterization of spatial distortion in magnetic resonance imaging and its implications for stereotactic surgery. *Neurosurgery* 1994;35:696-703-4.
- [183] Bond JE, Smith V, Yue NJ, Knisely JPS. Comparison of an image registration technique based on normalized mutual information with a standard method utilizing implanted markers in the staged radiosurgical treatment of large arteriovenous malformations. *Int J Radiat Oncol Biol Phys* 2003;57:1150–8. doi:10.1016/S0360-3016(03)01568-2.
- [184] van den Elsen PA, Pol E-JD, Viergever MA. Medical image matching-a review with classification. *IEEE Eng Med Biol Mag* 1993;12:26–39. doi:10.1109/51.195938.

List of Figures

Figure 1-1: Illustration of the Zeeman effect for a proton in presence of external magnetic field B_0 . Adopted from [71].	32
Figure 1-2: (a) System at the equilibrium state. Magnetization is aligned with B_0 . (b) A B_1 field is applied on x' -axis in the rotating frame. Magnetization rotates around B_1 . (c) B_1 field is disrupted at a specific time to result in a flip angle of 90° . .34	
Figure 1-3: Graphical illustration of the exponential increase of the longitudinal Magnetization with T_1 characteristic time. Precession of isochromats is also shown.	36
Figure 1-4: Graphical illustration of the T_2 relaxation time. Exponential reduction of the transverse Magnetization, M_{xy} , at a rate of $1/T_2$ (continuous line). In fact, the reduction will take place at a relaxation rate of $1/T_2^*$ (dashed line) due to local magnetic field inhomogeneities.	37
Figure 1-5: Graphical illustration of selective excitation of a slice transversal to the z -axis. Figure adopted from [radiologycafe.com educational site].....	38
Figure 1-6: Graphical illustration of the phase encoding (left) and frequency encoding (right) principles by applying gradient magnetic fields on x and y axes, respectively. Figure adopted from [71]......	40
Figure 1-7: Excitation pulses, inversion pulses and gradient magnetic fields of some of the most common sequences in MR imaging, (a) Gradient Echo, (b) Spin Echo, (c) FLASH, (d) FSE and (e) EPI. Figure adopted from [71].	43
Figure 2-1: Deviation from the assumed gradient field linearity will result in image distortion. (A) Solid line represents the actual gradient field, while the dashed line corresponds to the assumed linear one. A voxel lying at the actual r_0 location will be imaged at the distorted r_0' location. (B) The gradient field	

polarity is reversed (decreasing with distance r from the isocenter). This change did not affect the distorted space. Figure is adopted from [27].49

Figure 2-2: (A) The static magnetic field B_0 vector is not homogeneous at the edges of the imaged space. The dashed line represents the assumed homogeneous B_0 , while the solid line corresponds to the actual inhomogeneous B_0' field. (B) The inhomogeneous field is summed with the linear gradient field, applied for spatial encoding. A voxel lying at the actual r_0 location will be imaged at the distorted r_0' location, with $r_0' < r_0$. (C) The gradient field polarity is reversed (increasing with distance r from MR isocenter). This change will directly affect the sign of the distortion in the acquired image, as $r_0' > r_0$. Figure is adopted from [27].50

Figure 2-3: Cranial MRI scan of a patient with mascara on their eyelids. The susceptibility of mascara resulted in the front half of the globes appearing obscured. Figure adapted from [“MRI Artifacts: Mechanism and Control” by C. Ruan].....53

Figure 2-4: Susceptibility-related distortion depends on the orientation between frequency encoding direction and materials interface. (left) Interface is perpendicular to the frequency encoding direction. The actual shape of phantom containers (depicted by red the red contour) is deformed due to the difference in the magnetic susceptibility. (right) The material interface is parallel to the frequency encoding direction. The actual shapes match the ones identified in the image. Figure adopted from [87,88].54

Figure 2-5: NMR spectrum for a mixture of water and fat placed at an external magnetic field of 3.0T. The main fat peak corresponds to a resonance frequency for fat of 420 Hz lower than that of water. Asterisks denote the secondary fat resonance peaks, some of which lie very close to the water resonance peak. Figure adopted from [89].55

Figure 2-6: 1-D phase unwrapping. (a) Actual phase distribution. (b) Wrapped phase values. (c) Wrapped phase values including noise. (d) The noise resulted in errors in the unwrapping procedure. Consequently, the unwrapped phase

distribution differs by 2π rad from the actual one. Furthermore, the unwrapping errors propagates to all subsequent points. Figure adopted from [97].....64

Figure 2-7: Indicative results of the 3D guided phase unwrapping algorithm. (a) Wrapped phase difference distribution for a large homogeneous cylindrical phantom and a 3.0T MR scanner. Several wrapping points are observed. An area of increased noise is detected at the top. (b) Corresponding unwrapped phase difference using the algorithm developed for the purposes of this thesis. Unwrapping errors are induced in the noisy area but did not propagate to the rest of the image.....67

Figure 3-1: Examples of the superior soft contrast in MR compared to CT for brain tumor delineation. (a, c) Axial slices of a patient with multiple brain metastases. (b, d) Same slices acquired with MRI, following administration of contrast agent.....70

Figure 3-2: (a) A graphic illustration of the actual geometry of the Perfexion irradiation unit. Each sector accommodates 24 ^{60}Co sources, which are arranged in five rings and can be independently moved upon a conical surface to align with the channels of any of the three available collimator sizes. (b)–(d) Pictorial description of the comprehensive Perfexion simulation model developed for Monte Carlo dosimetric calculations. (b) A cross-sectional view (plane xz) of the simulation model geometry for the case that all sources are aligned with the 16 mm collimation channels. The following parts are distinguishable: (i) the source bushing (yellow), (ii) the primary collimator consisting mainly of Pb (cyan), (iii) the secondary collimation system consisting mainly of tungsten (dark blue) and (iv) the spherical phantom used to obtain dosimetry results (red). (c) A ^{60}Co source is accurately aligned with the collimation channel of the 4 mm collimator. The ^{60}Co pellets are depicted in magenta. (d) The same source has been moved and positioned to deliver a 16 mm shot. A small geometric shift and tilt is induced between the source's central axis and the collimation channel. In sub-figures (c) and (d), note that the capsule (light blue) interleaves the space between the source and the collimation channel, while this is not the case for the bushing part.....74

Figure 3-3: (a) The frame base of the Leksell stereotactic frame model G. (b) The MR indicator box. Images taken from [elekta.com].	75
Figure 3-4: All parts comprising the Leksell stereotactic frame model G. The frame base and the MR indicator box are fixed on a distortion detection phantom. .	76
Figure 3-5: The minimally invasive Leksell stereotactic frame is firmly fixed on the patient using the four pins, prior to MR image acquisitions. The MR indicator box should also be fixed (not shown here). Images taken from [Elekta official youtube channel].....	79
Figure 4-1: (a) The developed phantom. (b) The Leksell indicator box mounted on the phantom. (c) The Leksell stereotactic frame model G also fixed on the phantom. (d) The phantom being placed in the head coil used in intracranial MRI scanning for Gamma Knife radiosurgery treatment planning.....	85
Figure 4-2: An indicative axial slice of the performed MR scan series #1 nF (a) and CT scan (b), depicting the high contrast between CPs and acrylic. The N shaped fiducials of the Leksell localization box are also visible. Presented images are not spatially co-registered.	90
Figure 4-3: Distortion vectors for the axial (a),(c),(e) plane close to the phantom and frame base (see Figure 4-1) and the coronal (b),(d),(f) plane of the phantom. Initial points correspond to CT-identified CP locations while terminal points to MRI-averaged ones. Distortion vectors correspond to analysis performed for image series 1-2 nF (a),(b), 3-4 F (c),(d) and 5-6 F (e),(f) (see Table 4-1). For figures (c)-(f), the contour of the frame base is also depicted. All vectors' lengths have been magnified by a factor of 3 to facilitate readability. The MR scanner's coordinate system is adopted. Note that in (c) and (e) frame base is projected on the axial plane as it actually lied at a distance of approximately 15 mm towards negative z axis. The gray dashed lines on figures (b),(d),(f) highlight location of the axial planes shown in figures (a),(c),(e), respectively. The yellow mark on frame base depicts the reference point for distances presented in Figure 4-4.	94

Figure 4-4: Total magnitude of detected CP displacements for three MRI-averaged datasets, image series #1-2 nF, 3-4 F and 7-8 mF. Distortion of 72 CPs is presented against their radial distance from the reference point on the frame base (depicted in figure 3). Although the frame was not fixed in image series #1-2 nF, corresponding data using the same reference point are also included for comparison. Dashed lines correspond to fitted trend lines of the form $y=a/x + b$ to guide the eye.95

Figure 4-5: Coronal slice acquired by employing the 3D T2w b-FFE sequence with (a) and without (b) the frame fixed on the phantom (the one sagittal and the three axial acrylic planes are evident in both images). Fiducials from the indicator box are highlighted using red circles. Red dashed lines have been manually drawn to examine co-linearity between fiducials. Red arrows point to severe deformation of the phantom's external shape close to the frame base.97

Figure 4-6: Snapshot of Leksell GammaPlan v.10 treatment planning system. Post-Gd axial image (left) and sagittal reformat (right) of the derived "average" MRI dataset (top row), along with corresponding CT-angiography images (bottom row) in the brain stem area of the scanned patient. The vertebral arteries lying in the vicinity of the frame base, but still within the treatable area with Perfexion, were contoured (red polygons) at the level of the foramen magnum on the CT series and superimposed to the MRI series.98

Figure 4-7: As in Figure 4-6, but in this case the contoured vessel (part of the superior cerebellar artery) is now lying at a significant distance (more than 15 cm) from the frame base.99

Figure 5-1: (a) The phantom utilized in this study filled with copper sulfate solution. (b) The phantom being MR scanned using the head coil..... 108

Figure 5-2: Overview of the workflow for distortion detection implemented in this study. 109

Figure 5-3: Total geometric distortion detected at all 947 CP locations for the three clinically used imaging protocols. Results are presented against radial distance from the corresponding MR scanner's isocenter. 112

- Figure 5-4: Total distortion maps ($dtotR$) on a sagittal plane at $x=0$ mm for FSPGR BRAVO (left), FSPGR 3DT1w (middle) and T1w MPRAGE (right). 113
- Figure 5-5: Distortion vectors on a sagittal plane at $x=0$ mm for FSPGR BRAVO (left), FSPGR 3DT1w (middle) and T1w MPRAGE (right). Vectors' lengths have been magnified by a factor of three to increase visibility. 114
- Figure 6-1: The distortion detection phantom used in this study. (a) Two cylindrical inserts were fixed on the removable top cap (S side of the phantom) shown on the left. (b) The phantom positioned at scanning orientation with the top mounted on..... 119
- Figure 6-2: Axial slice intersecting the cylindrical inserts of the phantom with frequency encoded direction set on A-P (a),(b),(d),e) and P-A (c),(f) directions. Inserts are filled with saline (no contrast agent) (top row) or 20 Mm of Gd-DTPA (bottom row). (a),(d) Distortion maps derived using the field mapping technique. (b),(c),(e),(f) T1w images of the same slice. Reversing read gradient polarity has no apparent effect on insert position but evidently displaces the contrast agent signal..... 126
- Figure 6-3: Axial slice intersecting the cylindrical inserts of the phantom with frequency encoded direction set on L-R (a),(b),(d),(e) and R-L (c),(f) directions. Inserts are filled with saline (no contrast agent) (top row) or 20 Mm of Gd-DTPA (bottom row). (a),(d) Distortion maps derived using the field mapping technique. (b),(c),(e),(f) T1w images of the same slice. Reversing read gradient polarity has no apparent effect on insert position but evidently displaces the contrast agent signal..... 127
- Figure 6-4: Estimated net centroid offset for both cylindrical inserts as a function of contrast agent concentration. (a) Frequency encoding direction set on the y-axis (P-A and A-P). (b) Frequency encoding direction set on the x-axis (L-R and R-L). Dashed lines were derived by linear fitting of the corresponding data.... 127
- Figure 6-5: Fitted slopes for net centroid offset vs Gd-DTPA concentration. Error bars correspond to the uncertainty of the slopes (at 67% confidence level) as determined by linear regression analysis. 128

Figure 6-6: (a) Field mapping derived distortion map corresponding to an axial slice with two brain metastases (metastases #4 and 5 in Table 6-3). (b) Fused forward (A-P) and reversed (P-A) polarity MR images using the clinically employed MR protocol for SRS treatment planning. Corresponding pixels with different values are depicted in color (green and purple for higher values in forward and reversed images, respectively). The area of the two metastases is depicted magnified in the insert. The red arrow points to the area of the two metastases. (c) Normalized pixel intensity profiles for the two images along the red dashed line that runs parallel to the y-axis..... 130

Figure 6-7: (a) Field mapping derived distortion map corresponding to an axial slice with one brain metastasis (met #10 in Table 6-3. (b) Fused forward (A-P) and reversed (P-A) polarity MR images acquired using the clinically employed MR protocol for SRS treatment planning. Corresponding pixels with different values are depicted in color (green and purple for higher values in forward and reversed images, respectively). The metastasis area is depicted magnified in the insert. The red arrow points to the metastasis location. (c) Normalized pixel intensity profiles for the two images along the red dashed line that runs parallel to the y-axis. 131

Figure 7-1: Calculated DVHs for the original plan (No Offset) as well as for the deliberately mispositioned targets towards the x direction (0.5 up to 3mm Offset) for four representative target sizes..... 137

Figure 7-2: Geometric uncertainty on x, y and z axes resulting in difference greater than 5% in D_{95} value as a function of target diameter. 140

Figure 8-1: Views of the 3D model of the high-resolution distortion detection phantom during the designing stage. 147

Figure 8-2: Pictures of the phantom developed for high resolution residual distortion detection. 147

Figure 8-3: CT (top row) and MR (bottom row) scans of the high-resolution distortion detection phantom developed. Indicative central axial (left) and sagittal (right) slices are presented. 149

Figure 8-4: MR images fused with CT scans of the new phantom for a slice lying at the S side before (left) and after (right) having enabled the vendor-supplied distortion correction routines. 150

Figure 9-1: Print-screen images from the GammaPlan treatment planning system presenting the central axial (left column), sagittal (middle column), and coronal (right column) planes of the radiation-induced polymerization distribution corresponding to the 4mm shot with reference coordinates $(x, y, z) = (100, 100, 100)$ as shown in forward (top row), reverse (middle row), and average images (bottom row). The target contour defined independently in forward, reverse, and average series following registration in the stereotactic space is marked with red, blue, and green, respectively. The prescription isodose, as planned in the forward MR series, is shown in yellow. 156

Figure 9-2: The geometrical uncertainty vector dR_{tot} determined for the 2 series acquired with forward (left) and reverse polarity (middle), as well as for their average series (right). Distortion measurements are presented as a spatial distribution of scaled vectors: the origin of each vector coincides with the reference coordinates of the corresponding shot's CM, whereas its length, denoting the measured distortion magnitude, is scaled to the length of the gray vectors residing on $(x, y, z) = (170, 30, 30)$, which corresponds to a 1.5 mm distortion. For reasons of clarity, the length of the presented vectors was scaled by a factor of 20. 157

Figure 9-3: Print-screen images from the GammaPlan treatment planning system presenting the central axial (left column), sagittal (middle column), and coronal (right column) views of a 1 cm metastasis as shown in forward (top row), reverse (middle row), and average images (bottom row). The target contour defined independently in forward, reverse, and average series following registration in the stereotactic space is marked with red, blue, and green, respectively. The prescription isodose, as planned in the forward MR series, is shown in yellow. 159

Figure 9-4: Geometric uncertainty and underdosage results associated with the forward series in a patient with 19 metastases. (a) The geometric uncertainty vectors,

dR_{tot} , are presented as scaled vectors similarly to those shown in Figure 9-2.
 (b) Target underdosage results were derived from target coverage of the prescription dose in the average images (the center and the diameter of each sphere coincides with the center and diameter of a target metastasis, whereas its color denotes the percentage of underdosage according to the presented color bar). 161

Figure 10-1: Distortion vectors (magnified by a factor of 15 to facilitate readability) for an indicative axial plane of the phantom corresponding to the original (a), as well as the average-image (b) and signal integration (c) corrected images with the read gradient direction set on the y-axis. 168

Figure 10-2: Histograms of the identified distortion for the original and corrected images with the read gradient direction set on y-axis (a) and x-axis (b). 169

List of Tables

Table 2-1: Magnetic susceptibility (volume susceptibility) of various materials or substances found in vivo. Values from [36].	52
Table 4-1: Summary of the MR imaging protocol used in the phantom study.....	86
Table 4-2: Mean and maximum absolute distortion values measured in "average" MRI datasets. R corresponds to the total CP displacement (Euclidean distance)	92
Table 4-3: Mean and maximum absolute distortion values measured in "average" MRI datasets at radial distances up to 50 mm and 70 mm from the center of the Leksell space. R corresponds to the total CP displacement (Euclidean distance).	93
Table 4-4: Uncertainty related to the CP localization algorithm	97
Table 5-1: Protocol parameters of all the performed MR image acquisitions using both scanners included in this study.	110
Table 5-2: Detected total distortion for the three imaging protocols of the GE and SIEMENS scanners included in this study. Percentage of CPs detected with more than 1 mm of absolute distortion (% CPs > 1 mm) is also given.	111
Table 6-1: MR scanning protocol and parameters used in the phantom study.....	121
Table 6-2: Sequence dependent distortion magnitude for all 947 control points, detected using both methods.	124
Table 6-3: Patient study results. For each metastasis, the total centroid offset provided by the reversed polarity technique is presented, along with the distortion detected using the field mapping technique. Net centroid offset in y-axis is deduced by subtracting the detected background distortion from the total centroid offset in y-axis.	129

Table 7-1: Effect of spatial offset towards the x direction on plan quality metrics for five target sizes.	138
Table 8-1: Specific details of MR scanners and imaging parameters used in this study.	148
Table 8-2: Detected total absolute distortion for the three MR scanners included in this study, with and without having enabled the distortion correction scheme. Percentages of CPs detected with more than 1 mm of absolute distortion (% CPs > 1 mm) are also given.	150
Table 9-1: Results (range and mean values) for the geometry uncertainties in x, y, and z axis directions (dx, dy and dz), as well as for the total spatial uncertainties, dR_{tot} , along with resultant percentage dose difference values DD (%). In all MR scans, frequency encoding was performed along the y-axis.....	160
Table 10-1: Statistical analysis for distortion detected for the original and corrected images.	167

Appendix

The 3D phase unwrapping algorithm developed in MATLAB for the purposes of this thesis. It is a guided unwrapping algorithm with the negated magnitude image stack serving as the noise estimator field. The algorithm is based on the work of [97] but was expanded to work in 3D. The negated magnitude image is used as the noise estimator field for guiding the unwrapping direction. Routines for importing the corresponding dicom images and other auxilliary commands are not included.

```
%-----%

%%% 3D guided Phase Unwrapping Algorithm - based on the work of
Cusack and Papadakis (2002), extended to work in 3D.

%%% The negated magnitude is used as the noise estimator field for
guiding the direction of unwrapping

%%% Developed in MATLAB by E P Pappas, National and Kapodistrian
University of Athens

% clear all
% load('unwrapdataDSTE06.mat');
% PhaseMap=angle(ComplexIm_ET1);      % set complex matrix name
% MagnitudeMap=abs(ComplexIm_ET1);    % set complex matrix name
% DTEn=DSTE06;
%---Define initial parameters-----
-----
PhaseMap=PhaseMap_out(:,: ,1:100);
MaskingCube = L_20mM_ET1_Mag(:,: ,1:100); % Mag cube used to determine
the
                                % VOI extraction" mask
NoiseEstimator= -MaskingCube; % negated magnitude as noise estimator
field
step=5;                        % set step for threshold
LowValue = 250;                % set Lowest magnitude Value for
extraction
minVox = 30;                   % Defines the minimum No of voxels that
a
                                % detected VOI must have

% clear PhaseMap_DSTE06

%-----%
-----

[ ~, ~, ~ , ~, Maskall, statsall ] = ...
```

```

MaskingObjectV2( MaskingCube, LowValue,
minVox );

figure, Mont_AsItIs(Maskall,[0 1]); impixelinfo;

PhaseMap(Maskall==0)=NaN;

clear Mag_STE26 MagC_STE36

%-----Determination of unwrapping seed-----
-----

[Objects, num]=bwlabeln(Maskall,26);

figure, Mont_AsItIs(Objects,[0 num]); impixelinfo;

for i=1:num;
    clear s centro bb
    s = regionprops(Objects == i,'Centroid');
    centro = round(s.Centroid);

    bb = zeros(size(NoiseEstimator));

    for m=(centro(2)-30):(centro(2)+30);
        for l=(centro(1)-30):(centro(1)+30);
            for n=(centro(3)-5):(centro(3)+5);
                if n <= size(NoiseEstimator,3) && n >= 1 ...
                    && m <= size(NoiseEstimator,1) && m >= 1 ...
                        && l <= size(NoiseEstimator,2) && l >= 1;

                    bb(m,l,n)=1;
                end
            end
        end
    end

    seedNoise = bb.*NoiseEstimator;

    ind = find(seedNoise == min(seedNoise(:))); % find position of
min noise
    [Yseed{i} Xseed{i} Zseed{i}]=ind2sub(size(seedNoise),ind);

    thres1{i} = seedNoise(Yseed{i}(1),Xseed{i}(1),Zseed{i}(1)); %
initial noise field threshold

end

thres1All = thres1;

thres1val = min(cell2mat(thres1));
clear bb l m n i t ind seedNoise MagnitudeMap statsbig Objectbig s
centro num MaskingCube thres1
%% UNWRAPPING

tic
UnwrapIndex = false(size(PhaseMap)); % binary map for indexing
unwrapped elements

```



```

UnwrappedMap = zeros(size(PhaseMap)); % initial phase unwrapped map

for k = 1:length(Yseed);
    UnwrappedMap(Yseed{k}(1),Xseed{k}(1),Zseed{k}(1))= ...

PhaseMap(Yseed{k}(1),Xseed{k}(1),Zseed{k}(1));

    UnwrapIndex(Yseed{k}(1),Xseed{k}(1),Zseed{k}(1))= 1; % min noise
seeds are considered already unwrapped
end

clear k
itt=0;
nvoxels=numel(PhaseMap); % total number of voxels
h = waitbar(0,'Please wait...','Name','Phase Unwrapping',... %
set up a waitbar
    'CreateCancelBtn','setappdata(gcf,'canceling',1)');
setappdata(h,'canceling',0)
while sum(UnwrapIndex(:))~=nvoxels; % loop until all voxels are
unwrapped
    thres=threslval+itt*step;
    itt=itt+1;
    NewUnwraps=UnwrapIndex; % binary map flagging new unwraps
    waitbar(sum(UnwrapIndex(:))/nvoxels,h,sprintf('Elapsed time:
%3.2f sec Itt: %3.0f out of %3.0f',toc,itt-1,-threslval/step+1))
    if getappdata(h,'canceling') % check if cancel has been pressed
        break
    end
    while sum(NewUnwraps(:))~=0; %loop until there are no new
unwraps
        % locate all recently unwrapped voxels
        clear Yseed Xseed Zseed unwr
        ind=find(NewUnwraps==1);
        [Yseed Xseed Zseed]=ind2sub(size(NewUnwraps),ind);
        clear ind
        counts=sum(NewUnwraps(:)); % number of recently
unwrapped voxels
        NewUnwraps=false(size(PhaseMap)); % reset flag
        for i=1:counts;
            % check all neighbors of recently unwrapped voxels,
            % ignore those exceeding cube dimensions
            if Yseed(i)<size(PhaseMap,1);
                if
NoiseEstimator(Yseed(i)+1,Xseed(i),Zseed(i))<=thres &&
UnwrapIndex(Yseed(i)+1,Xseed(i),Zseed(i))==0 &&
UnwrapIndex(Yseed(i),Xseed(i),Zseed(i))==1;

unwr=unwrap([UnwrappedMap(Yseed(i),Xseed(i),Zseed(i))
PhaseMap(Yseed(i)+1,Xseed(i),Zseed(i))]); % unwrap neighbor1

UnwrappedMap(Yseed(i)+1,Xseed(i),Zseed(i))=unwr(2);
    UnwrapIndex(Yseed(i)+1,Xseed(i),Zseed(i))=1;
% flag voxel as unwrapped
    NewUnwraps(Yseed(i)+1,Xseed(i),Zseed(i))=1;
% flag recently unwrapped voxel
    end
    end

    if Yseed(i)>1;
        if NoiseEstimator(Yseed(i)-
1,Xseed(i),Zseed(i))<=thres && UnwrapIndex(Yseed(i)-

```

```

1,Xseed(i),Zseed(i))==0 &&
UnwrapIndex(Yseed(i),Xseed(i),Zseed(i))==1;

unwr=unwrap([UnwrappedMap(Yseed(i),Xseed(i),Zseed(i))
PhaseMap(Yseed(i)-1,Xseed(i),Zseed(i))]);
UnwrappedMap(Yseed(i)-
1,Xseed(i),Zseed(i))=unwr(2);
UnwrapIndex(Yseed(i)-1,Xseed(i),Zseed(i))=1;
NewUnwraps(Yseed(i)-1,Xseed(i),Zseed(i))=1;
end
end

if Xseed(i)<size(PhaseMap,2);
if
NoiseEstimator(Yseed(i),Xseed(i)+1,Zseed(i))<=thres &&
UnwrapIndex(Yseed(i),Xseed(i)+1,Zseed(i))==0 &&
UnwrapIndex(Yseed(i),Xseed(i),Zseed(i))==1;

unwr=unwrap([UnwrappedMap(Yseed(i),Xseed(i),Zseed(i))
PhaseMap(Yseed(i),Xseed(i)+1,Zseed(i))]);

UnwrappedMap(Yseed(i),Xseed(i)+1,Zseed(i))=unwr(2);
UnwrapIndex(Yseed(i),Xseed(i)+1,Zseed(i))=1;
NewUnwraps(Yseed(i),Xseed(i)+1,Zseed(i))=1;
end
end

if Xseed(i)>1;
if NoiseEstimator(Yseed(i),Xseed(i)-
1,Zseed(i))<=thres && UnwrapIndex(Yseed(i),Xseed(i)-1,Zseed(i))==0 &&
UnwrapIndex(Yseed(i),Xseed(i),Zseed(i))==1;

unwr=unwrap([UnwrappedMap(Yseed(i),Xseed(i),Zseed(i))
PhaseMap(Yseed(i),Xseed(i)-1,Zseed(i))]);
UnwrappedMap(Yseed(i),Xseed(i)-
1,Zseed(i))=unwr(2);
UnwrapIndex(Yseed(i),Xseed(i)-1,Zseed(i))=1;
NewUnwraps(Yseed(i),Xseed(i)-1,Zseed(i))=1;
end
end

if Zseed(i)<size(PhaseMap,3);
if
NoiseEstimator(Yseed(i),Xseed(i),Zseed(i)+1)<=thres &&
UnwrapIndex(Yseed(i),Xseed(i),Zseed(i)+1)==0 &&
UnwrapIndex(Yseed(i),Xseed(i),Zseed(i))==1;

unwr=unwrap([UnwrappedMap(Yseed(i),Xseed(i),Zseed(i))
PhaseMap(Yseed(i),Xseed(i),Zseed(i)+1))]);

UnwrappedMap(Yseed(i),Xseed(i),Zseed(i)+1)=unwr(2);
UnwrapIndex(Yseed(i),Xseed(i),Zseed(i)+1)=1;
NewUnwraps(Yseed(i),Xseed(i),Zseed(i)+1)=1;
end
end

if Zseed(i)>1;
if NoiseEstimator(Yseed(i),Xseed(i),Zseed(i)-
1)<=thres && UnwrapIndex(Yseed(i),Xseed(i),Zseed(i)-1)==0 &&
UnwrapIndex(Yseed(i),Xseed(i),Zseed(i))==1;

```

```

unwr=unwrap([UnwrappedMap(Yseed(i),Xseed(i),Zseed(i))
PhaseMap(Yseed(i),Xseed(i),Zseed(i)-1)]);
                                UnwrappedMap(Yseed(i),Xseed(i),Zseed(i)-
1)=unwr(2);
                                UnwrapIndex(Yseed(i),Xseed(i),Zseed(i)-1)=1;
                                NewUnwraps(Yseed(i),Xseed(i),Zseed(i)-1)=1;
                                end
                                end
                                end
                                end
delete(h)
toc
clear k NewUnwraps Yseed Xseed Zseed ind UnwrapIndex h i cellarr
counts unwr NoiseEstim
% Mont_AsItIs(UnwrappedMap, []);

```